2016

Development of conducting carbon inks for direct writing of soft strain gauges

Reece D. Gately
University of Wollongong

UNIVERSITY
OF WOLLONGONG
AUSTRALIA

DEVELOPMENT OF CONDUCTING CARBON INKS FOR DIRECT WRITING OF SOFT STRAIN GAUGES

Reece D. Gately, IntBSc (Hon.)

Supervisor:
Prof. Marc in het Panhuis

This thesis is presented as required for the conferral of the degree:

PhD in Chemistry

The University of Wollongong
School of Chemistry

August 2016

Declaration

I, Reece D. Gately, IntBSc (Hon.), declare that this thesis submitted in fulfilment of the requirements for the conferral of the degree PhD in Chemistry, from the University of Wollongong, is wholly my own work unless otherwise referenced or acknowledged. This document has not been submitted for qualifications at any other academic institution.

Reece D. Gately, IntBSc (Hon.)
April 20, 2017

Abstract

Soft robotics is a rapidly emerging field, and the demand for intelligent, compliant actuators is on the rise. To this end, a strain gauge that can be 3D printed on a soft substrate is required, to match this ever-evolving field. Conductive carbon materials, such as carbon nanotubes (CNTs) have been previously presented as such a material. In this project, a vapour grown carbon nanofibre (VGCNF): gellan gum (GG) stable dispersion is produced through horn sonication, and is characterised through electrical, mechanical and rheological testing on a dry film, as well as surface morphology. The damaging effects of horn sonolysis is thoroughly investigated, to understand the reduction in properties caused to the production method. A co-dispersant, KetjenBlack (KB, a tradename for carbon black) is also added to further reduce the resistance of the dry films. This dispersion is optimised and evaluated through the same methods, and compared to a VGCNF dispersion. To produce a flexible strain gauge, a custom 3D printer was developed to perform patterned deposition of the dispersion. The dispersion is 3D printed onto a hydrogel substrate (poly-hydroxyethyl methacrylate, p-HEMA) and is found to have a gauge factor (GF) of 1.8 ± 0.2 and 0.76 ± 0.04 for one and two layers of the ink respectively, with a higher degree of repeatability with the two layer device.

This project has attributed to the field of soft robotics through the production of a 3D printed strain gauge that can be easily adapted for various substrates. It has highlighted the damage and filling effects that sonolysis can incur, and how it should be monitored. It also contributes to the general field of 3D printing through the production of a printer that can be used for multiple materials with varying rheological properties.

Acknowledgments

First and foremost I'd like to thank my supervisor, Marc. You've put up with me for almost 6 years of my uni life, both as a lecturer and then as a supervisor, and I don't believe I could have chosen a more suitable supervisor. Your chilled attitude has suited me perfectly, and I truly think I was able to accomplish a lot more with you at the helm. There were certainly times that I was freaking out with one hundred things to do, but you would leave me to sort out what I was able to and always managed to step in when I needed it. I couldn't be happier with you as a supervisor, and I truly hope we are able to work together in the future.

Next I'd like to thank everyone in the Soft Materials Group, both new and old. Whether through friendly chats at the lunch room in B41 regarding the most delicious jaffle we could make, or general science talk, it was always fantastic. When the SMG moved to iC, all the new crew of people we met were just as welcoming, fun, and helpful. Special mention to both Holly Warren and Lloyd James, you two have been fantastic and a heap of fun. I don't even need to say I hope we keep up as friends, since the only option is that we do!

None of this thesis would have been attempted or even considered if it weren't for the support of my family. Both my mother and father have wanted nothing less than this for me, and have always supported me where needed, either financially or emotionally. My brother and sister have always been there to help me through, whether it's listen to me boringly talk about what I did at uni that day, or helping proof read sections of this thesis. I couldn't have done it without them, and wouldn't have completed any of it if it weren't for Mum.

Finally, and most importantly, I'd like to thank my partner, Jayne. She has been through just as much as I have throughout this PhD, and has been my tether to reality. She has always been there to tell me when I'm being an idiot, when I need to take a night off, or when I need to get my ass in to gear. I'd take my work home with me, both the good and bad, and she had to deal with both, which I couldn't be more thankful for. I'm not sure what I'm more sorry about, my rantings when I'm infuriated with something, or my lengthy, detailed discussions about how cool the research that I did that day was. I always saw that point, she, not so much. I would have completely flipped out if it weren't for her, so I thank her for keeping me on track, sane, and smiling.

To all other technical staff that have helped me along the way (Tony, Joanne, Candace, Patricia, the list goes on!) I thank you too, for both science talk and always being around for a good laugh. To the guys in the workshop, thanks for always having a fantastic sense of humour, for putting up with me, and for being so good at what you do!

Contents

List of Publications **i**

List of Figures **v**

List of Tables **xiii**

List of Acronyms **xiii**

1 General Introduction **1**

1.1 Critical Overview 5

1.2 Literature Review 7

1.3 Carbon-Based Fillers 11

1.3.1 Carbon Nanotubes 12

1.3.2 Carbon Nanofibres 13

1.3.3 Graphene 15

1.3.4 Carbon Black 16

1.4 Gellan Gum 19

1.5 Probe Sonication as a dispersion method 21

1.5.1 Material Degradation Due to Probe Ultrasonication 22

1.6 Filling Effects of Sonolysis 23

1.6.1 Approaches for Filling Carbon Nanostructures 25

1.6.2 Recent developments 30

1.6.3 Future Prospects 33

1.7 Additive Manufacturing 33

1.7.1 Pen Writing 34

1.7.2 3D Printing 34
1.8 Strain Gauges 38
1.9 Aims 41

2 Materials and Methods 43

2.1 Sample Prepration 45
2.1.1 Prepration of Gellan Gum solutions 45
2.1.2 Prepration and Sonication of Carbon-Based Dispersions 45
2.1.3 Prepration of Free-standing Films 46
2.2 Direct Writing of the Dispersions 47
2.2.1 Fountain Pen Writing 47
2.2.2 Extrusion Printing 48
2.3 Analysis Methods 49
2.3.1 Dispersion Optimisation through UV-Vis-NIR Spectroscopy 49
2.3.2 Impedance Analysis 50
2.3.3 Mechanical Analysis 50
2.3.4 Rheological Analysis 51
2.3.5 Light Microscopy 52
2.3.6 Scanning Electron Microscopy 52
2.3.7 Transmission Electron Microscopy 52

3 Conducting carbon nanofibre networks: dispersion optimisation, evaporative casting and direct writing 55

3.1 Introduction 59
3.2 Experimental 60
3.2.1 Preparation of dispersions 60
3.2.2 Preparation of free-standing films 61
3.2.3 Direct writing 61
3.2.4 Characterisation techniques 62

3.2.5 Statistical treatment 63
3.3 Results and Discussion 63
3.3.1 Optimisation of dispersions 63
3.3.2 Electrical characteristics of free-standing films 66
3.3.3 Direct writing with a fountain pen 68
3.4 Conclusions 73
3.5 Acknowledgements 74

4 Electrical conductivity, impedance, and percolation behaviour of carbon nanofibre and carbon nanotube containing gellan gum hydrogels 75

4.1 Introduction 79
4.2 Experimental 80
4.2.1 Dispersion Preparation 80
4.2.2 Gel Preparation 81
4.2.3 Characterization 82
4.2.4 Statistical Treatment 82
4.3 Results and Discussion 83
4.3.1 Impedance and Electrical Conductivity of GG Hydrogels . . . 83
4.3.2 Effect of Sonolysis 86
4.3.3 Effect of Increasing Carbon Filler Volume Fraction 89
4.3.4 Effect of Decreasing Water Content 92
4.4 Conclusions 96
4.5 Acknowledgements 96

5 Sonication-induced effects on carbon nanofibres in composite materials 99

5.1 Introduction 103
5.2 Experimental 105
5.2.1 Preparation of dispersions 105

5.2.2 Preparation of free-standing films . . . 105
5.2.3 Electron Microscopy . . . 106
5.2.4 Electrical Characterisation . . . 106
5.2.5 Mechanical Analysis . . . 107
5.2.6 Spectroscopy . . . 107
5.3 Results and Discussion . . . 107
5.3.1 Electron microscopy . . . 107
5.3.2 Electrical and mechanical characterisation . . . 112
5.3.3 Spectroscopy . . . 116
5.4 Conclusions . . . 120
5.5 Acknowledgements . . . 121

6 3D Printed Carbon-Based Soft Strain Gauges 125

6.1 Introduction . . . 129
6.2 Materials and Methods . . . 131
6.2.1 Preparation of dispersions . . . 131
6.2.2 Preparation of free-standing films . . . 132
6.2.3 Preparation of HEMA-PU hydrogels . . . 132
6.2.4 3D printing of strain gauges . . . 133
6.2.5 Characterisation Methods . . . 134
6.3 Results and Discussion . . . 135
6.3.1 Sonication and Electrical Optimisation . . . 135
6.3.2 Damage due to sonication . . . 138
6.3.3 3D Printed Strain Gauges . . . 142
6.4 Conclusion . . . 147

7 Conclusions and Future Direction 151

7.1 General Conclusions . . . 153
7.2 Other and Future Directions . . . 155

Bibliography 159

A Additional Papers **203**

A.1 Introduction . . . 207

A.2 Results and Discussion . . . 209

A.2.1 Ink Preparation and Hydrogels Characterisation . . . 209

A.2.2 Model Evaluation . . . 213

A.2.3 Hydrogels 3D printing . . . 219

A.3 Conclusions . . . 221

A.4 Experimental Section . . . 222

A.4.1 Ink Formulation . . . 222

A.4.2 Ink Characterisation . . . 223

A.4.3 Hydrogel Preparation . . . 223

A.4.4 Hydrogel Characterisation . . . 224

A.4.5 Multi-Step Hydrogel Structures Fabrication . . . 224

A.4.6 Hydrogel 3D Printing . . . 225

A.5 Acknowledgements . . . 226

A.6 Introduction . . . 231

A.7 Experimental . . . 232

A.7.1 Materials . . . 232

A.7.2 Hydrogel Ink Formulations . . . 232

A.7.3 3D Printing . . . 233

A.7.4 Adhesion Testing . . . 235

A.8 Discussion . . . 235

A.9 Conclusions . . . 237

A.10 Introduction . . . 243

A.11 Results and Discussion . . . 245

A.12 Experimental Section . . . 253

A.12.1 Preparation of polydimethylsiloxane (PDMS) . . . 253

A.12.2 Preparation of the hydrogel precursor . . . 254

A.12.3 Rheological Characterization . . . 255

A.12.4 Device Fabrication 255
A.12.5 Sample Characterization 256

B Supporting Information **273**

B.1 Dynamic Scanning Calorimetry (DSC) 281
B.2 Mechanical Properties Comparison 281
B.3 Modulus vs. Linear Expansion Ratios 284
B.4 Hybrid Hydrogel Structures Preparation 286
B.5 3D Printer 287

List of Publications

Publications included as part of thesis

Chapter 1: Gately, R. D., & in het Panhuis, M. (2015). Filling of carbon nanotubes and nanofibres. Beilstein J Nanotechnol, 6, 508-516

Chapter 3: Warren, H., Gately, R. D., Moffat, H. N., & in het Panhuis, M. (2013). Conducting carbon nanofibre networks: dispersion optimisation, evaporative casting and direct writing. RSC Adv., 3(44), 21936

Chapter 4: Warren, H., Gately, R. D., O'Brien, P., Gorkin, R., & in het Panhuis, M. (2014). Electrical conductivity, impedance, and percolation behavior of carbon nanofiber and carbon nanotube containing gellan gum hydrogels. J. Polym. Sci. B, 52(13), 864-871

Chapter 5: Gately, R. D., Warren, H., Scardamaglia, M., Romeo, T., Bittencourt, C., & in het Panhuis, M. (2014). Sonication-induced effects on carbon nanofibers in composite materials. RSC Adv., 5, 19587-19595

Chapter 6: Gately, R. D., Naficy, S., Gorkin, R., & in het Panhuis, M., 3D Printed Carbon-Based Strain Gauges on Hydrogels (Under review: Nanotechnology)

Other Publications

Naficy, S., Gately, R., Gorkin, R., Xin, H., & Spinks, G. M. (2016). 4D Printing of Reversible Shape Morphing Hydrogel Structures. Macromol. Mater. Eng

Bakarich, S. E., Gorkin, R., Naficy, S., Gately, R., in het Panhuis, M., & Spinks, G. M. (2015). 3D/4D Printing Hydrogel Composites: A Pathway to Functional

Devices. MRS Adv., 1-6

Tian, K., Bae, J., Bakarich, S., Yang, C., Gately, R., Spinks, G., in het Panhuis, M., Suo, Z. & Vlassak, J. (2016). 3D Printing of Transparent and Conductive Heterogeneous Hydrogel-Elastomer Systems *(Under review, Adv. Mat.)*

List of Figures

1.1 Two worn robotic exosuits relying on pneumatic soft actuators for a,b) gait assist and c) grip assist. 8

1.2 A schematic showing how a 4D actuator is produced, as well as some possible conformations of the actuator 9

1.3 TEM micrographs highlighting the difference in structure of a typical SWCNT, DWCNT, MWCNT and VGCNF 11

1.4 A TEM micrograph of carbon black 17

1.5 The chemical structure of both the (a) high and (b) low acyl form of GG. 20

1.6 A simple mechanism showing the creation of both transient and stable cavitation bubbles during sonication. 22

1.7 Schematic of a method for producing filled SWCNTs and MWCNTs via arc discharge 29

1.8 Transmission electron micrographs of a hollow VGCNF highlighting the 'stepped' internal structure 32

1.9 A graphic showing a fully 3D printed valve that opens or closes depending on water temperature. 36

1.10 A 3D printer extruding UV-cured AAm. The resulting printed shape, and its 4D actuation path. 36

1.11 Two strain gauges and their patterns, displaying two that operate by either capacitance or resistance. 39

2.1 A labelled figure displaying both the pneumatic extrusion deposition system designed by C. Mire and M. in het Panhuis, and also the altered version using linear actuators 49

3.1 Sonication optimisation using UV-vis-NIR of a VGCNF-GG dispersion, as well as the efficiency plots. 65
3.2 SEM images and length analysis of a 4 min and 20 min sonicated VGCNF-GG evaporatively cast film. 67
3.3 Electrical conductivity of drop cast films as a function of VGCNF mass fraction and sonication time. 69
3.4 Viscosity as a function of shear rate for commercial fountain pen ink and the as-designed VGCNF-GG ink. 69
3.5 Direct writing of the VGCNFink with a fountain pen. 71
3.6 Morphology of typical direct written lines on the paper substrate. . . 72
3.7 Various analyses of the directly written VGCNF ink by the fountain pen, including line width and various electrical properties. 73

4.1 Photos and schematics of the impedance setup and samples 83
4.2 Electrical impedance analysis of a typical hydrogel (0.5 % w/v, crosslinked with 5 mM of $CaCl_2$) 85
4.3 Typical impedance graphs for a GG hydrogel used to calcuate impedance. 87
4.4 Storage modulus vs. sonication time for GG hydrogels. 89
4.5 Typical impedance plots of MWCNT and VGCNF hydrogels with different carbon material volume fractions. 91
4.6 Typical Bode plots for MWCNT containing hydrogels at water contents of 98.0, 96.0, 95.5, and 94.4 % 93
4.7 Impedance plots and conductivity of MWCNT and VGCNF containing hydrogels as a function of water content. 94

5.1 Typical high-resolution transmission electron microscopy images of VGCNFs at various sonication times. 109

5.2 Typical scanning electron micrographs of free-standing films prepared by evaporative casting and vacuum filtration of dispersions at various sonication times. 111

5.3 Electrical characterisation of free-standing composite films prepared by evaporative casting 114

5.4 Tensile properties of free-standing films at various sonication times. . 115

5.5 Raman spectra of unsonicated and sonicated VGCNF free-standing films 117

5.6 Typical XPS survey spectra recorded on unsonicated VGCNFs and BPs at various sonication times. 118

5.7 Detailed XPS survey spectra on VGCNF free-standing films produced by drop-cast and vacuum filtration, at various sonication times. . . . 119

6.1 An image displaying the custom-built 3D printer, with a close-up of the syringe holders. 134

6.2 Four images displaying the sonication optimisation of the CB-VGCNF dried films and the effects of over-sonication on the conductivity and resistance of the samples. 137

6.3 A graph showing how the length of VGCNFs decreases with increased sonication time, and the SEM micrographs that the data was taken from. 140

6.4 Two graphs showing a typical Raman spectra of a VGCNF: GG, CB: GG, and VGCNF: CB: GG free-standing film, and how the D: G ratio is affected through increasing sonication times of a VGCNF: CB: GG dispersion. 141

6.5 Three figures summarising the rheological affects of increased CB loading fractions of the CB-VGCNF ink. 143

6.6 A picture of the printed strain gauge with and without thse conductive fibre connectors, and a schema showing how it was made. 145

6.7 Three graphs summarising the mechanical properties of a 1 and 2 layer printed strain gauge. 146
6.8 The response of one and two layered printed strain gauges, and their gauge factor when compared across multiple cycles. 148

A.1 Extrusion printable inks were prepared with the components shown, and some images showing cast and fully 3D printed bilayer hinges. . . 210
A.2 Equilibrium swelling ratios of various poly(HEMA)- and poly(NIPAM)-based hybrid hydrogels at 20 and 60 °C. 212
A.3 Modulus of various poly(HEMA)- and poly(NIPAM)based hybrid hydrogels at 20 and 60 °C 212
A.4 A schematic representation of a produced hydrogel bilayer hinge, along with some images of a produced hinge both at 20 and 60 °C . . 217
A.5 Bending characteristics of hydrogel bilayers estimating only from the hydrogels' swelling ratios and fabrication parameters. 218
A.6 The printing pattern used and the resulting print at various temperatures for a cubic box. 222
A.7 Photographs of Alg/p-AAm ICE gel and Emax adhesion test sample before and after mechanical failure, coupled with the CAD images representing the print 236
A.8 Images of a 3D printed particulate reinforced Alg/p-AAm ICE gel composite ribbon, an artificial tendon printed with Alg/p-AAm ICE gel and Emax gradient structures, and a 3D printed artificial tendon attached to a skeleton. 238
A.9 A CAD model of hydrogel valve, photographs of the 4D printed valve at 20 °C (open) and 60 °C (closed) 238
A.10 Overall schematic of the 3D printing extrusion system used in this study, along with the 3D pattern used. 246
A.11 Rheological analysis of the rheological modifier for the hydrogel precursor. 247

A.12 Shematic illustration of the extrusion trace and the resulting geometry of multiple lines, along with optical profilometry of the as-printed gels 250
A.13 Electrical characterizations of the hydrogel in either bulk or printed state 252
A.14 An example of a printed hydrogel-elastomeric type device 254

B.1 UV-vis-NIR absorbance versus wavelength for GG-VGCNF dispersions, and optical microscopy of the dispersions at increasing times . 278
B.2 Differential scanning calorimetry results for poly(n-isopropylacrylamide) (p-nIPAAm)-based PEO-PU hydrogel with different PEO-PU component as indicated. 281
B.3 Representative stress-strain curves of fully swollen poly(hydroxyethyl methacrylate) (p-HEMA)-based and p-nIPAAm-based PEO_{10}-PU hydrogels tested in compression (a) and in tension (b). 282
B.4 Mechanical comparison between hydrogels produced here (large stars) with other hydrogel systems 283
B.5 Compression loading-unloading cycles for (a) p-HEMA-based PEO_{10}-PU, p-nIPAAm-based PEO_{10}-PU at 20 °C and p-nIPAAm-based PEO_{10}-PU at 60 °C. 285
B.6 Stress relaxation of p-HEMA-based PEO_{10}-PU, p-nIPAAm-based PEO5-PU and PEO_{10}-PU. All samples are fully swollen at room temperature 285
B.7 Young's modulus as a function of linear expansion ratio (λ) 286
B.8 A schema showing the multi-step preparation process for hydrogel hinges. 288
B.9 An example of a hybrid hydrogel box, made by a multi-step process similar to the one presented in Figure B.8 288
B.10 Photographs of the extrusion printer with syringes installed, coupled with the UV curing system 289
B.11 Variations on hydrogel geometry by extrusion rate variation 293

B.12 Resistance change of a stretched simple strain gauge 293
B.13 A single strain gauge mounted onto the index finger, with resistance readings in various conformations 294

List of Tables

1.1 A table detailing the different forms of Ketjenblack 18

A.1 Summary of the mechanical properties of cast Alg/p-AAm ICE gels and printed Alg/p-AAm ICE gels 231

B.1 Summary of energy expense obtained from the UV-vis absorbance data. 277

Chapter 1

General Introduction

A literature review of all material that is to be covered throughout this thesis. An overview for how each chapter/paper tie in with the overarching project is also discussed, along with the specific aims for this project.

Author Statement

This chapter contains the following published journal article, stylistically edited to suit the rest of this document:

R. D. Gately and M. in het Panhuis, "Filling of carbon nanotubes and nanofibres," *Beilstein J. Nanotechnol.*, vol. 6, no. 1, pp. 508–516, 2015

Author Statement:
I, Reece D. Gately, hereby declare that I contributed to the following work within this manuscript by:

- Wrote and edited the manuscript

All other work required for this manuscript was performed by other co-authors as follows:
Prof. Marc in het Panhuis: Assisted in proof-reading and editing the manuscript.

I, Prof. Marc in het Panhuis (supervisor), support and certify that the above author statement is correct.

Marc in het Panhuis
April 20, 2017

1.1 Critical Overview

This chapter highlights important literature surrounding the development of carbon-based filler (CBF)-polymer based composite materials, as a free-standing material or as an ink for 3D printing, and how these materials can easily lend themselves to soft robotics. Effects that need to be noted when developing such a composite have also been outlined, such as sonication induced filling and damaging of the CBF or the polymer dispersant.

Soft robotics is an emerging field with increased interest as more research is performed into the development of actuators, however there is still a lot to be desired. One such property is the ability for the actuators to sense how far they have actuated. This can be overcome through a strain gauge printed on top of the actuator, which is measured through an external circuit also controlling the actuation.

In order to develop these strain gauges, a carbon-based ink is required. The first paper presented shows the development of such an ink. This ink was produced using vapour-grown carbon nanofibres (VGCNFs) dispersed into a solution of gellan gum (GG). As presented, it shows the efficiency of GG as a dispersant, and that a VGCNF sample shows comparable properties to that of multi-walled carbon nanotubes (MWCNTs) but for a fraction of the cost. It then shows how this ink can be used in a variety of electrical applications.

A method of measuring the electrical properties of the samples was required, and thus the second paper is presented. Within this paper, the production of an Electrical Impedance Spectrometer was developed, tested, and benchmarked. Also presented are conductive hydrogels based on VGCNF and GG. This paper presents an instrument capable of measuring the bulk electrical properties of both dry and wet samples. This instrument was used to measure all electrical properties in each paper presented.

A highly efficient method to disperse CBFs into a solution is through horn sonication. However, it may cause damage to all compounds and particles within a solution, with a lot of literature emphasizing this statement. This is presented as a

literature review contained within this chapter, as well as a study was performed on these effects on the VGCNF-GG dispersions in the third paper presented. This third paper shows the detrimental effects on mechanical and electrical properties, as well as other methods such as X-ray photoelectron spectroscopy (XPS) and Raman. It also presents an advantageous side to this damage, as it shows that it has the ability to fill hollow tubular Carbon nanostructures (TCNSs), such as single-walled carbon nanotubes (SWCNTs), MWCNTs and VGCNFs, with other methods detailed in the literature review.

For the final paper presented, a co-dispersion containing both VGCNFs and KetjenBlack (KB) is optimised and characterised, as literature has indicated a co-dispersion of carbon nanotubes (CNTs) and graphene have a synergistic effect. These two materials have also shown great properties as conductors, and in being highly efficient dispersants into various polymers and resins, requiring very little energy per gram of material. All of these factors can be culminated into an ink that can be easily directly written, through extrusion printing, onto a hydrogel. This ink will have all of the previously mentioned abilities; strain gauging, flexibility, and versatility in printed design. This, when applied in conjunction with soft actuators, will prove to be a major step forward in the field of soft robotics.

1.2 Literature Review

Ever since the first machine was developed, mankind has strived to replicate the functions of nature, and to improve on them. Hard robots, on a macro scale, have been able to achieve this; cars can drive faster than any animal, planes can fly higher than birds, and robots can lift more than the strongest animals. The mechanics behind these were inspired by nature, however 'hard' robots can only achieve so much when compared to animals. Some hindrances include their lack of ability to move freely around complex environments [2], or performing delicate tasks such as picking easily bruised fruit [3] or surgery [4]. To this extent, soft robotics aims to marry hard and soft materials together, to give a hard backbone with soft, pliable actuators or completely replace the hard backbone with softer materials at the interface.

The first step to achieving this goal is to develop artificial muscles that mimic human ones. One of the oldest (but still relevant!) artificial muscles developed to this end is the McKibben pneumatic actuator, invented by J. L. McKibben in 1950, and later patented by R. Gaylord [5]. Its original purpose was as an orthotic for patients with poliomyelitis. The original muscle relied on having a flexible inflatable bladder surrounded by a stiff outer braid. When the muscle was inflated pneumatically, the braid restricted the directions that it could expand, causing the muscle to anisotropically deform and apply force to an attached line. These types of muscles have been used recently in human-robot interaction as an exosuit around the legs to assist the gait of those with partial loss (Figure 1.1 a and b) [6].

McKibben muscles have since evolved from their original 1950's design, with certain researchers altering the muscles for hydraulic actuation [8]. A recent development to alter these muscles for the field of soft robotics comes from the Walsh group, in the attempt to create a compliant glove to assist with grip strength (Figure 1.1-c) [6]. While these actuators are a step in the right direction, there are still a lot of flaws in the actuator; they are bulky as they require an air or water delivery system, they are not fully compliant, and they are not easy to reshape the actuators. A softer actuator must be developed, and one that can be designed and

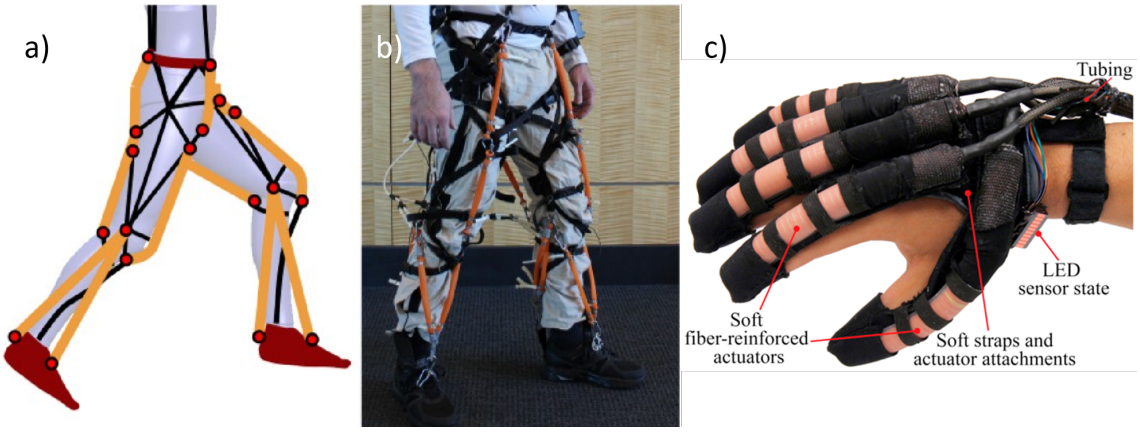

Figure 1.1: Two worn robotic exosuits relying on pneumatic soft actuators for a,b) gait assist and c) grip assist. Reproduced from [6, 7].

manipulated to fit each unique application. 3D printing has allowed bespoke devices to be developed, lending itself to this application.

If a 3D printer is used to print a device that has the capability to actuate, this has been referred to lately as a 4D printed actuator *i.e.* with respect to time, the 4th dimension. This can be as simple as printing a flexible material that is moved by hand (such as Ninjaflex, a thermoplastic with rubber-like physical properties), to materials that actuate with respect to an outside stimulus (temperature, pH) to form complex shapes [9–11]. The production and final result for such a device can be seen in Figure 1.2. Figure 1.2a shows how the actuator is printed, and then it's method of actuation. In this specific case, the material is printed with fibres in a prescribed orientation depending on the shape required. This is then encapsulated with another layer of inactive material, and cured. When the sample is heated, stretched, cooled, and then released, it is able to form various complex shapes, (Figure 1.2c-h). Upon re-heating of the sample, it then returns to its original shape.

The materials used to develop 4D printed actuators are designed in such a way that, as a response to an external stimulus, they deform either isotropically [12] or anisotropically [13]. This is achieved through multiple mechanisms, including contraction of the lattice structure or expulsion of water. To use a material like that to produce an actuator (and not just a hydrogel that shrinks), it is printed alongside a second material that has a much lower swelling ratio, and does not

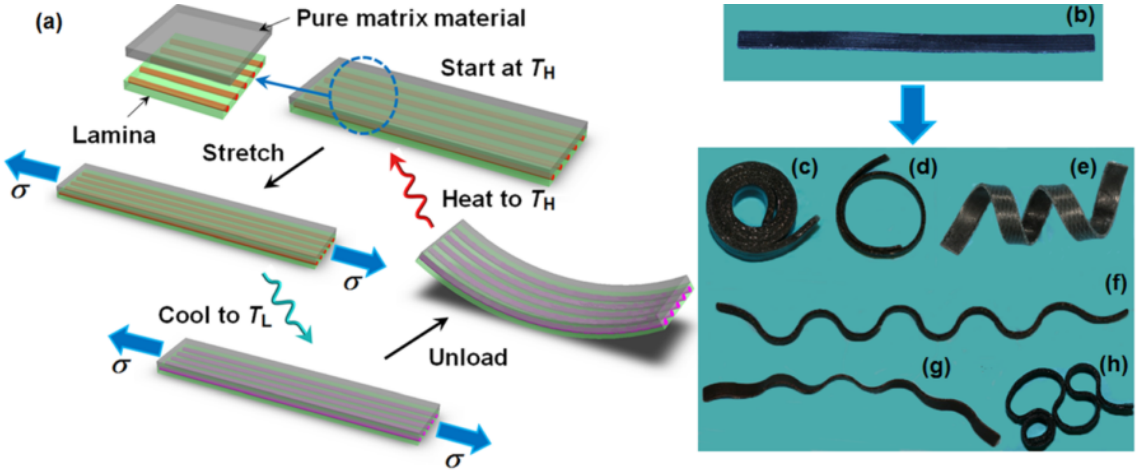

Figure 1.2: The development of a 4D printed actuator, showing the design principles and possible conformations. a) shows how the actuator is produced, and as it is printed. Two layers are printed; the first of which has fibres within it in a prescribed orientation, and the second is the pure matrix. b) shows such a sample. This printed sample is then heated, stretched, cooled, and released. (c-h) Upon release, it assumes a shape as calculated from the fibres. Upon re-heating, the shape returns to it's original conformation, and can be actuated again. Reproduced from [9].

respond to stimulus. The direction of actuation and thus the final shape depends on the difference in swelling ratios of the two materials, and how they are patterned [14]. In order to produce an actuator to meet all situations, a material that can have different properties depending on the make or concentration is required. To this extent, hydrogel actuators have seen a lot of use in soft robotics. They also have the added benefit to be able to match materials found in the human body.

The progression of 3D printed hydrogel actuators has been a rapid one, which can be measured in two ways: response time and force output of the actuator. One of the earliest hydrogel actuators was produced in 1995 by Yoshida *et al.*, which had a response time of 20 mins [15], which has come down to sub 10 s in recent actuators [16, 17]. Having a ultra-violet (UV) curable material is important to 3D printing as this allows you to deposit the material as a liquid and then, upon UV irradiation, solidify it into a sturdy, free-standing material. One of the most common 4D printed actuating materials used is p-nIPAAm, used as early as 1996 [18], using poly(acrylamide) (p-AAm) as the backbone (*i.e.* network that does not respond to stimuli), allowing both networks to be cured through UV irradiation [19].

A lot of current research has been placed into soft robotics, so much so that journals have started to appear solely for soft robotics. One such journal aptly named Soft Robotics (published by Mary Ann Liebert publishing) with the first volume published in July 2013 with a current impact factor of 6.130 (accurate as of July 2016). The need for a journal for this specific field indicates the growth of the field of soft robotics.

Current issues with soft robotics lie in that the materials are quite hard to actuate, requiring either a water bath (for pH/temperature change) or compressed air/liquid, and they are not 'smart', *i.e.* the actuators have no measurable response proportional to how far it has actuated. Both of these issues can be overcome by adding intelligence or external sensing to the material, and through Joule heating to cause actuation. This problem has been tackled previously through sensing material property changes, such as capacitance in a piezoelectric actuator [20, 21] or back-EMF for electromagnetic actuators [22]. These approaches, however, require a specific actuator to be used and designed, and cannot be applied to any soft actuator as required. The development of a universally applied sensor, such as a strain gauge designed for sensing of hydrogel actuators, would further the development of soft robotics.

These sensors also have another, very powerful, use for soft robotics, which is sensed human actuation. As seen above in Figure 1.1, robotic-human interaction is on the rise, however both of these devices do not react to the human body. The gait assisted exosuit has the artificial muscles timed in with a standard gait and actuates appropriately, not allowing for any changes or abnormalities, and the glove is actuated through the push of a button. With proper human-sensed robotic actuation, a doctor could perform remote surgery using a glove laden with sensors to pick up their every movement, which is then tied to a soft robot in the operating room. In order to make this a reality the sensors would need to be quite accurate, and the actuating materials would need to give feedback. Human-based sensors are a large area of research, to attempt to sense human movement as accurately

as possible [23, 24], with feedback being as simple as strategically placing pressure sensors on the soft robot [25].

1.3 Carbon-Based Fillers

Various CBFs have been used over the years as a supplemental material to produce strong, tough, or electrically conductive composite materials [26–28]. This is due to the outstanding mechanical and electrical properties that various CBFs offer, both on their own an in composite materials. Due to these factors, CBF are the main method that will be used to produce the required ink for strain gauging. The five CBFs that shall be reviewed are; CNTs (SWCNT, double-walled carbon nanotube (DWCNT), and MWCNT), carbon nanofibres (CNFs), graphene, and carbon black (CB). The structural differences between SW, DW, MW CNTs and CNFs can be seen in Figure 1.3.

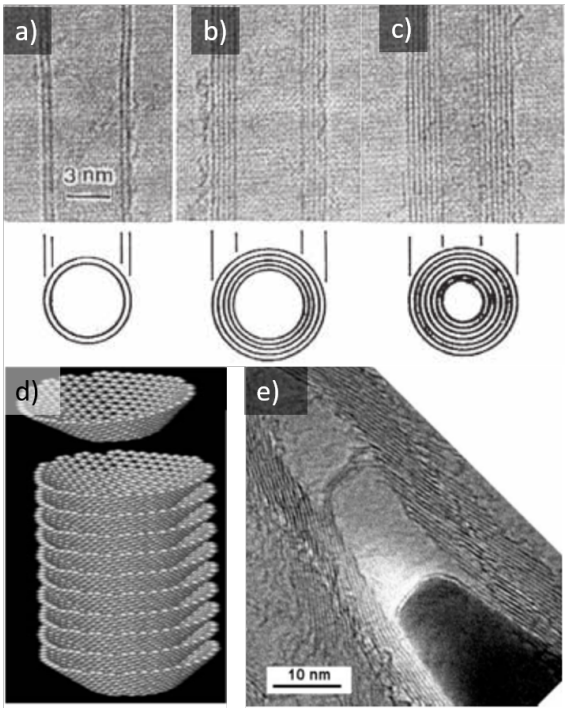

Figure 1.3: transmission electron microscopy (TEM) micrographs of a typical a) SWCNT, b) DWCNT, c) MWCNT and e) typical VGCNF. A schematic representation is given in (d) of the "cup-stacked" VGCNFs, resulting in a hollow core. a-c) Adapted with permission from [29], copyright 2006 the Royal Society of Chemistry and d,e) with permission from [30], copyright 2007 the Royal Society of Chemistry.

1.3.1 Carbon Nanotubes

Carbon nanotubes are well-known, 1D nanostructures, which are comprised of single, double, or multiple coaxial layers of rolled graphene [31]. The synthesis method and conditions greatly affect their structural characteristics such as number of layers, length and diameter distribution [32]. For example, the arc discharge synthesis method can be used to produce MWCNT with an inside diameter as small as 0.4 nm [29] and an outside diameter of up to 200 nm [33]. It has been shown that the inside diameter of MWCNTs produced using catalytic chemical vapour deposition (CCVD) is proportional to the size of the metal catalyst used during production [34]. Their high specific surface area (SSA) of 1315 m^2 g^{-1} [35] makes MWCNTs an ideal material for application in hydrogen storage [36], capacitors [37] and sensing [38].

Initially, both DWCNTs and MWCNTs were discovered at the same time, as the one method was yet to be refined and produced CNTs with a variety of walls and sizes [39]. These were produced through low pressure, high voltage arc discharge evaporation of carbon in an argon environment. Although DWCNTs were first imaged in 1991, they did not start to find common use until this process was further refined in 2005 to produce pure DWCNTs [40]. SWCNTs were discovered later during investigations into the filling of MWCNTs with iron and cobalt [41, 42]. Rather than producing a filled MWCNT (as expected), the metals acted as a catalyst to create a nanotube with a single wall. Similar to MWCNTs, the physical properties (inside diameter, length, degree of graphitization) of SWCNTs vary with the production method [43]. For example, during the synthesis of SWCNTs using pulsed laser vaporisation (PLV), the temperature of the deposition chamber was used to influence the average inside diameter range. It was demonstrated that at 780 °C the average diameter was 1.0 nm, whereas at 1000 °C the average diameter increased to 1.2 nm [44]. PLV has also been used to produce large quantities of pure SWCNTs and MWCNTs [45]. Other research showed that applying a magnetic field had a large effect on the size of the SWCNTs [46–49]. The SSA of the SWCNTs can

be between 124 and 1024 m^2 g^{-1} depending on the production method used by the various manufacturers [50]. Arc discharge has also been used to produce bundles of SWCNTs with a yield of up to 90 % [51]. This technique is now one of the more common production techniques, in addition to CCVD.

Each of these different materials have their own strengths and advantages when used as a dispersant. SWCNTs boast the most impressive electrical and mechanical properties, however they are harder to disperse in large concentrations when compared to MWCNTs [52]. DWCNTs have the added advantage of maintaining many of the properties of SWCNTs (such as thermal [53, 54] and mechanical [55, 56]), but are more chemically resistant [57]. This is because the second shell of carbon can be damaged without damaging the entire structure. MWCNTs boast very comparable properties to both SWCNTs and DWCNTs when in a composite material, but at a much cheaper cost ($1575, $1585, and $160 per gram for SW, DW, and MWCNT, respectively, Sigma Aldrich Australia, prices true as of November, 2016), and are much easier to disperse [58].

1.3.2 Carbon Nanofibres

CNFs, when compared to CNTs, are larger ($\approx$ 100 nm outer diameter), cylindrical, carbon structures that have multiple possible structures. In order to ease the complexity that surrounds all of these possible structures, the nomenclature proposed by Suares-Martinez *et al.* shall be used for the most part [59]. The structures that have been observed include: hollow- and filled-core, stacked nanocones; partitioned, stacked nanocones; and partitioned nanotubes. The filled-core, stacked nanocone structure consists of bowed sheets of graphene, which are stacked to produce a cylindrical, solid structure [30, 60]. Another morphology of CNF is produced by catalytic thermal chemical vapour deposition using a floating catalyst, henceforth referred to as VGCNFs [61], however they are also commonly referred to as graphitic carbon nanotubes (GCNTs). This technique can be used to produce partitioned, stacked nanocones or partitioned nanotubes. VGCNFs are produced (depending on the

structure of the catalyst) with a hollow interior cavity [62] and have been shown to consist of two primary structures, single layer and double layer. The internal arrangement is the same for both structures, that is, a series of parallel graphitic layers at an angle of 4-36 °relative to the hollow core. The double layer CNFs have an additional second layer (outside the angled layer) consisting of multiple sheets of graphene, which are aligned parallel with the core [43, 63]. Since it has been shown that thermal treatment between 1300 °C and 1700 °C leads to improved electrical and mechanical properties, VGCNFs are typically heat treated [64].

Typical dimensions of CNFs are: outside diameters of up to 200 nm, inside diameters of 12.5 nm (single layer) or 22 nm (double layer), and lengths of up to 20 μm [61, 63]. The SSA depends on the degree of heat treatment. For example, a SSA of 37 m_2 g^{-1} results from heat treatment at 1200 °C and is reduced to 15 m^2 g^{-1} after heat treatment at 2800 °C. Pyrolitic stripping can also be performed on as-grown nanofibres to remove unreacted polyaromatic hydrocarbons that may have fused onto the surface of the VGCNFs. This has been shown to increase the SSA from 20 m^2 g^{-1} to 62 m^2 g^{-1} [65]. Even higher values (348 m^2 g^{-1}) have been reported when using a metal catalyst and C_3H_8 decomposition [66]. Due to their unique internal structure, there has been significant interest in the filling of CNFs for the alignment of atoms [67, 68],

Figure 1.3 shows the morphological differences between a typical DWCNT, MWCNT and a typical VGCNF. Due to their large (average) inside radius, VGCNFs have a larger inside area as compared to SWCNTs and MWCNTs of the same length. The main interest in the filling of VGCNFs comes from their unique angled structure: the slight angle produces internal "shelves". This unique structure is clearly visible in the microscopy image (Figure 1.3e) and the schematic representation (Figure 1.3d).

Typically, SWCNTs boast the best properties, both electrically and mechanically, however this is offset by their high cost ($1575 per g, Sigma Aldrich Australia, accurate as of November 2016) and the difficulty to disperse (high dispersion times, low comparative amount able to be dispersed) tends to see SWCNTs used less of-

ten. MWCNTs are cheaper again (160 per g, Sigma Aldrich Australia, accurate as of November 2016), but are still expensive on an industrial production scale, but boast similar electrical and mechanical properties to that of SWCNTs. VGCNFs are cheaper again ($\approx$ 56 c per g, Pyrograf Products, Inc., accurate as of November 2016) with properties similar to that of both SWCNTs and MWCNTs, however the ease of dispersing (and thus, the amount that can be dispersed) is the highest [52].

1.3.3 Graphene

Next to CNTs, graphene is one of the most widely used carbon-based fillers, for much the same reasons. Graphene is derived from graphite, which is multiple layers of graphene stacked on top of each other, bonded through π-π stacking of the sp^2 carbon atoms. Graphite has been produced since the 1800's [69, 70] and its structure was first discerned in 1962 [71], however graphite had unremarkable properties as a dispersant, and so it was forgotten. After the success of CNTs, there was a lot of research going in to producing single-layer sheets of graphene, and this was finally achieved in 2004 by Novoselov *et al.* [72]. This work won Novoselov and Geim the Nobel Prize in Physics in 2010. Since then, a significant amount of research has been put towards various efficient methods of separating graphene sheets.

There are multiple methods to develop single sheets of graphene; micromechanical cleavage [73–75], chemical synthesis [76, 77], *in-situ* growth [73], and chemical exfoliation through graphene oxide [78–81]. Chemical exfoliation is currently the most widely used method, which involves chemically converting the graphene to graphene oxide. This would disrupt the π-π stacking (due to the presence of oxygen or hydroxy group), and would weaken the graphite. This is typically mechanically exfoliated, through a process such as ultrasonication, to produce individual sheets of graphene oxide. These sheets are then reduced back to graphene through chemical treatment [82, 83].

Each method mentioned has its' own advantages and disadvantages. Chemical synthesis of graphene shows the most promise, as it produces chemically pure

graphene, however it is currently quite slow and inefficient, only capable of producing grams at the highest end [84]. Currently, reduced graphene oxide (r-GO) presents the majority of graphene used, as it is quite easy to produce large amounts, and graphene oxide before reduction is easy to disperse in aqueous systems and can be rapidly reduced, making it easy to apply to many situations. It is known for CNTs and Buckyballs that it is the unique arrangement of carbon atoms that grant it the incredible electrical, mechanical, and thermal properties, and r-GO has flaws in the structure that compromise these properties [85, 86]. It still boasts amazing electrical properties (85 S cm^{-1} [87]) and mechanical properties (ultimate tensile strength of 130 GPa [88]) despite being 1 atom thick.

1.3.4 Carbon Black

Carbon black is a material that has been around since the Pharaonoic period of Egypt, which dates around 3200 BC, and was found in black inks used on papyrus [89]. The method to create carbon black then was to partially combust organic materials, then collect the remaining material and stabilise it in a liquid with gum arabic, a polysaccharide. This method has since been refined, as it was found that these compounds contained a lot of polyaromatic hydrocarbon (PAH) impurities, and is more closely related to soot. Carbon black, on the other hand, tends to have less than 0.25 % organic compounds [90].

The two primary methods of producing carbon black are through the processes furnace black and thermal/lamp black. Furnace black decomposes heavy aromatic oils in a hot gas stream, in a controlled manor to achieve specific particle sizes. Thermal black converts natural gases into carbon black atoms by heating the gases up in a furnace void of oxygen, to produce carbon black and hydrogen off-gas. This off-gas is then used to pre-heat another batch of natural gas to convert [91].

Carbon black has an aciniform morphology, that is, a 'grape-like' morphology. This can be seen in Figure 1.4. Carbon black boasts a lot of powerful properties similar to that of CNTs and for the same reasons; high surface area, high conductiv-

ity, and show mechanical reinforcement in composite materials. Carbon black has a typical diameter of between 80 and 800 nm [92, 93] and a conductivity of 1.25 to 5 S cm^{-1} [94], however it is quite hard to obtain a precise size due their morphology and inconsistency during production.

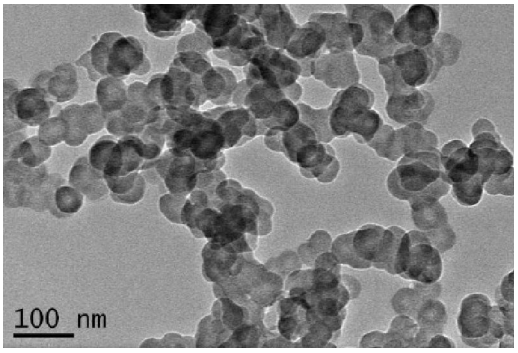

Figure 1.4: A TEM micrograph showing carbon black. Reproduced from [95].

There are multiple different producers and forms of carbon black, but one of the most conductive, easiest to disperse, and with the highest SSA has the trade name KetjenBlack, produced by AkzoNobel. Within the Ketjenblack selection of KB, they come in multiple formats, such as a powder, pelletised, or pre-dispersed in a polymer. As the only forms of Ketjenblack that can be dispersed are the powders (both pelletised or not), the other types have been omitted, and a summary of the physical properties of the remainder can be seen in Table 1.1.

The form that has been chosen in this study is the EC-600JD. This was chosen for several reasons. The first of which is the low concentration required for a percolated network. According to the manufacturer in the material specification, this is typically at 4 - 5 % wt (Table 1.1) with most researchers reporting up to 5 wt% loading [96, 97]. The second reason is the physical form it comes in. Using pelletised carbon powder makes handling a lot easier, safer, and easier to disperse. This is due to the fact that a lower density material, or one that has not been pelletised, tends to have a large volume, making it harder to completely submerge in the dispersant. Low density materials that have not been pelletised also carry a much greater risk of inhalation, and thus respiratory conditions may arise. This is overcome using a pelletised form. However, these pellets must be broken up either before or during

Table 1.1: A table detailing the different forms of Ketjenblack. Recreated from manufacturer's details.

Product Name	Ketjenblack EC-300J	Ketjenblack EC600-JD	Ketjenblack EC-600JD
Physical form	Soft pellets	Soft pellets	Very fine powder
Description	Superconductive black with very high purity	Top end superconductive black with very high purity	Ketjenblack EC-600JD in very fine powder form
Polymer	All polymers. Resins, coatings and inks	All polymers. Batteries and fuel cells	Batteries and fuel cells
Typical dosage (wt%)	8 - 10	4 - 5	4 - 5
Surface area (m^2 g^{-1})	800	1400	1400

dispersion, as they are tightly compacted to increase density. It is also the cheapest CBF, at only 23 c per g (AkzoNobel, accurate as of January 2016).

All of the discussed CBFs, and others, show strong properties as a particle. However, due to their size (typically in the nano-scale), they are currently not very useful in this form. For this reason, in order to harness their excellent mechanical properties and ultra-low resistance on a micro or macro scale, they are added as a reinforcing agent in composite materials. This has been used to achieve high electrical [98–100] or thermal [101] conductivity, use as an electromagnetic interference (EMI) shield [66], mechanical reinforcement [102], or have been used to add 'intelligence' or sensing to a material [23, 103, 104].

1.4 Gellan Gum

The biggest drawback of CBFs is their hydrophobicity, and thus require a dispersant to disperse them into an aqueous system. Gellan gum (GG) has been proven to be a highly efficient dispersant of both CNTs [100, 105] and CNFs [52], requiring very litte sonication energy per unit mass to disperse into an aqueous liquid. There are some unique properties of GG that make it ideal for this purpose, and make it ideal for designing an extrudable ink with modifiable rheological properties.

There are many common dispersants used to disperse CBFs into an aqueous solution, such as sodium dodecyl sulphate (SDS). GG was chosen to be evaluated as it is a more efficient dispersant (a stable dispersion can be created with 1 wt% MWCNT and 0.3 wt% GG [52] as compared to a 0.5 wt% MWCNT in 2 wt% SDS [106]), requires less energy (for MWCNT, 108 kJ g^{-1} in 0.3 wt% GG [52] compared to 2700 kJ g^{-1} in 1.5 wt% Triton-X 300 [107]), can be used as a rheological thickener, and the sonication degradation effects will be lessened on a higher molecular weight polymer. Tsaih *et al.*[108] performed a study that evaluated the sonication degradation effects on guar (MW 25 kDa), pectin (MW 30 - 100 kDa) and xanthan (M.W. 2 - 20 MDa) gums, and found that xanthan gum was affected least by sonication degredation due to its highter MW when evaluating their rheological properties.

GG is a linear, anionic, water soluble polysaccharide that is derived from the bacteria *Sphingomonas elodea* (formerly *Pseudomonas elodea* or *Auromonas elodea* [109]). The repeating unit of the polymer is a tetrasaccharide, which consists of two residues of G-glucose and one of each residues of L-rhamnose and D-glucuronic acid [110], see Figure 1.5.

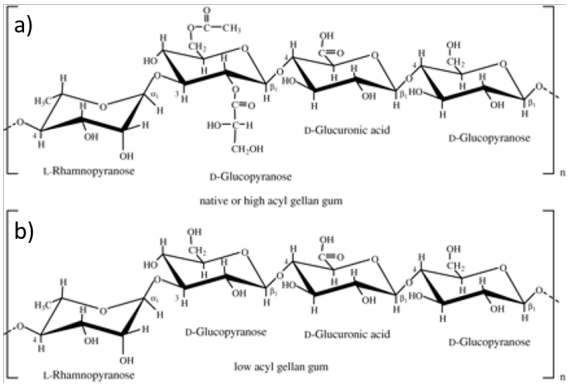

Figure 1.5: The chemical structure of both the (a) high and (b) low acyl form of GG. Reproduced from [111].

One primary method for the formation of GG hydrogels is physical entanglement, which can be reinforced through ionic bonding. Physically entangled GG hydrogels are thermally reversible, albeit weaker hydrogels. Physical entanglement was observed to occur at around 1.5 % w/w (21 °C). This mechanism simply involves the GG chains wrapping around each other tightly, which forms the stable hydrogel.

Adding an ionic crosslinker to these GG hydrogels removes their thermal reversibility, however they are mechanically stronger and tougher. Upon addition of a cation, the solution to gel (sol-gel) transition temperature is significantly increased, meaning that the gel will form at a higher temperature upon cooling [112]. Monovalent, divalent, and trivalent cations can be used to produce GG-crosslinked hydrogels, however the properties of the gels will be different; namely a decrease in mechanical properties if a monovalent cation is chosen over a divalent or trivalent one [113]. This is attributed to the crosslinking mechanism in a GG hydrogel.

When GG is ionically crosslinked to form a hydrogel, the carboxylate ion (formed in solution after the metal counterion dissociates, see Figure 1.5) ionically bonds

with the added cation. This cation also ionically bonds with another GG chain, and these two chains then form a double helix around each other. This is why it is believed that a monovalent cation will not form crosslinks that are as strong, as it is hypothesized that rather than forming a polyanion - cation - polyanion bond, it is required to form a polyanion - cation - water - cation - polyanion bond [113].

GG can come with varying degrees of acylation, and as produced by CP Kelco (the major, possibly sole large producer of GG) these are referred to as high acyl (as produced, native) and low acyl (chemically deacetylated), which can both be seen in Figure 1.5. High acyl GG tends to produce soft, flexible, non-brittle hydrogels, whereas the low acyl form, in contrast to the native form, produces firm, non-elastic, brittle hydrogels, and has been shown to be a very efficient dispersant of CBF [58, 100, 114, 115]. It is commonplace to mix both high and low acyl forms together to obtain a mixture with physical properties somewhere in between both of them, as there has been evidence of strong synergistic properties when a 50-50 mix is used [116].

Another advantage of GGs is that it has been approved for use in foodx by the European Union and the United States Food and Drug Administration as a rheological thickener [117]. Due to this approval, there has been a lot of interest in developing GG as a scaffold for cell growth [118], with documented *in-vivo* and *in-vitro* feasibility [119].

1.5 Probe Sonication as a dispersion method

In order to disperse the CNTs and CNFs into an aqueous GG solution, a method of mechanically mixing is required. The primary method used to achieve this goal is sonication, through either bath [120] or probe sonolysis [121]. Using bath sonolysis tends to have a longer mixing time with a much greater energy use (24 hour mixing time, at 300 W), when compared to probe sonication (less than 3 hours, typically 30 mins, run at around 7 W). Probe sonication comes with a large drawback, and that is that the method focuses all of the applied energy into a smaller proximity

[122], and these effects must be taken into consideration.

1.5.1 Material Degradation Due to Probe Ultrasonication

During sonication, a lot of stress is applied to the solution, which is stretched and compressed, creating cavitation bubbles as displayed in Figure 1.6. Two types of cavitation bubbles are formed; stable and transient. Stable cavitation bubbles are typically formed at lower energies (1-3 W cm^{-2}) and their size merely oscillates around some equilibrium size. At higher ultrasonication energies (over 10 W cm^{-2}) transient cavitation bubbles are formed, which grow in size until they reach a critical diameter (typically twice their starting diameter) and explode, applying a high amount of energy to the surrounding. Transient bubbles are considered to be the main source of energy during sonication.

Due to this rapid but efficient application of energy, every compound that is at the point of sonication undergoes high levels of shear stress. The negative effects has been well documented [1, 124], however if monitored properly can be used quite advantageously. Within a system such as the ones above (*i.e.* carbon material dispersed into a polymer) both materials are highly damaged when horn sonication is applied.

In a polymer solution, the chain length is shortened, which alters their rheological properties [125, 126]. This has been shown to reduce both the consistency

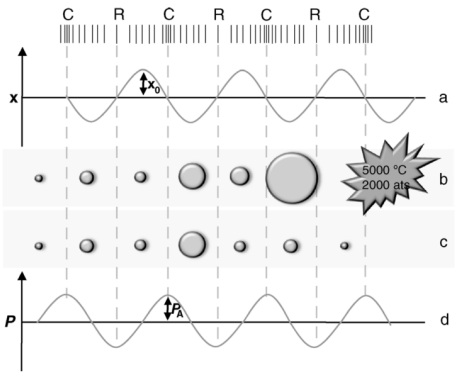

Figure 1.6: A simple mechanism showing the creation of both transient and stable cavitation bubbles during sonication. a) represents the displacement, b) shows the transient bubbles, c) shows the stable cavitation bubbles, and d) represents the pressure. Adapted from [123].

(K) and flow (n) behaviour of shear thinning polymers [127]. If this is a desirable property (*i.e.* to improve flow) then this can be an applicable technique to achieve such a result. In terms of 3D printing, where a shear thinning material is ideal, and this sonication damage can be to the detriment of the final product.

When evaluating the sonication effects on a long carbon material, such as CNTs, it has shown to reduce their average length from 3.5 μm down to 0.5 μm after brief exposure [128]. If these materials are added to increase electrical conductivity of the solution, then a longer CNT is desired, as this has shown to increase resistance, and thus reduce conductivity. According to a model proposed by Huang *et al.* [129], this reduction in length is due to mechanical/shearing process, as opposed to a thermal/chemical breakdown. It was also observed that the CNTs will shorten and eventually reach a limit, where shearing can no longer take place. This was calculated to be:

$$L_{lim} \approx 7 \times 10^{-4} d\sqrt{\sigma *}, \tag{1.1}$$

where d is the diameter and $\sigma *$ is the tensile strength of the CNTs. This indicates that a CNT with a larger diameter will be shortened further than one with a smaller diameter. Huang *et al.* also propose that this indicates that various parameters of sonication (*i.e.* pulse length, power level, and container geometry) will not affect this length shortening, and that all CNTs exposed to sonication will eventually plateau at L_{lim}.

1.6 Filling Effects of Sonolysis

It is well known that the as-produced CNTs have one end capped [130], thus in order to achieve filling, the CNTs must be opened. Controlled amounts of probe sonication can be used to open sealed CNTs, however this effect is required to be studied and monitored through techniques such as TEM, scanning electron microscopy (SEM), and XPS as to not over-damage the CNT.

The filling of SWCNTs, MWCNTs, and VGCNFs (hereafter referred to as TCNSs), has attracted much interest due to their applications in gas storage (in particular H_2) [131, 132], electrochemical energy storage [133, 134], battery electrodes [61, 135], catalysis [67, 136] and nanowelding [137]. Shortly after their discovery in 1991, MWCNTs were filled with metals in order to create metal nanowires encapsulated within the CNT [41]. While this was the original inspiration behind the filling of TCNSs, it is still very much prevalent today. The main advantages of using CNTs to produce metallic nanowires is that the CNTs act as a template for self-assembly of the nanowires [138, 139] and the CNT structure can act as a protective sheath to protect the nanowire from being damaged by chemicals in harsh conditions/environments [140]. CNTs have also been used as sacrificial templates. The CNTs can be removed by heat treating (generally requiring temperatures greater than 600 °C), thereby leaving the metal structures unaltered and exposed [141, 142]. It has also been shown that the irradiation of a filled MWCNT with a focused, high energy (200 keV) electron beam results in MWCNT-Co-MWCNT junction sites [143, 144].

There has been considerable interest in the filling of SWCNTs and MWCNTs for drug delivery applications, for example, tip functionalisation of the filled CNT for selective drug release [73, 145]. A recent review focussed on the use of CNTs filled with antitumour medication for use in chemotherapy and immunotherapy [146]. In particular, they noted that the high level of selectivity (when functionalised) gave the CNTs the ability to "seek out" and selectively deliver the contained drugs to the tumours. The same article also discussed the potential use of SWCNTs for the treatment of central nervous system disorders due to their ability to pass through blood-brain barriers [147].

Selected avenues for the filling of carbon nanotubes and nanofibres as well as applications of the filled TCNSs (including biomedical and catalytic applications) are discussed in the following sections. The progression of selected TCNS filling techniques beginning from the earliest papers that can be found as well as how the

techniques have adapted to modern methods and applications shall be reviewed, which will also extend to some of the most recent papers that have been published. The most common *ex situ* techniques for opening (decapping the TCNSs) and filling are also described in detail, as this is one of the main problems to overcome when filling TCNSs. The unique advantages with regards to the filling of these two TCNSs are also discussed, as it is important to emphasise that both serve their own, unique, purposes.

1.6.1 Approaches for Filling Carbon Nanostructures

1.6.1.1 Opening the capped ends

Various methods have been employed with the sole purpose of opening up sealed TCNSs. The initial work focussed on the opening of MWCNTs using bismuth in the presence of oxygen at 850 °C [148]. This was then further expanded by suspending the MWCNTs in 68 % nitric acid and refluxing at 140 °C for 4.5 h [149]. This wet chemistry method of opening MWCNTs was also attempted on SWCNTs using a heated hydrochloric acid solution, as nitric acid was found to be too harsh for SWCNTs. Similar to the MWCNTs, the SWCNTs were then easily filled directly after opening [150]. This was followed by more sophisticated methods such as oxygen plasma treatment [151], electrochemical treatment (which was able to remove the caps for both SWCNTs and MWCNTs) [152], heat treatment in carbon dioxide/air [153], sonication-induced shearing [124, 154], partial opening due to purification [155], precision cutting [156] and water-assisted etching [157].

The main issue with these methods is that etching the CNTs in this way damages their surface or alters their morphology in undesired ways (*e.g.* reduction in length). Due to this challenge, much research has been focussed on producing CNTs that are open at both ends. This has been achieved by using an anodic aluminium oxide (AAO) film as a template for the thermal decomposition of hydrocarbon gases, followed by removal of the template by etching in 46 % HF solution [158, 159]. This technique has since been refined to produce tailored CNTs of desired length

and diameter [160] and to allow the template to be dissolved in NaOH (rather than concentrated HF) [161]. This method has also been employed to produce SWCNTs [162] and VGCNFs [163], as well as long (10 μm) MWCNTs that can be nested or joined to create long MWCNTs [66].

There are multiple modes available to fill TCNSs, and those that shall be outlined are; electrochemical filling, functionalisation of the TCNSs, capillary suction, vapour phase, and *in situ* filling. Although it is also possible to combine more than one technique (*e.g.* chemical and capillary [164]), each mode will be described individually.

1.6.1.2 Electrochemical filling

Electrochemical deposition on both the interior and exterior surfaces of TCNSs has been achieved [165]. MWCNT samples decorated with gold nanoparticles on the interior and exterior surfaces were produced by first functionalising the CNTs with carboxylic acid groups [160]. This was followed by sonication of the functionalised MWCNTs in water and application of a large (225 V) potential across two gold electrodes [166]. This was shown to not only decorate the external surface, but also to fill some MWCNTs with a gold nanowire. Ordered, open MWCNTs produced from the AAO template method have also undergone an electrochemical filling process with nickel-iron alloys [156]. It was shown that this technique could be used to control the nickel/iron ratio and the amount of filling. Electrochemical methods have also been used to fill TCNSs with water [167] and can take advantage of the presence of oxygen within TCNSs applied as an electrode for Li-O_2 rechargeable batteries [168].

1.6.1.3 Filling through Functionalisation

The functionalisation of TCNSs is a proven, effective method to coat the exterior [37, 169, 170] or interior [171] surface with metal particles. This method produces TCNSs with a single-atom thick layer (plus the functional group, typically a car-

boxylate group) of metal particles. It has been utilised to create nanoscale capacitors with high energy storage rates, high specific capacitance (329 F g^{-1}) [37, 172] in addition to high surface area electrodes [169, 170, 173]. TCNSs have also been used as a membrane for water and gas filtration [174]. It has been proposed that by chemically functionalising the TCNSs, the selectivity of the membrane can be adapted to remove specific contaminants [175, 176]. Tip functionalisation has also been used as a method to selectively separate various analytes [177, 178] and can be performed at room temperature using ozone and small amounts of water vapour [179].

1.6.1.4 Capillary filling

It is well known that a tubular structure with a high aspect ratio will have strong capillary forces, and this is especially true for TCNSs [180, 181]. These forces can be exploited to achieve the filling of TCNSs. Capillary filling was achieved by depositing drops of metallic lead onto the external surface of MWCNTs, followed by heat treating the sample to 400 °C [182]. This heat treatment removed the capped ends and the resulting capillary action lead to the filling of the MWCNTs through the absorbance of the liquid lead. This process has been modelled to determine the extent of the capillary action [183]. In addition, the effect of the molecular weight of a polymer on the capillary action has also been investigated [184]. Microscopy has been used to visualise the filling of a MWCNT with gold via Joule heating and capillary action [185]. A mathematical model has been developed to evaluate the relationship between the TCNS radius, the radius of the nanoscale drop of material used to fill the TCNS, and the contact angle between the filler and the TCNS. This model successfully predicted the capillary absorption of nonwettable nanoparticles [186] and has been employed to achieve filling [187] as well as removal of the encapsulated nanoparticles [188]. Sonication has also been employed to fill MWCNTs in solution. Sonication acted to shear the MWCNT, resulting in the filling of the MWCNT with the surrounding metal solution [189].

Other methods have employed focused electron irradiation to produce SWCNTs

within the core of a filled MWCNT. This was achieved by first filling a MWCNT with iron, cobalt, nickel, or an iron-cobalt alloy using capillary action. Following this step, the sample was placed inside a transmission electron microscope (with the sample stage temperature set at 600 °C) and subjected to electron irradiation [190]. This resulted in the growth of a SWCNT within the inner core of the MWCNT.

1.6.1.5 Vapour-phase Filling

Filled SWCNTs and MWCNTs have been achieved by exposure to a metallic vapour. This resulted in metal nanowires within the core of the CNT [191–193]. A general summary of this method is as follows: the as-produced SW/MW CNTs were processed in a furnace under vacuum at a temperature that vaporizes the compound/element to be filled into the CNT. Next, a stream of the metallic vapour was sent into the furnace. In one such study, purified DWCNTs were added to an evacuated furnace at 400 °C and 10^{-3} Pa containing VCl_3 vapour [194]. The resulting material was then cooled to 100 °C for 48 h and cleaned with a HF solution. This filling method not only fills the interior cavity, but also coats the exterior of the CNTs with the vapour. Therefore, an additional cleaning step is required to remove these species.

It is important to note that this filling method, along with many other methods, is not restricted to metallic filling, although it is one of the more prevalent topics. Botka *et al.*have performed multiple studies on methods to efficiently fill SWCNTs with coronene [195, 196]. In both cases, the filling was performed by first opening the SWCNTs, then placing them in a furnace with coronene at temperatures of up to 450 °C and at a pressure of 10^{-4} mbar - the ideal conditions for the sublimation of coronene. After processing it was found that the coronene had both coated the SWCNT, as well as filled it. In some instances, this annealing and vapour filling caused a structural change in the coronene (which formed dicoronylene, the dimer of coronene) or in the SWCNT itself (which produced a DWCNT at high temperatures). This effect along with the unique structure of CNTs was exploited to

produce linear diamondoid assemblies of adamantine within the core of the DWCNTs using a method based on that proposed by Zhang *et al.*[197].

1.6.1.6 *In-situ* Filling

Although a significant amount of effort has gone into developing approaches for opening the end caps of TCNSs, some research has focussed on methods that either fill *in-situ* (during growth) or that simultaneously open and fill. These methods make use of the strong capillary action that exists within the nanoscale cavities. Filled SWCNTs and MWCNTs have been produced using layered sheets of graphene, decorated with palladium particles via arc discharge in solution [198, 199] (see Figure 1.7). This approach was able to produce filled SWCNTs or MWCNTs, depending on the number of layers of graphene used. In addition, it has been proposed that other metallic particles can be used. This has been demonstrated with Pd-Ag nanoparticles on graphene sheets, however, they were not "rolled" into CNTs [19].

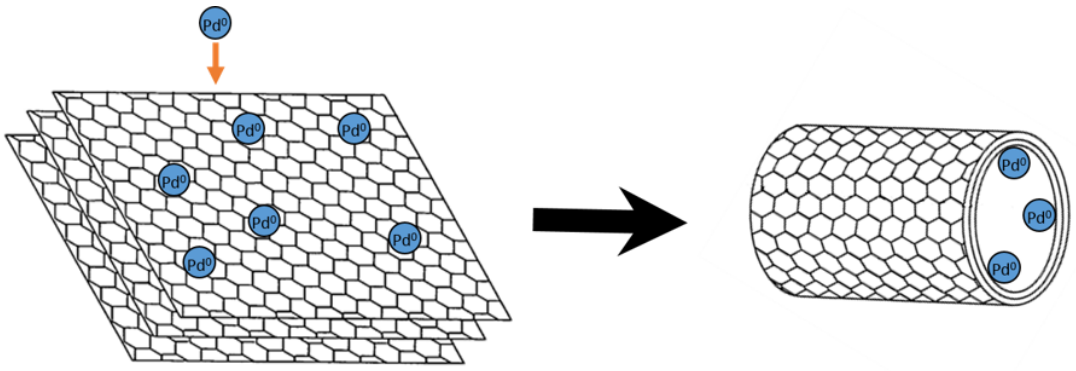

Figure 1.7: Schematic of a method for producing filled SWCNTs and MWCNTs via arc discharge in solution. Metallic palladium particles decorated the exterior surface of graphene sheets, which were then processed as filled CNTs. This schematic was inspired by a figure appearing in [199].

Both vapour phase filling and *in-situ* filling techniques have been combined to produce MWCNTs that are doped with various other elements, such as phosphorous and nitrogen, which can then later be released under high temperature conditions [200, 201]. One method to produce nitrogen-doped MWCNTs is a modified, floating catalyst, CCVD technique, which is most commonly used to produce VGCNFs. The

catalyst (ferrocene) was placed into the CCVD chamber under an argon/ethylene flow, and melamine was used as an efficient source for N-doping [131]. The chamber was then heated to 950 °C, with an effective heating of the ferrocene and melamine to 350 °C. At this temperature both compounds undergo sublimation. After the purification steps, it was found that the resulting MWCNTs were highly doped with nitrogen, demonstrating yet another method to produce MWCNTs to be used as a source of nitrogen storage. The nitrogen could be removed by heating to 700 °C. A very detailed review on one-dimensional nitrogen-containing carbon nanostructures by Ćirić-Marjanović *et al.* contains a very detailed list of other structures and methods used to achieve nitrogen storage [202].

The arc discharge method was also modified to produce filled SWCNTs and MWCNTs [203, 204]. This was achieved by first producing a powdered mixture of graphite and the various metals performed in the study (YB_2, YNi_2, and NiB). Next, standard arc discharge methods were utilised (25-35 V, 100 A). This method produced filled MWCNTs, as well as filled, graphitic nanoparticles. This method has been employed in conjunction with an AAO template lined with the filler material [205] or completely filled with the metal [206]. Moreover, a variety of bismuth-tin nanostructures covered by CNTs have been produced via *in-situ* filling. It was demonstrated that the $MSnO_2/MBi_2O_3$ ratio was instrumental in the formation of the encased nanostructures (nanoparticles, nanorods, and nanowires) [207].

1.6.2 Recent developments

Although several drug delivery and medical imaging applications of SWCNT and MWCNTs have been identified, this line of research has only very recently emerged [208–210]. Further investigations into the selective binding of functional groups and various viruses or tumours could provide for an effective drug delivery system for treating various difficult-to-treat ailments. However, effective CNT filling methods that do not negatively impact the drug require further investigation. To date, only SWCNTs and MWCNTs have been evaluated for their use in drug delivery. Although

potentially promising for affordable, targeted, drug release, VGCNFs have not yet been evaluated. Whilst they have not demonstrated the same nanoscale interactions as CNTs (such as crossing the blood-brain barrier, which is still under investigation), they may have other applications on the larger scale and allow for higher drug storage capacity.

The use of focused electron beam irradiation for the removal of the outside layers of SW/MW CNTs has promise as an effective method to produce pure or alloyed nanowires for conductive applications [211]. This, however, is also a relatively new research field where very little investigation into developing a scalable method for producing larger quantities of nanowires has been undertaken. As TCNSs have shown promise in the field of tissue engineering, with further development, this method may be used to produce channels for cell growth. Filled with appropriate drugs and medium, TCNSs may provide a platform for the growth of various cells.

Although significant research has gone into the filling of TCNSs, possibility for further exploration still remains. For example, most of the current methods are harsh (*i.e.* employing concentrated acids, high temperature/pressure conditions) and damage either the filler material or the TCNS itself. In addition, the filling process can be complex and can require multiple steps using custom-built equipment. These methods could be improved to provide a simple method to completely fill the TCNSs with the desired material, without damage to the TCNS, and in a timely manner. Simplicity is key for scale-up to large quantities of filled TCNSs, which is a requirement for any commercially viable application.

TCNSs provide a unique structure with a high aspect ratio, large filling volume, and good stability, which can be useful for many applications. For example, it is well known that they can improve the mechanical and electrical properties of various dispersants [101, 212–214]. However, the properties of the resulting materials prepared from dispersions of TCNSs filled with various materials have not been fully investigated. One interesting application area is in the field of repair (healing) of polymer materials [199]. Traditionally crack healing, which can repair the

detrimental effects of mechanical degradation and fatigue in polymer adhesives, was primarily investigated this field. One application of this concept could be in the area of polymer materials (such as hydrogels) for cartilage replacement.

Most interest in the filling of VGCNFs is due to their unique internal structure, which allows for the alignment of atoms along the ridges of the graphene sheets [67], as shown in Figure 1.8. The internal structure has been demonstrated to be a good site for the catalytic growth of nanoparticles of desired dimensions (Figure 1.8a,d). When the nanoparticles grow too large, they simply flow through and out of the VGCNF, as indicated in Figure 1.8d [215, 216]. The structure of VGCNFs in the context of filling has not been extensively studied [194], leaving much to be discovered as to how this unique internal "layering" can assist with self-assembly and size-controlled particle growth.

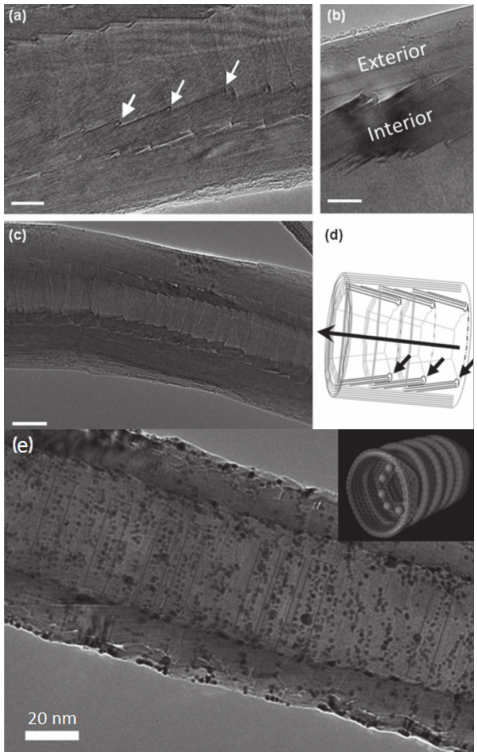

Figure 1.8: (a,b,c) Transmission electron micrographs of a hollow CCVD-grown CNF with the graphene caps indicated by the white arrows. (d) Schematic of the structure of the CNFs with the caps as well as nucleation sites indicated by the black arrows. (e) Transmission electron micrograph of the filled CNFs with gold nanoparticles. Inset: a computer generated model. Reprinted with permission from [67], copyright 2012 Wiley-VCH.

1.6.3 Future Prospects

The filling of TCNSs has shown much promise regarding the synthesis of nanowires, hydrogen storage, and drug delivery. Although most of the research has focussed on the development of the actual methods for filling, there are a number of biomedical applications of these fascinating materials that remain to be explored and developed. Most of the reviewed literature relates to MWCNTs, as this material has been extensively studied. VGCNFs are an emerging material for filling applications, but not all VGCNFs are suitable. For example, the VGCNFs with a "deck of cards" morphology (*i.e.* a series of parallel graphene sheets stacked on top of each other [217]) cannot be filled due to the lack of a hollow core [60]. VGCNFs have significant promise, however, their high production cost has limited research in the past. As research into the efficient production of pristine SWCNTs has progressed, their cost has correspondingly rapidly decreased, which should lead to future SWCNT filling applications.

1.7 Additive Manufacturing

When developing any new item, there are two approaches to the manufacturing process; additive or subtractive. Subtractive manufacturing relies on having an excess of the material and removing that which is unnecessary, such as a lathe. Additive manufacturing works on the opposite principle. That is, rather than removing what is not needed, it only adds what is required, and this is the basis for all 3D printers. This typically involves adding material layer-by-layer, and can also be performed through techniques such as inkjet printing and pen writing.

Additive manufacturing, as an approach, is not a new method, however it is now being applied in all new ways to achieve what was unable to be previously, *e.g.* restaurants have started to serve 3D printed food. This particular usage displays how advanced this technique has become, as this requires the printer to work with a variety of materials with various rheological properties. Advancements using addi-

tive manufacturing techniques have also shown promise to be able to produce living, implantable organs [218, 219], however this is still years from implementation.

1.7.1 Pen Writing

The basics for using a fountain pen have been around since 6th century AD, where a quill was the primary method of writing. Writing with a quill involved simply dipping the tip of the quill into an ink reservoir, where it was deposited on the parchment. This was then improved in the 10th century to contain the ink reservoir in the body of the pen [220], which was the first known prototype of the fountain pen, as it is known today. A fountain (nib) pen relies on controlled leakage of the ink within the reservoir out the uniquely designed tip and onto the substrate. This technique has been revisited in the last 15 years to develop more complex devices than simply writing, such as designing solar cells [221], nanoelectrodes [222], and DNA patterning [223].

Fountain pen writing is a relatively simple technique, and the ink design requirements are minimal. The only requirement is that the ink is similar to water at a shear rate of 1000 s^{-1}, the shear rate of standard pen writing, and is liquid at lower shear rates, to facilitate the liquid leaking down the nib. This same principle has been applied to an atomic force microscope to etch chrome lines 1 μm thick, with edge sharpness of 0.1 μm [224]. However, despite a variety of research showing that this technology can be used for fine chemical control of reactions [224] or accurate deposition [19, 225], the field of fountain pen writing has very little research.

1.7.2 3D Printing

3D printing is a rapid, additive fabrication technique that has been around since the 1980s by Hideo Kodama [226], who used a UV-hardening polymer to print the first 3D parts. This has since changed to favour thermoplastics for the printing process, due to the ease at which they can be melted, patterned, and then hardened through cooling. This iteration of 3D printer has recently gained traction in the general

public as a method of producing bespoke parts, mostly due to the reduced cost of printers, and increase in availability. Material, printers, and replacement parts can now be purchased quite easily.

Typical 3D printers are designed to print thermoplastics, however in order to print various other materials, such as hydrogels, the printer must be adapted to allow for this new material. There are two types of extrusion methods commonly used to achieve this; pneumatic or mechanical extrusion [227, 228].

3D printing, in its own right, has furthered device development, both in fabrication time and ability in many different fields, from medical [229, 230] to industrial production [231, 232], with many other uses [229]. 4D printing is the next step with this technology, as this will allow entire devices to be printed, that have the ability to actuate.

4D printed actuators are achieved through patterned 3D printing of a material, where the printed structure can change its shape or size, typically in heated water. Bakarich *et al.* produced a fully 3D printed valve, that utilised various ionic-scovalent entanglement (ICE) hydrogels with a commercially available gel, all of which are UV curable [14]. The produced valve and printing of it can be seen in Figure 1.9. The actuating hydrogel, an alginate/p-nIPAAm blend, changes its volume with respect to the water temperature it is submerged in. The other ICE hydrogel used was an alginate/p-AAm blend, which does not change its size or shape once swelled in water. A third structural gel, a commercially available UV curable adhesive (Emax 904) was also used as a rigid cap. This was able to produce a fully 3D printed device, with 4D printed actuators allowing it to control the flow of water.

The term 4D printing has only recently been coined, with simple 4D printed actuators showing up as recently as 2008 [233–235] without the term '4D actuator'. It has, however, picked up a lot of movement recently, as it strongly supports soft robotics through the production of highly adaptable and customisable actuators made of soft materials. Many other fields will also benefit from this research, in particular ones that require bespoke actuators from either hard or soft materials.

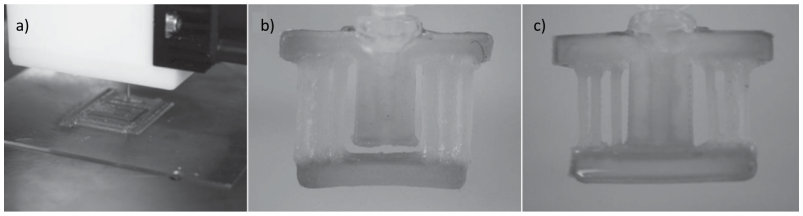

Figure 1.9: A graphic showing a fully 3D printed valve that opens or closes depending on the temperature of the surrounding water. a) shows the 3D printer in operation, printing the various materials required (algnate/p-nIPAAm, E-max, or alginate/p-AAm. b) shows the as-produced valve when submerged in 20 °C water, and c) shows it in 60 °C water. Reproduced from [14].

Current technology of soft robotics lies with developing hard robots that are covered in any soft material, such as hydrogels [236], most of which have biological inspiration, such as an octopus tentacle [2] (coined as biomimetic development). The J. Lewis research group at Harvard university have been striving to achieve biomimetic 4D actuators, and have recently reported success in such a field, which can be seen in Figure 1.10 [11] . The shape is made of a cellulose fibre reinforced fluorescently tagged acrylamide (AAm) solution, which is then UV cured to form a free-standing structure, as seen in Figure 1.10b. The material printed is also capable of changing shape over time in a water bath, allowing it to be deemed a 4D printed actuator.

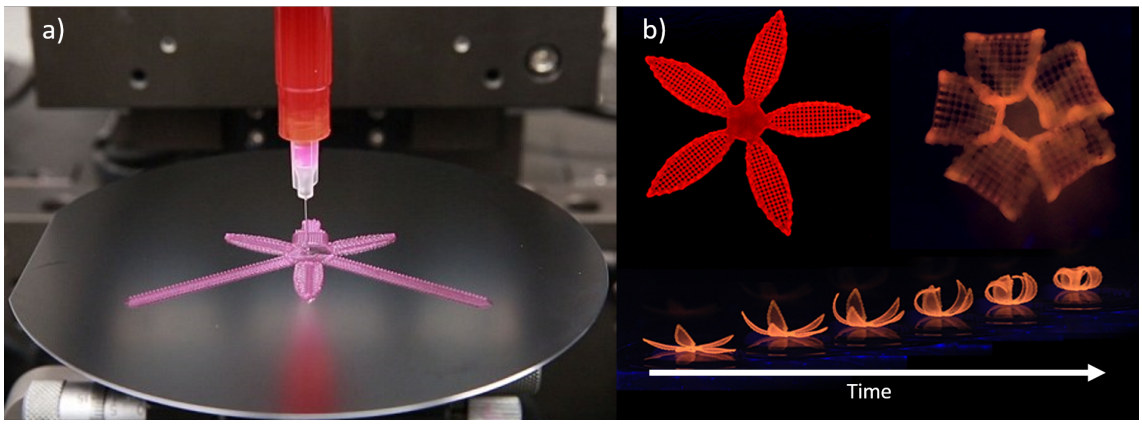

Figure 1.10: a) A 3D/4D printer extruding UV-cured AAm. b) The resulting printed shape, and its 4D actuation path. Reproduced from [11].

While this is producing a new wave of robotics, this involves developing two different mechanisms, and marrying them. This is important as trying to marry hard materials, such as metal, with soft hydrogels comes with its own set of problems,

deemed the 'fork through jelly' issue. Through the use of 4D printed actuators, and specifically hydrogel materials, a soft robot can be produced without any of these interfaces.

One of the main strengths to hydrogels is their highly tunable physical properties, and they can be developed to be stiff or soft, with no barrier between materials of various toughness [237]. Research has gone into producing a squid beak, which is a combination of both hard and soft materials, with no discernible distinction between either material. This will allow for a unique design of soft robot where every material used, including the actuators, are hydrogels [14].

4D hydrogel actuators rely on an active hydrogel, that expands or contracts under various conditions, that then works against another hydrogel layer that does not actuate [14, 238]. The most commonly used actuating hydrogel polymer is p-nIPAAm. When p-nIPAAm is exposed to temperatures around 60 °C, the interstitial water caught within the polymer network is ejected, which causes the hydrogel to turn white and reduce in volume [239]. In order to expand to its original size, the p-nIPAAm must then be placed into a cool ($\approx$ 21 °C) water bath, where it can reabsorb the interstitial water. This whole process can be done in as little time as 2 minutes (1 min to contract, 1 min to expand) [240]. This mechanism is the basis behind the valve produced by Bakarich *et al.* as seen in Figure 1.9 [14].

Hydrogel actuators have shown a lot of promise for soft robotics [241, 242], with 4D printing adding a lot more to the design and rapid prototyping of such actuators. Each actuator simply requires the addition of intelligence, so that the muscles can be accurately actuated to the required length, or the required force output. The development and addition to a strain gauge to these actuators would assist in finer control of these devices. Most modern strain gauges can also be 3D printed, which lends itself to the development of a 4D printed actuator with a strain gauge embedded.

1.8 Strain Gauges

Strain gauges are a patterned sensor that can detect when the pattern has been distorted or stretched in one direction. When the device is deformed, there is an alteration in the physical layout of the device (surface area, track length), and this change results in a measurable property changes, such as capacitance [243, 244] or, more commonly, resistance [23, 245]. Strain gauges are of increased interest for human-sensed actuation for the field of soft robotics [23] due to their ease in human-motion sensing ability.

For strain gauges to work in such a facility, the material needs to be patterned in a specific way for heightened sensitivity, even for small strain changes. Figure 1.11 shows two types of strain gauges. Figure 1.11a-c) shows a capacitive strain gauge that, when stretched, increases the contact surface area, while reducing the distance between the electrodes. As the well-known equation for capacitance shows,

$$C = \frac{k\epsilon_0 A}{d}, \tag{1.2}$$

where C is the capacitance, k is the relative permittivity of the dielectric between the plates (1 for air), ϵ_0 is $8.854\times10^{-12}Fm^{-1}$, the vacuum permittivity constant, A is the area of the electrodes, and d is the distance between the plates. This shows that, as A is increased and d is decreased, C will increase. When the change in C is measured with respect to l, the strain gauge can accurately measure how far it has been stretched in a linear direction. This can also be applied for hydrogel capacitance-based buttons and pressure sensors for various applications, including biomedical [246].

Figure 1.11d-e) shows a CNT based resistance strain gauge, that, when stretched, increases the track length, which causes the resistance to increase. To explain this variance mathematically, let Δr be the increase in resistance across a single track (as outlined in red in Figure 1.11d), ΔR is the change in resistance across the whole strain gauge, and $\frac{\delta l}{l_0}$ be the change in length. Thus,

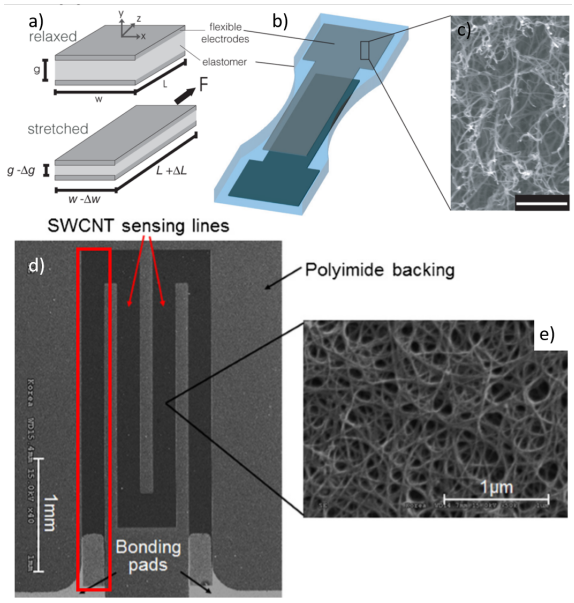

Figure 1.11: Two strain gauges and their patterns, displaying two that operate by either a) capacitance, and b) resistance. As a) is stretched, both distance between the two electrodes (denoted g) and the width (denoted w) are reduced, with the length (denoted l) is increased. This then causes the capacitance to increase measurably. b) shows a computer model of this strain gauge, with c) showing SEM imaging of the strain gauge. d) shows a resistive strain gauge, along with where it is connected. As it is strained in the direction of the tracks, the increase in track length increases the resistance of the sample, with e) showing SEM imaging of the surface. Reproduced from [247, 248] respectively.

$$\Delta r \; \alpha \; \frac{\delta l}{l_0}, \tag{1.3}$$

and

$$\Delta R = \Sigma \Delta r. \tag{1.4}$$

If 3 of the tracks in the strain gauge shown in Figure 1.11d) were to be removed, this would drop the sensitivity of the strain gauge considerably. This is because the length change would be felt by each track in the direction of strain, thus effectively multiplying δl by 4. For a single track to have the same change in resistance for a set δl, it would need to be 4 times as long. Thus, the more tracks you have, the higher the measurable change in resistance, and the higher the sensitivity of the sensor. The only factor that must be taken in to consideration with multiple tracks is print resolution *i.e.* the width of the tracks, to ensure that they do not bridge.

Two primary uses for strain gauges includes human-motion detection [24, 249] and development of a humanoid robot [23], however there are many more fields in which strain gauges are being studied for possible use. The medical field has a lot of interest in using wireless strain gauges [250] to monitor internal bodily operations, such as intestinal muscle movements [251] and automatic dietary monitoring [252] through the development and application of edible, or implantable, strain gauges.

1.9 Aims

The main aim of this thesis is to develop a conductive ink to facilitate 3D printing of strain gauges onto the surface of soft materials. This will be obtained through the use of conductive carbon fillers dispersed into an aqueous solution using a biopolymer with tunable rheological properties, which is then deposited through 3D printing.

The specific aims of this project were to:

- Design and optimize a variety of inks based on VGCNF and/or KB dispersed in GG;
- Characterise the as-produced ink for a variety of properties, such as:
  - Electrical conductivity
  - Mechanical properties
  - Rheological properties
  - Surface morphology
- Evaluate effects of sonication damage on the as-prepared composite materials through various microscopic techniques;
- Custom develop a 3D printer to pattern the inks as required;
- Fabricate and characterise a strain gauge using these inks onto a soft substrate.

Chapter 2

Materials and Methods

Each material and method that was used throughout each experimental chapter is discussed in full. For ease of reading, all chapters based on journal articles have had the experimental section collated to within this chapter.

2.1 Sample Prepration

2.1.1 Prepration of Gellan Gum solutions

GG solutions are prepared by first weighing out the appropriate amount of GG (low acyl form, CPKelco, Gelzan CM, Lot # 1I1443A) into 100 mL of Milli-Q water (resistivity $\approx$ 18.2 MΩ cm). This solution is then heated to $\approx$ 80 °C on a hotplate (Stuart CB162 heat stirrer) while stirring with an overhead stirrer at $\approx$ 800 RPM (IKA RW 20 Digital) for at least 30 minutes, until the solution is clear.

2.1.2 Prepration and Sonication of Carbon-Based Dispersions

To prepare a solution with CBFs, the appropriate amount of carbon material (VGCNFs (Pyrograf Products, PR24-LHT, Batch info: PS1345 Box 8, HT 170, diameters up to 200 nm) or KB (AkzoNobel, Ketjenblack EC-600JD powder, partially pelletised)) is initially added to a 20 mL glass vial (VWR, GERR502039B22RSP00, diameter 25 mm). 10 mL of the appropriate GG solution is then gently pipetted in. The solution is then briefly vortexed (IKA Vortex 3, Ident. No. 0003340000) to ensure that all of the CBF is wetted by the solution. Horn sonolosys is then applied to the solution (Branson Digital Sonifier, power output 6 W, 0.5 s pulse, 0.5 s between pulses) through a microtip horn (Consonic, diameter 3.175 mm) which is held $\approx$ 1 cm off the base of the glass sample vial. A water bath surrounds the sample vial to keep the solution cool when in operation, to minimise evaporation.

In extreme cases (i.e. GG concentrations above 0.9 mg mL^{-1}) the solution is too viscous to allow proper sonolysis, so to ensure that the sample could still be sonicated, it was initially heated to reduce the viscosity of the GG. This was done by placing the sample in the sonicator as normal, however rather than using a cold water bath, hot water ($\approx$ 60 °C) was used in place of cold water. The solution was allowed to heat for 5 minutes before sonolysis commenced.

Higher mass amounts of CBF (above 20 mg mL^{-1} for VGCNF, 40 mg mL^{-1} for KB, and 300 mg mL^{-1} for combined systems) proved to be quite challenging

to sonicate, as the volume of the CBF was greater than that of the 10 mL of GG solution. To overcome this, the CBF was lightly compressed prior to the addition of the GG solution.

2.1.3 Prepration of Free-standing Films

Two types of free-standing films were produced for use; evaporative cast (EC) films, and buckypaper (BP) films. Depending on the application, either of these films were used for analysis. Both of these films initially required to make a CBF dispersion to then cast into the film. The method used to create both of these films is outlined below.

2.1.3.1 Evaporatively Cast Films

EC films were prepared by pouring the as-prepared dispersion into a plastic petri dish (diameter 55 mm) and was allowed to dry under controlled conditions (21 °C, 50 % relative humidity (RH)) in a temperature-humidity controlled chamber (Humiditherm by Thermo Scientific, TRH-150-SD) for 24 hours, or until completely dry. The resulting films were then carefully removed from the petri dishes to produce free-standing films for analysis.

2.1.3.2 Buckypaper films

BP films were prepared by following the method as outlined by in het Panhuis [214, 253]. In brief, the as-prepared dispersions are diluted up to 100 mL with Milli-Q water, and was then briefly vortexed (IKA Vortex 3, Ident. No. 0003340000). This diluted solution was then filtered through a commercial membrane (Millipore, 5 μm pore size, polytetrafluorethylene) under vacuum (Vacuubrand, CVC2, 30 - 50 mbar) until all of the solution has been passed through the filter. The membrane is then gently removed and left to dry under controlled conditions (21 °C, 50 % RH) in a temperature-humidity chamber (Humiditherm by Thermo Scientific, TRH-150-SD) for 24 hours. One dried, the BP is then gently removed from the membrane to

produce a free-standing film.

2.1.3.3 p-HEMA Gel Preparation

To make a 20 mL solution, initially 5 g (25 wt%) of hydroxyethyl methacrylate (HEMA) was added to 10 mL of ethanol (EtOH) (50 wt%) along with 2 mol% of α-ketoglutaric acid (AKG), N,N'-methylenebis(acrylamide) (MBAAm). This was then heated to 60 °C, and stirred until dissolved fully dissolved. After the mixture turned transparent and has fully dissolved all solids ($\approx$ 10 mins), 10 g (50 wt%) of polyether-based polyurethane (PEO-PU) was added in small portions. The final volume is left on the heat stirring for 2 days, to ensure through mixing of all components. The final ink is completely transparent.

To cast the gels, rubber was cut to form the required shape, and was placed between two glass slides after injecting the ink. These samples placed under a UV lamp (Dymax BlueWave 75 UV spot curing lamp, 75 W lamp) in a reflective shroud to ensure complete irradiation. The total time of irradiation was 30 mins to ensure a complete cure.

2.2 Direct Writing of the Dispersions

2.2.1 Fountain Pen Writing

Fountain pen writing was carried out using a commercially available fountain (nib) pen (Parker, Jotter, purchased from Officeworks Australia) outfitted with a refillable cartridge. High quality photo paper (Spilman, matte, 180 g m^{-2}) was used as the substrate. Multiple tracks were deposited by firstly allowing the original track to dry before writing the second track on top. Care was taken to ensure that the second track is placed directly on top of the first one.

2.2.1.1 Circuits Produced from Fountain Pen Tracks

Circuits prepared using the fountain pen tracks as the electrodes were all drawn on high quality photo paper (Spilman, matte, 180 g m^{-2}). Multiple circuits were prepared using a variety of patterns, which were connected to green LEDs (Jaycar Electronics, Australia, diameter 5 mm, 3.5 V switch on voltage) with a 6 V power source, connected using copper tape (3M) and silver paint (SPI, Flash-dry^{TM} Silver Paint) to ensure good connectivity. The resistance of the tracks in the as-produced circuits was measured using a multimeter (Agilent 34401A) attached to the pieces of copper tape, witout the LED present.

2.2.2 Extrusion Printing

All inks deposited via extrusion deposition was performed using an in-house designed 3D printer. The printer was initially designed by C. Mire and M. in het Panhuis [227], but has since been adapted. The moving stage used for both versions is a Sherline Milling machine (Sherline 8020 CNC system) with the milling head removed. Both versions are displayed in Figure 2.1.

Iteration 1 (as described by C. Mire, Figure 2.1 A and B) used a pneumatic air fluid dispenser (EFD, Ultimus II) which was manually controlled in time with the moving stage. The sample mount was a clip that was held on to where the milling head was removed from, and the substrate is placed underneath. As the sonicated inks were too thin to print using only positive air pressure, the inks were thickened post-sonication to have a final [GG] of 0.7% w/w. For these inks, the air pressure applied to achieve consistent extrusion was between 15 and 70 psi, typically at 37 psi. Extrusion needles (EFD) were attached to the base of the syringe, which were applied to suit the resolution required (typically 25G, ID = 0.25 mm, or 32G, ID = 0.10 mm).

Iteration 2 removed the air pressure system and sample holder, and was instead replaced with a custom designed 3D printed mount that holds two linear actuators (Zaber, T-LA60A or T-NA08A50) that extrude out of two 5 mL sy-

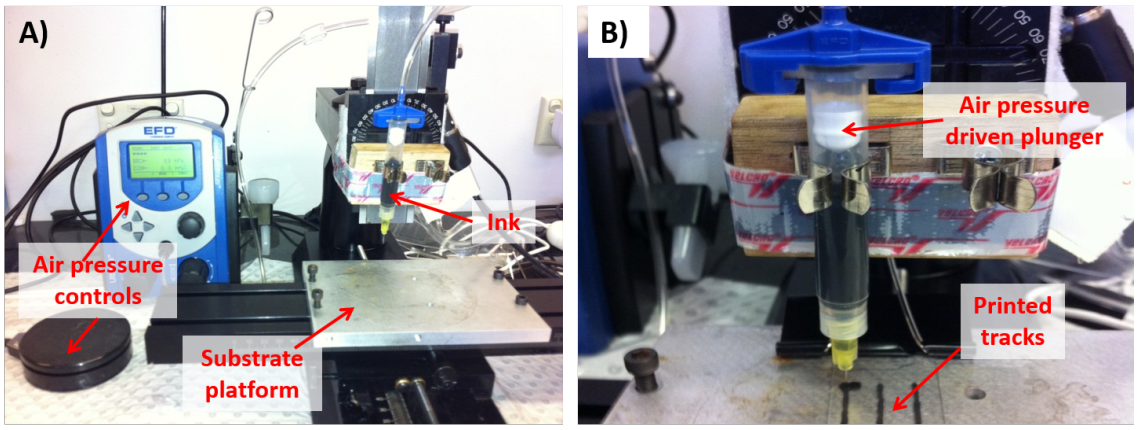

Figure 2.1: A, B) The pneumatic extrusion system used to extrusion write the tracks, with the various parts labelled, showing the general layout of the deposition method. Designed by C. Mire and M. in het Panhuis [227] C, D) The revised version of the same moving stage, displaying the mount with the various parts in place, as labelled.

ringes (fig:extruder C and D). The linear actuators were automatically controlled by custom-coded software, and was timed to match the moving stage. This iteration was designed for 3 printing methods in mind; regular printing, ratio printing (same ratio of two materials), and gradient printing (varying amounts of two materials throughout the print). Both ratio print and gradient printing were mixed at the point of printing.

More details on the extrusion deposition system, as well as the development and applications, can be found in the appendix.

2.3 Analysis Methods

2.3.1 Dispersion Optimisation through UV-Vis-NIR Spectroscopy

Carbon dispersions were prepared as described, however during sonication, a 30 μL 'thief' sample is taken from the vial after sonicating for various times (0.5, 1, 2, 4, 8, 12, 16, 20, 24, 28 mins). This thief sample is then diluted down to have a final CBF concentration of 10 μg mL^{-1}. These diluted samples were then analysed by UV-Vis-NIR spectrometry (Shimadzu UV-3600) between the wavelengths of 850

nm and 1200 nm.

2.3.2 Impedance Analysis

Impedance analysis was performed by applying a 1-V peak voltage ac signal using a waveform generator (Agilent U2761A) swept between frequencies of 1 Hz and 100 kHz, across a circuit consisting of a known resistor, and the sample. The impedance was obtained by measuring the voltage drop across the known resistor with an oscilloscope (Agilent U2701A), and also calculating the phase lag due to the sample.

For dry film samples, the films are cut into short strips (3 mm wide, 30 mm long) and placed between two glass slides held together with constant pressure, and contacted with copper tape (3M) on either side. After a measurement is taken at that length, the sample is then shortened and measured again, to ensure there are 5 different lengths analysed.

For gel samples, they are housed in a custom-designed sample compartment. The sample compartment that held the gels are rectangular in shape, with a width of 5 mm, height 6 mm (giving a cross-secitonal area of 30 mm^2), and lengths of 5 mm, incrementing up to 25 mm in 5 mm increments. Reticulated vitreous carbon (RVC, ERG Aerospace, foam structure with 20 pores per inch, relative density 3 % or void volume 97 %, resistivity 0.323 Ω cm) pieces were placed in the ends of the sample compartment so that the electrode materials could be incorporated into the gels to provide gel–electrode contact.

2.3.3 Mechanical Analysis

The mechanical properties of samples was analysed using a Shimadzu EZ-S Tabletop Universal tensile/compression tester. For both compression and tensile analysis, the instrument was moved at a speed of 2 mm min^{-1} unless otherwise specified. For tensile testing, custom-printed clamps (3D printed titanium) were implemented to ensure that the samples do not slip in the clamp, which consisted of a series of small jagged teeth angled in the opposite direction to the force applied.

Mechanical testing of HEMA-PU cured hydrogels was performed on a universal tensile tester (Shimadzu, EZ-S). 5 x 20 mm strips of the cured HEMA-PU hydrogels without the hydrophobic coating were tested at a rate of 2 mm min^{-1}. The strain gauges were also tested using this same instrumentation. Each strain gauge was tested up to a strain of 15%, at a rate of 6 mm min^{-1}. In order to evaluate the creep, a 15 s pause was added at both the start and end of each cycle. A USB multimeter (Agilent 34401A) was connected and was recording the resistance at 50 μs intervals. Each gauge was subject to 25 loading/unloading cycles.

2.3.4 Rheological Analysis

All rheological properties were mapped using an Anton Paar Physica MCR301 Digital Rheometer equipped with a peltier temperature-controlled plate (Anton Paar, P-PTD 200) and hood (Anton Paar, H-PTD 200) to ensure the tests were all performed at 21 °C. Two main measuring tools were used, depending on the type of analysis required; parallel plate tool (PP15, 15 mm dia.), typically for gel samples, and the conical plate tool (CP50, 50 mm dia., 0.992 ^{o} angle, 97 μm truncation), typically for liquid samples.

For gel samples, they were cast into a mould with a height of 10 mm and 16 mm diameter, to match the diameter of the parallel plate tool. Strain amplitude sweep experiments were carried out at a constant oscillating frequency of 10 Hz, with an oscillatory strain varying between 0.1 and 10 %.

For liquid samples to probe their shear thinning properties, 570 μL of the sample was placed onto the plate, and was measured using the conical plate tool, to ensure the shear stress is constant throughout varying shear rates. The sample is initially pre-sheared for 3 minutes at $\dot{\gamma} = 0.1$ s^{-1}, then the shear rate is ramped from $\dot{\gamma} = 0.1$ to 100 s^{-1} over 2 minutes.

2.3.5 Light Microscopy

All light microscopy images were taken on a Leica Z16 APO optical microscope, connected to a computer via firewire, where the images were obtained using Leica Application Suite version 4.3. Images were illuminated using external LEDs (Leica LED3000 RL). Length analysis for items of interest (*i.e.* nanotube length) was performed using the image analysis software in Leica Application Suite version 4.3.

2.3.6 Scanning Electron Microscopy

All SEM micrographs obtained of free-standing films and as-received CBF samples was performed using a field emission scanning electron microscope (FESEM JEOL JSM 7500-FA) operated at 5 kV and a spot size setting of 8.

For fibre length analysis, the micrographs obtained from the free-standing films sonicated for various times was taken into an image analysis program (Leica Application Suite 4.3) where the average fibre length was calculated. Only fibres that started and finished within the micrograph were analysed.

2.3.7 Transmission Electron Microscopy

TEM analysis of the dispersions was performed using a JEOL 2011 TEM operated at an acceleration voltage of 200 kV. All images were captured on a TEM digital imaging system (Gatan Orius). The samples were cast onto a copper grid (pore size 5 μm) and left to dry under controlled ambient conditions before TEM imaging.

Chapter 3

Conducting carbon nanofibre networks: dispersion optimisation, evaporative casting and direct writing

The optimisation of vapour-grown carbon nanofibres (VGCNFs) dispersed in the biopolymer gellan gum (GG) and its usage as an ink for the direct writing of conducting networks are reported. Sonication optimisation showed that dispersing 10 mg mL^{-1} VGCNFs required 3 mg mL^{-1} GGs solution and 4 minutes of low energy probe sonication. Free-standing films prepared by evaporative casting were found to exhibit electrical conductivity values of up to 35 ± 2 S cm^{-1}. It is demonstrated that sonolysis has a detrimental effect on electrical conductivity. The dispersions were easily modified to allow for direct writing of conducting networks on paper using a commercial fountain pen. The electrical characteristics of these direct written electrodes (on paper) improved with increasing number of layers. The written electrodes on paper were used to connect a battery to a light emitting diode to demonstrate that they can be used in simple devices.

Author Statement

This chapter contains the following published journal article, stylistically edited to suit the rest of this document:

H. Warren, R. D. Gately, H. N. Moffat, and M. in het Panhuis, "Conducting carbon nanofibre networks: Dispersion optimisation, evaporative casting and direct writing," *RSC Adv.*, vol. 3, pp. 21 936–21 942, 44 2013

Author Statement:
I, Reece D. Gately, hereby declare that I contributed to the following work within this manuscript by:

- UV-vis-NIR analysis of dispersion optimisation,
- Assisted in preparation of dispersions,
- Performed SEM imaging, including length analysis,
- Developed the method for direct writing,
- Performed profilometry on the written pen tracks,
- Co-writing of the paper, including figure preparation.

All other work required for this manuscript was performed by other co-authors as follows:
Dr. Holly Warren: Prepared each sample, optimised the sonication time for each dispersion, performed impedance analysis on the free-standing films, prepared all figures, and wrote the manuscript.
Hayley Moffat: Prepared the directly written lines for analysis, and performed the longevity study of the ink.
Prof. Marc in het Panhuis: Assisted in proof-reading and editing the manuscript.

I, Prof. Marc in het Panhuis (supervisor), support and certify that the above author statement is correct.

Marc in het Panhuis
April 20, 2017

3.1 Introduction

Additive manufacturing or rapid prototyping refers to techniques capable of building structures layer-by-layer, such as 3D printing [254], laser sintering [255], air-brush spraying [256], dip-pen nanolithography [257], slot-dye coating [258], gravure printing [259], inkjet printing [260–262], and extrusion printing [263]. These techniques have been extensively used for the fabrication of conductive electronics. Recently, conducting paper substrates have been used as part of low-cost, flexible, disposable devices [264–266]. This has led to the emergence of pen-on-paper (PoP) electronics, in which pens filled with conducting silver ink have been employed to create devices such as interconnects for light emitting diodes and antennas on paper [225]. The PoP approach requires inks with specific flow characteristics under ambient conditions, *i.e.* it should readily flow during writing and it should not coagulate in the pen. It has been shown that the resulting feature size of the written lines depend on the pen speed and the physiochemical properties of the ink and paper [267]. GG is a linear anionic polysaccharide produced from the bacterium *Pseudomonas elodea* [109, 268]. It is composed of tetrasaccharide repeating units of glucose, glucuronic acid and rhamnose in a molar ratio of 2 : 1 : 1 [269]. Aside from its wide- spread application in food and cosmetics, GGs unique suspending (dispersing), gelation and rheological properties have been used in the process of conducting carbon fillers such as SWCNTs, MWCNTs and graphene [105, 253, 270].

CNF are a conducting carbon filler which are closely related to CNTs, both in their structure and in their properties [271]. A CCVD synthesis method (with the use of a floating catalyst) has facilitated large-scale production of VGCNFs [272]. The structure of these VGCNFs is "cup-stacked", meaning their stacking morphology is one of truncated conical graphene layers around a large hollow core [61]. Their average diameter (100 nm) and average length (50 to 200 μm) can be tuned by precise control of the synthesis conditions [43] and are similar to MWCNTs produced by chemical vapour deposition (CVD) [273]. As-produced VGCNFs are often coated with layers of amorphous carbon which serves to reduce the electrical

conductivity due to low crystallinity [61]. This amorphous layer can be removed by post-treatment of the fibres with heat, which increases the crystallinity [274] and results in a double-layered nanofibre [63]. The VGCNFs used in this paper underwent a heat treatment at 1500 °C, which resulted in a highly graphitised outer layer of the hollow carbon fibre.

CNFs have potential applications as gas sensors [275], electrostatic paint and electronic shielding for the automotive industry and as components in batteries [274]. VGCNFs have been dispersed into various polymers including polystyrene (PS) [275], polypropylene (PP) [61, 274] and poly(methyl methacrylate) (PMMA) [276] using high-shear stirring methods. It has been shown that using a sonication bath followed by high-speed mechanical stirrign is a better dispersion method for VGCNFs (in an epoxy) compared to dispersing in a solvent for surfactant [277]. The reported electrical conductivity values for these composite materisl ranged from 0.01 S cm^{-1} (PMMA composite, 10 % w/w VGCNF) to 2 S cm^{-1} (PP composite, 60 % w/w VGCNF) [273, 275, 278].

In this paper, we describe a carbon nanofibre ink suitable for the direct writing of conducting networks using a pen-on-paper direct writing approach. The VGCNF dispersion is optimised in terms of maximum VGCNF loading fraction. It is demonstrated that written electrodes on appers have suitable electrical properties, *i.e.* they can be used to draw simple circuitry for connecting a light emitting diode (LED) to a battery power source.

3.2 Experimental

3.2.1 Preparation of dispersions

Low acyl gellan gum (GG, Gelzan, lot #1I1443A) was received as a gift from CP Kelco. Gellan gum solutions (0.5 % w/v) were prepared by dissolving dry powder (0.5 g) in Milli-Q water (100 mL, ≈ 80 °C, resistivity 18.2 MΩ cm), while stirring at ≈ 800 rpm (IkA RW 20 digital) for 30 minutes. Homogeneous dispersions of

vapour grown carbon nanofibres (Pyrograf Products, PR24-LHT, Batch info: PS 1345 Box 8, HT170) in GG were prepared using probe sonication. All dispersions were subjected to sonolysis using a digital sonicator horn (Branson Digital Sonifier) with a power output of 6 W in pulse mode (0.5 s on/off) and a tapered microtip (Consonic, diameter 3.175 mm) placed 1 cm from the bottom of a glass vial (diameter 25 mm).

3.2.2 Preparation of free-standing films

Drop-cast films were prepared by evaporative casting of composite dispersions onto the base of a cylindrical plastic petri-dish (diameter $\approx$ 5.5 cm) and dried under controlled ambient conditions (21 °C, 50 % relative humidity, RH) using a temperature/humidity chamber (Thermoline Scientific TRH-150-SD) for 24 h. The films were then peeled off the substrate to yield uniform free-standing films.

3.2.3 Direct writing

Direct writing was carried out using a commercially available fountain (nib) pen (Parker Jotter, Officeworks) with a refillable cartridge. VGCNF-GG inks were prepared as follows; GG solutions (3 mg mL^{-1}) were sonicated for 4 min (power output of 6 W) prior to addition of VGCNFs (10 mg mL^{-1}), followed by a further 4 min (power output of 6 W) of sonolysis. High quality photo paper (Spilman, matte, 180 g m^{-2}) was used as the substrate. Multiple circuits were prepared on paper substrates using directly written electrodes to connect LEDs (Jaycar Electronics, Australia, 5 mm diameter, green light source, 3.5 V switch on voltage) with a power source (6 V batter) using copper tape (3M). Connection was ensured through placing the legs of the LEDs in contact with the directly written tracks, and was held in place with conducting copper tape (3M). The power source was also connected in a similar manner, using leads with alligator clips to connect to the conducting copper tape instead.

3.2.4 Characterisation techniques

The absorbance behaviour of dispersions (diluted to VGCNF concentration of 6.67 mg mL^{-1}) was obtained using UV-vis-NIR spectroscopy (Cary 500 UV-vis-NIR spectrophotometer) with a 1 cm path length cuvette. The wavelength of 1000 nm was arbitrarily selected for analysis as it is in the wavelength range at which VGCNFs exhibit absorbance features, but GG does not. Small aliquots (20 μL) of the dispersion sample were removed at varying sonication times and analysed for the presence of aggregated carbon inhomogeneity using a Leica Z16 APO optical microscope (8× magnification).

The flow properties of composite inks were studied using an Anton Paar Physica MCR 301 Digital Rheometer with a cone and plate measuring system (49.972 mm diameter, 0.992 ^{o} angle, 97 μm truncation) and a heat controlled sample stage (Julabo Compact Recirculating Cooler AWC 100). Viscosity was measured between 0.1 and 100 s^{-1} shear rate at 21 °C.

The surface morphology of films and written electrodes containing VGCNFs were assessed using SEM (FESEM JEOL JSM 7500-FA) and optical profilometry (Veeco Wyko NT9000). VGCNF length was calculated through obtaining multiple SEM images of an evaporatively cast film, and measuring the length of all visible VGCNFs (Leica Application Suite, 4.3). In order to obtain cross-sectional SEMs of fountain pen lines, the paper substrate was cooled using liquid nitrogen and snapped across the track. The thickness of drop-cast films was determined using a digital micrometer (Mitutoyo IP 65).

Electrical resistance measurements were carried out as follows. Evaporatively cast films were cut into strips of 3 mm x 25 mm and contacted (top and bottom) with conducting copper tape (3M) and conducting silver paint (SPI). The electrodes prepared by direct writing were contacted using the conducting copper tape. Current (I)-voltage (V) characteristics were obtained by measuring current using a digital multimeter (Agilent 34410A) under a cycling potential applied by a waveform generator (Agilent 33220A) under controlled ambient conditions (21 °C, 50 % RH).

$I-V$ plots were evaluated as a function of sample length (L), and used to calculate total resistance (R_T) values. The conductivity (σ) and contact resistance (R_C) were calculated by straight line fitting of the R_T versus L data to:

$$R_T = (1/A_{cross}\sigma)L + R_C \tag{3.1}$$

where A_{cross} is the cross-sectional area and $1/(A_{cross}\sigma)$ represents the sample resistance (R_s).

3.2.5 Statistical treatment

The reported results are averages of the values obtained. Reported numerical errors and graphical error bars are given as ± 1 standard deviation (SD). Data and outliers were rejected either when instrumental error was known to have occured, or if data failed a !-test with a confidence interval $\geq$95 %.

3.3 Results and Discussion

3.3.1 Optimisation of dispersions

Previous research established that there is a strong correlation between UV-visible absorbance intensity and carbon-based materials [279]. In this work, the ability of the biopolymer gellan gum (GG) to disperse VGCNFs was assessed using UV-vis-NIR spectroscopy and light microscopy. It is assumed that the VGCNFs are completely dispersed when the UV-vis-NIR absorbance reaches a plateau coupled with the disappearance of visible aggregates.

Figure B.1 (Appendix B, supporting information) shows that a dispersion (volume 10 mL) containing 1 mg mL^{-1} VGCNFs and 1 mg mL^{-1} GG can be assumed to have reached completion after 4 min of sonication, *i.e.* the UV-vis-NIR absorbance plateaus (Figure B.1A and B) and the visible aggregates have disappeared (Figure B.1C-K). The amount (or expense, $E_\$$) of sonic energy (power x sonication)

required to disperse 10 mg VGCNFs in 10 mL of dispersion is 144 J mg^{-1}.

The VGCNF-GG dispersion system was optimised by establishing the minimum energy (expense, $E_\$$) required to completely disperse a given mass of VGCNFs. The optimum sonication time (and expense) was found to increase with GG concentration in the investigated range (0.25-1.5 mg mL^{-1}) at constant VGCNF concentration (1 mg mL^{-1}), see Figure 3.1A and Table B.1 (Appendix B, supporting information). It is well known that the viscosity of polymer solutions increases with increasing polymer concentration. As such, it is suggested that the increase in sonication time is related to the increase in viscosity which is likely to drive down VGCNF mobility, therefore requiring more sonolysis to completely disperse the VGCNFs.

It is clear that GG is efficient at dispersing VGCNFs, i.e. only 1 min ($E_\$ = 36 \pm 18$ J mg^{-1}) of sonication is needed to disperse 10 mg ofVGCNFin 10 mL at a VGCNF-GG ratio of 10 : 2.5. As expected, the input sonication energy required to reach the point of complete dispersion increased as theVGCNFconcentration was increased from 1 mg mL^{-1} to 20 mg mL^{-1} (Figure 3.1). It should be noted that it was not physically possible to incorporate more than 200 mg VGCNFs in 10 mL of GG solution. As the VGCNFs supplied by Pyrograf are not pelletised, it has a very low density, and the volume of 200 mg VGCNFs is greater than that of 10 mL. Even with light compression using a glass plunger, it was found that when the GG was added to $>$ 200 mg VGCNFs it would form a thick solution that could not be sonicated. Hence, we were unable to establish the upper concentration limit of the VGCNF.

The VGCNF expense was found to exhibit a minimum of 14.4 ± 3.4 J mg^{-1} for a VGCNF-GG dispersion with VGCNF concentration = 10 mg mL^{-1} (GG concentration = 3 mg mL^{-1}), see Figure 3.1C. It is not clear at present what the dependence of expense and VGCNF concentration should be. However, it is likely that this dependence is influenced by rheological percolation effects related to either the dispersant GG and/or the carbon materials [245, 280].

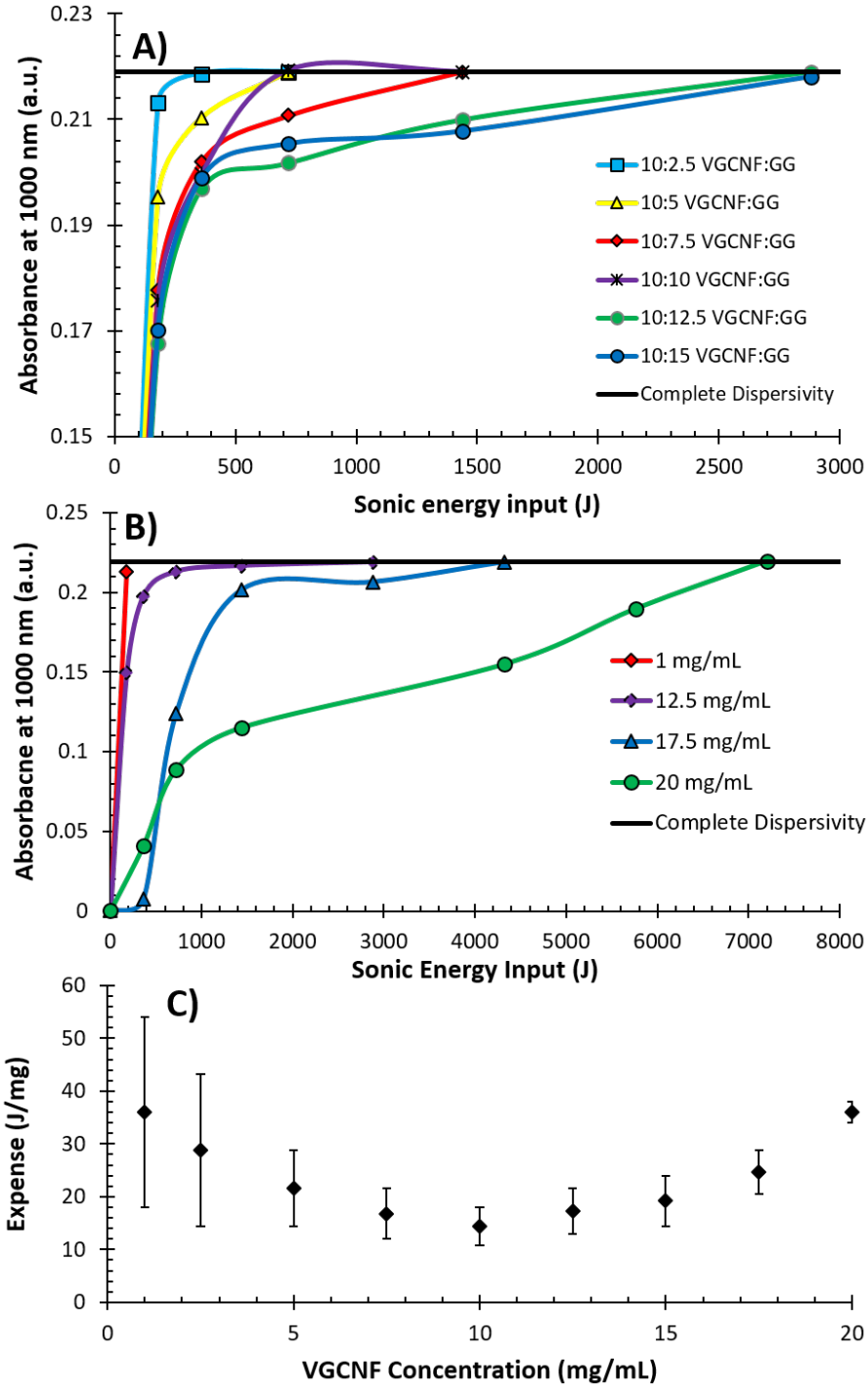

Figure 3.1: (A) UV-vis-NIR absorbance at 1000 nm as a function of sonication energy for 10 mg of VGCNFs dispersed in 10 mL GG solution at various VGCNF-GG ratios. The solid line indicates the expected absorbance for a complete dispersion. (B) UV-vis-NIR absorbance at 1000 nm versus input sonication energy for VGCNF-GG dispersions of increasing loading fraction. Horizontal black line represents the maximum absorbance for complete dispersion. (C) Expense to achieve a complete dispersion as a function of VGCNF concentration. All dispersions were diluted to a VGCNF concentration of 6.67 % mg mL^{-1}.

3.3.2 Electrical characteristics of free-standing films

The electrical conductivity of freestanding VGCNF-GG films (mass ratio 10 : 3, mass fraction 0.77) prepared by evaporative casting was adversely affected by sonication. For example, the electrical conductivity of films prepared from a VGCNF-GG dispersion ([VGCNF] = 5 mg mL^{-1}) subjected to 4 min of sonication is 35 ± 2 S cm^{-1}. As described above, increasing the VGCNFs loading requires longer sonication times, see Figure 3.1B. For example, dispersing 20 mg mL^{-1} of VGCNFs requires a sonication time of 20 min. The resulting films exhibited a lower conductivity (20 ± 2 S cm^{-1}) compared to films prepared using dispersions which were sonicated for 4 min, despite having the same VGCNF volume fraction. The decrease in conductivity was found to linearly decrease with increasing VGCNF concentration (Figure 3.3A). We have attributed this to sonication-induced damage of the VGCNF, resulting in reducing the overall length. Similar effects have been previously reported for carbon nanotubes [281–283].

The reduction in VGCNF length was examined using SEM analysis (Figure 3.2A and B). Length analysis (Figure 3.2C) clearly indicates that the average length of the fibres is smaller for the dispersions sonicated for 20 min (average 1.1 μm) compared to 4 minutes (average 2.1 μm). Figure 3.2C shows that the majority (60 %) of the VGCNFs which had been sonicated for 20 min were between 0.5 and 1 μm in length. In contrast, the VGCNF dispersion which underwent 4 min of sonication consisted of VGCNFs with a wider range of lengths, including some with lengths of >3 mm. It is well-known that electrical transport through a network of conductors is determined by the number of junctions and the resistance of these junctions in the network [284]. The reduction in conductivity can then be argued as follows. VGCNF sonication results in a reduction in the length of the VGCNFs, which increases the number of junctions in the VGCNF network leading to an increased electrical resistance (decreased conductivity).

The percolation behaviour of the VGCNF-GG system was investigated by preparing free-standing films with different VGCNF loading fraction (Figure 3.3B). The

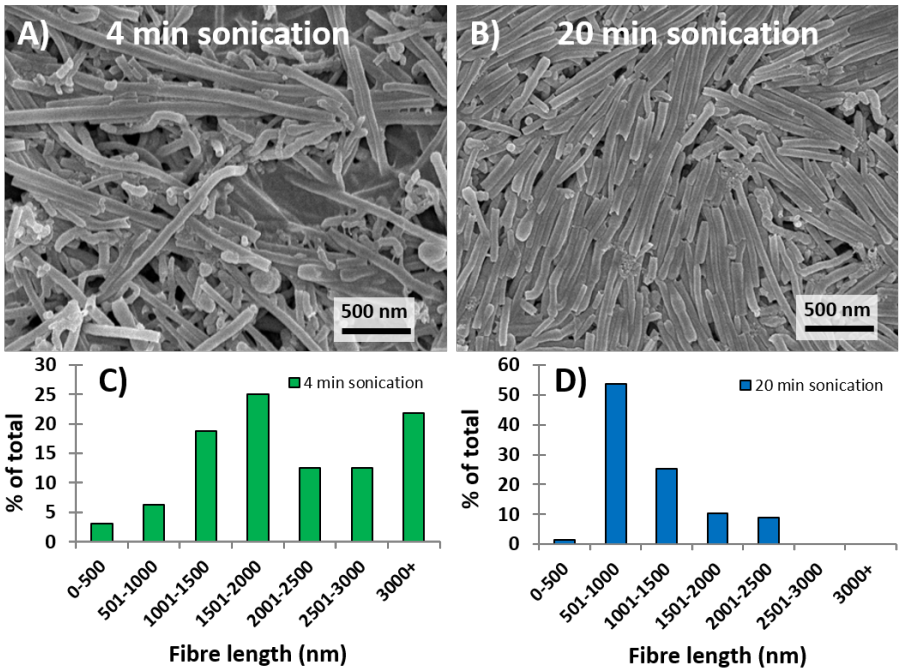

Figure 3.2: (A and B) SEM images of free-standing VGCNF-GG films (VGCNF volume fraction = 0.69) prepared from VGCNF-GG dispersions (VGCNF concentration = 10 mg mL^{-1}, GG concentration = 3 mg mL^{-1}) which were sonicated for 4 minutes and 20 minutes, respectively. (C) and (D) Histograms showing length of the VGCNFs based on analysis of SEM images (28 μm^2 area) for samples sonicated for 4 and 20 minutes, respectively.

conductivity as a function of VGCNF mass fraction was fitted to the statistical percolation model [285]:

$$\sigma = \sigma_o(\varphi - \varphi_c)^t, \tag{3.2}$$

where σ, σ_o, φ, φ_c and t are the conductivity, scaling factor, mass fraction, mass fraction percolation threshold and the critical exponent, respectively. The fit predicted values for σ_O, φ_C and t as 0.046 ± 0.004 S cm^{-1}, 0.0147 ± 0.003 and 1.7 ± 0.2, respectively. The t value is close to the theoretical predicted value ($t = 2.0$) for a 3D percolative network [285].

3.3.3 Direct writing with a fountain pen

Direct writing was investigated using a commercial fountain (nib) pen. The flow curve of a typically used commercial ink (Parker "Quink" blue-black) is shown in Figure 3.4, and was fitted to the well-known power law model [286]:

$$\eta = K\dot{\gamma}^{n-1}, \tag{3.3}$$

where $\dot{\gamma}$ is the shear rate, K is the consistency index and n is the power law index. This analysis revealed that the commercial ink exhibits near-Newtonian behaviour, *i.e.* $n = 0.9$. The viscosity of the commercial ink at shear rates common for pen writing (1000 s^{-1}) is approximately 0.81 mPa s. We achieved a similar viscosity (at this shear rate) by sonicating a GG solution (3 mg mL^{-1}) for 4 minutes prior to adding 100 mg of VGCNFsand sonicating for a further 4 minutes.

Analysis of the flow curve of our VGCNF pen ink revealed consistency and power indices consistent with shear thinning behaviour, *i.e.* $K = 26$ mPa s^n and $n = 0.54$, respectively. However, despite the rheological difference (near-Newtonian vs. shear thinning) our VGCNF ink has the required viscosity at the shear rates important for pen writing, *i.e.* $\dot{\gamma} = 1.1$ mPa s at shear rate = 1000 s^{-1}.

Lines were drawn (direct written) on a paper substrate using a fountain pen

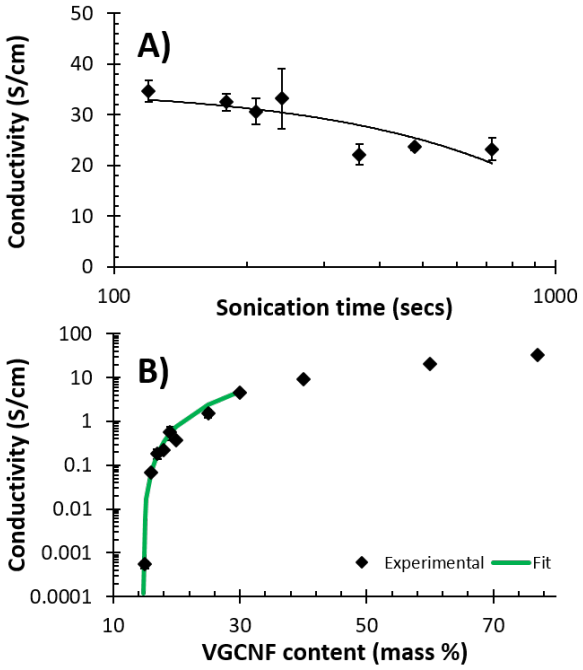

Figure 3.3: Electrical conductivity of drop cast films as a function of VGCNF (A) sonication time and (B) mass fraction. The straight line in (B) is a linear fit to the data. The solid line in (A) is a 3-parameter fit of the conductivity to the statistical percolation model, Equation 3.2.

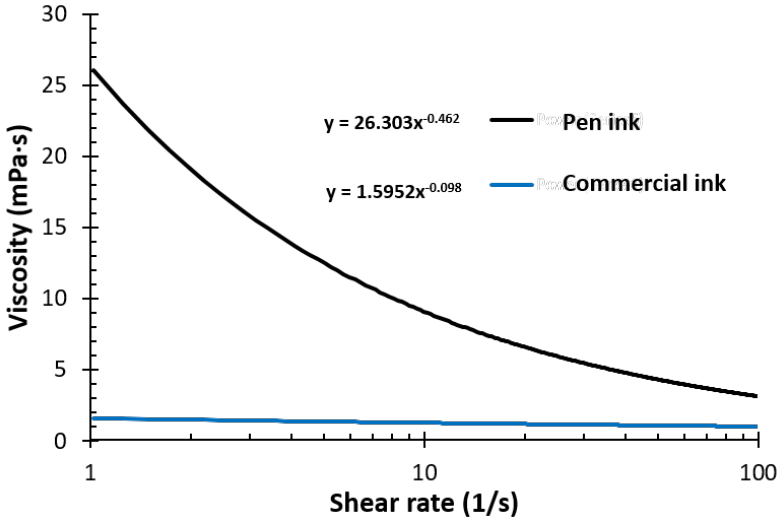

Figure 3.4: Viscosity as a function of shear rate for commercial pen ink (Parker "Quink" blue-black, dotted line) and VGCNFpen ink (solid line). The VGCNF ink was prepared by sonicating a gellan gum solution (3 mg mL^{-1}) for 4 minutes prior to adding 100 mg of VGCNFs (10 mg mL^{-1}) and sonicating for an additional 4 minutes.

filled with our pen ink (VGCNF concentration = 10 mg mL^{-1}, GG concentration = 3 mg mL^{-1} Figure 3.5). The morphology of pen tracks on paper was investigated using optical and electron microscopy (Figure 3.6). The characteristic "W" shape of nib fountain pen tracks is clearly visible in Figure 3.6A and B.

This shape is a result of the nib of the pen depressing the paper substrate during writing. SEM images revealed the presence of a VGCNFnetwork in all areas of the "W" shape, including on the surface of the central ridge (Figure 3.6C and D). Optical profilometry and cross-sectional SEM analysis was used to examine the effect of increasing the number of fountain pen ink layers on a paper substrate (Figure 3.6F). It was found that increasing the number of pen layers resulted in a linear increase in the line width (Figure 3.7A).

The number of layers had a significant effect on the electrical resistance (Figure 3.7B). The resistance decreased by almost two orders of magnitude over 10 layers. The resistance (corrected for contact resistance) of the lines (channel length 5 cm) was found to have a power-law dependence on the number of pen layers according to:

$$R_S = R_{S1} L^P, \tag{3.4}$$

where R_S, R_{S1}, L and P are the sample resistance, sample resistance of 1 layer, number of layers and power-law index, respectively. Our fit revealed values of R_{S1} = 75 ± 1 kΩ cm^{-1} and P = -1.218 ± 0.006. The fit underestimates the actual value for 1 direct written line (97 ± 20 kΩ cm^{-1}), which is a likely to be a result of initial ink uptake by the paper substrate. The contact resistance R_C also decreased with increasing number of pen layers (data not shown). These results indicate that with each written layer the amount of VGCNFdeposited increases which leads to a better contact between sample and electrode, and an improved electrical resistance [105].

The usefulness of our approach for direct writing paper electrodes for practical purposes was assessed by investigating the variability in the electrical resistance as a function of time for direct written lines, and the ability of electrodes to power an LED in a simple device. The variability was tested using two different approaches, (i)

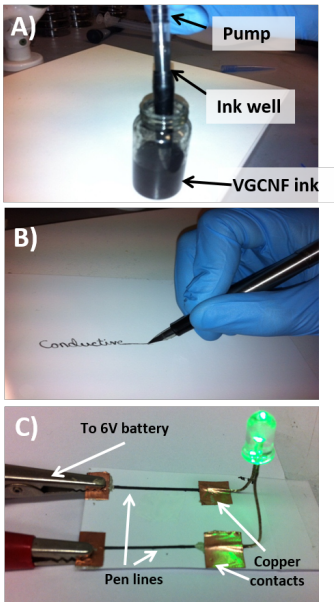

Figure 3.5: Direct writing of the VGCNF ink with a fountain pen. (A) Image of the commercial Parker Jotter fountain pen with pump-filled ink well and VGCNF ink, (B) image of the direct writing process, (C) Image of an LED powered by a power source (6 V battery) using direct written electrodes on a paper substrate (5 ink layers).

lines were direct written immediately after ink preparation, and electrical testing was carried out as function of resting time (Figure 3.7C), and (ii) there was a resting time between preparation of the ink and direct writing, followed by immediate electrical testing (Figure 3.7D). It is clear that once processed, the electrical resistance (3.4 $\pm$ 0.1 kΩ cm^{-1}) of the direct written pen lines (channel length 5 cm, 10 layers) does not change over 10 days. In contrast, the electrical resistance remains constant over the first 4 days, but then steadily increases with time between preparation of the ink and direct writing the electrodes. However, gentle shaking of the ink prior to direct writing can remove the increase in the electrical resistance (Figure 3.7D). For example, shaking the ink after 11 days resulted in a reduced resistance, similar to that of the initial resistance values (within error). This suggests that the ink can be stored for up to 3 days prior to direct writing, while it will require gentle shaking for longer time periods to re-disperse the VGCNFs in the ink. VGCNF written electrodes on paper were used in a simple circuit to connect an LED to a 6 V power source (Figure 3.5C). Current-voltage measurements were taken across each of the

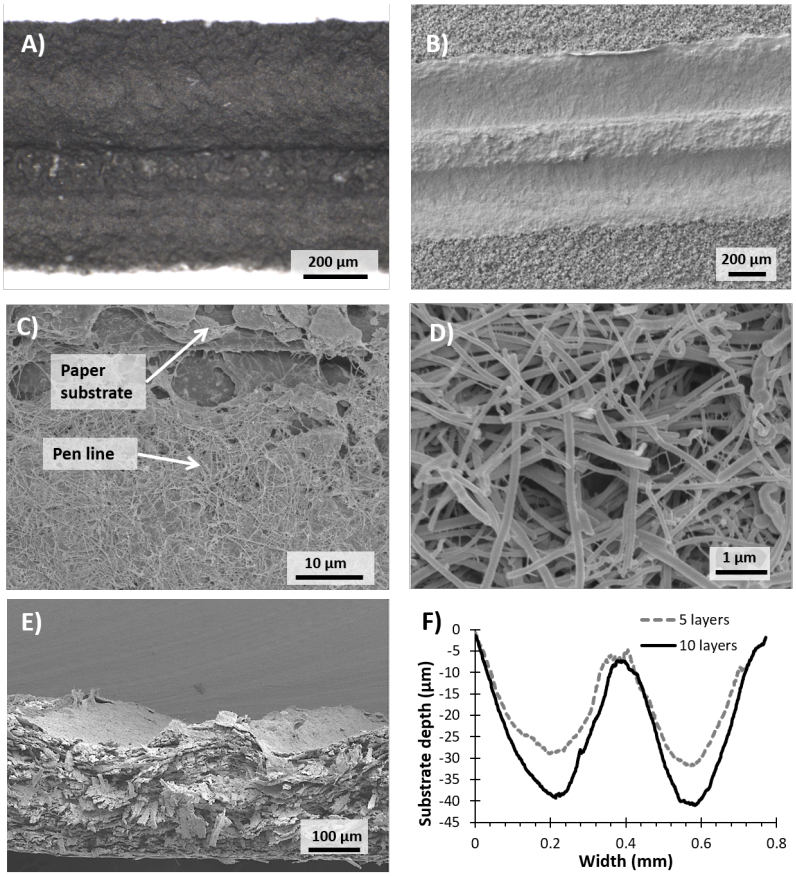

Figure 3.6: Morphology of typical direct written lines (electrodes, 5 layers) on the paper substrate. (A) Optical and (B) SEM images of the line. (C) SEM image of the edge of a line. (D) Enlarged view of the VGCNF network. (E) SEM of the cross-section. (F) Optical profilometry of direct written lines (5 and 10 layers).

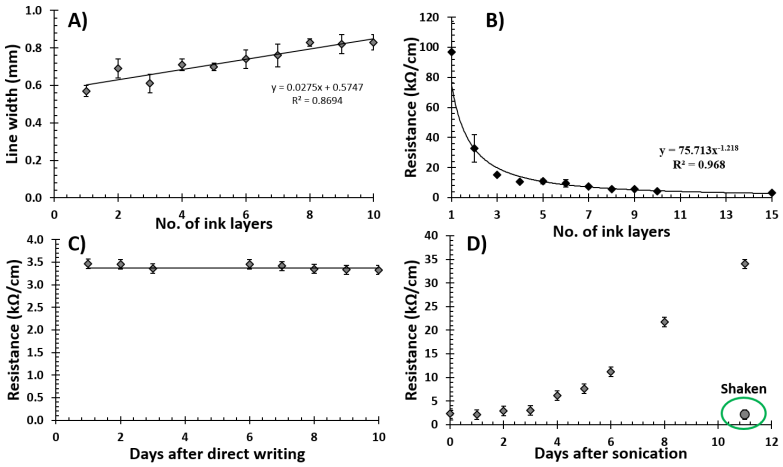

Figure 3.7: (A) Line width a function of number of ink layers for typical direct written lines on a paper substrate. Straight line is a linear fit to the data. (B) Electrical sample resistance of direct written lines as a function of number of ink layers on a paper substrate. Line is a power-law fit to the data. (C) Electrical (sample) resistance of typical direct written lines (10 layers) as a function of days after direct writing. Straight line is a guide to the reader's eye. (D) Electrical (sample) resistance of typical direct written lines (10 layers) as a function of resting time between ink preparation and direct writing. Circle indicates electrical resistance for an ink which was shaken on day 11 after preparation, prior to direct writing.

written lines (R_1 and R_2, Figure 3.5C) and across the LEDs. The average resistances across the 5-layered lines, R^1 and R^2, were found to be similar, *i.e.* 8.0 ± 0.3 and 8.0 ± 1.1 kΩ cm^{-1}, respectively. These measurements show that electrodes prepared by direct writing are stable over time and can be used in simple devices.

3.4 Conclusions

The dispersion optimisation of vapour-grown carbon nanofibres in solutions of the biopolymer gellan gum has been investigated. It was found that dispersing VGCNF in GG required only short sonication times and low sonication energy input. For example, 1 mg mL^{-1} of VGCNF could be completely dispersed in 1 mg mL^{-1} GG with 1 min of sonication at low power (6 W). It was demonstrated that gellan gum could easily disperse up to 20 mg mL^{-1} of VGCNF at a VGCNF-GG ratio of 10 : 3, which required 20 min of sonolysis. The electrical conductivity of free-standing films

decreased with increasing sonication time. For example, increasing the sonication time from 4 to 20 min decreased from 35 S cm^{-1} to 20 S cm^{-1}, which was attributed to the observed sonication-induced damaged in the length of the conducting carbon filler. Direct writing of VGCNF dispersions with a commercial fountain pen was also explored. The sonolysis protocol was changed to achieve VGCNF dispersion with similar viscosity at shear rates common to pen writing as a commercial pen ink. The electrical resistance of direct written electrodes on paper exhibited a power law dependence on the number of pen layers. Microscopy analysis suggested that with each successive pen stroke the amount of VGCNFincreases leading to the observed improved electrical characteristics. It was demonstrated that our direct written electrodes on paper can be used in simple device applications, such as connecting an LED to a power source. The electrical resistance of the paper electrodes was found to be stable for up to at least 10 days under ambient conditions. This paper contributes to the development of paper-based electrode materials.

3.5 Acknowledgements

This work was supported by the University of Wollongong and the Australian Research Council (Centre of Excellence and Future Fellowship programs). The authors acknowledge use of the facilities and the assistance of Mr T. Romeo at the UOW Electron Microscopy Centre. Prof P. Calvert (University of Massachusetts) and Dr R Clark (CP Kelco) are thanked for stimulating discussions and provision of gellan gum, respectively.

Chapter 4

Electrical conductivity, impedance, and percolation behaviour of carbon nanofibre and carbon nanotube containing gellan gum hydrogels

The electrical impedance behaviour of gellan gum (GG), GG-carbon nanotube, and GG-carbon nanofibre hydrogel composites is reported. It is demonstrated that the impedance behaviour of these gels can be modelled using a Warburg element in series with a resistor. Sonolysis (required to disperse the carbon fillers) does not affect GG hydrogel electrical conductivity (1.2 ± 0.1 mS cm^{-1}), but has a detrimental effect on the gel's mechanical characteristics. It was found that the electrical conductivity (evaluated using impedance analysis) increases with increasing volume fraction of the carbon fillers and decreasing water content. For example, carbon nanotube containing hydrogels exhibited a six- to sevenfold increase in electrical conductivity (to 7 ± 2 mS cm^{-1}) at water content of 82 %. It is demonstrated that at water content of 95 ± 2 % the electrical behaviour of multiwalled nanotube containing hydrogels transitions (percolates) from transport dominated by ions (owing to GG) to transport dominated by electrons (owing to the carbon nanotube network).

Author Statement

This chapter contains the following published journal article, stylistically edited to suit the rest of this document:

H. Warren, R. D. Gately, P. O'Brien, R. Gorkin, and M. in het Panhuis, "Electrical conductivity, impedance, and percolation behavior of carbon nanofiber and carbon nanotube containing gellan gum hydrogels," *J. Polym. Sci., Part B: Polym. Phys.*, vol. 52, no. 13, pp. 864–871, 2014

Author Statement:
I, Reece D. Gately, hereby declare that I contributed to the following work within this manuscript by:

- Developed the software and hardware interface for the impedance system,
- Sample preparation of all dispersions,
- Impedance testing of all samples,
- Benchmarked the custom-built instrument to commercially available systems.

All other work required for this manuscript was performed by other co-authors as follows:
Dr. Holly Warren: Prepared all gellan gum (GG) hydrogels, assisted in developing and benchmarking the impedance system, performed mechanical analysis on nanotube samples, ran all rheological analysis, and wrote the manuscript.
Patrick O'brien: Performed analysis on the nanofibre hydrogels (including mechanical and electrical).
Dr. Robert Gorkin III: Assisted in development of the impedance system.
Prof. Marc in het Panhuis: Assisted in proof-reading and editing the manuscript.

I, Prof. Marc in het Panhuis (supervisor), support and certify that the above author statement is correct.

Marc in het Panhuis
April 20, 2017

4.1 Introduction

Electrically conducting hydrogel materials have been studied for a wide range of applications ranging from strain sensors for soft robotics [287, 288], stretchable conductors [289], foldable actuators [145, 290] to neural prosthetic interfaces [291]. As non-ionic hydrogels are not natively electrically conductive, researchers have used various approaches to increase the electrical conductivity of hydrogels by adding salt [287, 289], doping with strong acids [292], and incorporating conducting fillers such as conducting polymers such as poly(3,4-ethylenedioxythiophene): poly(styrenesulfonate) (PEDOT:PSS) [293–295].

In addition, it is well known that the swelling ratio (wet mass divided by dry mass) or water content of hydrogels has an important effect on the mechanical and electrical characteristics of hydrogels [296]. For example, it has been shown that the electrical conductivity of double network hydrogels incorporated with a conducting polymer (PEDOT) is inversely proportional to the swelling ratio [296].

The conductivity of ion (ionic liquid containing) gels and hydrogels has been evaluated using a wide variety of methods. These approaches include alternating and direct current measurement techniques such as electrical impedance, conductivity meters, and four-point probe methods [293–295, 297, 298]. Overall, there are a number of differences between these methods. For instance, conductivity meters evaluate the impedance using an alternating current at a single frequency, whereas four-point methods use a direct current, which is applied to the surface.

Most of the reported electrical conductivity values for con- ducting filler composite hydrogel materials are in the order of 1–2 mS cm^{-1}. For example, PEDOT:PSS composite hydrogels (water content, 75–90 %) exhibited values in the range of 0.67–2.6 mS cm^{-1} depending on the conducting polymer content [294, 295]. Similar electrical conductivity values were obtained for hydrogels consisting of polyacrylate and a conducting polymer [297, 299]. Higher values ($>$ 4.3 mS cm^{-1}) have been reported, but this usually requires different synthesis strategies [296], or using hydrogels that consist of solely the conducting polymer, that is without a polymer

matrix [300].

One example of a commonly used polymer matrix is the biopolymer GG. It is anionic extracellular polysaccharide produced by a fermentation process of the bacterium Pseudomonas elodea [301] and is commonly used in the food industry as a thickener [109]. GG forms rigid gels by crosslinking with cations. For example, it has been shown that divalent cations, such as magnesium and calcium, are more effective cross-linkers than monovalent cations [109, 302].

The application of GG as a material for tissue engineering is rapidly gaining attention [263, 303]. In addition, several groups (including ours) have shown that GG is an efficient dispersant for conducting carbon fillers such as carbon nanotubes and carbon nanofibers [52, 114, 115, 245].

In this article, we report on the preparation and characterisation of conducting carbon filler containing GG hydrogels. Conducting carbon fillers such as SWCNTs, MWCNTs and VGCNFs are incorporated into hydrogels using sonication, followed by physical crosslinking with Ca^{2+} ions. The gels are characterized using oscillatory rheology and electrical impedance analysis.

4.2 Experimental

4.2.1 Dispersion Preparation

GG solutions were prepared by dissolving dry GG powder (low acyl GG, Gelzan, lot # 1I1443A), which was generously provided by CP Kelco, in Milli-Q water (100 mL, $\approx$ 80 °C, resistivity, 18.2 MΩ cm), while stirring at $\approx$ 800 rpm (IKA RW 20 digital). Composite dispersions of SWCNTs (Unidym, lot # P0261), MWCNTs (Nanocyl S.A., Belgium, lot #090901) and VGCNFs (Pyrograf Products, PR24-LHT, Batch info: PS 1345 Box 8, HT 170) in GG with carbon materials:GG weight ratios of 10:4, 10:3, and 10:3, respectively, were prepared using probe sonication with a digital sonicator horn (Branson Digital Sonifier). A power output of 6 W was utilized with a 0.5 s on/off pulsing cadence and a tapered microtip (Consonic,

diameter, 3.175 mm) placed 1 cm from the bottom of a glass vial (diameter, 25 mm).

4.2.2 Gel Preparation

Hydrogels were prepared such that the final concentration of GG was 0.5 % w/v. GG hydrogels were prepared by crosslinking GG solutions (some of which were subjected to sonolysis of up to 50 min) by adding 5 mM of $CaCl_2$. In the case of solutions undergoing sonolysis, GG hydrogel is prepared by sonicating 5 mg mL^{-1} of GG (0.5 % w/v) for 50 min prior to crosslinking with Ca^{2+} ions (5 mM $CaCl_2$,80 °C). The solutions were then poured into plastic moulds and allowed to cool under controlled ambient conditions (21 °C; relative humidity, 45 %).

Composite hydrogels were prepared by adding fresh GG powder to SWCNT, MWCNT, and VGCNF dispersions (with stirring and heating at 80 °C until fully hydrated) to increase the GG concentration to 0.5 % w/v, prior to crosslinking with Ca^{2+} ions (5 mM $CaCl_2$,80 °C). For instance, a hydrogel containing 10 mg mL^{-1} of MWNT is prepared by sonicating MWCNT (10 mg mL^{-1}) for 30 min in 3 mg mL^{-1} of GG, after which fresh GG powder is added to bring the total GG concentration to 5 mg mL^{-1} (0.5 % w/v). The dispersions were poured into plastic moulds and allowed to cool under con- trolled ambient conditions (21 °C, 45 % relative humidity using a Thermoline Scientific temperature/humidity chamber). Regardless of the amount of carbon filler, the same pro- portion of GG was subjected to sonication. It should be noted that the duration of sonication depends on the amount and type of conducting filler, as it is easier to disperse equivalent amounts of VGCNFs compared to MWCNT as described in the Results and Discussion section.

Hydrogels with water content from 0 to 100 % were prepared by selectively removing water under controlled ambient conditions using the temperature/humidity chamber. Water content was determined using weight measurement.

4.2.3 Characterization

Rheological analysis was carried out using an Anton Paar Physica MCR 301 Digital Rheometer (parallel plate tool; diameter, 15 mm) at 21 °C, with the aid of a Peltier temperature-controlled bottom plate system. Gels were poured into a mould with dimensions of 10 mm height and 16 mm diameter. Strain amplitude sweep experiments were carried out at constant frequency of 10 Hz and oscillating strain varying between 0.01 and 10 %.

The electrical impedance behaviour of gel samples was obtained for frequencies between 1 Hz and 100 kHz using a custom-designed instrument and sample compartment (Figure 4.1). The sample compartment held the gels which were moulded into a rectangular shape with a width of 1 cm, height 1 cm, and length up to 2.5 cm. Reticulated vitreous carbon (RVC, ERG Aerospace, foam structure with 20 pores per inch, relative density 3 % or void volume 97 %, resistivity 0.323 Ω cm) pieces were placed in the ends of the sample compartment so that the electrode materials could be incorporated into the gels to provide gel–electrode contact as shown in Figure 4.1(C). Impedance analysis was performed by applying a 1-V peak voltage (alternating current signal) using a waveform generator (Agilent U2761A), across the circuit consisting of a known resistor (R_k = 10 kΩ) and the gel sample. The impedance was obtained by measuring the voltage drop across the known resistor with an oscilloscope (Agilent U2701A).

4.2.4 Statistical Treatment

The reported results are averages of the values obtained. Reported numerical errors and graphical error bars are given as ±1 standard deviation. Data and outliers were rejected either when instrumental error was known to have occurred, or if data failed a Q-test with a confidence interval of ≥95 %.

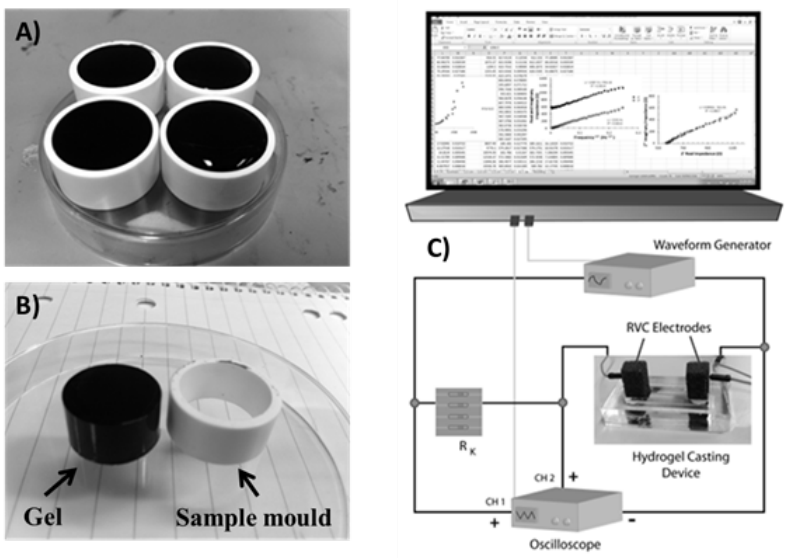

Figure 4.1: (A and B) Photographs of typical hydrogel samples (height, 10 mm; diameter, 16 mm). (C) Schematic representation of the custom-built electrical impedance analyser.

4.3 Results and Discussion

4.3.1 Impedance and Electrical Conductivity of GG Hydrogels

A custom-build instrument was used to carry out electrical impedance analysis on the GG hydrogels [Figure 4.1(C)]. Impedance measured in this manner provides information about the frequency-dependent behaviour of the charge carriers inside the gels. This method is different from other commonly employed techniques such as electrochemical impedance spectroscopy (which evaluates the interfacial behaviour of charge carriers), four-point probes (which applies a direct current usually to the surface of the material), and conductivity meters (which applies a single alternating frequency). This impedance setup was designed as a cheap and simple EIS, with the same principle as commercially available systems. The waveform generator was used to apply a sinusoidal waveform across both a known resistor (R_k) and the sample (R_s). By knowing the exact resistance of R_k, the voltage drop across R_k, and the voltage drop across R_s, various electrical properties of the material can be calculated. The waveform generator would apply a voltage at increasing frequencies to obtain

a frequency-dependent profile of each sample. This was all performed through in-house software coded in VBA (through Excel 2010) and also through C#. Through the use of a sample well with a known cross-sectional area, the conductivity and Warburg properties can be easily calculated. This also allowed the system to be used on both liquid and solid samples.

Figure 4.2(A) shows a Bode plot of a typical GG hydrogel crosslinked with 5 mM of Ca^{2+}. The impedance magnitude ($|Z|$) decreases with increasing frequencies and become independent of frequency above 1 kHz.

The corresponding Nyquist plot [Figure 4.2(B)] displays a linear relationship between the real (Z') and imaginary (Z") components of the impedance. At the intercept with the x-axis, the impedance is purely real (Z" = 0) and the Z'-value represents a resistance. The slope in the Nyquist plot is $\approx$ 1, suggesting a 45° constant phase shift between real and imaginary components of the impedance. This can also be recognized from a log-log version of the Bode plot, that is slope of -1/2 in the low frequency region (data not shown). This suggests that the hydrogel is behaving like a Warburg diffusion element (Z_W), in series with a resistor (R_I)[304].

Under this model, Z' and Z" are inversely proportional to the square root of the frequency (ω) [304],

$$Z' = R_I + \frac{\mu}{\sqrt{\omega}}, \tag{4.1}$$

and

$$Z" = \frac{\mu}{\sqrt{\omega}}, \tag{4.2}$$

where μ is the Warburg coefficient. This dependence is unique to the Warburg impedance and is generally referred to as the Warburg plot [Figure 4.2(C)]. A fit of this data to Equation Equation 4.1 and Equation Equation 4.2 revealed R_I = 554 ± 3 Ω and μ = 2410 ± 120 Ω $s^{-1/2}$. R_I and μ can also be determined by equivalent circuit modelling [Figure 4.2(A)], which yielded R_I = 672 ± 3 Ω and μ = 2200 ± 10 Ω $s^{-1/2}$. The magnitude of R_I and μ is influenced by the polymer and charge-

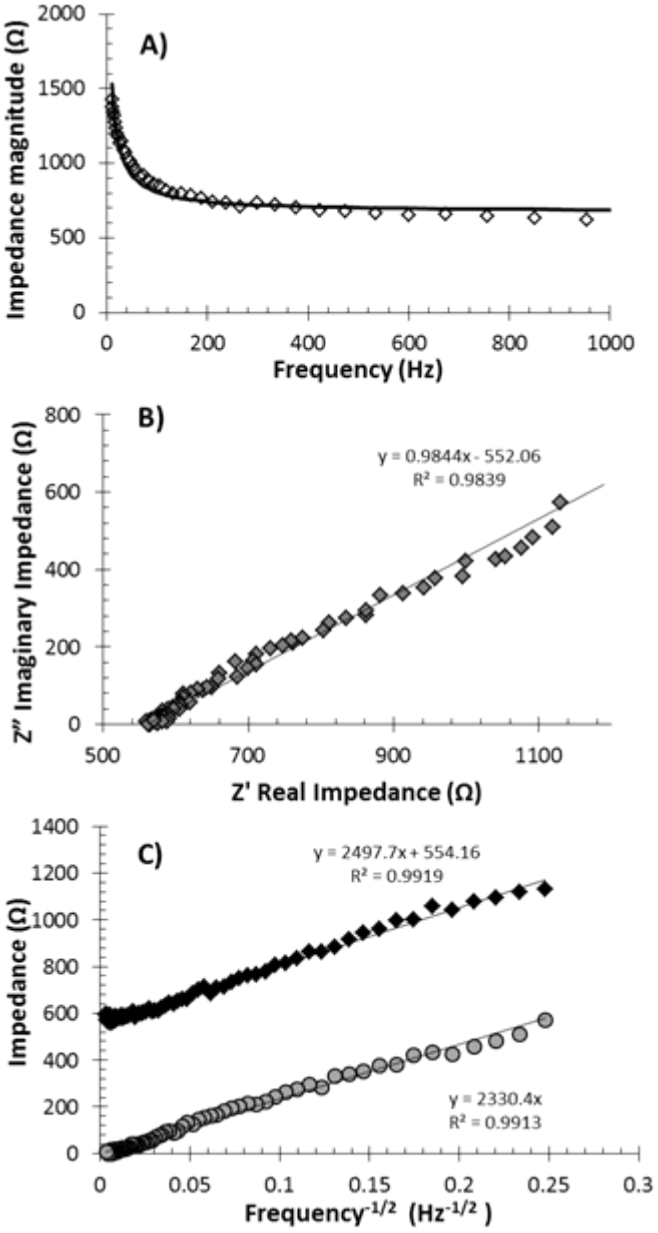

Figure 4.2: Electrical impedance analysis of a typical GG hydrogel (0.5 % w/v, crosslinked with 5 mM of $CaCl_2$) of dimensions 0.5 cm (l) x 1 cm (w) x 1 cm (h). (A) Bode plot, (B) Nyquist plot, and (C) Warburg plot. The solid line in (A) is a two parameter fit of data to an equivalent circuit model consisting of a Warburg element in series with a resistor, whereas the solid line in (B) is a straight line fit and in (C) it is a fit to Equation 4.1.

carrier concentrations. For example, μ was found to be inversely proportional to the concentration of Ca^{2+} (data not shown). In the remainder of this article, the values quoted for R_I and μ are determined using equivalent circuit modelling.

The impedance values measured in this manner include a contact resistance, R_C, owing to the interface between gel and electrodes (porous RVC). It was observed that the impedance magnitude (at any given frequency) increased with increasing gel length [Figure 4.3(A)]. Equivalent circuit modelling revealed that R_I was linearly proportional to gel length [Figure 4.3(B)], whereas m was invariant with length [Figure 4.3(C)]. Hence, the increase of R_I is directly related to the amount of gel material, which increases with length. This provides us with a method to correct the R_I value owing to the presence of electrode-hydrogel contact resistance by realizing that R_I versus l should obey,

$$R_I = \frac{1}{\sigma A_C} + R_C, \tag{4.3}$$

where A_C is the gel's cross-sectional area and σ is the gel's electrical conductivity (at high frequencies). Fitting Equation Equation 4.3 to the data shown in Figure 4.3(B) yielded $\sigma = 1.2 \pm 0.1$ mS cm^{-1} and a contact resistance value of $176 \pm 75\ \Omega$.

4.3.2 Effect of Sonolysis

One of the aims of this study is to investigate the electrical characteristics (including conductivity) of conducting carbon filler containing hydrogels, which requires the use of sonolysis. Hence, it is important to determine the effect of sonication on the gel's electrical and mechanical characteristics prior to incorporation of the conducting fillers such as carbon nanotubes and carbon nanofibres.

The effect of sonolysis was assessed by preparing GG hydrogels which were subjected to probe sonication of up to 40 min. Impedance analysis was used to evaluate the electrical conductivity as described in the previous section. Figure 4.3(D) shows that the gel electrical behaviour is not affected by sonication.

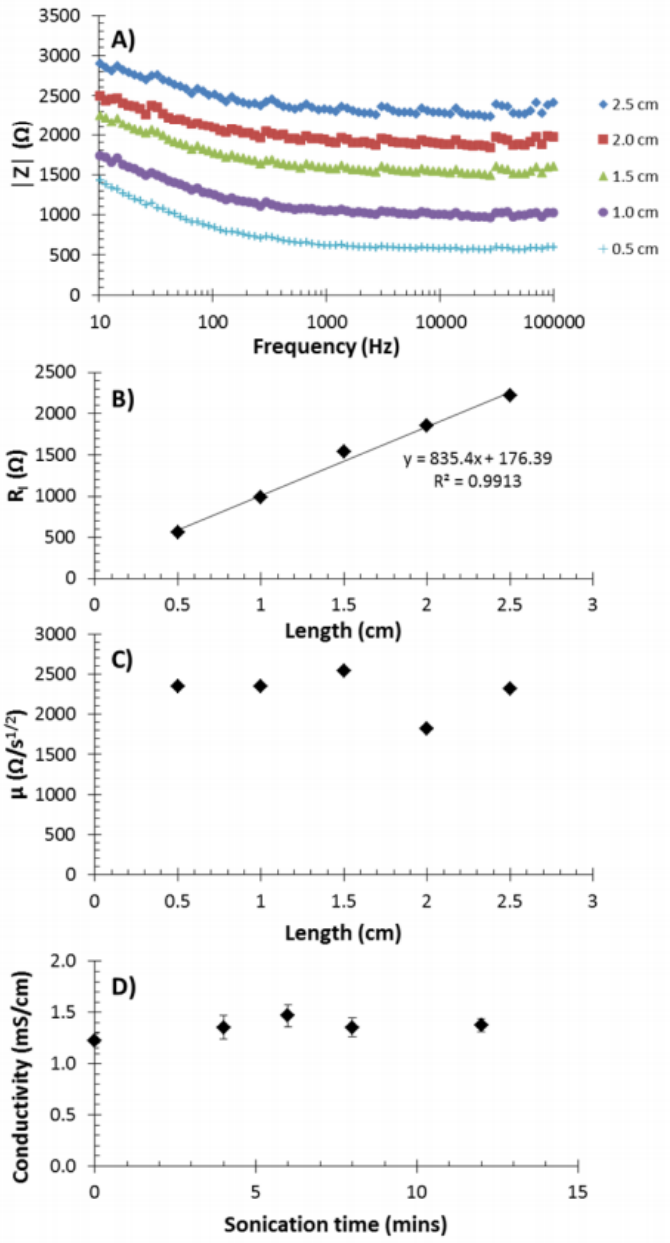

Figure 4.3: (A) Typical impedance magnitude ($|Z|$) of GG hydrogels of varying length. (B) Typical resistance (R_I) as a function of gel length. (C) Typical Warburg coefficient (μ) values as a function of gel length. (D) Electrical conductivity of GG hydrogels (0.5 % w/v, crosslinked with Ca^{2+}) as a function of sonication time, calculated from impedance analysis. Straight line in (B) is a linear fit to Equation Equation 4.3. μ and R_I are obtained from equivalent circuit modelling of data shown in (A).

In contrast, rheological analysis testing revealed that shear modulus values decrease significantly with increasing sonication time. Strain amplitude sweeps showed that all gels exhibited a clear plateau of storage [Figure 4.4(A)] and loss (data not shown) moduli. Their ratio in the plateau linear viscoelastic (LVE) region was indicative of a well-crosslinked polymer network. The storage modulus in the LVE region decreased with increasing sonication time [Figure 4.4(B)].

The decreasing trends observed in Figure 4.4 are a direct result of the shortening of the polymer chains owing to the process of horn sonolysis [305]. During the sonication process, cavities are created which leads to polymer chains experiencing large shear forces [306]. This results in a considerable reduction in the average chain length [108]. Crosslinked gels formed from sonicated GG solutions are less rigid and flow more easily with an applied shear strain, as evident from the reduction in storage modulus with increasing sonication time (Figure 4.4).

Composite hydrogels were prepared by dispersing 1 mg mL^{-1} of either SWCNTs, MWCNTs, or VGCNFs into GG solutions with the aid of low-energy sonolysis. The GG concentration was adjusted such that the carbon material volume fraction for all three materials was about 0.09 %. The density values of SWNT (1.50 g cm^{-3}), MWCNT (2.15 g cm^{-3}), VGCNF (1.95 g cm^{-3}), and GG (1.3 g cm^{-3}) were used to convert mass fraction into volume fraction [245].

It is well known that SWCNTs are difficult to disperse, which is evident from the 120 $\pm$ 10 min required to disperse 10 mg in GG solution (10 mL). In contrast, equivalent amounts of MWCNTs and VGCNFs took a lot less time (energy) to disperse, 12 $\pm$ 4 and 2 $\pm$ 0.5 min, respectively. Impedance analysis showed that the gel electrical conductivity is similar for all the three types of conducting filler (σ = 1.2 mS cm^{-1}), despite the large differences in the electrical conductivity of these materials in thin film form, that is 110 $\pm$ 15 mS cm^{-1} (SWCNT), 50 $\pm$ 5 mS cm^{-1} (MWCNT), and 35 $\pm$ 2 mS cm^{-1} (VGCNF).

This suggests that (in the hydrogels) the carbon-material volume fraction (0.09 %) is too low to contribute to the conduction mechanism. We aimed to address

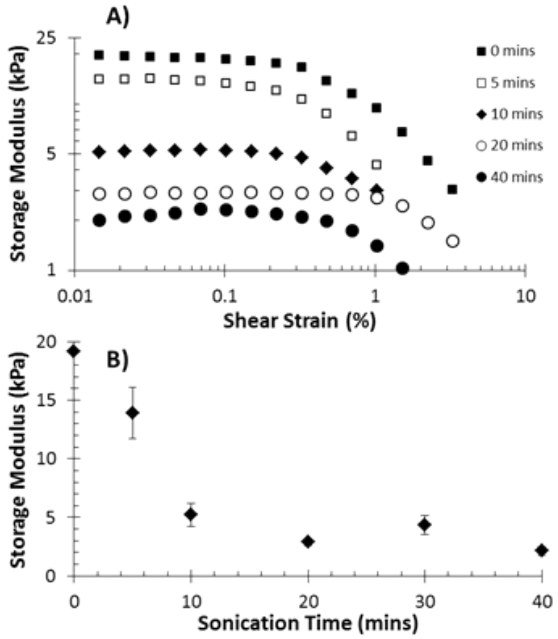

Figure 4.4: (A) Storage modulus as a function of shear strain for GG hydrogels (0.5 % w/v, crosslinked with 5 mM of Ca^{2+}) subjected to sonication. (B) Storage modulus in the region as a function of sonication time

this using two approaches (discussed in the next two sections), (i) increasing the carbon volume fraction (which in turn requires increasing the sonication time) and (ii) decreasing water content.

However, increasing the SWCNT concentration beyond 1 mg mL^{-1} was not practical owing to the already large sonication times required to achieve a complete dispersion at that concentration. Therefore, all further experiments involved VGCNFs and MWCNTs as they required more manageable sonication times.

4.3.3 Effect of Increasing Carbon Filler Volume Fraction

All hydrogels were prepared with a GG concentration of 5 mg mL^{-1} and water content of >98.5 %. Dispersing MWCNT at a concentration of 10 mg mL^{-1} in GG required 30 min of sonication. It is shown in Figure 4.4 that this length of sonolysis results in significant weakening of the gels. Hence, it was not possible to form MWCNT containing hydrogels by simply crosslinking the dispersion. Instead, fresh GG powder was added to the dispersions. These dispersions were crosslinked

using Ca^{2+} ions and cast in plastic moulds while hot ($\approx$ 80 °C), to form rigid gels upon cooling to room temperature (21 °C).

The Bode plots for the MWCNT hydrogels are shown in Figure 4.5(A). It is clear that increasing the MWCNT volume fraction results in a decrease in the magnitude at all frequencies. This indicates that the presence of MWCNT is improving the electrical characteristics of the gels.

VGCNF gels were prepared using a similar approach as the MWCNT gels, that is GG concentration is always fixed at 5 mg mL^{-1}. As VGCNF required less sonolysis compared to the MWCNT, it was possible to prepare hydrogels with higher volume fractions compared to the MWCNT. Dispersing 17.5 mg mL^{-1} of VGCNF required only 12 min of sonication. This difference allowed for the preparation of gels with volume fraction of up to 0.89 %. Regardless of the volume fraction, the same proportion of GG was subjected to sonication.

The Bode plots for the VGCNF hydrogels [Figure 4.5(B)] exhibit the same trends as shown for the MWCNT gels, that is the impedance magnitude decreases with increasing VGCNF volume fraction.

A comparison between the two different types of carbon material containing gels (water content, >98.5 %) leads to the following observations: (i) VGCNFs require less sonolysis to disperse than MWCNTs and (ii) MWCNTs require a lower volume fraction to influence the electrical conductivity. For example, the volume fractions required reaching an electrical conductivity value of 2.1 $\pm$ 0.4 mS cm^{-1} is about 0.89 % for VGCNFs, but only 0.41 % for MWCNTs. This could be attributed to the higher intrinsic electrical conductivity of MWCNTs over VGCNFs.

This approach is clearly limited by the amount of water (98.5 %) present in these gels. It was not possible to increase the carbon filler volume fraction beyond 0.89 % (and thereby decrease the water content) owing to the dispersibility of the conducting fillers and the sonication method. Therefore, in the following section the effect of reducing water content on the electrical behaviour of the gels was investigated.

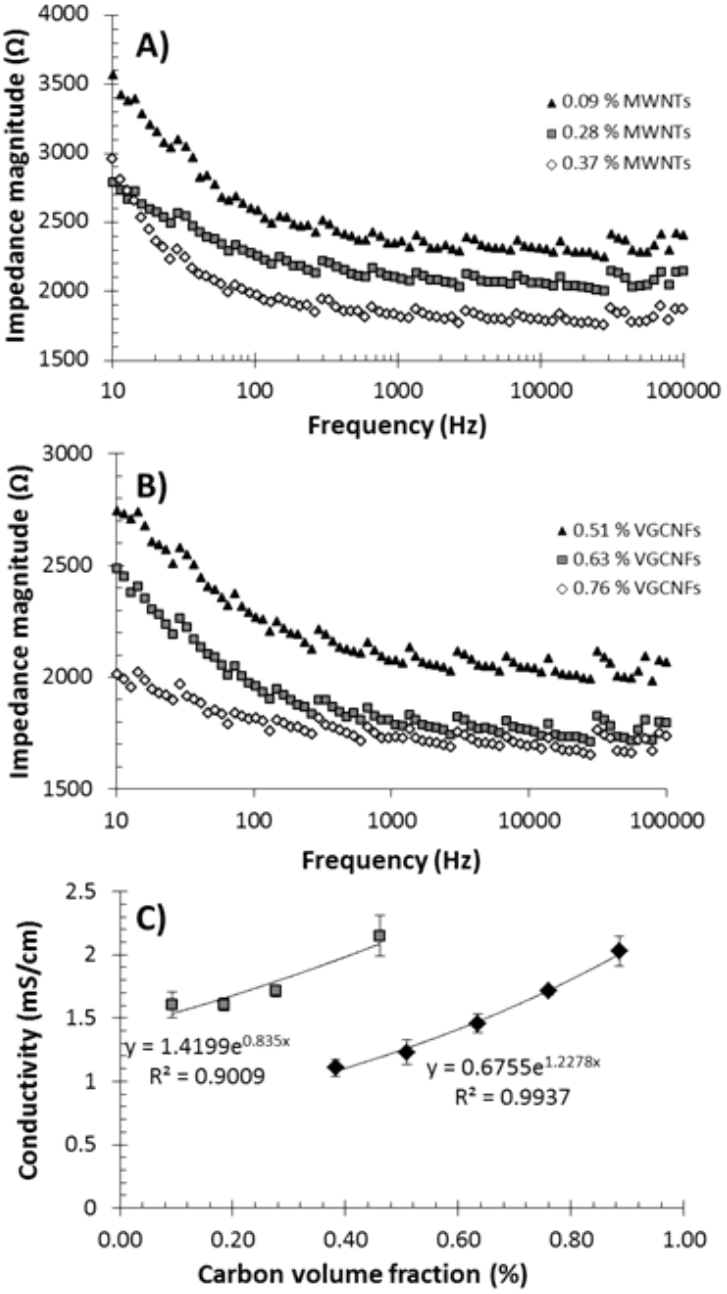

Figure 4.5: (A and B) Typical impedance magnitude ($|Z|$) of MWCNT and VGCNF hydrogels (length, 1 cm) with different carbon material volume fractions, respectively. (C) Electrical conductivity as a function of carbon filler volume fraction for GG hydrogels (0.5 % w/v, crosslinked with Ca^{2+}). Squares and diamonds indicate MWCNT and VGCNF, respectively. Lines are fits to the data.

4.3.4 Effect of Decreasing Water Content

The hydrogels were prepared at the highest possible carbon filler concentration with water content of >98.5 %, that is MWCNT and VGCNF volume fractions of 0.41 and 0.89 %, respectively, as outlined in the previous section. These gels (starting weight, $\approx$ 4.2 g) were then placed in a temperature-humidity chamber and their water content was selectively reduced under controlled circumstances at a rate of 0.43 ± 0.01 g h^{-1}. This experiment (which can be seen as deswelling) allows us to maintain accurate knowledge of the water, polymer, and conducting filler contents in our gels.

The Bode plots of MWCNT gels at different water contents are shown in Figure 4.6. At 98 %, the Bode plot shows a dependence of impedance magnitude on frequency similar to those shown in Figure 4.3(A) and Figure 4.5(A). It shows a clear frequency dependent region for frequencies below 1 kHz, and we have shown that this transport behaviour is indicative of a Warburg element in series with a resistor. However, as the water content decreases, the frequency dependence at lower frequencies disappears. It is clear that at 94.5 % of water content, the Bode plot is indicative of a resistor, that is transport dominated by electrons. Equivalent circuit modelling revealed that the Warburg coefficient values decreased from 1400 Ω $s^{-1/2}$ at WC = 98 % to 19 Ω $s^{-1/2}$ at WC = 94.5 % [Figure 4.7(A)]. These could suggest that a percolative MWCNT network is formed, which is further explored below.

Our analysis of conducting filler network formation was based on Warburg coefficient data for the following reason. During the deswelling experiment, gels undergo a dimensional change as a result of water loss. Figure 4.3(B) shows that the resistance is dependent on gel dimension, whereas Figure 4.3(C) shows that the Warburg coefficient is not.

Figure 4.7(A) shows that the dependence of the Warburg coefficient on water content for MWCNT containing gels undergoes a sharp transition around WC = 95 %. This transition identifies the WC point at which the electrical behaviour of the gels becomes dominated by electrons, that is the formation of a conducting filler

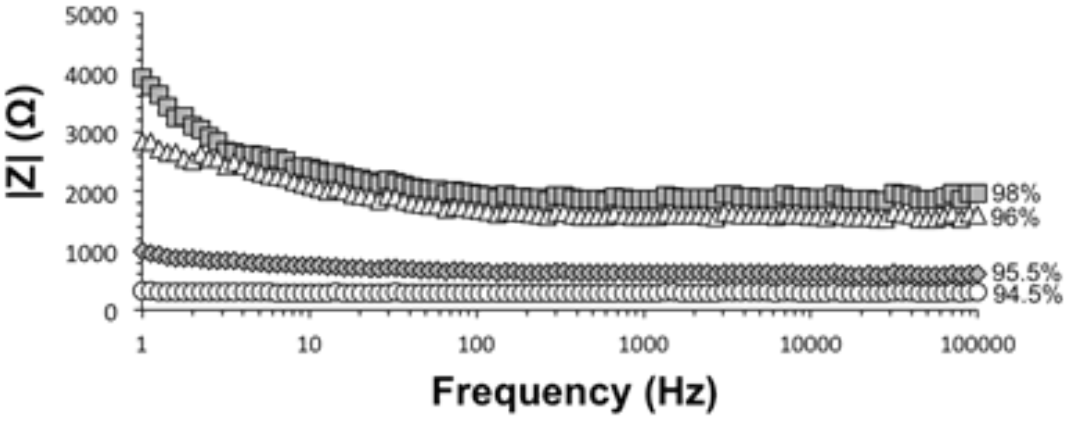

Figure 4.6: Typical Bode plots for MWCNT containing hydrogels at water contents of 98.0, 96.0, 95.5, and 94.4 %.

network in the hydrogel. This trend is similar to the well-known scaling behaviour of electrical conductivity with conducting filler mass fraction in composite materials. The composite materials become electrically conducting at the threshold concentration where a percolative network is formed. This behaviour is traditionally fitted using the statistical percolation model [285, 307]. Our data could be fitted using a similar model:

$$\mu = \mu_o(WC - WC_p)^t + C, \tag{4.4}$$

where μ_o is a scaling factor, WC_p is the percolation threshold in terms of water content, C is a constant, and t is the exponent. A fit of the data for MWCNT gels [Figure 4.7(A)] resulted in the following values, $\mu_o = 420 \pm 180\ \Omega\ s^{-1/2}$, $WC_p = 95 \pm 2$ %, $T = 1.5 \pm 0.6$, and $C = 20 \pm \Omega\ s^{-1/2}$, respectively.

In contrast to the MWCNT gels, the VGCNF containing gels exhibited a more gradual reduction in Warburg coefficient. For example, μ decreased from 1400 $\Omega\ s^{-1/2}$ at WC = 98 % to 325 $\Omega\ s^{-1/2}$ at WC = 85 %, with a further reduction to 3 $\Omega\ s^{-1/2}$ at WC = 60 %. A fit of this data to Equation Equation 4.4 revealed the following values, $\mu_o = 88 \pm 20\ \Omega\ s^{-1/2}$, WC_p 81 $\pm$ 2 %, $t = 1.0 \pm 0.4$, and $C = 3 \pm 1\ \Omega\ s^{-1/2}$, respectively.

The electrical conductivity of the gels as a function of water content was determined using R_I values (as determined by equivalent circuit modelling), the gel's

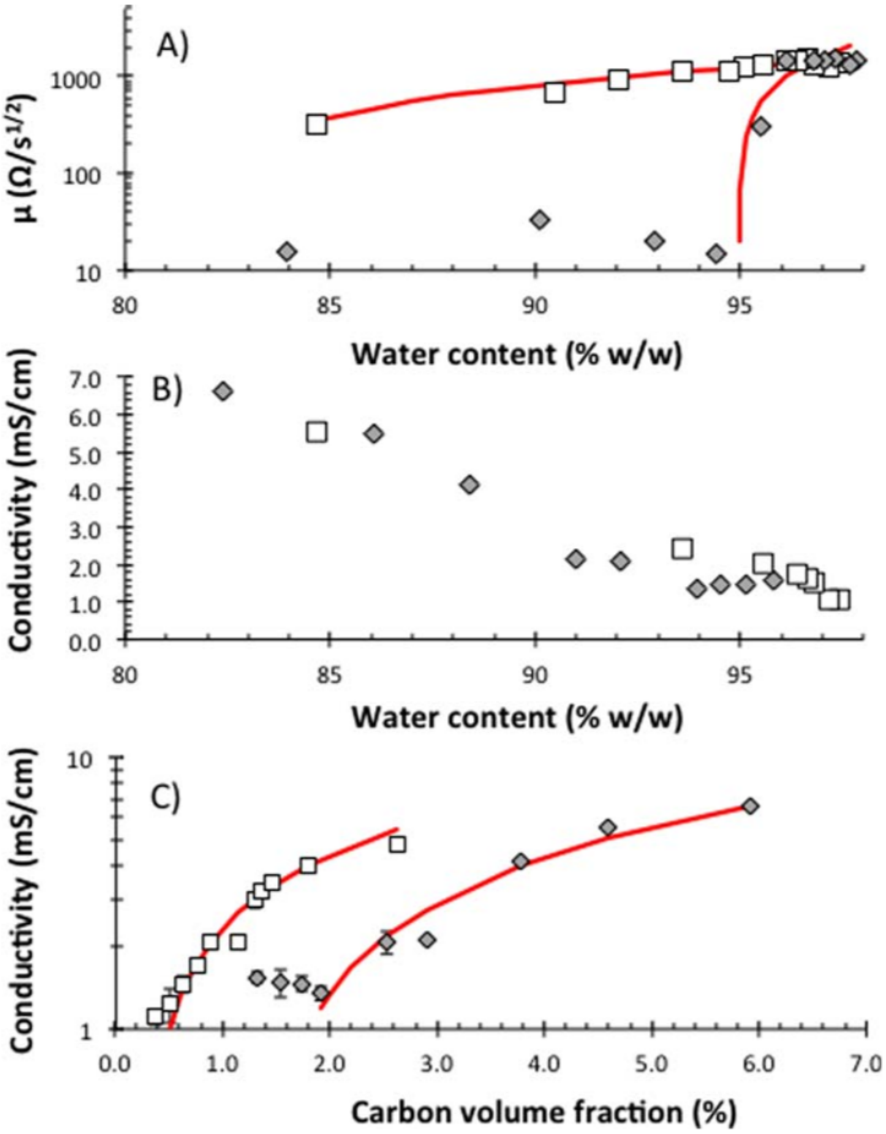

Figure 4.7: (A) Typical Warburg coefficient (m) values as a function of water content for MWCNT (diamonds) and VGCNF (squares) containing hydrogels. The solid lines are three parameter fits of the Warburg coefficient to Equation Equation 4.4. (B) Electrical conductivity as a function of water content for MWCNT (diamonds) and VGCNF (squares) containing hydrogels. (C) Electrical conductivity as a function of carbon filler volume fraction for MWCNT (diamonds) and VGCNF (squares) containing hydrogels. The solid lines are three-parameter fits to Equation Equation 4.5.

dimension, and Equation Equation 4.3, Figure 4.7(B) shows that the conductivity of the MWCNT and VGCNF gels increased with decreasing water content [Figure 4.7(B)]. For example, at WC = 82 % the MWCNT containing gel yielded an electrical conductivity value of 7 ± 1 mS cm^{-1}. Similar values were obtained for the VGCNF containing gels.

The combined electrical conductivity data for the effects of increasing carbon filler [Figure 4.5(C)] and decreasing water [Figure 4.7(B)] are shown in Figure 4.7(C) and were fitted using the statistical percolation model:

$$\sigma = \sigma_O(\varphi - \varphi_p)^t, \tag{4.5}$$

where σ_o is a scaling factor, φ is the carbon filler volume fraction, φ_p is the percolation threshold in terms of carbon filler volume fraction, and t is the exponent. The resulting t-values of the MWCNT ($t = 0.8 \pm 0.3$) and VGCNF ($t = 0.7 \pm 0.3$) containing gels are lower than the predicted scaling values for in two and three dimensions, that is $t = 1.3$ and $t = 2$, respectively [285, 307]. However, it should be noted that the predicted values are calculated by assuming ideal systems containing identical particles [307]. It is well known that VGCNF and MWCNT are far from being considered as containing identical particles.

In addition, the fitting revealed that the percolation thresholds occur at volume fractions of 0.3 % (water content, 93 %) and 1.4 % (water content, 96 %) for VGCNF and MWCNT containing hydrogels, respectively. It is interesting to note that the water content for the MWCNT hydrogels is similar to the water content at which the transport changes from dominated by ions to dominated by electrons (as predicted by Equation Equation 4.4). However, this similarity was not observed for the VGCNF containing hydrogels. We suggest that the low values for the exponent t are related to the occurrence of different types of conducting pathways, that is those dominated by ions and electrons and/or both. It is also possible that the percolation process in hydrogels is more adequate described by a kinetic percolation approach. Further research is necessary for the complete understanding of this concept.

4.4 Conclusions

The mechanical and electrical characteristics of GG, carbon nanotube-GG, and vapor-grown carbon nanofibre hydrogels have been investigated. The electrical characteristics of these hydrogels were assessed using a custom-built impedance analyser. Our analysis revealed that the impedance behaviour of these gels could be modelled using a Warburg diffusion element in series with a resistor. These resistor values were used to calculate the electrical conductivity after correcting for electrode-sample contact resistance.

Sonolysis had a detrimental effect on the mechanical characteristics, as measured using the shear modulus. For example, subjecting a GG solution to 40 min of horn sonication prior to gelation resulted in a decrease in shear modulus from 19.2 $\pm$ 3.1 to 2.2 $\pm$ 0.4 kPa. In contrast, it was observed that sonolysis did not affect the electrical conductivity of the GG hydrogels (1.2 $\pm$ 0.1 mS cm^{-1}).

Incorporating MWCNT and VGCNF through addition of more filler was found to result in a modest enhancement of the electrical conductivity. Larger increases in conductivity could be obtained by selectively removing water content.

Impedance analysis was used to show that MWCNT containing hydrogels undergo a sharp transition from transport dominated by ions (owing to GG) to transport dominated by electrons (owing to conducting fillers). For example, percolation analysis showed that the MWCNT form a percolative network within the hydrogels at water content of 95 $\pm$ 2 %. MWCNT containing gels exhibited an electrical conductivity of 7 $\pm$ 1 mS cm^{-1} at water content of 82 %.

This article contributes to the development and characterization of electrically conducting hydrogel materials.

4.5 Acknowledgements

This study was supported by the University of Wollongong and the Australian Research Council (Centre of Excellence and Future Fellowship programs). S. O'Brien,

C. Bronnbauer, L. J. Alcock, and C. S. Hansen are thanked for the preparation of materials and/or technical assistance with software.

Chapter 5

Sonication-induced effects on carbon nanofibres in composite materials

The preparation and characterization of carbon nanofibre - gellan gum composite materials is presented. Electron microscopy analysis reveals that nanofibres are affected by sonolysis, i.e. fibre length reduces, while filling (with gellan gum) amount increases. It is demonstrated that sonolysis and the resulting modification adversely affects the electrical (decrease in conductivity) and mechanical (decrease in the Young's modulus) characteristics of the composite materials. Spectroscopic analysis supports the observation that carbon nanofibres are filled by the dispersant during the preparation of the dispersions.

Author Statement

This chapter contains the following published journal article, stylistically edited to suit the rest of this document:

R. D. Gately and M. in het Panhuis, "Filling of carbon nanotubes and nanofibres," *Beilstein J. Nanotechnol.*, vol. 6, no. 1, pp. 508–516, 2015

Author Statement:
I, Reece D. Gately, hereby declare that I contributed to the following work within this manuscript by:

- Made all samples (dispersions, free-standing films)
- Performed and analysed mechanical and electrical characterisation
- Performed SEM imaging, including length analysis
- Analysed TEM micrographs and Raman spectra
- Wrote and edited the manuscript.

All other work required for this manuscript was performed by other co-authors as follows:
Dr. Holly Warren: Assisted in developing all samples, assisted in performing mechanical and electrical characterisation, and assisted in analysis of the TEM micrographs.
Anthony C. Romeo: Performed SEM and TEM imaging, and assisted in analysis of the micrographs.
Mattina Scardamaglia: Performed and analysed XPS data on the free-standing films and buckypaper samples.
Dr. Carla Bittencourt: Assisted in analysis of the XPS data on the free-standing films and buckypaper samples.
Prof. Marc in het Panhuis: Assisted in proof-reading and editing the manuscript.

I, Prof. Marc in het Panhuis (supervisor), support and certify that the above author statement is correct.

Marc in het Panhuis
April 20, 2017

5.1 Introduction

The filling of carbon nanostructures such as CNTs has been investigated for applications including metal nanowires [182, 193, 308], hydrogen storage [309], energy storage [133], catalysts [136] and electrical insulation [310, 311]. The methods used to fill CNTs can be broadly categorised as either chemical or physical. Chemical methods include functionalisation [177] or electrochemical methods [133, 165, 312], whereas physical methods employ strong capillary suction within the CNTs [140, 180, 182, 313]. CNTs are not readily filled as they are usually produced as closed structures resembling cylinders with hemi-spherical caps on either end. Opened CNT structures can be achieved through either direct growth [314] or by removing the caps [148–150]. Examples of the latter method include oxidative treatment [315] and boiling in acids [316].

The improvement of the mechanical [317, 318] and electrical [319, 320] characteristics of materials by incorporation of conducting carbon fillers is an active area of research. However, it is well-known that carbon fillers can be difficult to (homogeneously) disperse in aqueous solutions due their hydrophobicity and van der Waals interactions [321]. This disperse-ability issue has been successfully addressed by using dispersants (*e.g.* surfactants, polymers) in combination with sonolysis methods [124, 322, 323]. However, one of the drawbacks of sonolysis is that it can lead to damage to the carbon filler [281, 283] and/or the dispersant [324]. In general, this results in a detrimental effect on the properties of the composite material [128, 281, 282, 325, 326]. For example, it has been shown that extensive sonolysis (21 hours) reduced the average CNT length from 3.5 μm to less than 0.5 μm [128]. This reduction in length was coupled with a significant decrease in the conductivity of the resulting CNT network. Furthermore, the detrimental effect of sonolysis on the molecular mass of polymers is well-known [108, 125, 126, 214, 327, 328].

Here we investigate the effect of sonolysis on the properties of composite materials prepared by dispersing VGCNFs with the biopolymer GG. GG is a linear, anionic, water soluble biopolymer which is derived from the bacteria *Sphingomonas*

elodea (formerly *Pseudomonas elodea* or *Auromonas elodea*) [109]. The repeating unit of the polymer is a tetrasaccharide, which consists of two residues of D-glucose and one of each residues of L-rhamnose and D-glucuronic acid. It is well-known for its applications in food technology ever since it was approved by the European Union and the United States Food and Drug Administration nearly two decades ago [329]. More recently, it has been demonstrated that gellan gum is an efficient dispersant for conducting carbon fillers such as carbon nanotubes, graphene and VGCNFs [58, 100, 114, 115].

VGCNFs are a conducting carbon filler material which were first manufactured in 1889 as a potential replacement for filaments in glow lamps [330]. Their structure was first elucidated in 1952 using electron microscopy, which showed stacks of highly graphitised carbon forming a tubular shape [331]. VGCNFs are produced by a catalytic thermal chemical vapour deposition technique with a floating catalyst [61]. This method produces two characteristic structures, (i) 'stacked cup' (or 'herringbone') structure, which looks similar to a series of graphite cups without bases stacked on top of each other, and (ii) a 'stacked deck' (or 'parallel' structure) which is a series of multiple concentric tubes of graphitised carbon (similar to those observed for multi-walled CNTs), but at a slight (approx. 4 °) angle [63]. These structures are subsequently heat treated to remove (most of) the amorphous carbon outer layer and further improve their physical, mechanical, and electrical properties [43]. It has been shown that conductivity and mechanical strength of the nanofibres is enhanced through heat treatment at 1500 °C [64].

VGCNF composite materials have been produced using poly(caprolactone), poly(urethane), poly(ethylene) and epoxy resins [99, 102, 212, 213, 332–335]. For example, recently it was demonstrated that shape memory properties of VGCNF-epoxy composite materials were enhanced by chemical functionalisation of VGCNFs [332]. Other potential applications include the use of VGCNFs as constituents in electromagnetic interference shielding materials as discussed in a recent review article [336].

In this paper, VGCNF-GG dispersions and composite materials are prepared using sonolysis, vacuum filtration and evaporative casting. The effect of sonolysis on the VGCNFs was assessed using spectroscopic, microscopic, electrical and mechanical analysis techniques.

5.2 Experimental

5.2.1 Preparation of dispersions

Gellan gum was obtained from CP Kelco (low acyl form, Gelzan CM, Lot #1I1443A). A GG solution (3 mg mL^{-1}) was prepared by adding 300 mg of GG to 100 mL of Milli-Q water (resistivity $\approx$ 18.2 MΩ cm) and heated to 80 °C on a hotplate (Stuart CB162 heat stirrer) while stirring with an overhead stirrer at $\approx$ 800 rpm (IKA RW 20 digital) for at least 30 minutes.

Homogeneous dispersions were prepared by adding 100 mg of VGCNFs (Pyrograf Products, PR24-LHT, Batch info: PS1345 Box 8, HT 170) to 10 mL GG solution (3 mg mL^{-1}) and applying horn sonolysis using a digital sonicator (Branson Digital Sonifier, power output 6 W, 0.5 s pulse, 0.5 s break between pulses). The microtip horn (Consonic, diameter 3.175 mm) was held 1 cm off the base of a 20 mL glass sample vial (diameter 25 mm).

5.2.2 Preparation of free-standing films

Buckypaper (BP) free-standing films were prepared by a vacuum filtration process. Briefly, 3 mL of the VGCNF dispersion (10 mg mL^{-1} VGCNF in 3 mg mL^{-1} GG) was diluted to 90 mL with Milli-Q water, resulting in final concentrations of 0.33 mg mL^{-1} and 0.1 mg mL^{-1} for the VGCNF and GG respectively. This was then subjected to bath sonication (50 Hz, FXP4, Ultrasonics) for 5 minutes. The dispersion was filtered through a commercial membrane (5 μm pore size, polytetrafluorethylene, Millipore) using a vacuum pump (CVC2, Vacuubrand) operating between 30 – 50 mbar. Once filtration had completed, the membrane was allowed to dry under

controlled conditions (21 °C, 50% relative humidity, RH) in a temperature humidity chamber (Thermoline Scientific, TRH-150-SD) for up to 24 hours. Once dry, the BP was carefully peeled off the membrane to produce a free-standing film (diameter 40 mm).

Additional free-standing films were prepared by evaporative casting. Briefly, as-prepared dispersions were poured into a plastic petri-dish (diameter 55 mm) and allowed to dry under controlled conditions (21 oC, 50% RH) in a temperature-humidity chamber for up to 24 hours. The resulting films were then carefully removed from the substrate to produce free-standing films.

5.2.3 Electron Microscopy

Transmission electron microscopy (TEM) analysis of dispersions was performed using a transmission electron microscope (JEOL 2011) operated at an acceleration voltage of 200 kV. All images were captured on a TEM digital imaging system (Gatan Orius). A VGCNF dispersion was prepared by manual shaking of 10 mg VGCNF into $\approx$ 20 mL of isopropanol (Sigma Aldrich Australia) for 1 min, hereafter referred to as 'unsonicated'. Dispersions (unsonicated and sonicated) were then cast into a copper grid (pore size 5 μm) and left to dry under controlled ambient conditions before TEM imaging. Scanning electron microscopy (SEM) analysis of all free-standing films was carried out using a field emission scanning electron microscope (FESEM JEOL JSM 7500-FA) operated at 5 kV and a spot size setting of 8. Length analysis of VGCNFs was performed using an image analysis package (Leica Application Suite Version 4.3).

5.2.4 Electrical Characterisation

Samples for electrical characterisation were prepared by cutting the films into small strips (3 mm x 25 mm), and contacted with conducting copper tape (3M) and conducting silver paint (SPI). A uniform pressure ($\approx$ 105 Pa) was applied to the electrode-sample contact area using bull clips (Officeworks, Wollongong). Current

– voltage ($I - V$) profiles were obtained by measuring the current using a digital multimeter (Agilent 34410A) coupled with a cycling potential applied by a waveform generator (Agilent 3320A) in controlled ambient conditions (21 °C, 50% RH). The sample thickness was measured using a digital screw micrometer (Mitutoyo IP 65).

5.2.5 Mechanical Analysis

Tensile stress-strain measurements of the free-standing films were conducted using a universal mechanical testing apparatus (Shimazdu EZ-S). Films were cut into strips (width 4 mm) and a length assuring a gauge length of 10 mm. The samples were then stretched at a rate of 1 mm min^{-1} until failure.

5.2.6 Spectroscopy

Raman analysis was conducted using a Raman spectrometer (JY HR800, Horiba Jobin Yvon). The laser used was a HeNe laser (632.8 nm wavelength) at a power of 20 mW. The detector was an optical microscope (Olympus Bx41) with a spatial resolution of 1 μm. The spectrometer was calibrated using SiO2 at a wavenumber of 520.7 cm^{-1}. All scans were performed between 500 and 3000 cm^{-1} under controlled ambient conditions.

X-ray photoelectron spectroscopy (XPS) was carried out in UHV conditions (base pressure in the 10^{-9} mbar range) using a spectrometer (VERSAPROBE PHI 5000, Physical Electronics), equipped with a Monochromatic Al Kα X-Ray. The energy resolution was 0.7 eV. All binding energies were calibrated to the C 1s peak at 284.6 eV.

5.3 Results and Discussion

5.3.1 Electron microscopy

VGCNFs were stabilised in GG using a sonolysis process for up to 30 mins. TEM analysis (Figure 5.1a) of the as-received VGCNFs (unsonicated sample) revealed

that the sample contained the characteristic 'parallel' (indicated with 1) and 'herringbone' (indicated with 2) structures. All of the imaged VGCNFs appear to be closed structures (see the example in Figure 5.1b), while a number of other types of carbon structures (*e.g.* amorphous carbon) are apparent. Although these other structures either completely cover the VGCNFs (Figure 5.1b) or partially cover the surface (Figure 5.1c), they are easily removed after only a short period (2 min) of sonolysis (Figure 5.1d-f).

Apart from removing the other types of carbon, sonolysis also resulted in opening the VGCNFs. For example, four VGCNFs can be identified in Figure 5.1d, of which the 'herringbone' structure is not damaged, but at least one of the three 'parallel' structures is open ended. Furthermore, we made the interesting observation that two of these VGCNFs appear to be filled. The enlarged view in Figure 5.1e clearly shows evidence of a filled VGCNF. Quantitative image analysis of TEM micrographs revealed that approximately 1/3 of the imaged VGCNFs appeared to be either completely or partially filled. However, analysis of dispersions prepared using longer sonication times (*e.g.* 30 mins) revealed that most of the imaged fibres were either filled and/or opened (sheared). For example, the VGCNFs in Figure 5.1g have been opened and are filled, whereas one of the fibres shown in Figure 5.1h has not been opened (and is therefore not filled). In addition, other fibres (such as the one shown in Figure 5.1i) revealed a fibre with the 'parallel' section filled and an undamaged (non-filled) 'herringbone' section. Examination of the TEM images shows that fibre damage and degree of filling increased with increasing sonication time.

Quantitative TEM analysis showed that the fraction of filled VGCNFs increased from 33 % (after 2 min of sonolysis) to 85 % after 30 min of sonolysis. This is further evidence that the filling effect is most likely due to the opening of the VGCNFs, *i.e.* whenever a fibre is damaged as a result of sonolysis, it is filled with the surrounding dispersant GG). We suggest that this is a result of capillary forces, as has been previously observed for carbon nanotubes [182, 337].

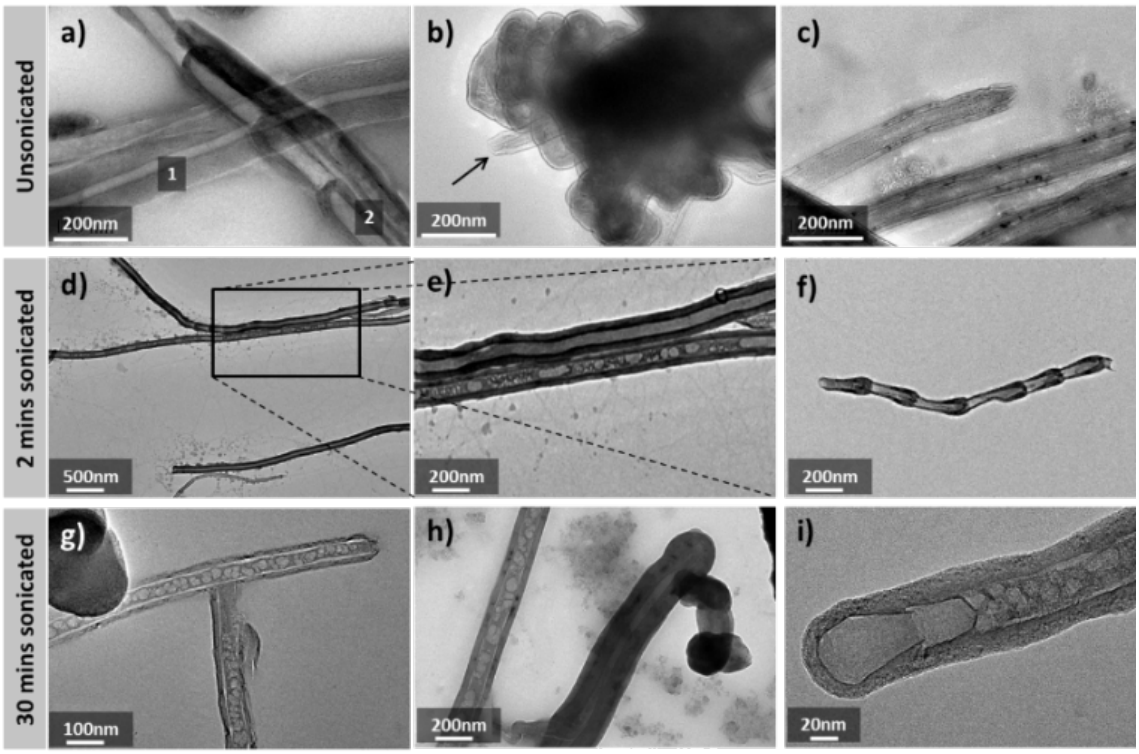

Figure 5.1: Typical high-resolution transmission electron microscopy images of VGCNFs unsonicated (a-c), sonicated for 2 min (d-f) and 30 min (g-i). a) VGCNFs displaying the characteristic 'parallel' (1) and 'herringbone' (2) structures. b) A VGCNF (indicated by arrow) completely covered with other types of carbon structures. c) VGCNFs partially covered with other types of carbon structures. d) Filled and un-filled VGCNFs. Rectangle indicates area of enlargement. e) Enlarged view of the filled and un-filled 'parallel' VGCNFs shown in image d). f) 'Herringbone' VGCNFwith one open end. g) Filled 'parallel' VGCNFs. h) Filled and closed 'parallel' VGCNFs. i) A VGCNF with a filled 'parallel' section filled and an undamaged 'herringbone' end section.

The effect of the wall thickness was also examined quantitatively. It was found that after 2 minutes of sonolysis the VGCNFs with thinner walls were more likely to be sheared and filled, whereas the VGCNFs with the thicker walls were less likely to have been sheared. Figure 5.1e shows two fibres with different wall thicknesses; the top one is thicker and undamaged, whereas the bottom one is thinner and has been sheared and filled. This effect was personified after 30 min sonication; as previously mentioned, all VGCNFs that had been sheared were completely filled. It was found that all fibres with thin walls had been sheared, whereas fibres with thicker walls were less likely to be damaged. Figure 5.1h shows a filled fibre next to an unfilled fibre, and it can be seen that the right hand fibre was unfilled and not sheared, but has a significantly thicker wall compared to the fibre on the left, which has been sheared and filled. It has been suggested that DW/MW CNTs can be tougher than SWCNTs with greater resistance to crack propagation due to interwall sp^3 bonding [338]. This toughness is proportional to the density of these interwall bonding sites. The more layers a CNT/CNF has, the higher the density of the sp^3 bonding sites there are, and thus a greater resistance to damage. This agrees with these observations; the thicker VGCNFs are less likely to be damaged, whereas the thinner ones are more likely to be sheared and filled.

SEM analysis of free-standing films (Figure 5.2) was used to assess the effect of sonication on the average length of the VGCNFs. After 2 min of sonication, it was found that the ends of the VGCNFs were reasonably circular in shape (Figure 5.2c), whereas after 30 min sonication the ends appeared to be more deformed and more ellipsoidal in shape (Figure 5.2d). At present it is not clear if the deformation is a direct result of sonolysis or an in-direct effect due to fracturing. Further research is necessary to confirm this.

The length of the fibres decreased with increasing sonication times. For example, for free-standing films prepared by evaporative casting, the average length decreased from 3.2 μm (2 min sonication) to 1.5 μm (30 min sonication), see Figure 5.2e. This data exhibited a power-law ($y = mx^{-b}$) dependence with b = 0.22 $\pm$ 0.01.

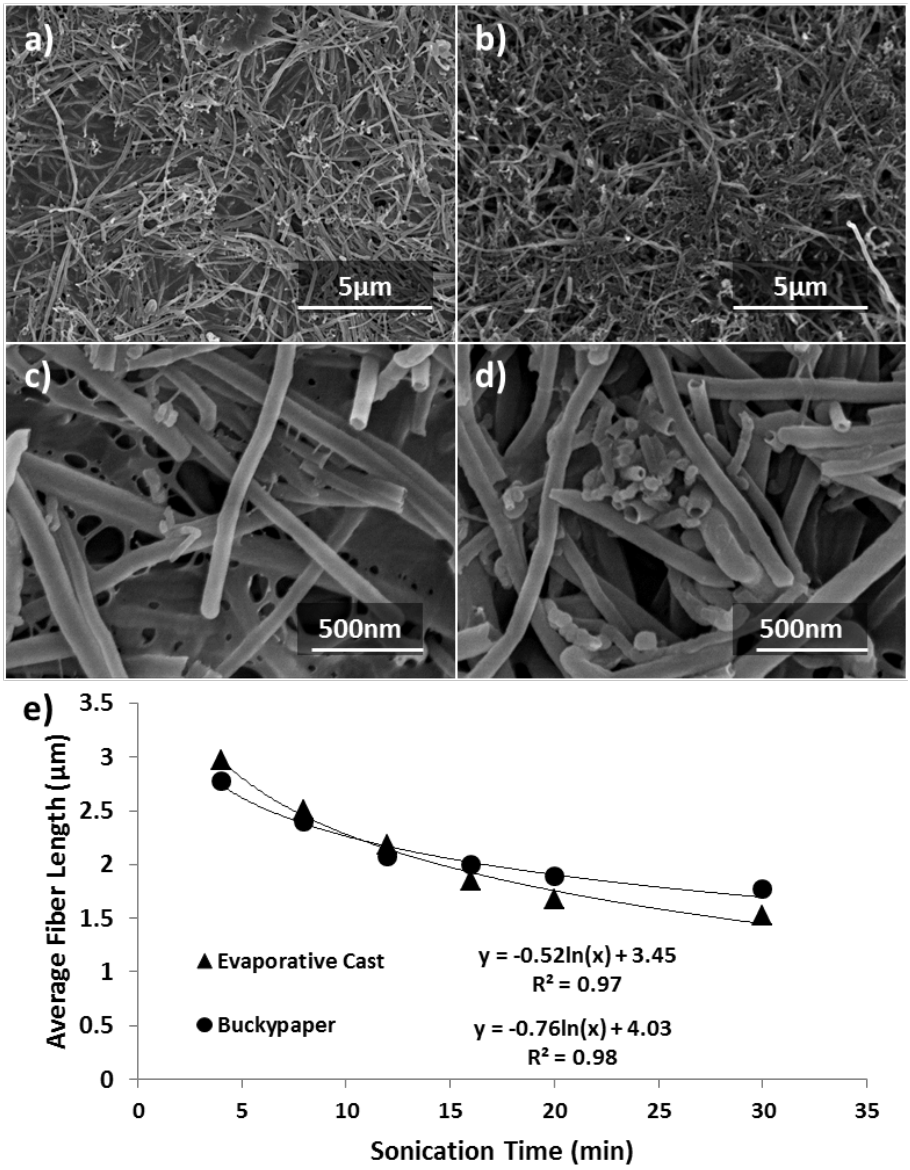

Figure 5.2: Typical scanning electron micrographs of free-standing films prepared by evaporative casting of dispersions prepared by sonicating for a) 2 min and b) 30 min. c) and d) are enlarged views of a and b), respectively. e) Average fibre length (assessed using image analysis on the micrographs) as a function of sonication time for films prepared by evaporative casting (triangles) and vacuum filtration (BPs, circles). The solid lines are fits to the data.

Similar results were obtained for films prepared by the vacuum filtration process (Figure 5.2e, circles, power law exponent b = 0.22 ± 0.01). This shortening through sonolysis is attributed to acoustic shearing as a result of inertial cavitation. The effect of this length reduction on the is discussed in the next section.

5.3.2 Electrical and mechanical characterisation

The dispersions were used to prepare free-standing films by evaporative casting. The resulting free-standing films were used to assess the effect of sonolysis on the electrical and mechanical characteristics of these materials.

Films prepared by evaporative casting were used since they retain all of the VGCNF and the GG materials present in the dispersion. In contrast, it is well-known that during the vacuum filtration process (to produce BPs) some proportion of both the dispersant and carbon fillers are removed.

The current-voltage ($I - V$) characteristics of all free-standing films (tested under controlled ambient conditions) exhibited Ohmic behaviour, *i.e.* linear $I - V$ characteristics. The total resistance (R_T) of the films was calculated from the $I - V$ characteristics and plotted against film length (L) (Figure 5.3a). The conductivity was then evaluated by fitting the R_T versus L data to [100, 214]:

$$R_T = 1/(\sigma A_C)L + R_C, \tag{5.1}$$

where A_C, σ, and R_C indicate the cross-sectional area, conductivity and contact resistance, respectively. The slopes of the linear fits shown in Figure 5.3a for films prepared by 4 min and 30 min sonication correspond to conductivity values of 35 ± 2 S cm^{-1} and 25 ± 1 S cm^{-1}, respectively. Figure 5.3b shows that the conductivity decreased with increasing sonication time, exhibiting a plateau value for films prepared by dispersion that have been sonicated for at least 20 min. The decrease in conductivity could be fitted to a power-law ($y = mx^{-b}$), which yielded b = 0.21 ± 0.03. Thus, there is good agreement with the power-law exponent as determined from the SEM analysis of length reduction (Figure 5.2e). This then could be seen

as a validation of our SEM analysis.

This behaviour is linked to the sonication-induced reduction in VGCNF length and can be explained as follows (similar to arguments used for carbon nanotubes as detailed in [128]); the VGCNFs form a percolative network in which the resistance is determined by a combination of the resistances along each of the VGCNFs and the junctions between the VGCNFs. This study also concluded that the junction resistance along a CNT is the primary source of resistance in a percolative network, that is, $R_{JCT} \gg R_{CNT}$. A reduction in the length of the VGCNFs is coupled with an increase in the number of junctions. Therefore, if the junction resistance is the determining factor in the conductivity of the film then it has been shown that the conductivity should follow a power law dependence on the length of the fibres [128]. In other words, conductivity decreases with increasing length of the fibres if junction resistance is dominant, while conductivity is independent of fibre length if junction resistance is neglible. Figure 5.3c shows that the conductivity as a function of fibre length follows a power law with exponent 0.8. Hence, the junctions between the VGCNFs dominate the electrical behaviour of the films.

Tensile testing was performed on free-standing films prepared by evaporative casting to assess the effect of sonication on the mechanical characteristics (Figure 5.4a). The Young's modulus decreased linearly with increasing sonication time from 1.3 $\pm$ 0.3 MPa (4 min sonication) to 0.21 $\pm$ 0.07 MPa (20 min sonication), see Figure 5.4b. This indicated that the films became more ductile with increasing sonication time, *i.e.* the films failed at a higher strain but lower stress. Previous research [214, 325] has attributed this to a combined effect of damage to the polymer (shortening of the polymer chain length with increasing sonolysis) and the carbon filler (reduction in length as discussed above). The combined effect of this is a reduction in the Young's modulus and the tensile strength of the composite.

It is clear that the reduction in the mechanical and electrical properties must be taken into account when using horn sonolysis. Our results indicate that 4 min of horn sonolysis results in composite materials which exhibit robust conductivity (35

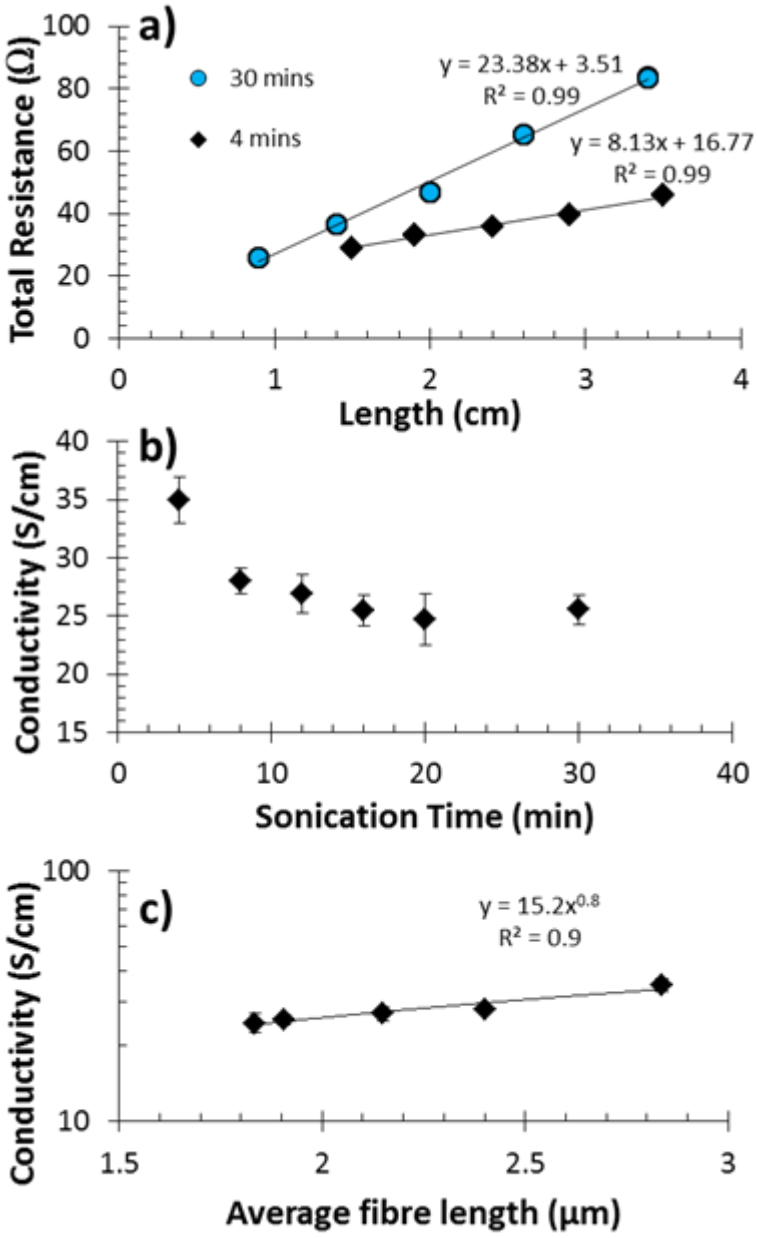

Figure 5.3: Electrical characterisation of free-standing composite films prepared by evaporative casting. a) Total resistance (21 °C, 50 % RH) as a function of film length for films prepared by evaporative casting of dispersions sonicated for 4 (diamonds) and 30 (circles) minutes. b) Electrical conductivity as a function of sonication time. c) Conductivity as a function of average VGCNF length as determined by SEM analysis. Straight lines in a), b) and c) are linear fits to Equation Equation 5.1 and power law fit with exponent 0.8.

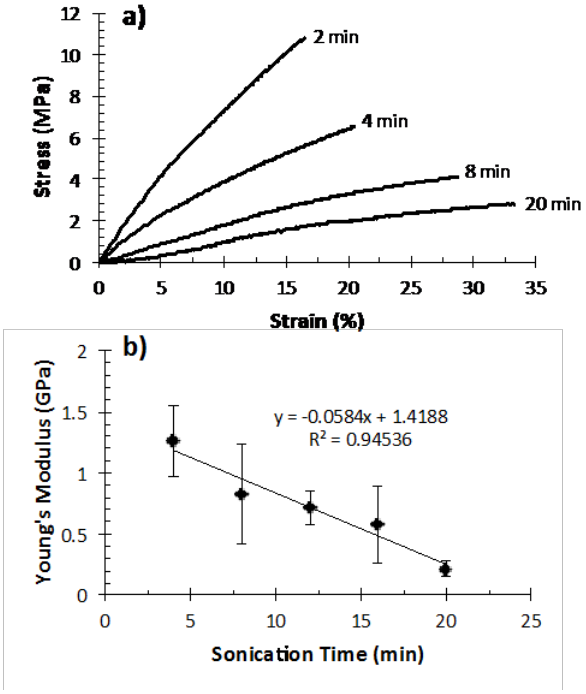

Figure 5.4: a) Typical tensile stress-strain plots of free-standing films prepared by evaporative casting of dispersions sonicated for 2, 4, 8 and 20 min. b) Young's modulus as a function of sonication time. The straight line in b) is a linear fit to the data.

$\pm$ 2 S cm^{-1}) and are mechanical sound. These values are comparable to conductivity values achieved for GG composite materials with multi-walled carbon nanotubes (50 $\pm$ 5 S cm^{-1}), but (as expected) lower then with single-walled carbon nanotubes (110 $\pm$ 15 S cm^{-1}) [58]. Due to the smaller amount of sonication time composite films with VGCNF have better mechanical properties compared to films prepared with carbon nanotubes. Shorter sonication times result in less mechanical shearing (and thus shortening) of the CNTs within the dispersion. Huang *et al.* [129] proposed a mathematical relationship stating the minimum length a CNT will reach, which is proportional to its tensile strength and diameter. This length is unaffected by various sonication parameters, such as pulse length and power level, thus each CNT exposed to sonication will be sheared eventually to this length. It stands to reason then that if two solutions are made with the same CNT, but one is exposed to twice the required amount of sonication energy, that the length of these CNTs will be shorter and thus the sample will have a lower conductivity. This further emphasizes

why it is important to fully optimise sonication time.

5.3.3 Spectroscopy

Raman analysis was used to indicate the change in the level of graphitization of the VGCNFs due to sonolysis (Figure 5.5a). The spectra of the as-received VGCNFs (powder form), and free-standing films prepared by evaporative casting/vacuum filtration of dispersions exhibited two characteristic Raman bands at 1330 $\pm$ 2 cm^{-1} and 1579 $\pm$ 5 cm^{-1}, *i.e.* the D- and G- bands, respectively [337]. It is well-known that the ratio of the intensity of the D-band over intensity of the G-band, I(D)/I(G), is indicative of the level of graphitization. An increase in the I(D)/I(G) ratio corresponds to a decrease in the graphitization of the VGCNFs. The I(D)/I(G) data (Figure 5.5b) revealed that there is virtually no change and a small increase in the ratio with increasing sonication time for films prepared by evaporative casting and vacuum filtration, respectively. This appears to suggest that although sonication results in the opening of VGCNFs, it does not result in significant changes to the level of graphitisation. Inertial sonication brought about by sonication has been shown to perform similar effects with carbon nanotubes [339].

As Raman has a depth of analysis large enough to probe the entire VGCNF and GG does not exhibit suitable characteristic bands it is unlikely that this spectroscopic technique provides information about the effect of filling. To better understand the effects of sonication on the interactions between VGCNF and gellan gum in the dispersions, samples were characterised using XPS analysis. Figure 5.6 shows the typical XPS survey spectra recorded from unsonicated and sonication-treated VGCNFs (2 and 30 minutes, shown in figure Figure 5.5). From the three spectra we can identify 2 main peaks which change their ratio: one at 284.4 eV, which is associated with photoelectrons emitted from carbon 1s core level and a second peak at about 533 eV generated by photoelectron emitted by O1s core level.

More information on the changes due to the sonication treatment can be understood from closer analysis of the C1s and O1s XPS spectra recorded on the different

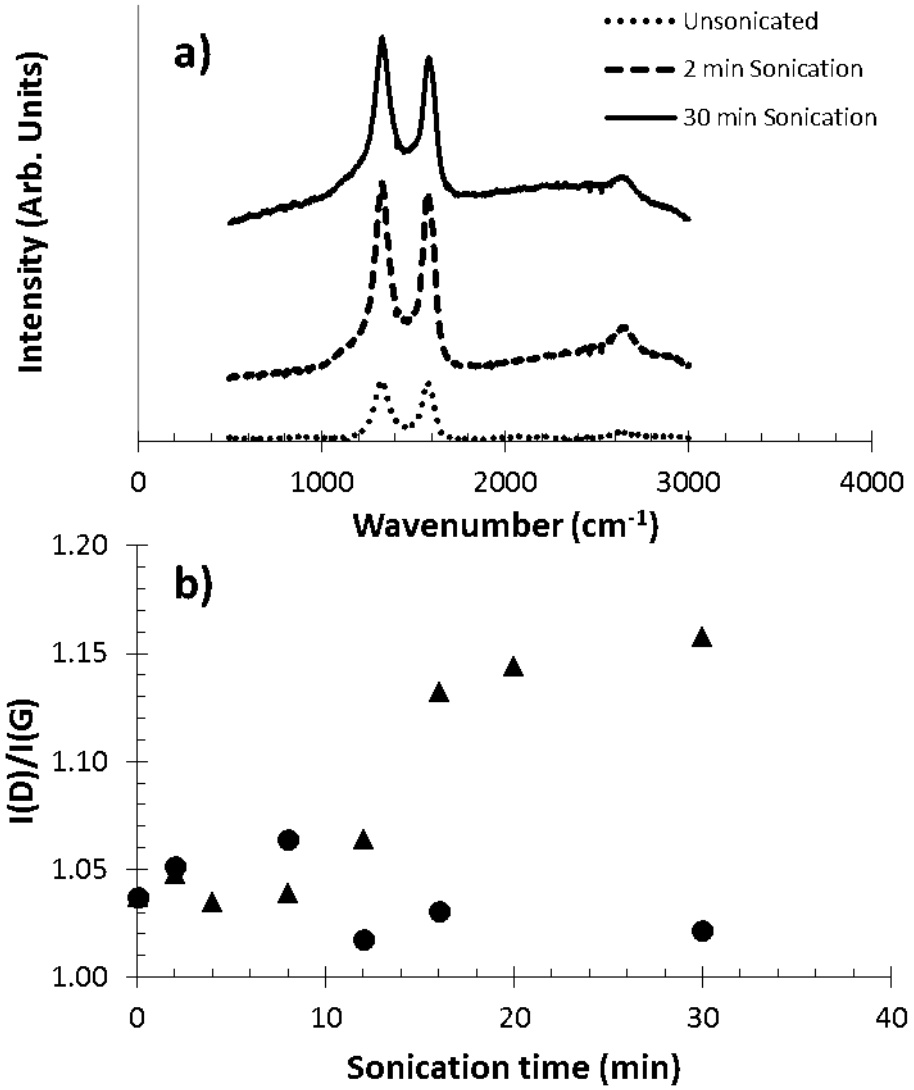

Figure 5.5: a) Raman spectra of VGCNF (unsonicated) and free-standing films prepared from dispersions sonicated for 2 min and 30 min. b) Ratio of the intensity of the D-band over the intensity of the G-band, I(D)/I(G) as a function of sonication time for free-standing films prepared by evaporative casting (triangles) and vacuum filtration (BPs, circles).

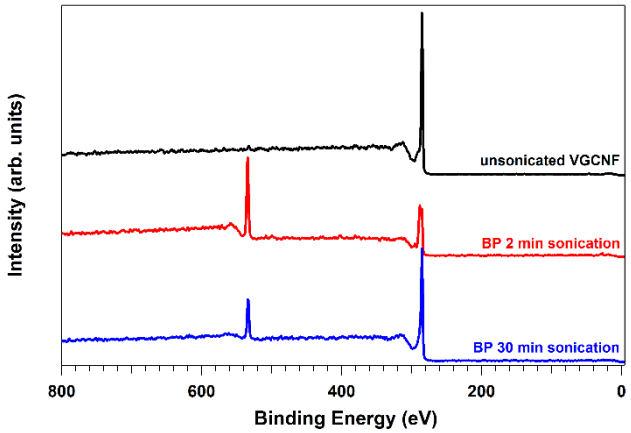

Figure 5.6: Typical XPS survey spectra recorded on unsonicated VGCNFs (black line) and BP produced from dispersions prepared using 2 min and 30 min of sonication (red and blue line, respectively).

samples (Figure 5.7a-b). The pristine C1s spectrum (grey dotted line at the bottom of Figure 5.7a) centred at 284.4 eV has the typical asymmetric line shape of photoelectrons emitted from carbon atoms participating in sp^2 bonds. This asymmetry is associated with the many-electron response to the sudden creation of a photohole [340].

This spectrum also shows a second component at 290.6 eV associated with the electron energy loss due to π-plasmon excitations. The dispersion of the VGCNFs in GG clearly results in a growing shoulder at the high binding energy side of the sp^2 peak. Figure 5.7c shows an example of the results of the curve fittings performed to explain the spectra of the sonicated samples. The modifications produced by the sonication treatment can be identified by a broad structure that peaks at 288 eV. This structure was previously attributed to photoelectrons emitted from carbon atoms belonging to carbon functional groups singly and/or doubly bound to one or two oxygen atoms [341].

To reproduce the C1s peak recorded after 8 min of sonication (Figure 5.7c), 6 components were used. Only three components (1, 2 and 6, Figure 5.7c) are required for fitting the spectrum of pristine (unsonicated) VGCNF: in addition to the asymmetric sp^2 peak at 284.4 eV, two Gaussian functions were used to reproduce the other features observed in the pristine spectrum. One Gaussian at 285.0 eV is associated

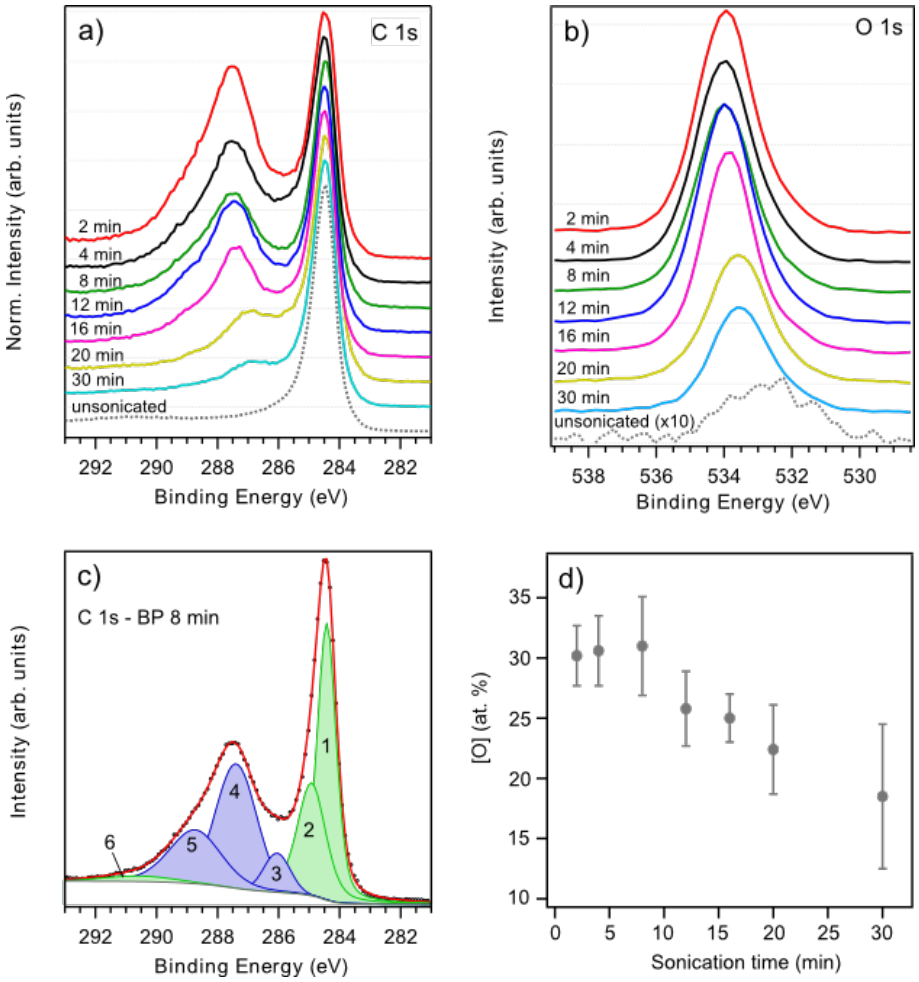

Figure 5.7: a) Typical C1s XPS survey spectra recorded on unsonicated VGCNFs (dotted line) and BPs produced from dispersions prepared using 2-30 min of sonication (colored lines). The spectra are normalised and offset for clarity. b) Typical O1s XPS survey spectra recorded on unsonicated VGCNFs (dotted line, 10 times enhanced) and BPs produced from dispersions prepared using 2-30 min of sonication (colored lines). c) Typical C1s XPS spectrum of BPs prepared using a dispersion sonicated for 8 min. Numbers 1-6 indicate the deconvulotion of the signal using Gaussian components centered at 284.4 eV (sp^2 bonded carbon), 285.0 eV (sp^3 bonded carbon), 286.1 eV (hydroxilic oxygen), 287.2 eV (carbonylic oxygen), 288.6 eV (carboxylic oxygen) and 290.6 eV (π-plasmon excitations), respectively. Black dots and red line indicate experimental data and the result of the fitting procedure, respectively. d) Oxygen content in the sample, obtained by the area under the O1s peak with respect to the C1s.

with photoelectrons emitted from carbon atoms at sp^3 bonds in amorphous carbon. During VGCNF synthesis, competing pathways can lead to amorphous carbon formation rather than to crystalline graphitic nanofibres (as discussed in electron microscopy section, see also Figure 5.1b-c). The other Gaussian, centred at 290.6 eV, corresponds to the π-plasmon excitations. The three other Gaussian components (3 to 5, Figure 5.7c) are related to oxygen containing functional groups present in GG, and centred at 286.1 eV (hydroxilic), 287.2 eV (carbonylic) and 288.6 eV (carboxylic). It is clear from Figure 5.7a that the broad structure at 288 eV decreases with increasing sonication. In addition, the O1s peak (previously observed for modified GG [303]) is also decreasing with increasing sonication time (Figure 5.7b). In other words, the amount of oxygen containing groups is decreasing near the surface of the VGCNFs as shown in Figure 5.7d. The relative amount of oxygen in the unsonicated sample was evaluated to be 2 %.

XPS is predominantly a surface technique (about 8 nm depth of analysis). Combined with the diameter of the VGCNF this would suggest that XPS can only provide data about the surface of the VGCNF and not the interior. Hence, it is suggested that the observed decrease in the O1s spectra (Figure 5.7b) and the oxygen containing groups in the C1s spectra (Figure 5.7d) can be explained by the reduction of gellan gum on, or near the surface of VGCNF due to filling of the VGCNF with GG. Electron microscopy results (Figure 5.1) appear to be in support of this suggestion, with the fibres becoming filled to a larger extent with increasing sonication time.

5.4 Conclusions

Incorporation of tubular carbon nanostructures into materials to form hybrid materials is an attractive area of chemical materials research. Tailoring the properties using sonication of functionalised materials is potentially very exciting as this allows for both physical and/or chemical changes.

The effect of sonolysis on vapour grown carbon nanofibres in gellan gum composite materials has been investigated. Finding the minimum time for sonication

is a typical first step when producing dispersions containing carbon nanostructures, however rarely is the effect of sonolysis on the properties of the constituents and the resulting materials studied in detail.

It was found that the average length of the VGCNFs was halved with just 30 minutes of low energy sonication. Electron microscopy analysis revealed that the VGCNFs were opened, shortened and filled. Spectroscopy analysis revealed that sonication treatment resulted in modification of the VGCNFs.

Our investigations revealed that the electrical characteristics reduced (from 35 $\pm$ 2 S cm^{-1} to 25 $\pm$ 2 S cm^{-1}) due to sonication-induced reduction in length of the carbon nanofibres. In contrast, it is likely that the reduction in mechanical characteristics is mostly due to the effect of sonolysis on polymer chain length. This paper demonstrates that despite the sonication-induced opening, filling and modification of carbon nanofibers, composite materials that are mechanical robust and electrically conducting can be easily prepared by limiting the amount of horn sonolysis (to just 4 min).

Methods for the filling of carbon nanotubes are well established, there has been limited research regarding the filling of carbon nanofibers [1, 336]. One of the remaining challenges is to prepare filled tubular carbon nanostructures with properties suitable for selective drug delivery (*e.g.* nanosized needles) and for autonomic healing of polymeric materials (*e.g.* load-bearing biomedical materials). It is suggested that filled VGCNFs offer great opportunities for addressing these challenges.

5.5 Acknowledgements

This project was supported by the University of Wollongong (UOW), Australian Research Council (ARC) Centre of Excellence for Electromaterials Science, ARC Future Fellowship program, and the Belgian Fund for Scientific Research (FRS-FNRS) under FRFC contract "Chemographene" (convention N° 2.4577.11). Carla Bittencourt and Marc in het Panhuis acknowledge support from the European Union COST action MP0901 "NanoTP" and Australia Academy of Science. Ross Clark

(CP Kelco) and Patricia Hayes (UOW) are thanked for the provision of gellan gum and assistance with Raman measurements. The authors acknowledge the use of facilities within the UOW Electron Microscopy Centre and the Materials Node of the Australia National Fabrication Facility.

Chapter 6

3D Printed Carbon-Based Soft Strain Gauges

Soft robotics is a rapidly emerging field, with an increasing interest in the development of fully compliant machinery. To sense the motion of such an appendage, the development of a soft strain gauge is necessary, utilizing 3D printing to match the dynamic range of substrates. In this study, a hybrid carbon black(CB)-vapour grown carbon nanofibre(VGCNF) dispersion is produced, and is evaluated for it's ability as a strain gauge. The effects of sonolysis on the carbon materials is studied, and the detrimental effects on the physical and electrical properties are presented. From this, an optimised dispersion was 3D printed onto the surface of a hydroxyethyl methacrylate (HEMA) hydrogel to for a strain gauge, which was found to have a GF of 1.8 ± 0.2 and 0.76 ± 0.04 for one and two layers respectively.

Author Statement

This chapter contains the following under review journal article, stylistically edited to suit the rest of this document:

R. Gately, S. Naficy, R. Gorkin, and M. in het Panhuis, "3d printed carbon-based soft strain gauges," *Nanotechnology*, (*Currently under review*)

Author Statement:
I, Reece D. Gately, hereby declare that I contributed to the following work within this manuscript by:

- Produced all samples,
- Ran all experimental methods,
- Analysed all produced data,
- Developed the 3D extrusion printer used,
- Wrote and edited the manuscript.

All other work required for this manuscript was performed by other co-authors as follows:
Dr. Sina Naficy: Developed the hydrogel formulation to be printed (both HEMA and NIPAM) and performed mechanical analysis on both HEMA and NIPAM pure samples.
Dr. Robert Gorkin III: Assisted in development of the 3D extrusion printer.
Prof. Marc in het Panhuis: Assisted in proof-reading and editing the manuscript.

I, Prof. Marc in het Panhuis (supervisor), support and certify that the above author statement is correct.

Marc in het Panhuis
April 20, 2017

6.1 Introduction

Soft robotics is currently a large and rapidly growing field of research. This is largely driven by the fact that 'hard' robotics struggle with delicate tasks, such as gripping soft objects, and have a hard time integrating with (soft) human bodies. To this aim, softer materials, such as hydrogels, are being studied as artificial muscles or actuators [3, 343, 344]. Hydrogels offer a soft, adaptable, material that can act as either a muscle itself, or as a platform for other materials. Hydrogels have been successfully implemented as a grip assistant [6] and been able to grip soft objects without damaging them [345].

One of the biggest challenges identified for soft robotics is the development of suitable sensors that can be integrated with soft actuators. Examples of how this can be integrated include sensing the capacitance in a piezoelectric actuator [20, 21], embedding external sensors within the soft actuator [346], or aerogels that increase in conductivity [347].

A strain gauge works on having a measurable material property that changes with respect to how far it has been strained or compressed. There are two primary methods this can be attained; change in capacitance [348] or change in bulk resistance [249]. Resistive strain gauges have high adaptability, as they can be readily processed using additive manufacturing (*e.g.* 3D printing) [349].

Previous studies have shown that carbon nanotube (CNT) dispersions act as an effective strain gauge on soft substrates [350, 351], with some being fully 3D printed [245] and high gauge factors [352]. The ideal material for a strain gauge has high electrical conductivity (> 1 S cm^{-1}), while maintaining a high degree of elasticity. Hybrid systems containing both CNTs and graphene in an epoxy resin have shown that they can produce flexible conductors, with no loss of electrical properties through multiple cycles [353]. However, when comparing the conductivity of a CNT dispersion to that of one with graphene, there are mixed results, as some studies indicate a synergistic effect, others indicate a hindrance [354, 355]. Multiple studies, however, verify that the thermal conductivity increases with a

higher graphene content [356, 357], which supports thermally activated actuators. Alternatives to CNTs and graphene are vapour-grown carbon nanofibres (VGCNFs) [52, 358, 359] and carbon black (CB) [360]. The effect of adding CB to a multi-walled CNT dispersion has been studied [361], however combinations of VGCNFs and CB are yet to be studied. Scores of studies have been performed on VGCNF, CNT, and graphene based strain gauges, however there are very few papers concerned with VGCNF-CB combined dispersions. Individually these materials can produce highly conductive, flexible printed tracks, however any potential synergies between the materials have not been studied.

Gellan gum (GG) is a linear, anionic, water soluble polysaccharide that is derived from the bacteria *Sphingomonas elodea* (formerly *Pseudomonas elodea* or *Auromonas elodea* [109]). It is a shear thinning material with highly adaptable rheological properties [362, 363], making it an ideal rheological modifier for 3D extrusion printing of various materials [364]. GG has been shown to be a highly effective dispersant of various carbon materials, such as VGCNFs [52] and Carbon Nanotubes (CNTs) [365], using only 30 % wt of the carbon materials in water to achieve a full dispersion. The low acyl version of GG has been shown to be a vastly superior dispersant of carbon materials than the high acyl couterpart [114, 115].

In order to disperse the CB and VGCNFs into the GG to form an aqueous solution, a method of mechanically mixing is required. The primary method used to achieve this goal is sonication, through either bath [120] or probe sonolysis [121]. Using bath sonolysis tends to have a higher mixing time with a much lower energy effciency [339], when compared to probe sonication [52]. While probe sonication offers a faster method to deliver the energy, it does come with drawbacks. It can damage both the dispersant and the filler, which can have detrimental effects on the mechanical and electrical properties [1, 122]. As such, it is important to monitor this level of damage, which can be done through techniques such as transmission electron spectroscpy (TEM), scanning electron microscopy (SEM), and X-ray photoelectron spectroscopy (XPS).

Hydrogels have shown excellence in assisting with the development of soft robotics [2]. This is due to their similarity to skin, and thus can be integrated effortlessly with the human body [366]. One particular hydrogel that has shown promise for biomimetic soft robotics is hydroxyethyl methacrylate (HEMA) [218, 367]. Their strong mechanical properties [241] and ease of curing the hydrogel make it an ideal candidate for hydrogel soft robotics.

In this paper, a method to disperse a combined system of both CB and VGCNFs in the dispersant GG for 3D printing high gauge factor strain gauges is presented. The primary aim of this study is to produce and characterise a 3D printable dispersion utilizing both VGCNFs and CB. First the dispersions are optimised with respect to the mass fraction of CB, VGCNFs and the sonication time. The level of damage due to sonication is also evaluated and presented. This ink is then directly written using a custom-built 3D printer onto a HEMA-polyurethaine (PU) hydrogel surface, to form a strain gauge. The ability for the ink to act as a strain gauge is then characterised.

6.2 Materials and Methods

6.2.1 Preparation of dispersions

Low acyl gellan gum (GG, Gelzan, Lot#1I1443A) was gifted to our research group from CP Kelco. Gellan gum solutions at the required concentration (up to 1.2 % w/v) were prepared by dissolving the required amount of dry powder in Milli-Q water (100 mL, 80 ^{o}C, resistivity 18.2 MΩ cm) while vigorously stirring with an overhead stirrer (800 RPM, IKA RW 20 digital) for 30 minutes, until the solution was clear.

10 mL of the GG solution was placed in a glass vial (25 mL diameter), and to that the required amounts of CB (KetjenBlack EC600-JD, AkzoNobel) and VGCNFs (Pyrograf Products, PR24-LHT, PS 1345 Box 8, HT 170) were added. This was then subjected to digital probe sonication (Branson Digital Sonifier, 6 W power

output, 0.5 s pulse on/off) through a titanium tapered microtip (Consonic, 3.175 mm diameter). The glass vial was placed in an ice bath.

6.2.2 Preparation of free-standing films

Free-standing films were prepared by evaporatively casting of the VGCNF:CB:GG dispersions. The as-prepared dispersions were poured into a plastic petri dish (diameter 55 mm) and allowed to evaporate under controlled conditions (21 ^{o}C, 50 % RH) in a temperature-humidity controlled chamber for 24 hours. The films were then carefully freed from the petri dish to produce free-standing films.

6.2.3 Preparation of HEMA-PU hydrogels

HEMA-PU hydrogels were prepared as follows. To 10 mL of ethanol we added 5 g of hydroxyethyl methacrylate (HEMA, Sigma Aldrich, Australia), 0.11 g of the UV initiator, α-ketoglutaric acid (AKG), and 0.12 g of the crosslinker, N,N'-methylenebisacrylamide (NBAAm, Sigma Aldrich, Australia). This solution was stirred and heated (IKA C-MAG HS hotplate stirrer, Sigma Aldrich, Australia) at 60 ^{o}C until fully dissolved. 5 g of a rheological thickener, polyether-based polyurethane (PEO-PU, AdvanSource Biomaterials, HydroMed D-4), was then broken up and slowly added. This final solution was then sealed, blocked from light, and stirred for 2 days at 60 ^{o}C until all PEO-PU is dissolved, producing a transparent, viscous solution.

To cure the HEMA-PU into a hydrogel, the solution was poured into a 25 x 40 x 4 mm ^{3} cast, and placed between two glass slides held together tightly by bulldog clips. Care must be taken when applying the glass slide to not introduce any air bubbles, and these were thoroughly inspected before curing. This was then placed in a reflective chamber, and the sample was irradiated with UV light (DyMax BlueWave 75, 9 W cm^{-2}) for up to 10 mins until fully cured. The sample was then left to dry overnight, before rehydrating in water. A transparent, hydrophobic coating (nail polish top coat, Priceline Pharmacy Australia, SKU: 598425) was applied to one

surface of the swollen hydrogel to facilitate 3D printing.

6.2.4 3D printing of strain gauges

A custom-built 3D printer was used to print the strain gauges onto the hydrogel, and can be seen in Figure 6.1. The printer consists of a commercially available milling machine (Sherline 8020) and a custom designed and 3D printed holder (Figure 6.1 b). This held both the material syringe (5 mL or 30 mL) and the linear actuators used to extrude the material (Zaber T-NA08A50-KT01U, 50 N thrust). These actuators were controlled by custom-designed software (coded in C#) to control speed and timing of actuation.

The strain gauge pattern was designed and coded in G-code, as this could be directly imported into the printer. The whole strain gauge was 20 mm in length, and 15 mm wide, with track width $\approx$ 1 mm. The strain gauge was designed with two connectors (5 x 5 mm) and three tracks in the axis of actuation. Each track was separated by 5 mm, which provided adequate spacing to ensure they did not short circuit during printing or afterwards.

Optimum printing conditions were found when the print needle was set to a jog speed of 60 mm min^{-1}, with the flow rate of the ink at 24 μL min^{-1}. The dispersion used to produce the strain gauges consisted of [VGCNF] = 10 mg mL^{-1}, [CB] = 20 mg mL^{-1}, and [GG] = 9 mg mL^{-1}, sonicated for 8 min. The material was extruded through a 25 gauge (ID 0.26 mm) smooth-flow tapered tip (Nordson EFD, 7018391). To ensure solid connection, a 5 cm length of conductive yarn (Type C50T024, SGL Carbon Fibers LLC, Evanston, WY, USA, cross-sectional area $\approx$ 0.221 mm^2) was placed onto the connectors during printing when the ink was wet and allowed to dry in place to reinforce the connection. These tracks were then sealed with the same hydrophobic coating to prevent swelling.

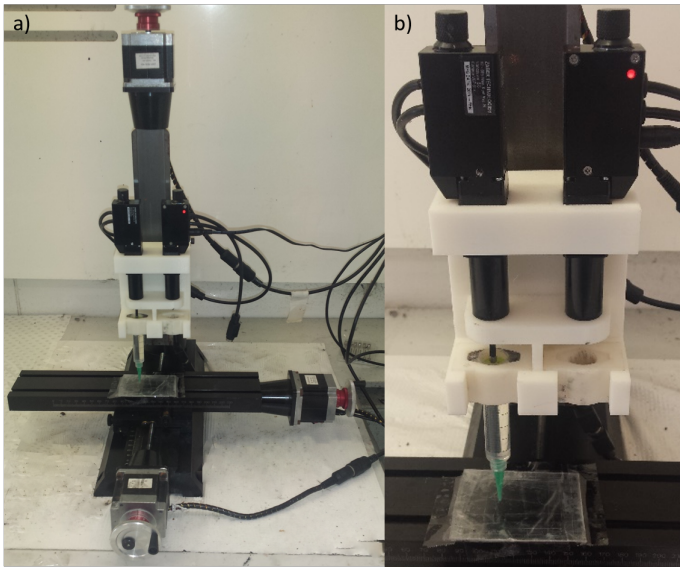

Figure 6.1: An image displaying a) the custom-built 3D printer as-used, with b) an inset showing a close-up of the actuator and syringe holder.

6.2.5 Characterisation Methods

Assessment of the VGCNF:VB disperse-ability was performed through monitoring the UV-Vis-NIR absorbance at various sonication times, with wavelengths of 1000 nm and 1150 nm using a standard spectrophotometer (Shimadzu UV-3600). The dispersions were diluted down in water to a total carbon (carbon black and VGCNF) concentration of 10 μg mL^{-1} prior to analysis.

Electrical characterisation of the free-standing films was performed using a custom-built impedance setup [58]. This impedance setup utilizes a USB waveform generator (Agilent U2761A) and oscilloscope (Agilent U2701A) to apply a sinusoidal waveform across a known resistor and the sample. Initially, a sweeping waveform was applied (1 V peak voltage, 1 Hz to 100 kHz), and for further analysis a 10 kHz waveform was used.

Scanning electron microscopy (SEM) analysis of all free-standing films was carried out using a field emission scanning electron microscope (FESEM JEOL JSM 7500-FA) operated at 5 kV and a spot size setting of 8. Length analysis of VGCNFs was performed using an image analysis package (Leica Application Suite Version 4.3)

Raman analysis was conducted using a Raman spectrometer (JY HR800, Horiba

Jobin Yvon). The laser used was a HeNe laser (632.8 nm wavelength) at a power of 20 mW. The detector was an optical microscope (Olympus Bx41) with a spatial resolution of 1 mm. The spectrometer was calibrated using SiO_2 at a wavenumber of 520.7 cm^{-1}. All scans were performed between 500 and 3000 cm^{-1} under controlled ambient conditions.

Rheological testing of the ink was performed on an Anton Paar MCR301 Digital Rheometer with a peltier heated base (Julabo Compact Recirculating Cooler AWC 100, 21 ^oC. Viscosity profiles were obtained by performing a rotation test with a cone and plate measuring system (49.972 mm diameters, 0.992^o angle) from $\dot{\gamma}$ = 0.01 to 100 s^{-1} with 3 min of pre-shear.

Mechanical testing of cured HEMA-PU hydrogels was performed on a universal tensile tester (Shimadzu, EZ-S). 5 x 20 mm^2 strips of the cured HEMA-PU hydrogels without the hydrophobic coating were tested at a rate of 2 mm min^{-1}. The strain gauges were also tested using this same instrumentation. When testing a strain gauge, the carbon fibre connectors were placed within the clamps to restrict the movement. Each strain gauge was tested up to a strain of 15%, at a rate of 6 mm min^{-1}. In order to evaluate the creep, a 15 s pause was added at both the start and end of each cycle. A USB multimeter (Agilent 34401A) was connected and was recording the resistance at 50 μs intervals. Each gauge was subject to 25 loading/unloading cycles.

6.3 Results and Discussion

6.3.1 Sonication and Electrical Optimisation

When developing the conductive ink, as the VGCNF or CB are the components that add conductivity and the GG is merely the dispersant, the [GG] needed to be minimised. The first step taken to this extent was to disperse a low mass (*i.e.* 1 mg) CB into solutions of decreasing [GG]. Using a high [GG] with a low [CB], the absorbance of a fully dispersed CB solution can be established. To achieve this,

initially 1 mg CB was added to 10 mL of 1 % GG, which was sonicated and had the UV-Vis absorbance monitored, which reached a plateau after 30 s sonication. The [GG] was then decreased to a point where it no longer reached this same absorbance *i.e.* when [GG] is too low to achieve a full dispersion. The minimum [GG] was found to be 0.3 %, which reached a plateau after 2 min sonication. The [CB] was then increased, maintaining [GG] at 0.3 %. The maximum [CB] found was 10 mg mL^{-1} in a 0.3 % GG solution which plateaued out at the same absorbance after 4 min sonication. This ratio was maintained for all further optimisation studies, *i.e.* a 10: 3 ratio.

Initially, the sonication dispersion efficiency as a function of energy input for the CB in GG needed to be determined, and the results can be seen in Figure 6.2a. It can be seen that the lowest energy per mg CB was that of [CB] = 20 mg mL^{-1}. These samples were attempted to turn into dry films as per the experimental, however it was found that CB lacked the structure to be able to create solid films, with a large majority cracking. From the few films that were able to be produced, it was noted that they were quite thick, readily cracked, and low in surface area, so this formulation was deemed unfit to turn into a strain gauge.

In order to turn this dispersion into a free-standing film more consistently with better properties to suit a strain gauge VGCNFs were added. After the optimal sonication parameters for the CB-GG dispersion was determined, both systems were combined to determine the optimal concentration of both fillers relative to each other. This was established by maintaining [VGCNF] at 10 mg mL^{-1} and incrementing [CB] from 5 to 30 mg mL^{-1} (Figure 6.2a). It was found that above 30 mg mL^{-1} the volume of CB was too high, and the solution, upon brief sonication to break up the pelletised CB, would be unable to be sonicated any further. Dispersion efficiency was not greatly affected by the addition of both carbon materials, with only a minor decrease in efficiency. From Figure 6.2a, we can see that the optimum [CB] is 20 mg mL^{-1}, as this has the lowest energy requirement per mg of CB. This was also verified by maintaining the [CB] at 20 mg mL^{-1} and varying [VGCNF],

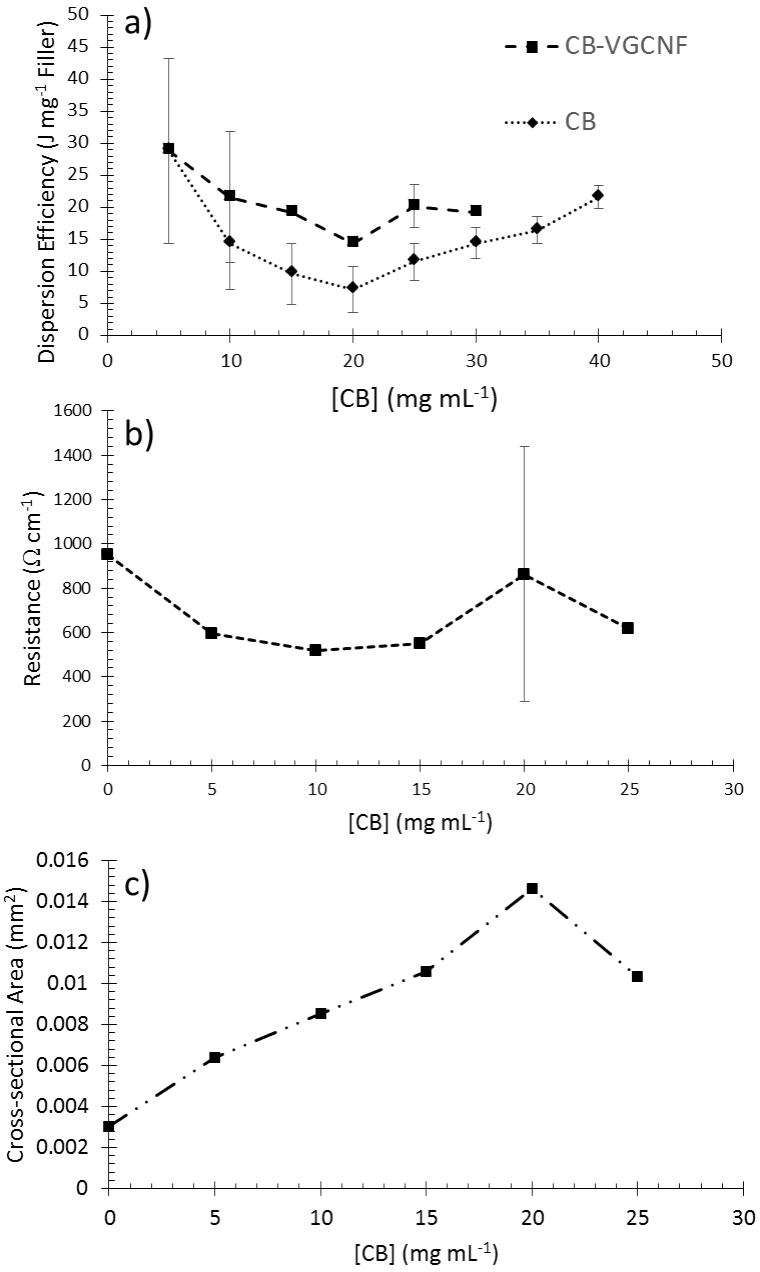

Figure 6.2: Sonication optimisation of both the CB and CB-VGCNF dispersions as dry films, as well as their cross sectional area. In all samples shown, the [VGCNF] was 10 mg mL^{-1}, as it is the optimum concentration, with [GG] chosen to give a ratio of 10: 3 carbon filler to GG. a) shows the dispersion efficiency of both the CB and CB-VGCNF against [CB]. b) shows how the resistance of the samples is affected through the addition of CB. c) shows how the cross-sectional area is increased with increasing [CB].

which also showed that this dispersion was the most energy efficient. This solution was chosen as the dispersion for the rest of this study, *i.e.* [VGCNF] = 10 mg mL^{-1}, [CB] = 20 mg mL^{-1}, [GG] = 9 mg mL^{-1}, with a sonication time of 8 min.

For the development of a resistance-based strain gauge, it is the unit resistance that is the important property, rather than the conductivity, and this was measured and is shown in Figure 6.2b. It was noted that after the addition of a small amount of CB the resistance drops from 950 $\pm$ 50 Ω cm^{-1} down to 520 $\pm$ Ω cm^{-1} at [CB] = 10 mg mL^{-1}. At higher concentrations the resistance remains relatively unchanged (within errors).

While increasing the [CB] the resistance remains unchanged, it is worth noting that the cross-sectional area increases (Figure 6.2c). As the size of the petri dish was kept constant for all samples produced, as more material was added, it would produce a thicker film. Both the increase in thickness and [CB] are attributed to the reduction in resistance.

6.3.2 Damage due to sonication

In order to quantify the damage on the carbonous fillers due to sonication, a variety of techniques were employed. The first of which was length analysis of SEM micrographs, as seen in Figure 6.3. The length analysis was performed by examining multiple SEM micrographs at increasing sonication times, with typical micrographs of the 4 and 24 min sonicated films shown in Figure 6.3b-c. Through measuring the length of each visible fibre, a distribution of the fibre length was produced (Figure 6.3a). It can be seen here that, as the sonication time increases, the distribution tends towards smaller fibres, with a majority of fibres greater than 3 μm in length for a 4 min sonicated film. When compared to a 24 min sonicated film, where the majority lie between 0.5 and 1.5 μm in length, this shows that with increasing sonication time the fibre length is dramatically reduced. When this effect is compared to a VGCNF: GG dispersion [52], the effect is amplified for lower sonication times, but decreased for higher sonication times. That is, at 4 min sonication time, longer

fibres were present in a VGCNF: GG film, however at 24 min sonication, longer fibres were present in a VGCNF: CB: GG film. This indicates that during initial sonication the VGCNFs absorb most of the sonication energy, however as sonication time is increased, the force is distributed across both the VGCNFs and CB.

This reduction in length also contributes to the reduction in the conductivity at increased sonication times (data not shown). It has been previously shown that the resistance of a CNT network is almost solely determined by the number of junctions, as $R_{JCT} \gg R_{CNT}$ [128].

Raman analysis was also performed on all three dispersions (VGCNF: GG, CB: GG, and VGCNF: CB: GG) at the optimal time, and can be seen in Figure 6.4a. From examining the ratio of the D and G peaks, which are typically around 1324 cm^{-1} and 1597 cm^{-1} respectively, we can evaluate the damage to the π stacking in the VGCNFs. It can be seen from Figure 6.4b that at increasing sonication times the D: G ratio of the liquid dispersion increases while the dry films decrease. In dry films, there is initially a decrease in the D: G ratio when compared to pristine CB powder (1.37 ± 0.08), but an increase when compared to pristine VGCNF powder (1.03 ± 0.02). This increase can be attributed to various physical changes in both carbon materials. In the case of carbon structures, these are evident in the amount of amorphous carbon present. It is known that the average size of the microcrystalline structure, L_a, can be calculated from this ratio by:

$$L_a = 44[I(D)/I(G)]^{-1}, \tag{6.1}$$

where $I(D)$ and $I(G)$ are the D and G bands, respectively [368, 369]. This then states that, as the D: G ratio increases, L_a decreases, which, in the instance of carbon materials, is the amount of crystalline carbon. As the D: G ratio is higher for a VGCNF: CB: GG dispersion than that of one without CB, it can be noted that CB consists of more amorphous carbon than VGCNFs. As sonication time increases, the crystalline structure in both the VGCNFs and CB is disrupted, converting it to amorphous carbon.

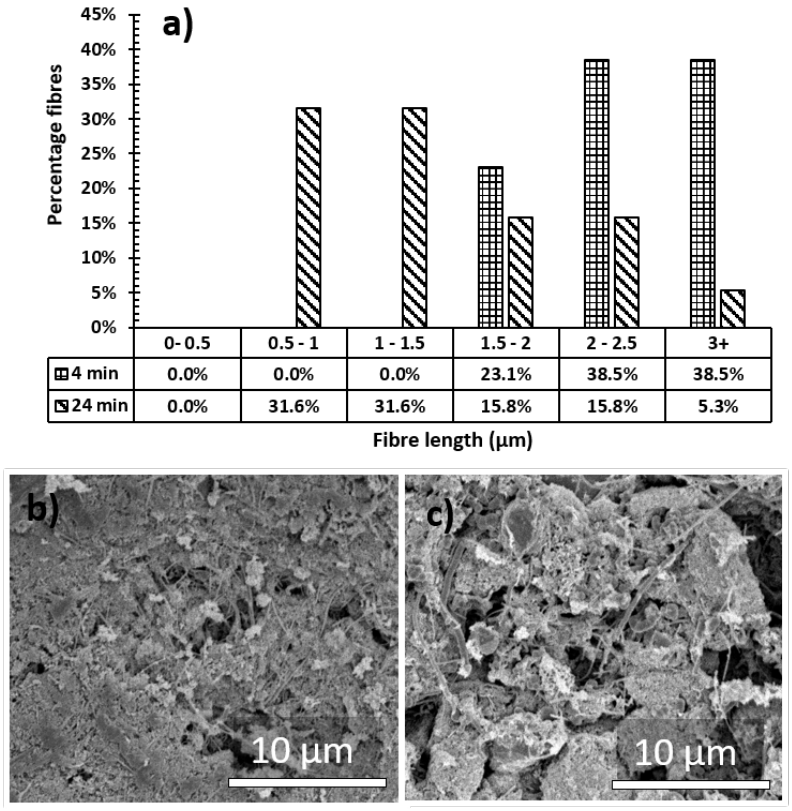

Figure 6.3: a) represents a bar graph with the number of VGCNFs within a certain length bracket, as a percentage as all viewed fibres.b,c) show two example SEM micrographs for a 4 and 24 min sonicated sample at 2,500x magnification.These micrographs were used for the length analaysis.

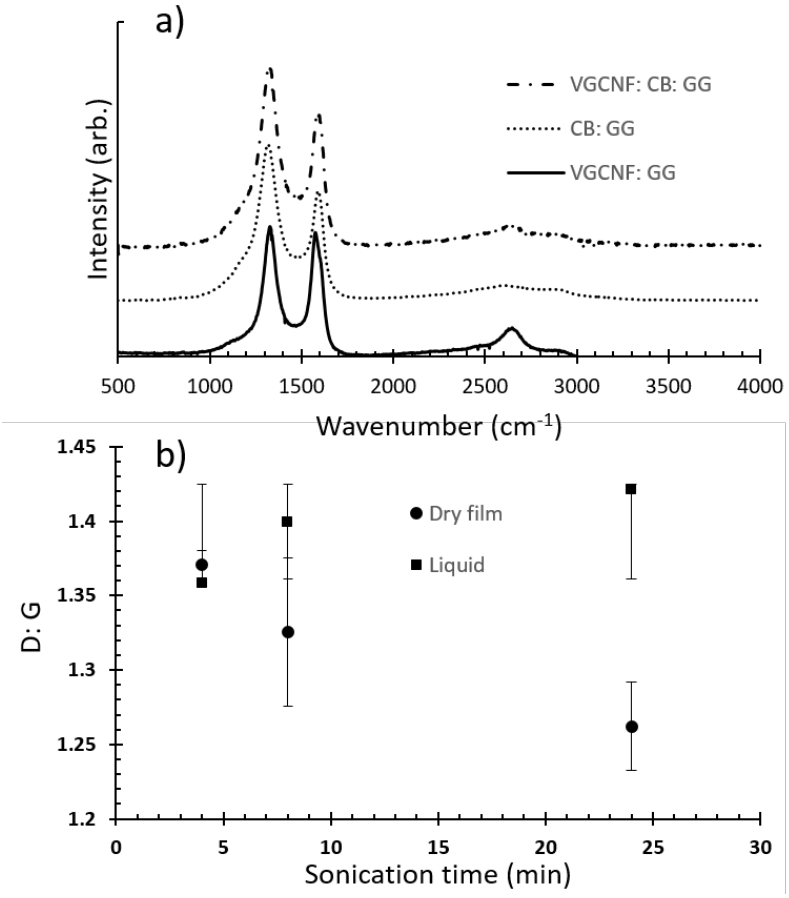

Figure 6.4: a) shows typical Raman spectra of VGCNF: GG, CB: GG, and VGCNF: CB: GG dispersions as a free-standing film. b) shows the D: G ratio of the VGCNF: CB: GG dry film as a function of sonication time.

Examining the length of visible fibres within the film also indicates that there is a significant reduction in fibre length as sonication time is increased (Figure 6.3b). A 4 min sonicated sample has a broad spread of fibre lengths, with the highest percentage above 2 μm, whereas a 24 min sonicated sample has the greatest percentage below 1.5 μm.

6.3.3 3D Printed Strain Gauges

Before attempting to print the tracks on a hydrogel, the rheological properties were examined to determine suitability, and are displayed in Figure 6.5. Figure 6.5a shows a typical viscosity sweep from $\dot{\gamma} = 1$ to 100 s^{-1}. Since the plot is linear when plotted as a lin-log plot, this represents a shear thinning material, and can be quantified by the following equation:

$$\eta = K\dot{\gamma}^{n-1}, \tag{6.2}$$

where η is the viscosity (Pa s), K is the flow consistency index (Pa s^n), $\dot{\gamma}$ is the shear rate (s^{-1}), and n is the flow behaviour index (1 for Newtonian fluids, less than 1 for shear thinning materials). It was found that, for the optimum ink, $K = 0.87 \pm 0.02$ Pa s^n and $n = 0.86 \pm 0.02$. This shows that the material is shear thinning, with a high initial viscosity, and thins rapidly at higher shear rates, thus is ideal for 3D extrusion printing.

The effects of increasing [CB] on the rheological properties was also examined (Figure 6.5b-c). Upon examining η at $\dot{\gamma} = 100$ s^{-1}, it was shown to steadily increase until [CB] = 20 mg mL^{-1}, where it jumped significantly (from 16 ± 1 to 49 ± 4 mPa s^{-1}). The K value experienced a similar trend, however it started to increase after [CB] = 15 mg mL^{-1}. This shows that at low concentrations the CB does not affect the rheological properties, however at higher concentrations it can be used to make a far more viscous and shear thinning ink. This examination also showed that the ink was suitable for 3D extrusion printing.

The strain gauge was printed onto a hydrated HEMA-PU hydrogel (thickness

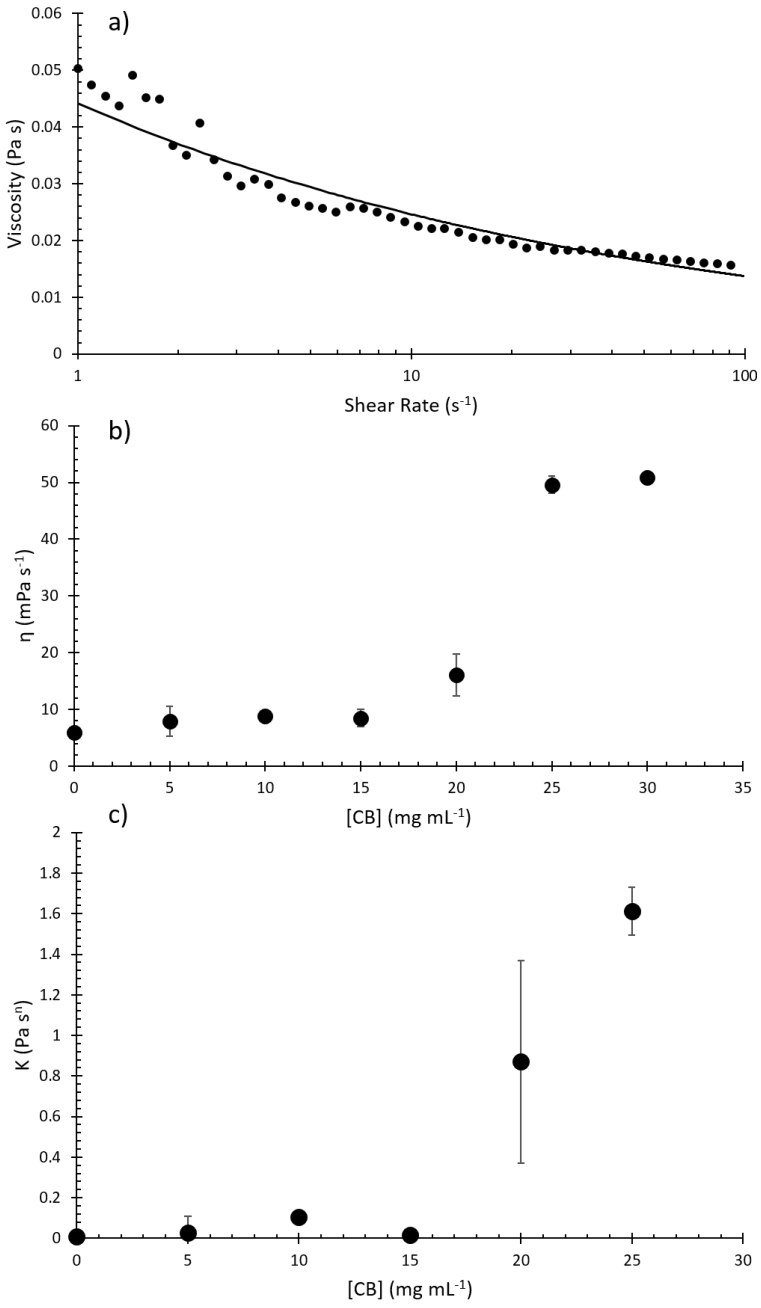

Figure 6.5: a) shows a typical viscosity sweep for an optimal CB-VGCNF ink from a shear rate of 1 to 100 s^{-1}. b,c) shows how the viscosity (at $\dot{\gamma} = 100$ s^{-1}) and K value are affected by increasing loading fractions of CB. Solid line in a) is a fit to Equation 6.2.

$\approx$ 1.75 mm), however a hydrophobic layer was required on the printed surface to encapsulate the carbon tracks. Since the main mechanism for conduction in the VGCNF: CB: GG dry films is through electronic rather than ionic, this is hindered by water. Thus, the coating ensured that the hydrogel would stay hydrated, but the strain gauge would not. This limited the maximum resolution of the tracks, restricting the minimum size of the strain gauge, which can be seen in Figure 6.6a. Each tested strain gauge has three tracks in the direction of strain to increase sensitivity to smaller strains. To explain this, let

$$\Delta R \propto \frac{\delta l}{l_0}, \tag{6.3}$$

where ΔR is the measured change in resistance, δl is the change in length during strain, and l_0 is the original length. Thus, to maximise ΔR, and therefore a higher gauge factor, a longer track is more desirable, however to keep the size of the strain gauges down to an applicable size the tracks were curled. This effect has been previously reported [245]. These samples consisted of one layer of tracks, as a single layer was faster and simpler to produce, with the end results of the two roughly comparable.

The mechanical properties of both one and two layered strain gauges are summarised in Figure 6.7. The HEMA-PU hydrogel was mechanically tested to failure to find the elastic region, which was found to be up to 20 % strain (data not shown). For this reason, each strain gauge was cyclically tested up to 15 %, to ensure that it was within the elastic region of the HEMA-PU hydrogel.

Both single layer and dual layer strain gauges were printed and mechanically tested during strain gauge evaluation, and can be seen in Figure 6.7b. From this plot, two other important properties were extracted; the Young's Modulus, and the energy dissipated on each cycle (Figure 6.7b and c). For a single layer strain gauge, the Young's Modulus is observed to initially increase, then begin to decline, giving an average of 160 $\pm$ 2 kPa, however the opposite was noted for a dual layer gauge, averaging at 235 $\pm$ 9 kPa. This is attributed to initially pre-stressing the

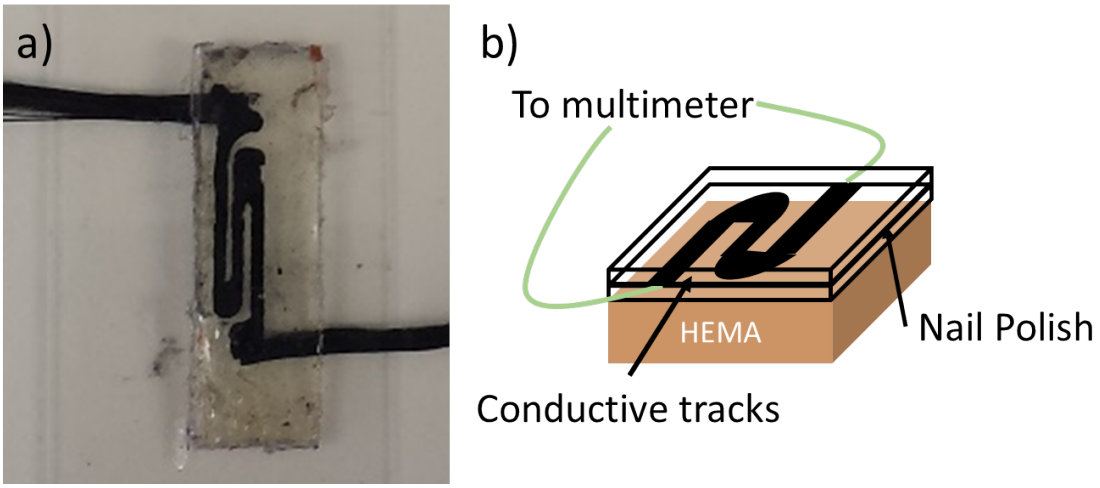

Figure 6.6: a) Photograph of an as-printed strain gauge with the conductive fibre connectors. b) A schematic representation of the strain gauge composition.

gel, allowing the bonds to rearrange within the hydrogel, and minor cracks in the conductive tracks forming. Upon addition of a second layer of conductive track, the Young's Modulus is found to increase, and this is attributed to the hydrophobic coating. When applied and dried, it forms a stiff, brittle layer, which was found to alter the mechanical properties. The energy dissipated on each hysteresis loop was also examined, and presented as a percentage of the loading energy (Figure 6.7c). For a single layer, this was found to remain constant between the 2^{nd} and 23^{rd} cycle, averaging at 14.7 ± 0.4 %. However, the two layer strain gauge was seen to steadily increase after the 4^{th} cycle, increasing at a rate of 0.718 ± 0.006 % each cycle. This increase in energy dissipated for a dual layered strain gauge was attributed to the tracks breaking through multiple cycles.

The initial samples printed had a single layer of the CB-VGCNF ink, as this was found to be enough to produce a strain gauge. The gauge factor (GF) was calculated using:

$$GF = \frac{\Delta R/R_o}{\epsilon}, \tag{6.4}$$

where ΔR is the change in resistance across the total strian, R_o is the unstrained resistance of the strain gauge (which was 240 ± 80 kΩ), and ϵ is the strain placed on the sample. Using Equation 6.4, the GF was calculated for each cycle throughout

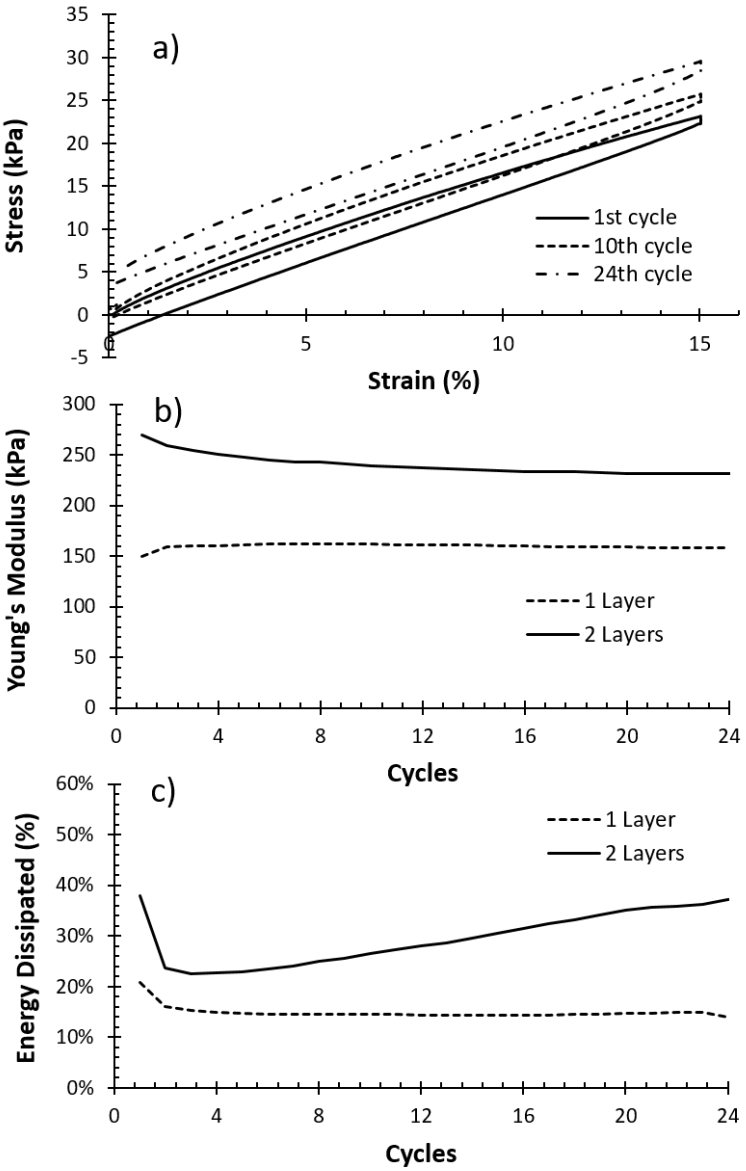

Figure 6.7: Three graphs summarising the mechanical properties of both the HEMA-PU hydrogel by itself, and with a 1 layer printed strain gauge. a) A typical stress-strain graph for a strain gauge up to a strain of 15%, at the first, 10^{th}, and 24^{th} cycle, displaying the hysteresis loop. b) The Young's Modulus and c) the energy dissipated as a percentage of the loading energy, for both 1 and 2 layered strain gauges.

the cyclic tests, and the GF for a single layer track was found to be 1.8 ± 0.2. The creep was also evaluated through placing a pause at the top and bottom of each cycle, and the resistance was found to creep 0.12 ± 0.05 %.

These same samples were also printed using two layers of the CB-VGCNF ink, to determine the effect of increasing the number of layers. This result can be found in Figure 6.8b. These samples were found to have a very sharp response, however the GF was considerably lower (Figure 6.8c), *i.e.* 0.76 ± 0.04. It is clear from Figure 6.8 that the two layer device is a more reusable device, as the strain gauge maintains an equivalent GF value over 45 cycles.

6.4 Conclusion

A co-dispersion containing both CB and VGCNFs was able to be produced efficiently using the dispersant GG, to produce a homogeneous dispersion. The overall sonication time was short, requiring only 8 min to disperse the most efficient amount of material (on a low power output, 6 W). The addition of CB to a VGCNF: GG dispersion was shown to drop the resistance values as low as 510 ± 20 Ω cm^{-1} when processed into a dry film. This dispersion, as a dry film, was able to maintain its' flexibility, which is key in a strain gauge for soft substrates. The damaging effects of sonication was evaluated, and analysis of SEM micrographs found a decrease in the length of VGCNFs when increasing sonication time. Raman analysis also indicated that the D: G ratio of the dry films decreased at increasing sonication times, indicating both surface and inter-layer damage to the VGCNFs.

The rheological properties of the ink were evaluated, to determine suitability for 3D extrusion printing. The optimum solution had an n value of 0.86 ± 0.02, which shows that it is shear thinning. This is due to the dispersant, GG, and the addition of CB. With a K value of 0.86 ± 0.02 Pa s^n, the ink was found to be rheologically suitable for printing.

When evaluated for strain gauging, the ink was found to be suitable, producing a strain gauge with a GF of 1.8 ± 0.2 up to a strain of 15% across 25 cycles. When

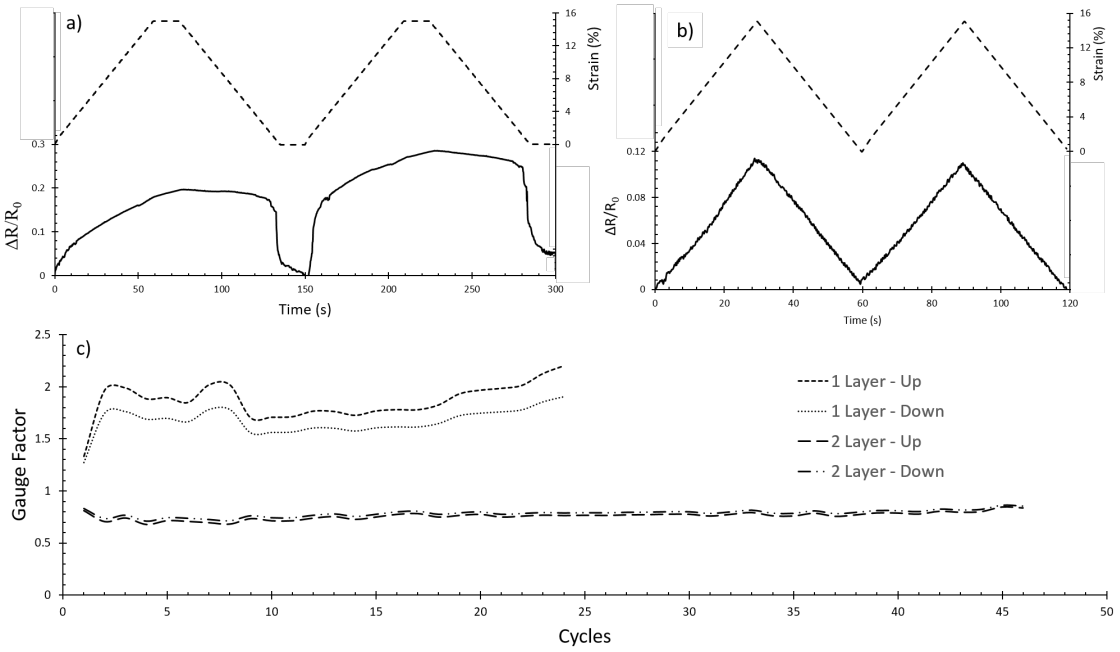

Figure 6.8: Two graphs showing the resistance change for an as-printed strain gauge with a) one layer, and b) two layers. c) shows the gauge factor for both the up and down of both strain gauges across multiple cycles.

two layers were printed, it was found to decrease the GF to 0.76 ± 0.04, however the GF was found to be more consistent over 45 cycles compared to the performance of the 1 layered soft strain gauge.

This paper contributes to the use of 3D printing in the fabrication of soft strain gauges through the production and application of a 3D fabricated strain gauge on a soft substrate. Through a multi-faceted approach (ink, instrument, and substrate design), a strain gauge was able to be developed that can be printed onto any soft substrate with minimal surface preparation or modelling.

Chapter 7

Conclusions and Future Direction

A brief conclusion summarising all work presented, and any future research to be taken from this point.

7.1 General Conclusions

Throughout this project, multiple steps were required to ensure that the material used to produce the final strain gauge met all requirements, and that all specific aims were achieved. Each of these aims shall be reiterated, and how it was achieved.

Chapter 3 details the specific aims of designing, optimising, and characterising an ink based on VGCNF and GG, as well as evaluating the effects of sonication damage on this dispersion. Initially, a VGCNF-GG dispersion was produced and homogeneously dispersed through horn sonication. To achieve the highest conductivity, a study was first performed to determine the minimum ratio of VGCNF: GG, which was found to be 10: 3. The sonication time was also optimised, as it is know that horn sonication can have detrimental effects on carbon dispersants. It was found that a solution containing 10 mg mL^{-1} VGCNF and 3 mg mL^{-1} GG was the most energy efficient solution, requiring only 14 $\pm$ 3 J of sonic energy per mg VGCNF. The electrical conductivity of this dispersion, when dried into a free-standing film, was found to be 35 $\pm$ 2 S cm^{-1}. The sonication damage effects on both the tube length, and thus the conductivity, was also examined, and it was found to severely reduce both of these properties, with the conductivity lowering to 20 $\pm$ 2 S cm^{-1} after 5x sonication (Figures 3.2 and 3.3). This ink was rheologically tested, and found to match that of fountain pen ink at high shear rates ($\approx$ 1000 s^{-1}, that of normal writing). Due to this, the ink was filled into a commercially available fountain pen and was able to power an LED (Figure 3.5).

Chapter 4 presents the development of an in-house EIS (Figure 4.1), which was used as the primary method of electrical characterisation throughout this project. This set-up was developed to measure the electrical behaviour of both dry and wet samples, *i.e.* hydrogels or dry films. A USB waveform generator would apply a set potential at a known frequency across a known resistor and the sample, and the voltage drop was measured by a USB oscilloscope. The frequency of the waveform was then stepped up to produce a full electrical impedance spectrum. The system was benchmarked through measuring the spectra of a variety of GG hydrogels con-

taining SWCNTs, MWCNTs and VGCNFs. It was found that for a wet system (*i.e.* 95 % water content) the addition of carbon fillers had a modest increase to the electrical conductivity, but this affect could be further amplified through the reduction in water (Figure 3.3).

Chapter 5 shows a highly detailed analysis of the sonication damaging effects of sonolysis on a VGCNF: GG dispersion, including some filling effects that were noted. In all previous experimentation presented, it was apparent that horn sonication reduced the electrical and rheological properties of the resulting sample. This was due to damaging both the carbon fillers (SWCNT, MWCNT and VGCNF) and the dispersant (GG). This effect was studied in great detail through various spectroscopic techniques (Raman, XPS, EIS), microscopic techniques (TEM, SEM), and mechanical characterisation. Qualitative analysis of TEM micrographs showed that after a brief (2 min) sonication time, the surrounding GG was drawn into the internal cavity of the VGCNFs due to strong capillary forces at the point of shear (Figure 5.1). This was further backed up through XPS, that showed that the concentration of both oxygen and carboxyl groups decreased at increasing sonication times. As XPS is a surface technique, any GG within the VGCNFs is not detected. It was also found that there was also a reduction in conductivity and Young's Moduli at higher sonication times (Figures 5.3 and 6.7). These were explained through investigation of SEM micrographs of the dry films, as it was found that the average VGCNF length was reduced from 3.2 μm at 2 min sonication, down to 1.5 μm at 30 min sonication (Figure 5.2) This showed that the sonication times must be heavily monitored and minimised where possible.

Chapter 6 shows the production of a KB: VGCNF: GG dispersion, the effects of sonolysis on the materials in the dispersion, production of a custom 3D printer that was then used to print a strain gauge on a p-HEMA hydrogel, along with the full characterisation. The VGCNF: GG dispersion offered promising properties, however in order to further reduce the resistance of the dry tracks, KB was added as a co-dispersant. It was found that a KB dispersion could not form a dry film,

so VGCNFs were added to mechanically strengthen the films, and improve their electrical performance. After optimised for sonication time, it was found that the most efficient dispersion had 20 mg mL^{-1} KB, 10 mg mL^{-1} VGCNF (as found before), and 6 mg mL^{-1} GG, *i.e.* a 20: 6 ratio for total carbon content. This resulted in a slight decrease in efficiency when compared to pure VGCNFs (14.4 ± 0.6 J mg^{-1}), however the resistance per unit length was reduced (from 1000 ± 100 Ω cm^{-1} down to 863 ± 1 Ω cm^{-1}, Figure 6.2). This is a more desirable property for strain gauges, so this ink was deemed more suitable. The rheological properties were also ideal for 3D extrusion printing, as they could be tailored using a different concentration of GG.

In order to deposit this material onto a soft substrate, a 3D extrusion printer was developed (Figure 6.1). This printer was designed by replacing the head of a commercially available milling machine with a custom designed and 3D printed holder that housed two linear screw actuators, which forced the material out through a standard syringe with replaceable needles. Software was also written in order to tie the extrusion rate in with the movement of the printer head.

This research culminated in the production of a conductive strain gauge that was 3D printed onto a flexible, soft substrate. The ink was printed onto a p-HEMA hydrogel base with a hydrophobic layer encapsulating the tracks, as to allow them to stay dry while immersed in water. The strain gauges were tested for repeatability (up to 25 loading/unloading cycles) and was found to remain constant throughout this time. The gauge factor of the strain gauge was found to be 1.8 ± 0.2 and 0.76 ± 0.04 for one and two layers respectively, with a higher degree of repeatability with the two layer device (up to 45 cycles, Figure 6.8).

7.2 Other and Future Directions

The research within this thesis has already initiated a number of other research directions, *e.g.* the printer developed as part of this project was used for developing 4D printed hydrogel actuators [370, 371], with an identical copy assembled at

Harvard University, USA, resulting in a collaborative paper developing soft ionic strain gauges [372] (see Appendix A for details on these papers). The printer was developed with a broad scope in mind, allowing most materials to be printed with ease.

The final product, the 3D printed strain gauge, also offers various other research directions. The next major direction for soft robotics is towards 4D printed soft actuators, and the presented strain gauge has the capability to sense such a strain gauge. It is well known that carbon materials exhibit Joule heating (as do many materials with a resistance!). As most common 4D soft actuators are thermally actuated, the strain gauge could be used as a controlled method for these types of actuators. As the strain gauge would be able to not only cause the actuator to bend, but could then sense how far, it would offer fine control over a soft hinge.

While this project has added to the amount of research on KB as a conductive dispersant, there are very few articles released on this material. As KB is a readily available material, there are still a lot of properties of KB in a dispersion that should be evaluated, *i.e.* using it as a stable co-dispersant to achieve a higher conductivity through altering the KB: VGCNF ratio. KB offers a viable alternative to other harder to process materials, such as graphene, and should be evaluated as such.

Bibliography

[1] R. D. Gately and M. in het Panhuis, "Filling of carbon nanotubes and nanofibres," *Beilstein J. Nanotechnol.*, vol. 6, no. 1, pp. 508–516, 2015.

[2] S. Kim, C. Laschi, and B. Trimmer, "Soft robotics: A bioinspired evolution in robotics," *Trends Biotechnol.*, vol. 31, no. 5, pp. 287–294, 2013.

[3] J. Baeten, K. Donné, S. Boedrij, W. Beckers, and E. Claesen, "Autonomous fruit picking machine: A robotic apple harvester," in *Field and Service Robotics: Results of the 6th International Conference*, C. Laugier and R. Siegwart, Eds. Berlin, Heidelberg: Springer Berlin Heidelberg, 2008, pp. 531–539.

[4] B. T. Bethea, A. M. Okamura, M. Kitagawa, T. P. Fitton, S. M. Cattaneo, V. L. Gott, W. A. Baumgartner, and D. D. Yuh, "Application of haptic feedback to robotic surgery," *J. Laparoendosc. Adv. Surg. Tech.*, vol. 14, no. 3, pp. 191–195, 2004.

[5] R. H. Gaylord, *Fluid actuated motor system and stroking device*, US Patent 2,844,126, 1958.

[6] P. Polygerinos, Z. Wang, K. C. Galloway, R. J. Wood, and C. J. Walsh, "Soft robotic glove for combined assistance and at-home rehabilitation," *Rob. Auton. Syst.*, vol. 73, pp. 135–143, 2015.

[7] M. Wehner, B. Quinlivan, P. M. Aubin, E. Martinez-Villalpando, M. Baumann, L. Stirling, K. Holt, R. Wood, and C. Walsh, "A lightweight soft exosuit for gait assistance," in *2013 IEEE International Conference on Robotics and Automation (ICRA)*, IEEE, 2013, pp. 3362–3369.

[8] M. Mori, K. Suzumori, M. Takahashi, and T. Hosoya, "Very high force hydraulic mckibben artificial muscle with a p-phenylene-2, 6-benzobisoxazole cord sleeve," *Adv. Rob.*, vol. 24, no. 1-2, pp. 233–254, 2010.

[9] Q. Ge, H. J. Qi, and M. L. Dunn, "Active materials by four-dimension printing," *Appl. Phys. Lett.*, vol. 103, no. 13, p. 131 901, 2013.

[10] Q. Ge, C. K. Dunn, H. J. Qi, and M. L. Dunn, "Active origami by 4D printing," *Smart Mater. Struct.*, vol. 23, no. 9, p. 094 007, 2014.

[11] A. S. Gladman, E. A. Matsumoto, R. G. Nuzzo, L. Mahadevan, and J. A. Lewis, "Biomimetic 4D printing," *Nat. Mater.*, vol. 15, no. 4, pp. 413–418, 2016.

[12] K. K. Westbrook and H. J. Qi, "Actuator designs using environmentally responsive hydrogels," *J. Intell. Mater. Syst. Struct.*, vol. 19, no. 5, pp. 597–607, 2007.

[13] A. Buyanov, I. Gofman, L. Revel'skaya, A. Khripunov, and A. Tkachenko, "Anisotropic swelling and mechanical behavior of composite bacterial cellulose–poly (acrylamide or acrylamide–sodium acrylate) hydrogels," *J. Mech. Behav. Biomed. Mater.*, vol. 3, no. 1, pp. 102–111, 2010.

[14] S. E. Bakarich, R. Gorkin, G. M. Spinks, *et al.*, "4D printing with mechanically robust, thermally actuating hydrogels," *Macromol. Rapid Commun.*, vol. 36, no. 12, pp. 1211–1217, 2015.

[15] R. Yoshida, K. Uchida, Y. Kaneko, K. Sakai, A. Kikuchi, Y. Sakurai, and T. Okano, "Comb-type grafted hydrogels with rapid deswelling response to temperature changes," *Nature*, vol. 374, no. 6519, pp. 240–242, 1995.

[16] Y. S. Kim, M. Liu, Y. Ishida, Y. Ebina, M. Osada, T. Sasaki, T. Hikima, M. Takata, and T. Aida, "Thermoresponsive actuation enabled by permittivity switching in an electrostatically anisotropic hydrogel," *Nat. Mater.*, vol. 14, no. 10, pp. 1002–1007, 2015.

[17] E. Lee, D. Kim, H. Kim, and J. Yoon, "Photothermally driven fast responding photo-actuators fabricated with comb-type hydrogels and magnetite nanoparticles," *Sci. Rep.*, vol. 5, p. 15 124, 2015.

[18] Y. Kaneko, K. Sakai, A. Kikuchi, Y. Sakurai, and T. Okano, "Fast swelling/deswelling kinetics of comb-type grafted poly (n-isopropylacrylamide) hydrogels," in *Macromolecular Symposia*, Wiley Online Library, vol. 109, 1996, pp. 41–53.

[19] L. Li, M. Chen, G. Huang, N. Yang, L. Zhang, H. Wang, Y. Liu, W. Wang, and J. Gao, "A green method to prepare pd–ag nanoparticles supported on reduced graphene oxide and their electrochemical catalysis of methanol and ethanol oxidation," *J. Power Sources*, vol. 263, pp. 13–21, 2014.

[20] K. Jung, K. J. Kim, and H. R. Choi, "A self-sensing dielectric elastomer actuator," *Sens. Actuators, A*, vol. 143, no. 2, pp. 343–351, 2008.

[21] J. J. Dosch, D. J. Inman, and E. Garcia, "A self-sensing piezoelectric actuator for collocated control," *J. Intell. Mater. Syst. Struct.*, vol. 3, no. 1, pp. 166–185, 1992.

[22] B. Hanson and M. Levesley, "Self-sensing applications for electromagnetic actuators," *Sens. Actuators, A*, vol. 116, no. 2, pp. 345–351, 2004.

[23] T. Yamada, Y. Hayamizu, Y. Yamamoto, Y. Yomogida, A. Izadi-Najafabadi, D. N. Futaba, and K. Hata, "A stretchable carbon nanotube strain sensor for human-motion detection," *Nat. Nanotechnol.*, vol. 6, no. 5, pp. 296–301, 2011.

[24] R. Tajima, S. Kagami, M. Inaba, and H. Inoue, "Development of soft and distributed tactile sensors and the application to a humanoid robot," *Adv. Rob.*, vol. 16, no. 4, pp. 381–397, 2002.

[25] Y.-L. Park, C. Majidi, R. Kramer, P. Bérard, and R. J. Wood, "Hyperelastic pressure sensing with a liquid-embedded elastomer," *J. Micromech. Microeng.*, vol. 20, no. 12, p. 125 029, 2010.

[26] M. H. Al-Saleh and W. H. Saadeh, "Hybrids of conductive polymer nanocomposites," *Mater. Des*, vol. 52, pp. 1071–1076, 2013.

[27] D. Bigg, "The effect of compounding on the conductive properties of EMI shielding compounds," *Adv. Polym. Technol.*, vol. 4, no. 3-4, pp. 255–266, 1984.

[28] H. J. Barraza, F. Pompeo, E. A. O'Rea, and D. E. Resasco, "Swnt-filled thermoplastic and elastomeric composites prepared by miniemulsion polymerization," *Nano Lett.*, vol. 2, no. 8, pp. 797–802, 2002.

[29] Y. Ando and X. Zhao, "Synthesis of carbon nanotubes by arc-discharge method," *New Diamond Front. Carbon Technol.*, vol. 16, no. 3, pp. 123–138, 2006.

[30] M. Monthioux, L. Noé, L. Dussault, J.-C. Dupin, N. Latorre, T. Ubieto, E. Romeo, C. Royo, A. Monzón, and C. Guimon, "Texturising and structurising mechanisms of carbon nanofilaments during growth," *J. Mater. Chem.*, vol. 17, no. 43, pp. 4611–4618, 2007.

[31] M. Dresselhaus, A. Jorio, and R. Saito, "Characterizing graphene, graphite, and carbon nanotubes by raman spectroscopy," *Annual Review of Condensed Matter Physics*, vol. 1, no. 1, pp. 89–108, 2010.

[32] M. Cadek, R. Murphy, B. McCarthy, A. Drury, B. Lahr, R. Barklie, M. In het Panhuis, J. Coleman, and W. Blau, "Optimisation of the arc-discharge production of multi-walled carbon nanotubes," *Carbon*, vol. 40, no. 6, pp. 923–928, 2002.

[33] X. Wang, X. Lin, V. Dravid, J. Ketterson, and R. P. Chang, "Carbon nanotubes synthesized in a hydrogen arc discharge," *Appl. Phys. Lett.*, vol. 66, no. 18, pp. 2430–2432, 1995.

[34] R. Andrews, D. Jacques, D. Qian, and T. Rantell, "Multiwall carbon nanotubes: Synthesis and application," *Acc. Chem. Res.*, vol. 35, no. 12, pp. 1008–1017, 2002.

[35] A. Peigney, C. Laurent, E. Flahaut, R. Bacsa, and A. Rousset, "Specific surface area of carbon nanotubes and bundles of carbon nanotubes," *Carbon*, vol. 39, no. 4, pp. 507–514, 2001.

[36] M. Ritschel, M. Uhlemann, O. Gutfleisch, A. Leonhardt, A. Graff, C. Täschner, and J. Fink, "Hydrogen storage in different carbon nanostructures," *Appl. Phys. Lett.*, vol. 80, no. 16, pp. 2985–2987, 2002.

[37] B. Sankapal, H. Gajare, D. Dubal, R. Gore, R. Salunkhe, and H. Ahn, "Presenting highest supercapacitance for tio$_2$/mwnts nanocomposites: Novel method," *Chemical Engineering Journal*, vol. 247, pp. 103–110, 2014.

[38] A. Verma, S. Saxena, G. Saini, V. Gaur, and V. Jain, "Hydrogen peroxide vapor sensor using metal-phthalocyanine functionalized carbon nanotubes," *Thin Solid Films*, vol. 519, no. 22, pp. 8144–8148, 2011.

[39] S. Iijima, "Helical microtubules of graphitic carbon," *Nature*, vol. 354, no. 6348, pp. 56–58, 1991.

[40] M. Endo, H. Muramatsu, T. Hayashi, Y. A. Kim, M. Terrones, and M. S. Dresselhaus, "Nanotechnology: 'buckypaper' from coaxial nanotubes," *Nature*, vol. 433, no. 7025, pp. 476–476, 2005.

[41] S. Iijima and T. Ichihashi, "Single-shell carbon nanotubes of 1-nm diameter," *Nature*, vol. 363, no. 6430, pp. 603–605, 1993.

[42] D. S. Bethune, C. H. Klang, M. S. de Vries, G. Gorman, R. Savoy, J. Vazquez, and R. Beyers, "Cobalt-catalysed growth of carbon nanotubes with single-atomic-layer walls," *Nature*, vol. 363, no. 6430, pp. 605–607, 1993.

[43] M. Endo, Y. Kim, T. Hayashi, Y. Fukai, K. Oshida, M. Terrones, T. Yanagisawa, S. Higaki, and M. Dresselhaus, "Structural characterization of cup-stacked-type nanofibers with an entirely hollow core," *Appl. Phys. Lett.*, vol. 80, no. 7, pp. 1267–1269, 2002.

[44] S. Bandow, S. Asaka, Y. Saito, A. M. Rao, L. Grigorian, E. Richter, and P. Eklund, "Effect of the growth temperature on the diameter distribution and chirality of single-wall carbon nanotubes," *Phys. Rev. Lett.*, vol. 80, no. 17, p. 3779, 1998.

[45] W. K. Maser, A. M. Benito, and M. T. Martínez, "Production of carbon nanotubes: The light approach," *Carbon*, vol. 40, no. 10, pp. 1685–1695, 2002.

[46] M. Keidar, A. Shashurin, J. Li, O. Volotskova, M. Kundrapu, and T. S. Zhuang, "Arc plasma synthesis of carbon nanostructures: Where is the frontier?" *J. Phys. D: Appl. Phys.*, vol. 44, no. 17, p. 174 006, 2011.

[47] M. Keidar, I. Levchenko, T. Arbel, M. Alexander, A. M. Waas, and K. K. Ostrikov, "Increasing the length of single-wall carbon nanotubes in a magnetically enhanced arc discharge," *Appl. Phys. Lett.*, vol. 92, no. 4, p. 043 129, 2008.

[48] O. Volotskova, J. A. Fagan, J. Y. Huh, F. R. Phelan Jr, A. Shashurin, and M. Keidar, "Tailored distribution of single-wall carbon nanotubes from arc plasma synthesis using magnetic fields," *ACS Nano*, vol. 4, no. 9, pp. 5187–5192, 2010.

[49] E. I. Waldorff, A. M. Waas, P. P. Friedmann, and M. Keidar, "Characterization of carbon nanotubes produced by arc discharge: Effect of the background pressure," *J. Appl. Phys.*, vol. 95, no. 5, pp. 2749–2754, 2004.

[50] B. Panella, M. Hirscher, and S. Roth, "Hydrogen adsorption in different carbon nanostructures," *Carbon*, vol. 43, no. 10, pp. 2209–2214, 2005.

[51] C. Journet, W. Maser, P. Bernier, A. Loiseau, M. L. De La Chapelle, d. l. S. Lefrant, P. Deniard, R. Lee, and J. Fischer, "Large-scale production of single-walled carbon nanotubes by the electric-arc technique," *Nature*, vol. 388, no. 6644, pp. 756–758, 1997.

[52] H. Warren, R. D. Gately, H. N. Moffat, and M. in het Panhuis, "Conducting carbon nanofibre networks: Dispersion optimisation, evaporative casting and direct writing," *RSC Adv.*, vol. 3, pp. 21 936–21 942, 44 2013.

[53] K. Méténier, S. Bonnamy, F. Béguin, C. Journet, P. Bernier, M. L. de La Chapelle, O. Chauvet, and S. Lefrant, "Coalescence of single-walled carbon nanotubes and formation of multi-walled carbon nanotubes under high-temperature treatments," *Carbon*, vol. 40, no. 10, pp. 1765–1773, 2002.

[54] Y. Kim, H. Muramatsu, T. Hayashi, M. Endo, M. Terrones, and M. Dresselhaus, "Thermal stability and structural changes of double-walled carbon nanotubes by heat treatment," *Chem. Phys. Lett.*, vol. 398, no. 1-3, pp. 87–92, 2004.

[55] X. Wei, Q. Chen, L.-M. Peng, R. Cui, and Y. Li, "Tensile loading of double-walled and triple-walled carbon nanotubes and their mechanical properties," *J. Phys. Chem. C*, vol. 113, no. 39, pp. 17 002–17 005, 2009.

[56] M. M. J. Treacy, T. W. Ebbesen, and J. M. Gibson, "Exceptionally high young's modulus observed for individual carbon nanotubes," *Nature*, vol. 381, no. 6584, pp. 678–680, 1996.

[57] H. Muramatsu, T. Hayashi, Y. Kim, D. Shimamoto, Y. Kim, K. Tantrakarn, M. Endo, M. Terrones, and M. Dresselhaus, "Pore structure and oxidation stability of double-walled carbon nanotube-derived bucky paper," *Chem. Phys. Lett.*, vol. 414, no. 4-6, pp. 444–448, 2005.

[58] H. Warren, R. D. Gately, P. O'Brien, R. Gorkin, and M. in het Panhuis, "Electrical conductivity, impedance, and percolation behavior of carbon nanofiber and carbon nanotube containing gellan gum hydrogels," *J. Polym. Sci., Part B: Polym. Phys.*, vol. 52, no. 13, pp. 864–871, 2014.

[59] I. Suarez-Martinez, N. Grobert, and C. P. Ewels, "Nomenclature of sp 2 carbon nanoforms," *Carbon*, vol. 50, no. 3, pp. 741–747, 2012.

[60] S.-H. Yoon, S. Lim, S.-h. Hong, I. Mochida, B. An, and K. Yokogawa, "Carbon nano-rod as a structural unit of carbon nanofibers," *Carbon*, vol. 42, no. 15, pp. 3087–3095, 2004.

[61] M. Endo, Y. Kim, T. Hayashi, K. Nishimura, T. Matusita, K. Miyashita, and M. Dresselhaus, "Vapor-grown carbon fibers (vgcfs): Basic properties and their battery applications," *Carbon*, vol. 39, no. 9, pp. 1287–1297, 2001.

[62] N. M. Rodriguez, A. Chambers, and R. T. K. Baker, "Catalytic engineering of carbon nanostructures," *Langmuir*, vol. 11, no. 10, pp. 3862–3866, 1995.

[63] T. Uchida, D. P. Anderson, M. L. Minus, and S. Kumar, "Morphology and modulus of vapor grown carbon nano fibers," *J. Mater. Sci.*, vol. 41, no. 18, pp. 5851–5856, 2006.

[64] J. Y. Howe, G. G. Tibbetts, C. Kwag, and M. L. Lake, "Heat treating carbon nanofibers for optimal composite performance," *J. Mater. Res.*, vol. 21, no. 10, pp. 2646–2652, 2006.

[65] K. L. Elias, R. L. Price, and T. J. Webster, "Enhanced functions of osteoblasts on nanometer diameter carbon fibers," *Biomaterials*, vol. 23, no. 15, pp. 3279–3287, 2002.

[66] B. O. Lee, W. J. Woo, and M.-S. Kim, "EMI shielding effectiveness of carbon nanofiber filled poly (vinyl alcohol) coating materials," *Macromol. Mater. Eng.*, vol. 286, no. 2, pp. 114–118, 2001.

[67] A. La Torre, M. d. C. Giménez-López, m. W. Fay, G. A. Rance, W. A. Solomonsz, T. W. Chamberlain, P. D. Brown, and A. N. Khlobystov, "Assembly, growth, and catalytic activity of gold nanoparticles in hollow carbon nanofibers," *ACS Nano*, vol. 6, no. 3, pp. 2000–2007, 2012.

[68] W. A. Solomonsz, G. A. Rance, M. Suyetin, A. La Torre, E. Bichoutskaia, and A. N. Khlobystov, "Controlling the regioselectivity of the hydrosilylation reaction in carbon nanoreactors," *Chem.–Eur. J.*, vol. 18, no. 41, pp. 13 180–13 187, 2012.

[69] B. Brodie, "Sur le poids atomique du graphite," *Ann. Chim. Phys*, vol. 59, no. 466, e472, 1860.

[70] L. Staudenmaier, "Verfahren zur darstellung der graphitsäure," *Ber. Dtsch. Chem. Ges.*, vol. 31, no. 2, pp. 1481–1487, 1898.

[71] H. P. Boehm, A. Clauss, G. O. Fischer, and U. Hofmann, "Das adsorptionsverhalten sehr dünner kohlenstoff-folien," *Zeitschrift fúr anorganische und allgemeine Chemie*, vol. 316, no. 3-4, pp. 119–127, 1962.

[72] K. S. Novoselov, "Electric field effect in atomically thin carbon films," *Science*, vol. 306, no. 5696, pp. 666–669, 2004.

[73] J. Chen, R. Zjang, and W. Wang, "Fabricating microporous PDMS using water-in-PDMS emulsion," *RSC Publishing Blogs Home. Chips and Tips*, 2012.

[74] A. Martinez, K. Fuse, and S. Yamashita, "Mechanical exfoliation of graphene for the passive mode-locking of fiber lasers," *Appl. Phys. Lett.*, vol. 99, no. 12, p. 121 107, 2011.

[75] S. Bae, H. Kim, Y. Lee, X. Xu, J.-S. Park, Y. Zheng, J. Balakrishnan, T. Lei, H. R. Kim, Y. I. Song, Y.-J. Kim, K. S. Kim, B. Özyilmaz, J.-H. Ahn, B. H. Hong, and S. Iijima, "Roll-to-roll production of 30-inch graphene films for transparent electrodes," *Nat. Nanotechnol.*, vol. 5, no. 8, pp. 574–578, 2010.

[76] S. Park and R. S. Ruoff, "Chemical methods for the production of graphenes," *Nat. Nanotechnol.*, vol. 4, no. 4, pp. 217–224, 2009.

[77] K. P. Loh, Q. Bao, P. K. Ang, and J. Yang, "The chemistry of graphene," *J. Mater. Chem.*, vol. 20, no. 12, p. 2277, 2010.

[78] G. Wang, J. Yang, J. Park, X. Gou, B. Wang, H. Liu, and J. Yao, "Facile synthesis and characterization of graphene nanosheets," *J. Phys. Chem. C*, vol. 112, no. 22, pp. 8192–8195, 2008.

[79] X. Li, X. Wang, L. Zhang, S. Lee, and H. Dai, "Chemically derived, ultrasmooth graphene nanoribbon semiconductors," *Science*, vol. 319, no. 5867, pp. 1229–1232, 2008.

[80] D. A. Dikin, S. Stankovich, E. J. Zimney, R. D. Piner, G. H. B. Dommett, G. Evmenenko, S. T. Nguyen, and R. S. Ruoff, "Preparation and characterization of graphene oxide paper," *Nature*, vol. 448, no. 7152, pp. 457–460, 2007.

[81] D. R. Dreyer, S. Park, C. W. Bielawski, and R. S. Ruoff, "The chemistry of graphene oxide," *Chem. Soc. Rev.*, vol. 39, no. 1, pp. 228–240, 2010.

[82] S. Pei and H.-M. Cheng, "The reduction of graphene oxide," *Carbon*, vol. 50, no. 9, pp. 3210–3228, 2012.

[83] P. Cui, J. Lee, E. Hwang, and H. Lee, "One-pot reduction of graphene oxide at subzero temperatures," *Chem. Commun.*, vol. 47, no. 45, p. 12 370, 2011.

[84] M. Choucair, P. Thordarson, and J. A. Stride, "Gram-scale production of graphene based on solvothermal synthesis and sonication," *Nat. Nanotechnol.*, vol. 4, no. 1, pp. 30–33, 2009.

[85] C. Gómez-Navarro, J. C. Meyer, R. S. Sundaram, A. Chuvilin, S. Kurasch, M. Burghard, K. Kern, and U. Kaiser, "Atomic structure of reduced graphene oxide," *Nano Lett.*, vol. 10, no. 4, pp. 1144–1148, 2010.

[86] A. Pirkle, J. Chan, A. Venugopal, D. Hinojos, C. W. Magnuson, S. McDonnell, L. Colombo, E. M. Vogel, R. S. Ruoff, and R. M. Wallace, "The effect of chemical residues on the physical and electrical properties of chemical vapor deposited graphene transferred to SiO2," *Appl. Phys. Lett.*, vol. 99, no. 12, p. 122 108, 2011.

[87] C. Gómez-Navarro, R. T. Weitz, A. M. Bittner, M. Scolari, A. Mews, M. Burghard, and K. Kern, "Electronic transport properties of individual chemically reduced graphene oxide sheets," *Nano Lett.*, vol. 7, no. 11, pp. 3499–3503, 2007.

[88] C. Lee, X. Wei, J. W. Kysar, and J. Hone, "Measurement of the elastic properties and intrinsic strength of monolayer graphene," *Science*, vol. 321, no. 5887, pp. 385–388, 2008.

[89] P. T. Nicholson and I. Shaw, *Ancient egyptian materials and technology.* Cambridge University Press, 2000.

[90] A. Y. Watson and P. A. Valberg, "Carbon black and soot: Two different substances," *AIHAJ*, vol. 62, no. 2, pp. 218–228, 2001.

[91] J.-B. Donnet, *Carbon black: Science and technology, 2nd edn.* CRC Press, 1993.

[92] T. A. J. Kuhlbusch and H. Fissan, "Particle characteristics in the reactor and pelletizing areas of carbon black production," *J. Occup. Environ. Hyg.*, vol. 3, no. 10, pp. 558–567, 2006.

[93] R. J. McCunney, H. J. Muranko, C. M. Long, A. K. Hamade, P. A. Valberg, and P. Morfeld, "Carbon black," in *Patty's Toxicology.* John Wiley & Sons, Inc., 2001.

[94] N. Probst and E. Grivei, "Structure and electrical properties of carbon black," *Carbon*, vol. 40, no. 2, pp. 201–205, 2002.

[95] B. Guo, R. Zebda, S. J. Drake, and C. M. Sayes, "Synergistic effect of co-exposure to carbon black and fe_2o_3 nanoparticles on oxidative stress in cultured lung epithelial cells," *Part. Fibre Toxicol.*, vol. 6, no. 1, p. 1, 2009.

[96] J. A. Heiser and J. A. King, "Thermally conductive carbon filled nylon 6, 6," *Polym. Compos.*, vol. 25, no. 2, pp. 186–193, 2004.

[97] C. Guo, L. Zhou, and J. Lv, "Effects of expandable graphite and modified ammonium polyphosphate on the flame-retardant and mechanical properties of wood flour-polypropylene composites," *Polymers & Polymer Composites*, vol. 21, no. 7, p. 449, 2013.

[98] S. Stankovich, D. A. Dikin, G. H. Dommett, K. M. Kohlhaas, E. J. Zimney, E. A. Stach, R. D. Piner, S. T. Nguyen, and R. S. Ruoff, "Graphene-based composite materials," *Nature*, vol. 442, no. 7100, pp. 282–286, 2006.

[99] P. Cardoso, J. Silva, A. Paleo, F. Van Hattum, R. Simoes, and S. Lanceros-Méndez, "The dominant role of tunneling in the conductivity of carbon nanofiber-epoxy composites," *Phys. Status Solidi A*, vol. 207, no. 2, pp. 407–410, 2010.

[100] C. J. Ferris *et al.*, "Gel–carbon nanotube composites: The effect of carbon nanotubes on gelation and conductivity behaviour," *Soft Matter*, vol. 5, no. 7, pp. 1466–1473, 2009.

[101] P. Sanoj and B. Kandasubramanian, "Hybrid carbon-carbon ablative composites for thermal protection in aerospace," *J. Compos.*, vol. 2014, Article ID 825607, 2014.

[102] A. Khattab, C. Liu, W. Chirdon, and C. Hebert, "Mechanical and thermal characterization of carbon nanofiber reinforced low-density polyethylene composites," *J. Thermoplast. Compos. Mater.*, vol. 26, no. 7, pp. 954–967, 2013.

[103] I. Kang, Y. Y. Heung, J. H. Kim, J. W. Lee, R. Gollapudi, S. Subramaniam, S. Narasimhadevara, D. Hurd, G. R. Kirikera, V. Shanov, *et al.*, "Introduction to carbon nanotube and nanofiber smart materials," *Compos. Part B Eng.*, vol. 37, no. 6, pp. 382–394, 2006.

[104] E. Peiner, A. Tibrewala, R. Bandorf, S. Biehl, H. Lüthje, and L. Doering, "Micro force sensor with piezoresistive amorphous carbon strain gauge," *Sens. Actuators, A*, vol. 130, pp. 75–82, 2006.

[105] N. Songmee, P. Singjai, *et al.*, "Gel–carbon nanotube materials: The relationship between nanotube network connectivity and conductivity," *Nanoscale*, vol. 2, no. 9, pp. 1740–1745, 2010.

[106] L. Jiang, L. Gao, and J. Sun, "Production of aqueous colloidal dispersions of carbon nanotubes," *J. Colloid Interface Sci.*, vol. 260, no. 1, pp. 89–94, 2003.

[107] M. O. Lisunova, N. I. Lebovka, O. V. Melezhyk, and Y. P. Boiko, "Stability of the aqueous suspensions of nanotubes in the presence of nonionic surfactant," *J. Colloid Interface Sci.*, vol. 299, no. 2, pp. 740–746, 2006.

[108] M. L. Tsaih and R. H. Chen, "Effect of degree of deacetylation of chitosan on the kinetics of ultrasonic degradation of chitosan," *J. Appl. Polym. Sci.*, vol. 90, no. 13, pp. 3526–3531, 2003.

[109] E. R. Morris, K. Nishinari, and M. Rinaudo, "Gelation of gellan–a review," *Food Hydrocolloids*, vol. 28, no. 2, pp. 373–411, 2012.

[110] M. A. O'Neill, R. R. Selvendran, and V. J. Morris, "Structure of the acidic extracellular gelling polysaccharide produced by pseudomonas elodea," *Carbohydr. Res.*, vol. 124, no. 1, pp. 123–133, 1983.

[111] J. Mano, G. Silva, H. S. Azevedo, P. Malafaya, R. Sousa, S. Silva, L. Boesel, J. M. Oliveira, T. Santos, A. Marques, *et al.*, "Natural origin biodegradable systems in tissue engineering and regenerative medicine: Present status and some moving trends," *Journal of the Royal Society Interface*, vol. 4, no. 17, pp. 999–1030, 2007.

[112] S. Kanesaka, T. Watanabe, and S. Matsukawa, "Binding effect of Cu^{2+} as a trigger on the sol-to-gel and the coil-to-helix transition processes of polysaccharide, gellan gum," *Biomacromolecules*, vol. 5, no. 3, pp. 863–868, 2004.

[113] J. Tang, M. A. Tung, and Y. Zeng, "Compression strength and deformation of gellan gels formed with mono-and divalent cations," *Carbohydr. Polym.*, vol. 29, no. 1, pp. 11–16, 1996.

[114] L. Lu and W. Chen, "Large-scale aligned carbon nanotubes from their purified, highly concentrated suspension," *ACS Nano*, vol. 4, no. 2, pp. 1042–1048, 2010.

[115] J. P. Ferrance, "Single-walled carbon nanotube strings for biosensor development," *Electroanalysis*, vol. 23, no. 12, pp. 2906–2914, 2011.

[116] R. Mao, J. Tang, and B. Swanson, "Texture properties of high and low acyl mixed gellan gels," *Carbohydr. Polym.*, vol. 41, no. 4, pp. 331–338, 2000.

[117] S. A. Survase, P. S. Saudagar, I. B. Bajaj, and R. S. Singhal, "Gellan gum: Fermentative production, downstream processing and applications," *Food Technology and Biotechnology*, vol. 45, no. 2, pp. 107–118, 2007.

[118] A. M. Smith, R. M. Shelton, Y. Perrie, and J. J. Harris, "An initial evaluation of gellan gum as a material for tissue engineering applications," *J. Biomater. Appl.*, vol. 22, no. 3, pp. 241–254, 2007.

[119] J. T. Oliveira, L. S. Gardel, T. Rada, L. Martins, M. E. Gomes, and R. L. Reis, "Injectable gellan gum hydrogels with autologous cells for the treatment of rabbit articular cartilage defects," *J. Orthop. Res.*, vol. 28, no. 9, pp. 1193–1199, 2010.

[120] Y. Ding, H. Alias, D. Wen, and R. A. Williams, "Heat transfer of aqueous suspensions of carbon nanotubes (cnt nanofluids)," *Int. J. Heat Mass Transfer*, vol. 49, no. 1, pp. 240–250, 2006.

[121] B. Krause, M. Mende, P. Pötschke, and G. Petzold, "Dispersability and particle size distribution of cnts in an aqueous surfactant dispersion as a function of ultrasonic treatment time," *Carbon*, vol. 48, no. 10, pp. 2746–2754, 2010.

[122] R. G. Compton, J. C. Eklund, and F. Marken, "Sonoelectrochemical processes: A review," *Electroanalysis*, vol. 9, no. 7, pp. 509–522, 1997.

[123] E. Ginsburg, M. Kinsley, and A. Quitral, "The power of ultrasound.," *Administrative radiology journal: AR*, vol. 17, no. 5, p. 17, 1998.

[124] F. Hennrich, R. Krupke, K. Arnold, J. A. Rojas Stütz, S. Lebedkin, T. Koch, T. Schimmel, and M. M. Kappes, "The mechanism of cavitation-induced scission of single-walled carbon nanotubes," *J. Phys. Chem. B*, vol. 111, no. 8, pp. 1932–1937, 2007.

[125] G. J. Price and P. F. Smith, "Ultrasonic degradation of polymer solutions: 2. the effect of temperature, ultrasound intensity and dissolved gases on polystyrene in toluene," *Polymer*, vol. 34, no. 19, pp. 4111–4117, 1993.

[126] S. Koda, K. Taguchi, and K. Futamura, "Effects of frequency and a radical scavenger on ultrasonic degradation of water-soluble polymers," *Ultrason. Sonochem.*, vol. 18, no. 1, pp. 276–281, 2011.

[127] B. Tiwari, K. Muthukumarappan, C. O'Donnell, and P. Cullen, "Rheological properties of sonicated guar, xanthan and pectin dispersions," *Int. J. Food Prop.*, vol. 13, no. 2, pp. 223–233, 2010.

[128] D. Hecht, L. Hu, and G. Gruner, "Conductivity scaling with bundle length and diameter in single walled carbon nanotube networks," *Appl. Phys. Lett.*, vol. 89, no. 13, p. 133 112, 2006.

[129] Y. Y. Huang, T. P. Knowles, and E. M. Terentjev, "Strength of nanotubes, filaments, and nanowires from sonication-induced scission," *Adv. Mater.*, vol. 21, no. 38-39, pp. 3945–3948, 2009.

[130] S. Reich, L. Li, and J. Robertson, "Structure and formation energy of carbon nanotube caps," *Phys. Rev. B*, vol. 72, no. 16, p. 165 423, 2005.

[131] C. Liu, Y. Chen, C.-Z. Wu, S.-T. Xu, and H.-M. Cheng, "Hydrogen storage in carbon nanotubes revisited," *Carbon*, vol. 48, no. 2, pp. 452–455, 2010.

[132] A. Rashidi, A. Nouralishahi, A. Khodadadi, Y. Mortazavi, A. Karimi, and K. Kashefi, "Modification of single wall carbon nanotubes (swnt) for hydrogen storage," *Int. J. Hydrogen Energy*, vol. 35, no. 17, pp. 9489–9495, 2010.

[133] G. Che, B. B. Lakshmi, C. R. Martin, and E. R. Fisher, "Metal-nanocluster-filled carbon nanotubes: Catalytic properties and possible applications in electrochemical energy storage and production," *Langmuir*, vol. 15, no. 3, pp. 750–758, 1999.

[134] S. L. Candelaria, Y. Shao, W. Zhou, X. Li, J. Xiao, J.-G. Zhang, Y. Wang, J. Liu, J. Li, and G. Cao, "Nanostructured carbon for energy storage and conversion," *Nano Energy*, vol. 1, no. 2, pp. 195–220, 2012.

[135] T. P. Kumar, R. Ramesh, Y. Lin, and G. T.-K. Fey, "Tin-filled carbon nanotubes as insertion anode materials for lithium-ion batteries," *Electrochem. Commun.*, vol. 6, no. 6, pp. 520–525, 2004.

[136] X. Pan and X. Bao, "Reactions over catalysts confined in carbon nanotubes," *Chem. Commun.*, no. 47, pp. 6271–6281, 2008.

[137] L. Dong, X. Tao, L. Zhang, X. Zhang, and B. J. Nelson, "Nanorobotic spot welding: Controlled metal deposition with attogram precision from copper-filled carbon nanotubes," *Nano Lett.*, vol. 7, no. 1, pp. 58–63, 2007.

[138] X.-R. Ye, Y. Lin, C. Wang, and C. M. Wai, "Supercritical fluid fabrication of metal nanowires and nanorods templated by multiwalled carbon nanotubes," *Adv. Mater.*, vol. 15, no. 4, pp. 316–319, 2003.

[139] A. Elias, J. Rodriguez-Manzo, M. McCartney, D. Golberg, A. Zamudio, S. E. Baltazar, F. Lopez-Urias, E. Munoz-Sandoval, L. Gu, C. Tang, *et al.*, "Production and characterization of single-crystal feco nanowires inside carbon nanotubes," *Nano Lett.*, vol. 5, no. 3, pp. 467–472, 2005.

[140] X. Gao, Y. Zhang, X. Chen, G. Pan, J. Yan, F. Wu, H. Yuan, and D. Song, "Carbon nanotubes filled with metallic nanowires," *Carbon*, vol. 42, no. 1, pp. 47–52, 2004.

[141] B. K. Grandhe, V. R. Bandi, K. Jang, S. S. Kim, D.-S. Shin, Y. Lee, J.-M. Lim, and T. Song, "Synthesis and characterization of Eu^{3+} doped Gd_2O_3 nanotubes using multi wall carbon nanotubes as removable templates," *Met. Mater. Int.*, vol. 19, no. 3, pp. 507–511, 2013.

[142] P. Ajayan, O. Stephan, P. Redlich, C. Colliex, *et al.*, "Carbon nanotubes as removable templates for metal-oxide nanocomposites and nanostructures," *Nature*, vol. 375, no. 6532, pp. 564–567, 1995.

[143] J. A. Rodríguez-Manzo, F. Banhart, M. Terrones, H. Terrones, N. Grobert, P. M. Ajayan, B. G. Sumpter, V. Meunier, M. Wang, Y. Bando, *et al.*, "Heterojunctions between metals and carbon nanotubes as ultimate nanocontacts," *Proc. Natl. Acad. Sci. U.S.A*, vol. 106, no. 12, pp. 4591–4595, 2009.

[144] D.-M. Tang, L.-C. Yin, F. Li, C. Liu, W.-J. Yu, P.-X. Hou, B. Wu, Y.-H. Lee, X.-L. Ma, and H.-M. Cheng, "Carbon nanotube-clamped metal atomic chain," *Proc. Natl. Acad. Sci. U.S.A*, vol. 107, no. 20, pp. 9055–9059, 2010.

[145] X. Zhang, C. L. Pint, M. H. Lee, B. E. Schubert, A. Jamshidi, K. Takei, H. Ko, A. Gillies, R. Bardhan, J. J. Urban, *et al.*, "Optically-and thermally-responsive programmable materials based on carbon nanotube-hydrogel polymer composites," *Nano Lett.*, vol. 11, no. 8, pp. 3239–3244, 2011.

[146] Y. Zhang, Y. Bai, and B. Yan, "Functionalized carbon nanotubes for potential medicinal applications," *Drug Discovery Today*, vol. 15, no. 11, pp. 428–435, 2010.

[147] C. Ménard-Moyon, E. Venturelli, C. Fabbro, C. Samorí, T. Da Ros, K. Kostarelos, M. Prato, and A. Bianco, "The alluring potential of functionalized carbon nanotubes in drug discovery," *Expert Opin. Drug Discovery*, vol. 5, no. 7, pp. 691–707, 2010.

[148] P. Ajayan, T. Ebbesen, T. Ichihashi, S. Iijima, K. Tanigaki, and H. Hiura, "Opening carbon nanotubes with oxygen and implications for filling," *Nature*, vol. 362, no. 6420, pp. 522–525, 1993.

[149] S. Tsang, Y. Chen, P. Harris, M. Green, *et al.*, "A simple chemical method of opening and filling carbon nanotubes," *Nature*, vol. 372, no. 6502, pp. 159–162, 1994.

[150] J. Sloan, J. Hammer, M. Zwiefka-Sibley, M. L. H. Green, and J. Sloan, "The opening and filling of single walled carbon nanotubes (swts)," *Chem. Commun.*, no. 3, pp. 347–348, 1998.

[151] A. Mathur, S. Roy, K. Hazra, S. Wadhwa, S. C. Ray, S. Mitra, D. Misra, and J. McLaughlin, "Oxygen plasma assisted end-opening and field emission enhancement in vertically aligned multiwall carbon nanotubes," *Mater. Chem. Phys.*, vol. 134, no. 1, pp. 425–429, 2012.

[152] A. F. Holloway, K. Toghill, G. G. Wildgoose, R. G. Compton, M. A. Ward, G. Tobias, S. A. Llewellyn, B. Ballesteros, M. L. Green, and A. Crossley, "Electrochemical opening of single-walled carbon nanotubes filled with metal halides and with closed ends," *J. Phys. Chem. C*, vol. 112, no. 28, pp. 10 389–10 397, 2008.

[153] Y. Yamada, O. Kimizuka, K. Machida, S. Suematsu, K. Tamamitsu, S. Saeki, Y. Yamada, N. Yoshizawa, O. Tanaike, J. Yamashita, *et al.*, "Hole opening of carbon nanotubes and their capacitor performance†," *Energy & Fuels*, vol. 24, no. 6, pp. 3373–3377, 2010.

[154] J. Liu, A. G. Rinzler, H. Dai, J. H. Hafner, R. K. Bradley, P. J. Boul, A. Lu, T. Iverson, K. Shelimov, C. B. Huffman, *et al.*, "Fullerene pipes," *Science*, vol. 280, no. 5367, pp. 1253–1256, 1998.

[155] S. Cambré, B. Schoeters, S. Luyckx, E. Goovaerts, and W. Wenseleers, "Experimental observation of single-file water filling of thin single-wall carbon nanotubes down to chiral index (5, 3)," *Phys. Rev. Lett.*, vol. 104, no. 20, p. 207 401, 2010.

[156] X.-H. Wang, H. Orikasa, N. Inokuma, Q.-H. Yang, P.-X. Hou, H. Oshima, K. Itoh, and T. Kyotani, "Controlled filling of permalloy into one-end-opened carbon nanotubes," *J. Mater. Chem.*, vol. 17, no. 10, pp. 986–991, 2007.

[157] L. Zhu, Y. Xiu, D. W. Hess, and C.-P. Wong, "Aligned carbon nanotube stacks by water-assisted selective etching," *Nano Lett.*, vol. 5, no. 12, pp. 2641–2645, 2005.

[158] T. Kyotani, L.-f. Tsai, and A. Tomita, "Formation of ultrafine carbon tubes by using an anodic aluminum oxide film as a template," *Chem. Mater.*, vol. 7, no. 8, pp. 1427–1428, 1995.

[159] ——, "Preparation of ultrafine carbon tubes in nanochannels of an anodic aluminum oxide film," *Chem. Mater.*, vol. 8, no. 8, pp. 2109–2113, 1996.

[160] P. Hou, C. Liu, C. Shi, and H. Cheng, "Carbon nanotubes prepared by anodic aluminum oxide template method," *Chin. Sci. Bull.*, vol. 57, no. 2-3, pp. 187–204, 2012.

[161] P.-X. Hou, W.-J. Yu, C. Shi, L.-L. Zhang, C. Liu, X.-J. Tian, Z.-L. Dong, and H.-M. Cheng, "Template synthesis of ultra-thin and short carbon nanotubes with two open ends," *J. Mater. Chem.*, vol. 22, no. 30, pp. 15 221–15 226, 2012.

[162] M. R. Maschmann, A. D. Franklin, P. B. Amama, D. N. Zakharov, E. A. Stach, T. D. Sands, and T. S. Fisher, "Vertical single-and double-walled carbon nanotubes grown from modified porous anodic alumina templates," *Nanotechnology*, vol. 17, no. 15, p. 3925, 2006.

[163] J. K. Kasi, A. K. Kasi, W. Wongwiriyapan, N. Afzulpurkar, P. Dulyaseree, M. Hasan, and A. Tuantranont, "Synthesis of carbon nanotube and carbon nanofiber in nanopore of anodic aluminum oxide template by chemical vapor deposition at atmospheric pressure," in *Advanced Materials Research*, Trans Tech Publ, vol. 557, 2012, pp. 544–549.

[164] A. Capobianchi, S. Foglia, P. Imperatori, A. Notargiacomo, M. Giammatteo, T. Del Buono, and E. Palange, "Controlled filling and external cleaning of multi-wall carbon nanotubes using a wet chemical method," *Carbon*, vol. 45, no. 11, pp. 2205–2208, 2007.

[165] D. Du, M. Wang, Y. Qin, and Y. Lin, "One-step electrochemical deposition of prussian blue–multiwalled carbon nanotube nanocomposite thin-film: Prepa-

ration, characterization and evaluation for H_2O_2 sensing," *J. Mater. Chem.*, vol. 20, no. 8, pp. 1532–1537, 2010.

[166] K. M. Samant, V. R. Chaudhari, S. Kapoor, and S. K. Haram, "Filling and coating of multiwalled carbon nanotubes with silver by DC electrophoresis," *Carbon*, vol. 45, no. 10, pp. 2126–2129, 2007.

[167] S. Babu, P. Ndungu, J.-C. Bradley, M. P. Rossi, and Y. Gogotsi, "Guiding water into carbon nanopipes with the aid of bipolar electrochemistry," *Microfluid. Nanofluid.*, vol. 1, no. 3, pp. 284–288, 2005.

[168] R. R. Mitchell, B. M. Gallant, C. V. Thompson, and Y. Shao-Horn, "All-carbon-nanofiber electrodes for high-energy rechargeable Li-O_2 batteries," *Energy Environ. Sci.*, vol. 4, no. 8, pp. 2952–2958, 2011.

[169] D. J. Guo and H. L. Li, "Highly dispersed ag nanoparticles on functional mwnt surfaces for methanol oxidation in alkaline solution," *Carbon*, vol. 43, no. 6, pp. 1259–1264, 2005.

[170] K. M. Metz, P. E. Colavita, K.-Y. Tse, and R. J. Hamers, "Nanotextured gold coatings on carbon nanofiber scaffolds as ultrahigh surface-area electrodes," *J. Power Sources*, vol. 198, pp. 393–401, 2012.

[171] B. K. Balan, S. M. Unni, and S. Kurungot, "Carbon nanofiber with selectively decorated pt both on inner and outer walls as an efficient electrocatalyst for fuel cell applications," *J. Phys. Chem. C*, vol. 113, no. 40, pp. 17 572–17 578, 2009.

[172] J.-G. Wang, Y. Yang, Z.-H. Huang, and F. Kang, "Coaxial carbon nanofibers/mno 2 nanocomposites as freestanding electrodes for high-performance electrochemical capacitors," *Electrochim. Acta*, vol. 56, no. 25, pp. 9240–9247, 2011.

[173] F. Nitze, M. Mazurkiewicz, A. Malolepszy, A. Mikolajczuk, P. Kędzierzawski, C.-W. Tai, G. Hu, K. J. Kurzydłowski, L. Stobinski, A. Borodzinski, *et al.*, "Synthesis of palladium nanoparticles decorated helical carbon nanofiber as

highly active anodic catalyst for direct formic acid fuel cells," *Electrochimica Acta*, vol. 63, pp. 323–328, 2012.

[174] K. Sears, L. Dumée, J. Schütz, M. She, C. Huynh, S. Hawkins, M. Duke, and S. Gray, "Recent developments in carbon nanotube membranes for water purification and gas separation," *Materials*, vol. 3, no. 1, pp. 127–149, 2010.

[175] A. Srivastava, O. Srivastava, S. Talapatra, R. Vajtai, and P. Ajayan, "Carbon nanotube filters," *Nat. Mater.*, vol. 3, no. 9, pp. 610–614, 2004.

[176] H.-W. Liang, L. Wang, P.-Y. Chen, H.-T. Lin, L.-F. Chen, D. He, and S.-H. Yu, "Carbonaceous nanofiber membranes for selective filtration and separation of nanoparticles," *Adv. Mater.*, vol. 22, no. 42, pp. 4691–4695, 2010.

[177] M. Majumder, N. Chopra, and B. J. Hinds, "Effect of tip functionalization on transport through vertically oriented carbon nanotube membranes," *J. Am. Chem. Soc.*, vol. 127, no. 25, pp. 9062–9070, 2005.

[178] B. Corry, "Water and ion transport through functionalised carbon nanotubes: Implications for desalination technology," *Energy Environ. Sci.*, vol. 4, no. 3, pp. 751–759, 2011.

[179] K. Peng, L.-Q. Liu, H. Li, H. Meyer, and Z. Zhang, "Room temperature functionalization of carbon nanotubes using an ozone/water vapor mixture," *Carbon*, vol. 49, no. 1, pp. 70–76, 2011.

[180] M. Whitby and N. Quirke, "Fluid flow in carbon nanotubes and nanopipes," *Nat. Nanotechnol.*, vol. 2, no. 2, pp. 87–94, 2007.

[181] M. Mezgebe, L.-H. Jiang, Q. Shen, C. Du, and H.-R. Yu, "Studies and comparison of the liquid adsorption behavior and surface properties of single-and multiwall carbon nanotubes by capillary rise method," *Colloids Surf., A*, vol. 415, pp. 86–90, 2012.

[182] S. Iijima and P. Ajayan, "Capillarity-induced filling of carbon nanotubes," *Nature: International weekly journal of science*, vol. 361, no. 6410, pp. 333–334, 1993.

[183] T. A. Hilder and J. M. Hill, "Modeling the loading and unloading of drugs into nanotubes," *Small*, vol. 5, no. 3, pp. 300–308, 2009.

[184] S. Dhondi, G. Pereira, and S. C. Hendy, "Effect of molecular weight on the capillary absorption of polymer droplets," *Langmuir*, vol. 28, no. 27, pp. 10 256–10 265, 2012.

[185] R. Zou, Z. Zhang, Q. Liu, K. Xu, A. Lu, J. Hu, Q. Li, Y. Bando, and D. Golberg, "Melting of metallic electrodes and their flowing through a carbon nanotube channel within a device," *Adv. Mater.*, vol. 25, no. 19, pp. 2693–2699, 2013.

[186] D. Schebarchov and S. Hendy, "Capillary absorption of metal nanodroplets by single-wall carbon nanotubes," *Nano Lett.*, vol. 8, no. 8, pp. 2253–2257, 2008.

[187] D. Schebarchov, B. Lefévre, W. Somerville, and S. Hendy, "Filling a nanoporous substrate by dewetting of thin films," *Nanoscale*, vol. 5, no. 5, pp. 1949–1954, 2013.

[188] K. Edgar, S. C. Hendy, D. Schebarchov, and R. D. Tilley, "Reverse capillary action in carbon nanotubes: Sucking metal nanoparticles out of nanotubes," *Small*, vol. 7, no. 6, pp. 737–740, 2011.

[189] T. T. Nguyen and P. Serp, "Confinement of metal nanoparticles in carbon nanotubes," *ChemCatChem*, vol. 5, no. 12, pp. 3595–3603, 2013.

[190] J. A. Rodríguez-Manzo, M. Terrones, H. Terrones, H. W. Kroto, L. Sun, and F. Banhart, "*In-situ* nucleation of carbon nanotubes by the injection of carbon atoms into metal particles," *Nat. Nanotechnol.*, vol. 2, no. 5, pp. 307–311, 2007.

[191] M. Sauer, H. Shiozawa, P. Ayala, G. Ruiz-Soria, H. Kataura, K. Yanagi, S. Krause, and T. Pichler, "*In-situ* filling of metallic single-walled carbon nanotubes with ferrocene molecules," *Phys. Status Solidi A*, vol. 249, no. 12, pp. 2408–2411, 2012.

[192] G. Du, W. Li, and Y. Liu, "Filling carbon nanotubes with Co_9S_8 nanowires through *in situ* catalyst transition and extrusion," *J. Phys. Chem. C*, vol. 112, no. 6, pp. 1890–1895, 2008.

[193] C.-H. Kiang, J.-S. Choi, T. T. Tran, and A. D. Bacher, "Molecular nanowires of 1-nm diameter from capillary filling of single-walled carbon nanotubes," *J. Phys. Chem. B*, vol. 103, no. 35, pp. 7449–7451, 1999.

[194] G. Zhang and X. W. D. Lou, "Controlled growth of $NiCo_2O_4$ nanorods and ultrathin nanosheets on carbon nanofibers for high-performance supercapacitors," *Sci. Rep.*, vol. 3, p. 1470, 2013.

[195] B. Botka, M. Füstös, G. Klupp, D. Kocsis, E. Székely, M. Utczás, B. Simándi, Á. Botos, R. Hackl, and K. Kamarás, "Low-temperature encapsulation of coronene in carbon nanotubes," *Phys. Status Solidi A*, vol. 249, no. 12, pp. 2432–2435, 2012.

[196] B. Botka, M. E. Füstös, H. M. Tóháti, K. Németh, G. Klupp, Z. Szekrényes, D. Kocsis, M. Utczás, E. Székely, and T. Váczi, "Interactions and chemical transformations of coronene inside and outside carbon nanotubes," *Small*, vol. 10, no. 7, pp. 1369–1378, 2014.

[197] J. Zhang and X. Zhao, "Conducting polymers directly coated on reduced graphene oxide sheets as high-performance supercapacitor electrodes," *J. Phys. Chem. C*, vol. 116, no. 9, pp. 5420–5426, 2012.

[198] D. Bera, S. C. Kuiry, M. McCutchen, S. Seal, H. Heinrich, and G. C. Slane, "*In situ* synthesis of carbon nanotubes decorated with palladium nanoparticles using arc-discharge in solution method," *J. Appl. Phys.*, vol. 96, no. 9, pp. 5152–5157, 2004.

[199] S. Seal, D. Bera, S. C. Kuiry, M. Meyyappan, and M. L. McCutchen, *In-situ synthesis of carbon nanotubes filled with metallic nanoparticles using arc discharge in solution*, US Patent 7,968,072, 2011.

[200] N. G. Tsierkezos, P. Szroeder, R. Fuge, and U. Ritter, "Electrochemical studies on novel films consisting of phosphorus-doped multi-walled carbon nanotubes," *Ionics*, vol. 21, no. 4, pp. 1081–1088, 2015.

[201] X. Liu, H. Kuzmany, P. Ayala, M. Calvaresi, F. Zerbetto, and T. Pichler, "Selective enhancement of photoluminescence in filled single-walled carbon nanotubes," *Adv. Funct. Mater.*, vol. 22, no. 15, pp. 3202–3208, 2012.

[202] G. Ćirić-Marjanović, I. Pašti, and S. Mentus, "One-dimensional nitrogen-containing carbon nanostructures," *Prog. Mater Sci.*, vol. 69, pp. 61–182, 2015.

[203] W. Maser, J. Lambert, P. Ajayan, O. Stephan, and P. Bernier, "Role of y-ni-b mixtures in the formation of carbon nanotubes and encapsulation into carbon clusters," *Synth. Met.*, vol. 77, no. 1, pp. 243–247, 1996.

[204] N. Demoncy, O. Stephan, N. Brun, C. Colliex, A. Loiseau, and H. Pascard, "Filling carbon nanotubes with metals by the arc-discharge method: The key role of sulfur," *The European Physical Journal B-Condensed Matter and Complex Systems*, vol. 4, no. 2, pp. 147–157, 1998.

[205] G. Zheng, Y. Yang, J. J. Cha, S. S. Hong, and Y. Cui, "Hollow carbon nanofiber-encapsulated sulfur cathodes for high specific capacity rechargeable lithium batteries," *Nano Lett.*, vol. 11, no. 10, pp. 4462–4467, 2011.

[206] J. Bao, C. Tie, Z. Xu, Z. Suo, Q. Zhou, and J. Hong, "A facile method for creating an array of metal-filled carbon nanotubes," *Adv. Mater.*, vol. 14, no. 20, pp. 1483–1486, 2002.

[207] N. Jeong, K. S. Hwang, S. Yang, and S.-p. Lee, "Controlled growth, characterization and thermodynamic behavior of bismuth–tin nanostructures sheathed in carbon nanotubes," *Mater. Charact.*, vol. 89, pp. 69–80, 2014.

[208] B. R. Smith, E. E. B. Ghosn, H. Rallapalli, J. A. Prescher, T. Larson, L. A. Herzenberg, and S. S. Gambhir, "Selective uptake of single-walled carbon nan-

otubes by circulating monocytes for enhanced tumour delivery," *Nat. Nanotechnol.*, vol. 9, no. 6, pp. 481–487, 2014.

[209] R. K. Singh, K. D. Patel, J.-J. Kim, T.-H. Kim, J.-H. Kim, U. S. Shin, E.-J. Lee, J. C. Knowles, and H.-W. Kim, "Multifunctional hybrid nanocarrier: Magnetic cnts ensheathed with mesoporous silica for drug delivery and imaging system," *ACS Appl. Mater. Interfaces*, vol. 6, no. 4, pp. 2201–2208, 2014.

[210] S. Goenka, V. Sant, and S. Sant, "Graphene-based nanomaterials for drug delivery and tissue engineering," *J. Controlled Release*, vol. 173, pp. 75–88, 2014.

[211] T. Xu, X. Xie, K. Yin, J. Sun, L. He, and L. Sun, "Controllable atomic-scale sculpting and deposition of carbon nanostructures on graphene," *Small*, vol. 10, no. 9, pp. 1724–1728, 2014.

[212] H. D. Deshpande, D. R. Dean, V. Thomas, W. C. Clem, M. V. Jose, E. Nyairo, and M. Mishra, "Carbon nanofiber reinforced polycaprolactone fibrous meshes by electrostatic co-spinning," *Curr. Nanosci.*, vol. 8, no. 5, pp. 753–761, 2012.

[213] J.-M. Thomassin, C. Jerome, T. Pardoen, C. Bailly, I. Huynen, and C. Detrembleur, "Polymer/carbon based composites as electromagnetic interference (EMI) shielding materials," *Mater. Sci. Eng. R-Rep.*, vol. 74, no. 7, pp. 211–232, 2013.

[214] A. Aldalbahi and M. in het Panhuis, "Electrical and mechanical characteristics of buckypapers and evaporative cast films prepared using single and multi-walled carbon nanotubes and the biopolymer carrageenan," *Carbon*, vol. 50, no. 3, pp. 1197–1208, 2012.

[215] B. K. Balan, V. S. Kale, P. P. Aher, M. V. Shelke, V. K. Pillai, and S. Kurungot, "High aspect ratio nanoscale multifunctional materials derived

from hollow carbon nanofiber by polymer insertion and metal decoration," *Chem. Commun.*, vol. 46, no. 30, pp. 5590–5592, 2010.

[216] W. Baaziz, S. Begin-Colin, B. P. Pichon, I. Florea, O. Ersen, S. Zafeiratos, R. Barbosa, D. Begin, and C. Pham-Huu, "High-density monodispersed cobalt nanoparticles filled into multiwalled carbon nanotubes," *Chem. Mater.*, vol. 24, no. 9, pp. 1549–1551, 2012.

[217] K. P. De Jong and J. W. Geus, "Carbon nanofibers: Catalytic synthesis and applications," *Catalysis Reviews*, vol. 42, no. 4, pp. 481–510, 2000.

[218] T. Billiet, M. Vandenhaute, J. Schelfhout, S. Van Vlierberghe, and P. Dubruel, "A review of trends and limitations in hydrogel-rapid prototyping for tissue engineering," *Biomaterials*, vol. 33, no. 26, pp. 6020–6041, 2012.

[219] F. P. Melchels, M. A. Domingos, T. J. Klein, J. Malda, P. J. Bartolo, and D. W. Hutmacher, "Additive manufacturing of tissues and organs," *Prog. Polym. Sci.*, vol. 37, no. 8, pp. 1079–1104, 2012.

[220] C. E. Bosworth, "A mediæval islamic prototype of the fountain pen?" *J. Semitic Stud. Manchester*, vol. 26, no. 2, pp. 229–234, 1981.

[221] X. Cai, Z. Lv, H. Wu, S. Hou, and D. Zou, "Direct application of commercial fountain pen ink to efficient dye-sensitized solar cells," *J. Mater. Chem.*, vol. 22, no. 19, pp. 9639–9644, 2012.

[222] A. P. Suryavanshi and M.-F. Yu, "Electrochemical fountain pen nanofabrication of vertically grown platinum nanowires," *Nanotechnology*, vol. 18, no. 10, p. 105305, 2007.

[223] M. O. Reese, R. M. van Dam, A. Scherer, and S. R. Quake, "Microfabricated fountain pens for high-density DNA arrays," *Genome Res.*, vol. 13, no. 10, pp. 2348–2352, 2003.

[224] A. Lewis, Y. Kheifetz, E. Shambrodt, A. Radko, E. Khatchatryan, and C. Sukenik, "Fountain pen nanochemistry: Atomic force control of chrome etching," *Appl. Phys. Lett.*, vol. 75, no. 17, pp. 2689–2691, 1999.

[225] A. Russo, B. Y. Ahn, J. J. Adams, E. B. Duoss, J. T. Bernhard, and J. A. Lewis, "Pen-on-paper flexible electronics," *Adv. Mater.*, vol. 23, no. 30, pp. 3426–3430, 2011.

[226] H. Kodama, "Automatic method for fabricating a three-dimensional plastic model with photo-hardening polymer," *Rev. Sci. Instrum.*, vol. 52, no. 11, pp. 1770–1773, 1981.

[227] C. A. Mire, A. Agrawal, G. G. Wallace, P. Calvert, *et al.*, "Inkjet and extrusion printing of conducting poly (3, 4-ethylenedioxythiophene) tracks on and embedded in biopolymer materials," *J. Mater. Chem.*, vol. 21, no. 8, pp. 2671–2678, 2011.

[228] S. V. Murphy and A. Atala, "3D bioprinting of tissues and organs," *Nat. Biotechnol.*, vol. 32, no. 8, pp. 773–785, 2014.

[229] C. Schubert, M. C. van Langeveld, and L. A. Donoso, "Innovations in 3D printing: A 3D overview from optics to organs," *Br. J. Ophthalmol.*, vol. 98, no. 2, pp. 1–3, 2013.

[230] F. Rengier, A. Mehndiratta, H. von Tengg-Kobligk, C. M. Zechmann, R. Unterhinninghofen, H.-U. Kauczor, and F. L. Giesel, "3D printing based on imaging data: Review of medical applications," *International journal of computer assisted radiology and surgery*, vol. 5, no. 4, pp. 335–341, 2010.

[231] D. Bak, "Rapid prototyping or rapid production? 3D printing processes move industry towards the latter," *Assembly Automation*, vol. 23, no. 4, pp. 340–345, 2003.

[232] E. Bassoli, A. Gatto, L. Iuliano, and M. Grazia Violante, "3D printing technique applied to rapid casting," *Rapid Prototyping J.*, vol. 13, no. 3, pp. 148–155, 2007.

[233] E. Torres-Jara, K. Gilpin, J. Karges, R. J. Wood, and D. Rus, "Compliant modular shape memory alloy actuators," *IEEE Robotics & Automation Magazine*, vol. 17, no. 4, pp. 78–87, 2010.

[234] N. Kamamichi, T. Maeba, M. Yamakita, and T. Mukai, "Fabrication of bucky gel actuator/sensor devices based on printing method," in *2008 IEEE/RSJ International Conference on Intelligent Robots and Systems*, IEEE, 2008, pp. 582–587.

[235] J. Rossiter, P. Walters, and B. Stoimenov, *Printing 3D dielectric elastomer actuators for soft robotics*, presented at Electroactive Polymer Actuators and Devices, San Diego, California, USA, 2009.

[236] A. Albu-Schaffer, O. Eiberger, M. Grebenstein, S. Haddadin, C. Ott, T. Wimbock, S. Wolf, and G. Hirzinger, "Soft robotics," *IEEE Robotics Automation Magazine*, vol. 15, no. 3, pp. 20–30, 2008.

[237] A. Miserez, Y. Li, J. H. Waite, and F. Zok, "Jumbo squid beaks: Inspiration for design of robust organic composites," *Acta Biomater.*, vol. 3, no. 1, pp. 139–149, 2007.

[238] L.-W. Xia, R. Xie, X.-J. Ju, W. Wang, Q. Chen, and L.-Y. Chu, "Nano-structured smart hydrogels with rapid response and high elasticity," *Nat. Commun.*, vol. 4, p. 2226, 2013, RSC Publishing Blogs Home, Chips and Tips.

[239] E. M. White, J. Yatvin, J. B. Grubbs, J. A. Bilbrey, and J. Locklin, "Advances in smart materials: Stimuli-responsive hydrogel thin films," *J. Polym. Sci., Part B: Polym. Phys.*, vol. 51, no. 14, pp. 1084–1099, 2013.

[240] E. S. Gil, S.-H. Park, L. W. Tien, B. Trimmer, S. M. Hudson, and D. L. Kaplan, "Mechanically robust, rapidly actuating, and biologically functionalized macroporous poly (n-isopropylacrylamide)/silk hybrid hydrogels," *Langmuir*, vol. 26, no. 19, pp. 15 614–15 624, 2010.

[241] P. Calvert, "Hydrogels for soft machines," *Adv. Mater.*, vol. 21, no. 7, pp. 743–756, 2009.

[242] Z. Liu and P. Calvert, "Multilayer hydrogels as muscle-like actuators," *Adv. Mater.*, vol. 12, no. 4, pp. 288–291, 2000.

[243] J. J. R. Stovall, *Capacitance strain gauge*, US Patent 2,576,489, 1951.

[244] J. D. Johnson, S. R. Zarabadi, and I. D. Jay, *Capacitive strain gauge*, US Patent 7,204,162, 2007.

[245] G. C. Pidcock *et al.*, "Extrusion printing of flexible electrically conducting carbon nanotube networks," *Adv. Funct. Mater.*, vol. 22, no. 22, pp. 4790–4800, 2012.

[246] M. I. Tiwana, S. J. Redmond, and N. H. Lovell, "A review of tactile sensing technologies with applications in biomedical engineering," *Sens. Actuators, A*, vol. 179, pp. 17–31, 2012.

[247] D. J. Cohen, D. Mitra, K. Peterson, and M. M. Maharbiz, "A highly elastic, capacitive strain gauge based on percolating nanotube networks," *Nano Lett.*, vol. 12, no. 4, pp. 1821–1825, 2012.

[248] D. Lee, H. P. Hong, M. J. Lee, C. W. Park, and N. K. Min, "A prototype high sensitivity load cell using single walled carbon nanotube strain gauges," *Sens. Actuators, A*, vol. 180, pp. 120–126, 2012.

[249] F. Lorussi, E. P. Scilingo, M. Tesconi, A. Tognetti, and D. De Rossi, "Strain sensing fabric for hand posture and gesture monitoring," *IEEE Trans. Inf. Technol. Biomed.*, vol. 9, no. 3, pp. 372–381, 2005.

[250] R. Melik, E. Unal, N. K. Perkgoz, B. Santoni, D. Kamstock, C. Puttlitz, and H. V. Demir, "Nested metamaterials for wireless strain sensing," *IEEE J. Sel. Topics in Quantum Electron.*, vol. 16, no. 2, pp. 450–458, 2010.

[251] J. R. Mathias, C. A. Sninsky, H. D. Millar, M. H. Clench, and R. H. Davis, "Development of an improved multi-pressure-sensor probe for recording muscle contraction in human intestine," *Dig. Dis. Sci.*, vol. 30, no. 2, pp. 119–123, 1985.

[252] O. Amft and G. Tröster, "On-body sensing solutions for automatic dietary monitoring," *IEEE Pervasive Comput.*, vol. 8, no. 2, pp. 62–70, 2009.

[253] J. Boge, L. J. Sweetman, S. F. Ralph, *et al.*, "The effect of preparation conditions and biopolymer dispersants on the properties of swnt buckypapers," *J. Mater. Chem.*, vol. 19, no. 48, pp. 9131–9140, 2009.

[254] R. A. Giordano, B. M. Wu, S. W. Borland, L. G. Cima, E. M. Sachs, and M. J. Cima, "Mechanical properties of dense polylactic acid structures fabricated by three dimensional printing," *J. Biomater. Sci. Polym. Ed.*, vol. 8, no. 1, pp. 63–75, 1997.

[255] M. Agarwala, D. Bourell, J. Beaman, H. Marcus, and J. Barlow, "Direct selective laser sintering of metals," *Rapid Prototyping J.*, vol. 1, no. 1, pp. 26–36, 1995.

[256] G. Susanna, L. Salamandra, T. M. Brown, A. Di Carlo, F. Brunetti, and A. Reale, "Airbrush spray-coating of polymer bulk-heterojunction solar cells," *Sol. Energy Mater. Sol. Cells*, vol. 95, no. 7, pp. 1775–1778, 2011.

[257] R. D. Piner, J. Zhu, F. Xu, S. Hong, and C. A. Mirkin, "" dip-pen" nanolithography," *Science*, vol. 283, no. 5402, pp. 661–663, 1999.

[258] F. C. Krebs, "Polymer solar cell modules prepared using roll-to-roll methods: Knife-over-edge coating, slot-die coating and screen printing," *Sol. Energy Mater. Sol. Cells*, vol. 93, no. 4, pp. 465–475, 2009.

[259] M. M. Voigt, R. C. Mackenzie, S. P. King, C. P. Yau, P. Atienzar, J. Dane, P. E. Keivanidis, I. Zadrazil, D. D. Bradley, and J. Nelson, "Gravure printing inverted organic solar cells: The influence of ink properties on film quality and device performance," *Sol. Energy Mater. Sol. Cells*, vol. 105, pp. 77–85, 2012.

[260] J.-W. Song, J. Kim, Y.-H. Yoon, B.-S. Choi, J.-H. Kim, and C.-S. Han, "Inkjet printing of single-walled carbon nanotubes and electrical characterization of the line pattern," *Nanotechnology*, vol. 19, no. 9, p. 095 702, 2008.

[261] T. H. Van Osch, J. Perelaer, A. W. de Laat, and U. S. Schubert, "Inkjet printing of narrow conductive tracks on untreated polymeric substrates," *Adv. Mater.*, vol. 20, no. 2, pp. 343–345, 2008.

[262] B.-J. de Gans, P. C. Duineveld, and U. S. Schubert, "Inkjet printing of polymers: State of the art and future developments," *Adv. Mater.*, vol. 16, no. 3, pp. 203–213, 2004.

[263] C. J. Ferris, K. G. Gilmore, G. G. Wallace, *et al.*, "Biofabrication: An overview of the approaches used for printing of living cells," *Appl. Microbiol. Biotechnol.*, vol. 97, no. 10, pp. 4243–4258, 2013.

[264] Z. Nie, C. A. Nijhuis, J. Gong, X. Chen, A. Kumachev, A. W. Martinez, M. Narovlyansky, and G. M. Whitesides, "Electrochemical sensing in paper-based microfluidic devices," *Lab. Chip*, vol. 10, no. 4, pp. 477–483, 2010.

[265] A. C. Siegel, S. T. Phillips, M. D. Dickey, N. Lu, Z. Suo, and G. M. Whitesides, "Foldable printed circuit boards on paper substrates," *Adv. Funct. Mater.*, vol. 20, no. 1, pp. 28–35, 2010.

[266] J. P. Rolland and D. A. Mourey, "Paper as a novel material platform for devices," *MRS Bull.*, vol. 38, no. 04, pp. 299–305, 2013.

[267] J. Kim, M.-W. Moon, K.-R. Lee, L. Mahadevan, and H.-Y. Kim, "Hydrodynamics of writing with ink," *Phys. Rev. Lett.*, vol. 107, no. 26, p. 264 501, 2011.

[268] T. J. Pollock, "Gellan-related polysaccharides and the genus sphingomonas," *Microbiology*, vol. 139, no. 8, pp. 1939–1945, 1993.

[269] P.-E. Jansson, B. Lindberg, and P. A. Sandford, "Structural studies of gellan gum, an extracellular polysaccharide elaborated by pseudomonas elodea," *Carbohydr. Res.*, vol. 124, no. 1, pp. 135–139, 1983.

[270] N. J. Whiteside, G. G. Wallace, and M. in het Panhuis, "Preparation and characterisation of graphene composite hydrogels," *Synth. Met.*, vol. 168, pp. 36–42, 2013.

[271] M. S. Dresselhaus, G. Dresselhaus, and P. C. Eklund, *Science of fullerenes and carbon nanotubes: Their properties and applications*. Academic press, 1996.

[272] G. G. Tibbetts, D. W. Gorkiewicz, and R. L. Alig, "A new reactor for growing carbon fibers from liquid-and vapor-phase hydrocarbons," *Carbon*, vol. 31, no. 5, pp. 809–814, 1993.

[273] N. Grobert, "Carbon nanotubes–becoming clean," *Mater. Today*, vol. 10, no. 1, pp. 28–35, 2007.

[274] M. H. Al-Saleh and U. Sundararaj, "A review of vapor grown carbon nanofiber/polymer conductive composites," *Carbon*, vol. 47, no. 1, pp. 2–22, 2009.

[275] B. Zhang, R. Fu, M. Zhang, X. Dong, L. Wang, and C. U. Pittman, "Gas sensitive vapor grown carbon nanofiber/polystyrene sensors," *Mater. Res. Bull.*, vol. 41, no. 3, pp. 553–562, 2006.

[276] G. A. Jimenez and S. C. Jana, "Electrically conductive polymer nanocomposites of polymethylmethacrylate and carbon nanofibers prepared by chaotic mixing," *Compos. Part A Appl. S.*, vol. 38, no. 3, pp. 983–993, 2007.

[277] S. Rana, R. Alagirusamy, and M. Joshi, "Effect of carbon nanofiber dispersion on the tensile properties of epoxy nanocomposites," *J. Compos. Mater.*, vol. 45, no. 21, pp. 2247–2256, 2011.

[278] K. Lozano and E. Barrera, "Nanofiber-reinforced thermoplastic composites. i. thermoanalytical and mechanical analyses," *J. Appl. Polym. Sci.*, vol. 79, no. 1, pp. 125–133, 2001.

[279] J. Yu, N. Grossiord, C. E. Koning, and J. Loos, "Controlling the dispersion of multi-wall carbon nanotubes in aqueous surfactant solution," *Carbon*, vol. 45, no. 3, pp. 618–623, 2007.

[280] Y. Huang, S. Ahir, and E. Terentjev, "Dispersion rheology of carbon nanotubes in a polymer matrix," *Phys. Rev. B*, vol. 73, no. 12, p. 125 422, 2006.

[281] Q. Cheng, S. Debnath, E. Gregan, and H. J. Byrne, "Ultrasound-assisted swnts dispersion: Effects of sonication parameters and solvent properties," *J. Phys. Chem. C*, vol. 114, no. 19, pp. 8821–8827, 2010.

[282] P. Vichchulada, M. A. Cauble, E. A. Abdi, E. I. Obi, Q. Zhang, and M. D. Lay, "Sonication power for length control of single-walled carbon nanotubes in aqueous suspensions used for 2-dimensional network formation," *J. Phys. Chem. C*, vol. 114, no. 29, pp. 12 490–12 495, 2010.

[283] K. Lu, R. Lago, Y. Chen, M. Green, P. Harris, and S. Tsang, "Mechanical damage of carbon nanotubes by ultrasound," *Carbon*, vol. 34, no. 6, pp. 814–816, 1996.

[284] P. N. Nirmalraj, P. E. Lyons, S. De, J. N. Coleman, and J. J. Boland, "Electrical connectivity in single-walled carbon nanotube networks," *Nano Lett.*, vol. 9, no. 11, pp. 3890–3895, 2009.

[285] D. Stauffer and A. Aharony, *Introduction to percolation theory*, English, 2nd ed. London, England, Taylor & Francis London, 1992.

[286] J. S. Pérez, E. R. Porcel, J. C. López, J. F. Sevilla, and Y. Chisti, "Shear rate in stirred tank and bubble column bioreactors," *Chem. Eng. J.*, vol. 124, no. 1, pp. 1–5, 2006.

[287] P. Manandhar, P. D. Calvert, and J. R. Buck, "Elastomeric ionic hydrogel sensor for large strains," *IEEE Sens. J.*, vol. 12, no. 6, pp. 2052–2061, 2012.

[288] S. Bauer, S. Bauer-Gogonea, I. Graz, M. Kaltenbrunner, C. Keplinger, and R. Schwödiauer, "25th anniversary article: A soft future: From robots and sensor skin to energy harvesters," *Adv. Mater.*, vol. 26, no. 1, pp. 149–162, 2014.

[289] C. Keplinger, J.-Y. Sun, C. C. Foo, P. Rothemund, G. M. Whitesides, and Z. Suo, "Stretchable, transparent, ionic conductors," *Science*, vol. 341, no. 6149, pp. 984–987, 2013.

[290] E. Wang, M. S. Desai, and S.-W. Lee, "Light-controlled graphene-elastin composite hydrogel actuators," *Nano Lett.*, vol. 13, no. 6, pp. 2826–2830, 2013.

[291] R. A. Green, N. H. Lovell, G. G. Wallace, and L. A. Poole-Warren, "Conducting polymers for neural interfaces: Challenges in developing an effective long-term implant," *Biomaterials*, vol. 29, no. 24, pp. 3393–3399, 2008.

[292] P. Pissis, A. Kyritsis, and V. Shilov, "Molecular mobility and protonic conductivity in polymers: Hydrogels and ionomers," *Solid State Ionics*, vol. 125, no. 1, pp. 203–212, 1999.

[293] F. A. Aouada, M. R. Guilherme, G. M. Campese, E. M. Girotto, A. F. Rubira, and E. C. Muniz, "Electrochemical and mechanical properties of hydrogels based on conductive poly (3, 4-ethylene dioxythiophene)/poly (styrenesulfonate) and paam," *Polym. Test.*, vol. 25, no. 2, pp. 158–165, 2006.

[294] T. Dai, X. Qing, H. Zhou, C. Shen, J. Wang, and Y. Lu, "Mechanically strong conducting hydrogels with special double-network structure," *Synth. Met.*, vol. 160, no. 7, pp. 791–796, 2010.

[295] R. Kishi, K. Hiroki, T. Tominaga, K.-I. Sano, H. Okuzaki, J. G. Martinez, T. F. Otero, and Y. Osada, "Electro-conductive double-network hydrogels," *J. Polym. Sci., Part B: Polym. Phys.*, vol. 50, no. 11, pp. 790–796, 2012.

[296] S. Naficy, J. M. Razal, G. M. Spinks, G. G. Wallace, and P. G. Whitten, "Electrically conductive, tough hydrogels with ph sensitivity," *Chem. Mater.*, vol. 24, no. 17, pp. 3425–3433, 2012.

[297] Q. Tang, J. Wu, and J. Lin, "A multifunctional hydrogel with high conductivity, ph-responsive, thermo-responsive and release properties from polyacrylate/polyaniline hybrid," *Carbohydr. Polym.*, vol. 73, no. 2, pp. 315–321, 2008.

[298] F. Gayet, L. Viau, F. Leroux, F. Mabille, S. Monge, J.-J. Robin, and A. Vioux, "Unique combination of mechanical strength, thermal stability, and high ion conduction in pmma- silica nanocomposites containing high loadings of ionic liquid," *Chem. Mater.*, vol. 21, no. 23, pp. 5575–5577, 2009.

[299] Q. Tang, J. Lin, J. Wu, C. Zhang, and S. Hao, "Two-steps synthesis of a poly (acrylate–aniline) conducting hydrogel with an interpenetrated networks structure," *Carbohydr. Polym.*, vol. 67, no. 3, pp. 332–336, 2007.

[300] T. Dai, X. Jiang, S. Hua, X. Wang, and Y. Lu, "Facile fabrication of conducting polymer hydrogels via supramolecular self-assembly," *Chem. Commun.*, no. 36, pp. 4279–4281, 2008.

[301] K. S. Kang and G. T. Veeder, *Polysaccharide S-60 and bacterial fermentation process for its preparation*, US Patent 4,326,053, 1982.

[302] H. Grasdalen and O. Smidsrød, "Gelation of gellan gum," *Carbohydr. Polym.*, vol. 7, no. 5, pp. 371–393, 1987.

[303] D. F. Coutinho, S. V. Sant, H. Shin, J. T. Oliveira, M. E. Gomes, N. M. Neves, A. Khademhosseini, and R. L. Reis, "Modified gellan gum hydrogels with tunable physical and mechanical properties," *Biomaterials*, vol. 31, no. 29, pp. 7494–7502, 2010.

[304] D. Pletcher, R. Greff, R. Peat, L. Peter, and J. Robinson, *Instrumental methods in electrochemistry, 1st edn.* Elsevier, 2001.

[305] T. Q. Nguyen, Q. Z. Liang, and H.-H. Kausch, "Kinetics of ultrasonic and transient elongational flow degradation: A comparative study," *Polymer*, vol. 38, no. 15, pp. 3783–3793, 1997.

[306] M. W. Kuijpers, P. D. Iedema, M. F. Kemmere, and J. T. Keurentjes, "The mechanism of cavitation-induced polymer scission; experimental and computational verification," *Polymer*, vol. 45, no. 19, pp. 6461–6467, 2004.

[307] W. Bauhofer and J. Z. Kovacs, "A review and analysis of electrical percolation in carbon nanotube polymer composites," *Compos. Sci. Technol.*, vol. 69, no. 10, pp. 1486–1498, 2009.

[308] D. Ugarte, T. Stöckli, J. Bonard, A. Châtelain, and W. De Heer, "Filling carbon nanotubes," *Appl. Phys. A*, vol. 67, no. 1, pp. 101–105, 1998.

[309] Y. Chen, D. T. Shaw, X. Bai, E. Wang, C. Lund, W. Lu, and D. Chung, "Hydrogen storage in aligned carbon nanotubes," *Appl. Phys. Lett.*, vol. 78, no. 15, pp. 2128–2130, 2001.

[310] A. Leonhardt, S. Hampel, C. Mueller, I. Moench, R. Koseva, M. Ritschel, D. Elefant, K. Biedermann, and B. Buechner, "Synthesis, properties, and applications of ferromagnetic-filled carbon nanotubes," *Chem. Vap. Deposition*, vol. 12, no. 6, pp. 380–387, 2006.

[311] G. Korneva, H. Ye, Y. Gogotsi, D. Halverson, G. Friedman, J.-C. Bradley, and K. G. Kornev, "Carbon nanotubes loaded with magnetic particles," *Nano Lett.*, vol. 5, no. 5, pp. 879–884, 2005.

[312] S. A. Miller and C. R. Martin, "Redox modulation of electroosmotic flow in a carbon nanotube membrane," *J. Am. Chem. Soc.*, vol. 126, no. 20, pp. 6226–6227, 2004.

[313] B. M. Kim, S. Qian, and H. H. Bau, "Filling carbon nanotubes with particles," *Nano Lett.*, vol. 5, no. 5, pp. 873–878, 2005.

[314] W. Hu, D. Gong, Z. Chen, L. Yuan, K. Saito, C. A. Grimes, and P. Kichambare, "Growth of well-aligned carbon nanotube arrays on silicon substrates using porous alumina film as a nanotemplate," *Appl. Phys. Lett.*, vol. 79, no. 19, pp. 3083–3085, 2001.

[315] O. Byl, P. Kondratyuk, S. T. Forth, S. A. FitzGerald, L. Chen, J. K. Johnson, and J. T. Yates, "Adsorption of CF_4 on the internal and external surfaces of opened single-walled carbon nanotubes: A vibrational spectroscopy study," *J. Am. Chem. Soc.*, vol. 125, no. 19, pp. 5889–5896, 2003.

[316] B. Satishkumar, A. Govindaraj, J. Mofokeng, G. Subbanna, and C. Rao, "Novel experiments with carbon nanotubes: Opening, filling, closing and functionalizing nanotubes," *J. Phys. B: At., Mol. Opt. Phys.*, vol. 29, no. 21, p. 4925, 1996.

[317] G. Tang, D. Chang, D. Wang, J. He, W. Mi, J. Zhang, and W. Wang, "Mechanical property improvement of carbon fiber-reinforced ptfe composites by pa6 filler dispersion," *Polym.-Plast. Technol. Eng.*, vol. 51, no. 4, pp. 377–380, 2012.

[318] J. E. Puskas, E. A. Foreman-Orlowski, G. T. Lim, S. E. Porosky, M. M. Evancho-Chapman, S. P. Schmidt, M. El Fray, M. Piątek, P. Prowans, and K. Lovejoy, "A nanostructured carbon-reinforced polyisobutylene-based thermoplastic elastomer," *Biomaterials*, vol. 31, no. 9, pp. 2477–2488, 2010.

[319] X. Chen, S. Wei, A. Yadav, R. Patil, J. Zhu, R. Ximenes, L. Sun, and Z. Guo, "Poly (propylene)/carbon nanofiber nanocomposites: *Ex Situ* solvent-assisted preparation and analysis of electrical and electronic properties," *Macromol. Mater. Eng.*, vol. 296, no. 5, pp. 434–443, 2011.

[320] Y. Yang, M. C. Gupta, K. L. Dudley, and R. W. Lawrence, "The fabrication and electrical properties of carbon nanofibre–polystyrene composites," *Nanotechnology*, vol. 15, no. 11, p. 1545, 2004.

[321] L. Vaisman, H. D. Wagner, and G. Marom, "The role of surfactants in dispersion of carbon nanotubes," *Adv. Colloid Interface Sci.*, vol. 128, pp. 37–46, 2006.

[322] J. Xu, S. Chatterjee, K. W. Koelling, Y. Wang, and S. E. Bechtel, "Shear and extensional rheology of carbon nanofiber suspensions," *Rheol. Acta*, vol. 44, no. 6, pp. 537–562, 2005.

[323] S. Kumar, B. Lively, L. Sun, B. Li, and W. Zhong, "Highly dispersed and electrically conductive polycarbonate/oxidized carbon nanofiber composites

for electrostatic dissipation applications," *Carbon*, vol. 48, no. 13, pp. 3846–3857, 2010.

[324] E. Tang, M. Huang, and L. Lim, "Ultrasonication of chitosan and chitosan nanoparticles," *Int. J. Pharm.*, vol. 265, no. 1, pp. 103–114, 2003.

[325] P. He, Y. Gao, J. Lian, L. Wang, D. Qian, J. Zhao, W. Wang, M. J. Schulz, X. P. Zhou, and D. Shi, "Surface modification and ultrasonication effect on the mechanical properties of carbon nanofiber/polycarbonate composites," *Compos. Part A Appl. S.*, vol. 37, no. 9, pp. 1270–1275, 2006.

[326] G. J. Price, "Ultrasonically enhanced polymer synthesis," *Ultrason. Sonochem.*, vol. 3, no. 3, S229–S238, 1996.

[327] J. Lorimer, T. Mason, T. Cuthbert, and E. Brookfield, "Effect of ultrasound on the degradation of aqueous native dextran," *Ultrason. Sonochem.*, vol. 2, no. 1, S55–S57, 1995.

[328] A. J. Granero, J. M. Razal, G. G. Wallace, *et al.*, "Spinning carbon nanotube-gel fibers using polyelectrolyte complexation," *Adv. Funct. Mater.*, vol. 18, no. 23, pp. 3759–3764, 2008.

[329] I. B. Bajaj, S. A. Survase, P. S. Saudagar, and R. S. Singhal, "Proizvodnja gelan gume fermentacijom, njezino izdvajanje, pročišćavanje i primjena," *Food Technology and Biotechnology*, vol. 45, no. 4, pp. 341–354, 2007.

[330] T. V. Hughes and C. R. Chambers, *Manufacture of carbon filaments*, US Patent 405,480, 1889.

[331] L. Radushkevich and V. Lukyanovich, "O strukture ugleroda, obrazujucegosja pri termiceskom razlozenii okisi ugleroda na zeleznom kontakte," *Zurn Fisic Chim*, vol. 26, no. 1, pp. 88–95, 1952.

[332] J. Ding, Y. Zhu, and Y. Fu, "Preparation and properties of silanized vapor-grown carbon nanofibers/epoxy shape memory nanocomposites," *Polym. Compos.*, vol. 35, no. 2, pp. 412–417, 2014.

[333] M. D. Sanchez-Garcia, J. M. Lagaron, and S. V. Hoa, "Effect of addition of carbon nanofibers and carbon nanotubes on properties of thermoplastic biopolymers," *Compos. Sci. Technol.*, vol. 70, no. 7, pp. 1095–1105, 2010.

[334] M. Hosur, R. Barua, S. Zainuddin, S. Jeelani, A. Kumar, J. Trovillion, and Y. Pereza, "Processing and characterization of epoxy nanocomposites with mwcnts/cnfs using thinky and 3-roll shear mixing techniques," *Matéria (Rio de Janeiro)*, vol. 15, no. 2, pp. 247–253, 2010.

[335] M. Chipara, R. A. Vaia, and A. Nasar, "Electron spin resonance on polyurethanes–vapor grown carbon nanofiber composites," *Vacuum*, vol. 107, pp. 254–258, 2014.

[336] M. Monthioux, "Filling single-wall carbon nanotubes," *Carbon*, vol. 40, no. 10, pp. 1809–1823, 2002.

[337] F. Tuinstra and J. Koenig, "Characterization of graphite fiber surfaces with raman spectroscopy," *J. Compos. Mater.*, vol. 4, no. 4, pp. 492–499, 1970.

[338] E. M. Byrne, M. A. McCarthy, Z. Xia, and W. A. Curtin, "Multiwall nanotubes can be stronger than single wall nanotubes and implications for nanocomposite design," *Phys. Rev. Lett.*, vol. 103, no. 4, 2009.

[339] A. Sesis, M. Hodnett, G. Memoli, A. J. Wain, I. Jurewicz, A. B. Dalton, J. D. Carey, and G. Hinds, "Influence of acoustic cavitation on the controlled ultrasonic dispersion of carbon nanotubes," *J. Phys. Chem. B*, vol. 117, no. 48, pp. 15 141–15 150, 2013.

[340] S. Hüfner, *Photoelectron spectroscopy: Principles and applications*, 3rd. Springer Berlin Heidelberg, 2003.

[341] T. Ohno, T. Tsubota, M. Toyofuku, and R. Inaba, "Photocatalytic activity of a TiO_2 photocatalyst doped with C^{4+} and S^{4+} ions having a rutile phase under visible light," *Catal. Lett.*, vol. 98, no. 4, pp. 255–258, 2004.

[342] R. Gately, S. Naficy, R. Gorkin, and M. in het Panhuis, "3d printed carbon-based soft strain gauges," *Nanotechnology*, (*Currently under review*).

[343] T. S. Shim, S.-H. Kim, C.-J. Heo, H. C. Jeon, and S.-M. Yang, "Controlled origami folding of hydrogel bilayers with sustained reversibility for robust microcarriers," *Angew. Chem. Int. Ed.*, vol. 51, no. 6, pp. 1420–1423, 2012.

[344] D. Morales, I. Podolsky, R. W. Mailen, T. Shay, M. D. Dickey, and O. D. Velev, "Ionoprinted multi-responsive hydrogel actuators," *Micromachines*, vol. 7, no. 6, p. 98, 2016.

[345] R. V. Martinez, J. L. Branch, C. R. Fish, L. Jin, R. F. Shepherd, R. Nunes, Z. Suo, and G. M. Whitesides, "Robotic tentacles with three-dimensional mobility based on flexible elastomers," *Adv. Mater.*, vol. 25, no. 2, pp. 205–212, 2013.

[346] Y. She, C. Li, J. Cleary, and H.-J. Su, "Design and fabrication of a soft robotic hand with embedded actuators and sensors," *J. Mech. Robot*, vol. 7, no. 2, p. 021 007, 2015.

[347] P. Lv, K. Yu, X. Tan, R. Zheng, Y. Ni, Z. Wang, C. Liu, and W. Wei, "Super-elastic graphene/carbon nanotube aerogels and their application as a strain-gauge sensor," *RSC Adv.*, vol. 6, no. 14, pp. 11 256–11 261, 2016.

[348] J. Wu, C. Song, H. S. Saleem, A. Downey, and S. Laflamme, "Network of flexible capacitive strain gauges for the reconstruction of surface strain," *Meas. Sci. Technol.*, vol. 26, no. 5, p. 055 103, 2015.

[349] J. T. Muth, D. M. Vogt, R. L. Truby, Y. Mengüç, D. B. Kolesky, R. J. Wood, and J. A. Lewis, "Embedded 3D printing of strain sensors within highly stretchable elastomers," *Adv. Mater.*, vol. 26, no. 36, pp. 6307–6312, 2014.

[350] O. Kanoun, C. Müller, A. Benchirouf, A. Sanli, T. N. Dinh, A. Al-Hamry, L. Bu, C. Gerlach, and A. Bouhamed, "Flexible carbon nanotube films for high performance strain sensors," *Sensors*, vol. 14, no. 6, pp. 10 042–10 071, 2014.

[351] N. Lu, C. Lu, S. Yang, and J. Rogers, "Highly sensitive skin-mountable strain gauges based entirely on elastomers," *Adv. Funct. Mater.*, vol. 22, no. 19, pp. 4044–4050, 2012.

[352] S. Harada, W. Honda, T. Arie, S. Akita, and K. Takei, "Fully printed, highly sensitive multifunctional artificial electronic whisker arrays integrated with strain and temperature sensors," *ACS Nano*, vol. 8, no. 4, pp. 3921–3927, 2014.

[353] V. C. Tung, L.-M. Chen, M. J. Allen, J. K. Wassei, K. Nelson, R. B. Kaner, and Y. Yang, "Low-temperature solution processing of graphene- carbon nanotube hybrid materials for high-performance transparent conductors," *Nano Lett.*, vol. 9, no. 5, pp. 1949–1955, 2009.

[354] A. Yu, P. Ramesh, X. Sun, E. Bekyarova, M. E. Itkis, and R. C. Haddon, "Enhanced thermal conductivity in a hybrid graphite nanoplatelet–carbon nanotube filler for epoxy composites," *Adv. Mater.*, vol. 20, no. 24, pp. 4740–4744, 2008.

[355] U. Khan, I. O'Connor, Y. K. Gun'ko, and J. N. Coleman, "The preparation of hybrid films of carbon nanotubes and nano-graphite/graphene with excellent mechanical and electrical properties," *Carbon*, vol. 48, no. 10, pp. 2825–2830, 2010.

[356] S.-Y. Yang, W.-N. Lin, Y.-L. Huang, H.-W. Tien, J.-Y. Wang, C.-C. M. Ma, S.-M. Li, and Y.-S. Wang, "Synergetic effects of graphene platelets and carbon nanotubes on the mechanical and thermal properties of epoxy composites," *Carbon*, vol. 49, no. 3, pp. 793–803, 2011.

[357] H. Im and J. Kim, "Thermal conductivity of a graphene oxide–carbon nanotube hybrid/epoxy composite," *Carbon*, vol. 50, no. 15, pp. 5429–5440, 2012.

[358] Y. Liu and S. Kumar, "Polymer/carbon nanotube nano composite fibers–a review," *ACS Appl. Mater. Interfaces*, vol. 6, no. 9, pp. 6069–6087, 2014.

[359] E. Hammel, X. Tang, M. Trampert, T. Schmitt, K. Mauthner, A. Eder, and P. Pötschke, "Carbon nanofibers for composite applications," *Carbon*, vol. 42, no. 5, pp. 1153–1158, 2004.

[360] C. H. A. Wong, A. Ambrosi, and M. Pumera, "Thermally reduced graphenes exhibiting a close relationship to amorphous carbon," *Nanoscale*, vol. 4, no. 16, pp. 4972–4977, 2012.

[361] J. Sumfleth, X. C. Adroher, and K. Schulte, "Synergistic effects in network formation and electrical properties of hybrid epoxy nanocomposites containing multi-wall carbon nanotubes and carbon black," *J. Mater. Sci.*, vol. 44, no. 12, pp. 3241–3247, 2009.

[362] M. C. García, M. C. Alfaro, and J. Muñoz, "Rheology of sheared gels based on low acyl-gellan gum," *Food Sci. Technol. Int.*, vol. 22, no. 4, pp. 325–332, 2016.

[363] S. R. Moxon and A. M. Smith, "Controlling the rheology of gellan gum hydrogels in cell culture conditions," *Int. J. Biol. Macromol.*, vol. 84, pp. 79–86, 2016.

[364] R. Lozano, L. Stevens, B. C. Thompson, K. J. Gilmore, R. Gorkin, E. M. Stewart, M. in het Panhuis, M. Romero-Ortega, and G. G. Wallace, "3D printing of layered brain-like structures using peptide modified gellan gum substrates," *Biomaterials*, vol. 67, pp. 264–273, 2015.

[365] M. in het Panhuis, J. Wu, S. A. Ashraf, and G. G. Wallace, "Conducting textiles from single-walled carbon nanotubes," *Synth. Met.*, vol. 157, no. 8, pp. 358–362, 2007.

[366] B. C. Tee, C. Wang, R. Allen, and Z. Bao, "An electrically and mechanically self-healing composite with pressure-and flexion-sensitive properties for electronic skin applications," *Nat. Nanotechnol.*, vol. 7, no. 12, pp. 825–832, 2012.

[367] L. Migliorini, T. Santaniello, Y. Yan, C. Lenardi, and P. Milani, "Low-voltage electrically driven homeostatic hydrogel-based actuators for underwater soft robotics," *Sens. Actuators, B*, vol. 228, pp. 758–766, 2016.

[368] T. Jawhari, A. Roid, and J. Casado, "Raman spectroscopic characterization of some commercially available carbon black materials," *Carbon*, vol. 33, no. 11, pp. 1561–1565, 1995.

[369] L. G. Cançando, K. Takai, T. Enoki, M. Endo, Y. A. Kim, H. Mizusaki, A. Jorio, L. N. Coelho, R. Magalhaẽs-Paniago, and M. A. Pimenta, "General equation for the determination of the crystallite size l[sub a] of nanographite by raman spectroscopy," *Appl. Phys. Lett.*, vol. 88, no. 16, p. 163 106, 2006.

[370] S. E. Bakarich, R. Gorkin, S. Naficy, R. Gately, M. in het Panhuis, and G. M. Spinks, "3D/4D printing hydrogel composites: A pathway to functional devices," *MRS Advances*, vol. 1, no. 08, pp. 521–526, 08 2015.

[371] S. Naficy, R. Gately, R. Gorkin, H. Xin, and G. M. Spinks, "4D printing of reversible shape morphing hydrogel structures," *Macromol. Mater. Eng.*, 2016.

[372] K. Tian, J. Bae, S. Bakarich, C. Yang, R. Gately, G. M. Spinks, M. in het Panhuis, Z. Suo, and J. Vlassak, "3d printing of transparent and conductive heterogeneous hydrogel-elastomer systems," *Adv. Mater.*, (*Currently under review*).

Appendix A

Additional Papers

The following papers are all papers that I have helped to author, and display a variety of different applications of instrumentation developed throughout the course of this project, in specific the custom-built 3D printer. The design of the 3D printer was briefly discussed in the body of this document, however not all applications were explored. These papers show various uses of this same instrument, and how it can be applied to a variety of problems.

4D Printing of Reversible Shape Morphing Hydrogel Structures

A series of hydrogel-based inks are developed to print 3D structures capable of reversible shape deformation in response to hydration and temperature. The inks are made of large polymer chains and UV curable monomers which form interpenetrating polymer networks after polymerization. By taking advantage of the long polymer chains in the ink formulations, it is possible to adjust the rheological properties of the inks to enable 3D printing. Hydrogels produced from the inks exhibit robust mechanical performance with their mechanical properties controlled by the nature of the long polymer chains within their networks. In this paper, hydrogel hinges are made from various ink formulations and a simple model is developed to predict their bending characteristics, including the bending curvature and bending angle. This model can be used as a guide to determine optimal parameters for a wide range of materials combination to create all-hydrogel structures that undergo desired shape transitions

The following is a stylistically edited version of the published paper:

S. Naficy, R. Gately, R. Gorkin, H. Xin, and G. M. Spinks, "4D printing of reversible shape morphing hydrogel structures," *Macromol. Mater. Eng.*, 2016

A.1 Introduction

Structures capable of changing their 3D shape in response to their environment are found commonly in nature and include reversible processes, such as flower heliotropism, and irreversible actions, like seed pod opening [2–5]. The concept of shape morphing is also well reflected in origami art, where a flat sheet of paper turns into a complex 3D shape following a series of well-designed folds. Inspired by the principles of origami and shape morphing, various engineering devices have been designed and fabricated. Examples of such devices include foldable robots [6], compact deployable structures [7, 8], foldable electronics [9, 10], and biomedical devices [11, 12]. While impressively complex morphing motions have been demonstrated [13], the fabrication and control of such devices remains complicated. Here we conjointly develop 3D printing techniques and mechanical models to provide a facile method for the digital design, fabrication, and accurate control of reversible shape changing devices. The underlying mechanism of shape morphing is principally by one or more bending deformations that result from a change in mechanical properties (*e.g.*, stiffness) or physical characteristics (*e.g.*, volume) of an active component in a multimaterial device [14–16]. In some cases the structural deformation is irreversible [17], with one or more intermediary states, such as the shape transitions originated from stress relaxation of shape memory polymers [18, 19]. Completely reversible shape transitions are also possible with the structure returning back to its original shape when stimulation is ceased [20]. These shape transitions can occur when the active material changes in volume. Stimuli responsive gels and hydrogels and electroactive polymers belong to this category [21–27]. Fabrication by 3D printing is providing an exciting opportunity for preparing complex shape morphing

devices. Traditionally, *in situ* polymerization, casting, and film making methods have been widely utilized with shape memory polymers [28, 29], but as the level of complexity in shape transformation increases so does the number of manufacturing steps needed to complete the device. 3D printing offers precise placement of different materials and has been used to construct complex hybrid structures, including morphing systems made with shape memory materials [30–32] and volume change materials [33]. Gels and hydrogels are particularly interesting as the active material in morphing structures because they undergo large deformations due to their high degree of swelling. Although there are reports of 3D printed hydrogels, little has been explored to evaluate the use of 3D printing in creating hydrogel-based shape morphing structures with robust mechanical performance [34, 35].

Here, we introduce a series of interpenetrating networks with controllable water swellability, tunable rheology, and robust mechanical properties for the preparation of 3D printed shape morphing structures. Inks were developed for extrusion printing in which a linear hydrophilic polyurethane was combined with ultraviolet (UV) curable monomers in a blended solvent. The polyurethane provides suitable rheological properties needed for extrusion printing along with mechanical robustness required for the printed objects. The UV curable monomers form a second hydrophilic polymer network to rapidly solidify the structure after printing and tune the elastic modulus and water swellability. Previously, we demonstrated the positive impact of hydrophilic polyurethanes on the mechanical performance of pH-sensitive hydrogel films produced via casting and UV curing [36]. In this paper, we use p-nIPAAm as a temperature sensitive polymer network, along with a nonactive polymer, p-HEMA, to provide structural integrity (Figure A.1a). The p-nIPAAm shows a reversible thermal transition with a large reduction in water swelling when heated above 32 °C. Bilayers constructed from the p-nIPAAm and p-HEMA are able to morph from a flat state when dry to a controllable 3D structure when fully swollen below 32 °C and back to the flat state at temperatures above 32 °C (Figure A.1c). A model has been developed to establish a correlation between bending characteristics of

the bilayer hybrid hydrogels and the material properties and fabrication parameters (Figure A.1b). The model is utilized as a guide to extrusion print objects capable of reversible and controllable shape transformation.

A.2 Results and Discussion

A.2.1 Ink Preparation and Hydrogels Characterisation

For the ink preparation, different types of PEO-PU with varying molecular weight were used along with AKG as UV initiator, MBAAm as crosslinking agent and HEMA and n-isopropylacrylamide (nIPAAm) as monomers. All the PEO-PU used here were soluble in polar organic solvents and their mixture with water (e.g., ethanol:water), but insoluble in water alone. The number of ether units in the polyether segment of PEO-PU molecules was 70, 12, 10, or 5. To distinguish between different PEO-PUs used in this study, the number of ether units in the PEO-PU structure is herein referred to as an index, *e.g.*, $PEO7_{70}$-PU refers to a polyether-based polyurethane with 70 ether units. The concentration of UV initiator and crosslinking agent were optimized to reach the gelation point after 1 min of UV irradiation of the inks with a 300–450 nm UV lamp (BlueWave 75, Dymax). To prevent phase separation of p-nIPAAm during UV polymerization and printing, ethanol was chosen as the solvent. p-nIPAAm is a temperature sensitive polymer with a lower critical solution temperature (LCST) of 32 °C in aqueous solutions. The occurrence of phase separation during nIPAAm polymerization results in poor mechanical properties and unpredictable network structure. In previous reports [35], sub-ambient temperatures were required during printing and UV curing of nIPAAm to prevent this phenomenon. However, p-nIPAAm phase behaviour is completely different in ethanol and ethanol: water mixtures and in pure ethanol, the LCST phase separation is totally suppressed [37, 38]. Hence, by using ethanol as solvent, there was no need for further controlling of temperature during the processing of nIPAAm-based inks and no phase separation was observed during or after UV polymerization of

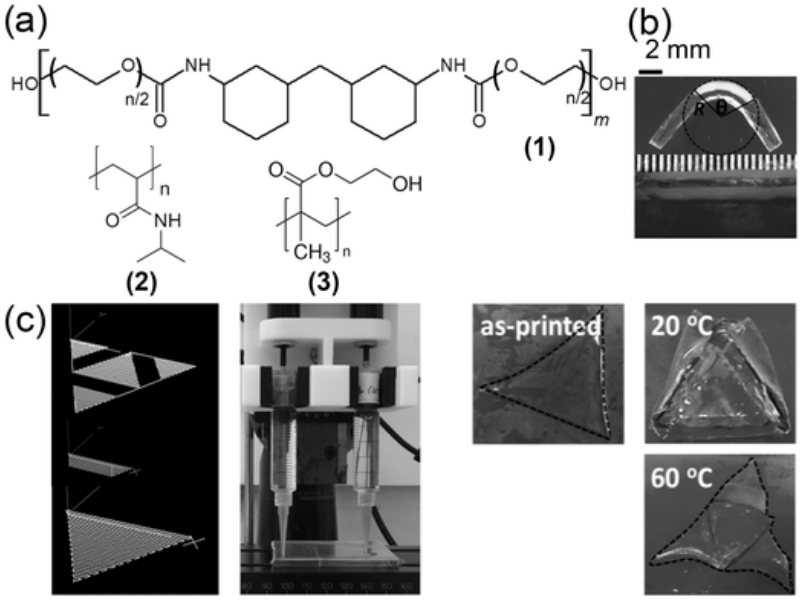

Figure A.1: Extrusion printable inks were prepared with the components shown in (a): polyether-based linear polyurethane (1), poly(NIPAM) (2), and poly(HEMA) (3). b) Hydrogel bilayer hinges are made from these inks, and their shape deformation is characterized. A model is developed to correlate R and θ to the physical and mechanical properties of the hydrogel components. c) From this model, print patterns are developed to print hydrogel objects that are capable of undergoing desired shape transitions at different environmental conditions. The broken lines are to highlight the edge of the hydrogels.

inks. For swelling tests and mechanical properties evaluation, hybrid hydrogels were prepared by UV irradiation of various ink formulations for 4 h, and then kept in water to reach equilibrium. The swelling ratios were not strongly affected by the mass ratio of PEO-PU to HEMA or nIPAAm monomer, over the range investigated. Based on this observation, the final mass ratio of PEO-PU to HEMA or nIPAAm monomer was fixed at 1: 1.

The swelling of the hybrid hydrogels was mainly controlled by the type of PEO-PU (Figure A.2). Longer polyether segment length resulted in higher water uptake. For the hydrogel films made of PEO_{70}-PU, PEO_{12}-PU, PEO_{10}-PU, and PEO_5-PU, the swelling ratio was 10.0 ± 0.2, 2.5 ± 0.1, 2.0 ± 0.1, and 1.4 ± 0.1, respectively. p-nIPAAm hydrogel, made under identical conditions except with no PEO-PU component in the formulation, had a swelling ratio of 9.6 ± 0.2 at 20 °C. The swelling ratio of resulting p-nIPAAm-based hydrogels equilibrated at 20 °C was between that of their constituent components and ranged from 9.1 ± 0.1 to 2.5 ± 0.2. The

swelling ratio of p-HEMA-based PEO_5-PU hydrogels was 1.9 ± 0.2, which was similar to that of pure p-HEMA hydrogel (1.9 ± 0.1) and the PEO_{10}-PU hydrogel (2.0 ± 0.1). As expected, p-nIPAAm-based hydrogels were temperature sensitive while p-HEMA-based hydrogels did not exhibit any response to a change in temperature between 20 and 60 °C (Figure A.2). By increasing the tem- perature to 60 °C, or well above the LCST, the swelling ratio of poly(NIPAM)-based hydrogels significantly decreased by up to 380 % relative to the swelling ratio at 20 °C. The observation demonstrates that the p-nIPAAm chains retain their phase transition behavior in the presence of PEO-PU chains. The differential scanning calorimetry (DSC) data confirmed the occurrence of a transition point for all p-nIPAAm-based hydrogels (Figure B.3, Supporting Information). This transition point was 31.9 °C for hybrid hydrogels containing PEO_{70}-PU and a gradual increase in the LCST was noticed as the length of polyether segment in the PEO-PU component decreased. For p-nIPAAm-based PEO5-PU, the transition point was 35.8 °C. These changes in the swelling ratio of p-nIPAAm-based hydrogels were reversible and corresponded to 24-55 % linear dimensional change.

The mechanical properties of the hybrid hydrogels were characterized in compression and tension to evaluate their performance in possible load-bearing applications (for full details see the Supporting Information). All tests were carried out at temperatures well below and well above the transition point of p-nIPAAm-based hydrogels (*i.e.*, at 20 and 60 °C). No significant difference was noticed in the mechanical properties of poly(HEMA)-based hydrogels when tested at 20 and 60 °C. The mechanical performance of all hybrid hydrogels was completely dependent on the nature of PEO-PU and their stiffness increased as swelling ratio decreased (Figure A.3).

In general, the mechanical properties of the hybrid hydrogels were found to be similar to those of other tough gels (Figures B.3 and B.4, Supporting Information) [39]. The hybrid hydrogels could be repeatedly loaded and unloaded to a maximum compressive strain of ≈ 60 % with little noticeable network damage and resembled

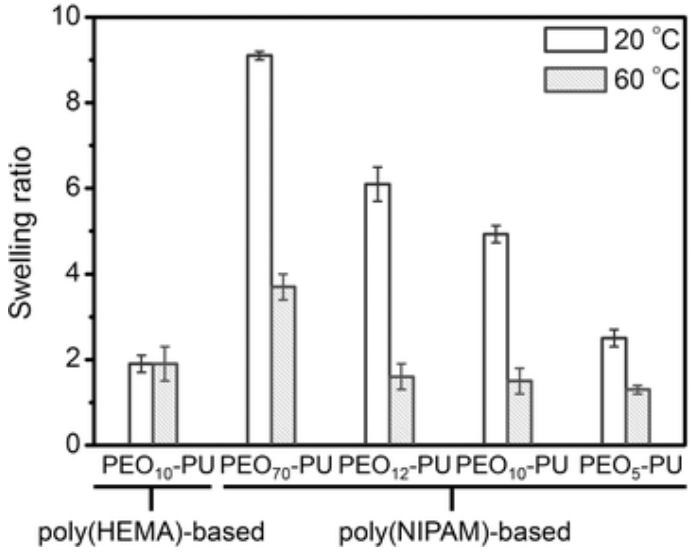

Figure A.2: Equilibrium swelling ratios of various poly(HEMA)- and poly(NIPAM)-based hybrid hydrogels at 20 and 60 °C.

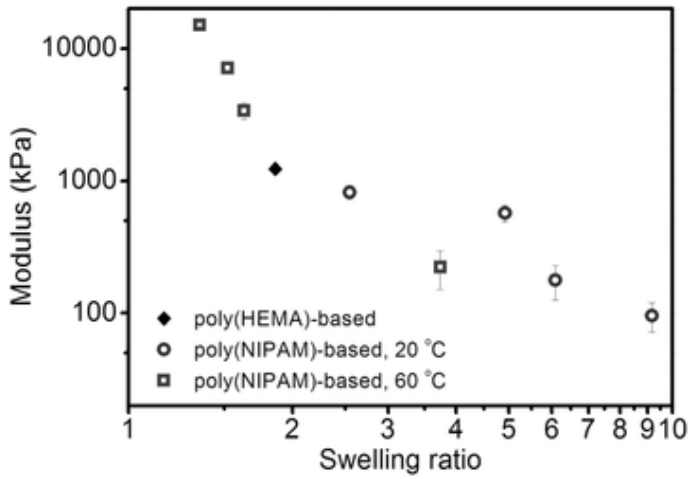

Figure A.3: Modulus of various poly(HEMA)- and poly(NIPAM)based hybrid hydrogels at 20 and 60 °C

the behaviour of thermoplastic polyurethanes [40]. Some hysteresis was evident in a single load/unload cycle, but the subsequent loading curve was very close to that of the previous cycle indicating immediate and near complete network recovery upon unloading (Figure B.5, Supporting Information). In contrast, double network hydrogels show permanent network damage during a loading/unloading cycle such that the subsequent loading curve follows the previous unloading curve. Hybrid gels made from interpenetrating covalently and ionically crosslinked networks show almost complete damage recovery, but require a lengthy recovery period at zero load. The absence of permanent network damage in repeated loading and unloading cycles demonstrated here for the p-HEMA- or p-nIPAAm-based PEO-PU hydrogels is very useful for applications where multiple loading patterns may be applied.

A.2.2 Model Evaluation

An analytical model is presented where the principal mode of shape morphing from fl at to a complex 3D structure is assumed to be bending. Therefore, by knowing the radius of curvature (R) and bending angle (Θ) for each bending hinge, it is possible to predict the final shape after stimulation. From a practical point of view, both R and Θ are known values and are determined from the desired final 3D structure. What is needed, however, is to determine which materials should be selected and what parameters should be assigned to the fabrication process to create a hinge capable of bending to the desired position. To establish a correlation between materials properties, fabrication parameters, and radius of curvature and bending angle, we started with an approach similar to that used for bending of metal bilayers with different expansion ratios [41]. A similar method was successfully employed to study the bending curvature of electrospun p-nIPAAm films on a solid substrate [42]. The bending curvature (κ) of a bilayer is determined as a function of its overall thickness (h), and the stiffness and thickness ratios of the two components (m and n, respectively)

$$\kappa = \frac{1}{R} = \frac{6\Delta\lambda(1+m)^2}{h\left[3(1+m^2)+(1+mn)(m^2+\frac{1}{mn})\right]} \tag{A.1}$$

where $m = h_1/h_2$ and $n = E_1/E_2$. E_1 and E_2 are the moduli of layers 1 and 2, while h_1 and h_2 are the thicknesses of the layers 1 and 2. The contribution from the anisotropic longitudinal expansion to the bending of the bilayer is through $\Delta\lambda$ in Equation A.1, where $\Delta\lambda = \lambda_1 - \lambda_2$, and λ_1 and λ_2 are the linear expansion ratios of each layer when separated. Equation A.1 is only valid for elastic deformations and is sensitive to expansion inhomogeneity and the overall thickness of the bilayers. We applied Equation A.1 to hydrogel bilayers made of two hybrid hydrogels with different swelling ratios. The hydrogels in each layer had identical dry polymer concentration and dry thickness since all ink formulations used to prepare the bilayers had the same solid content. Thus, m can be expressed as the ratio of hydrogels' linear swelling expansion ratios with respect to their dry dimensions

$$m = \frac{\lambda_1}{\lambda_2} \tag{A.2}$$

Assuming the hydrogel swell isotropically, λ_1 and λ_2 are the cubic root of their swelling ratios. In addition, from linear elasticity theory, the modulus of a swollen network (E) is determined by the linear expansion ratio of that hydrogel after swelling (λ), and the modulus of its dry network (E_0) : $E \approx E_0\lambda^{-1}$ [43]. For two hydrogels in equilibrium, the parameter n from Equation A.1 is

$$n \approx \frac{E_{0,1}}{E_{0,2}}\frac{\lambda_2}{\lambda_1} \tag{A.3}$$

In addition, the equilibrium swelling ratio of a polymer network can be related to the network structure, which in turn determines the modulus of the dry network. From thermodynamics of swollen networks, this correlation is $E_0 \approx \lambda^{-\nu}$, where ν is 5.25 for highly swollen networks and 8 for less swollen networks [44]. Hence, $E \approx \lambda^{-\alpha}$ regardless of E_0 and Equation A.3 can be rewritten as

$$n \approx \left(\frac{\lambda_2}{\lambda_1}\right)^{\alpha} \tag{A.4}$$

where $\alpha = \nu+1$ and is assumed to be constant for all hydrogels used in this study. Experimentally, an approximate correlation was found to exist between the Young's moduli of the swollen hybrid hydrogels (E) and their respective linear expansion ratios (λ), as shown in Figure B.7 (Supporting Information) with α of 6.9. Inserting Equations A.2 and A.4 in Equation A.1, the bending curvature of a hydrogel hinge can be defined by knowledge only of the hydrogel components' linear expansion ratios (material parameters: α, λ_1 and $\lambda_2, m = \frac{\lambda_1}{\lambda_2}$) and the thickness of the hinge (fabrication parameter: h)

$$\kappa = \frac{6(\lambda_1 - \lambda_2)(1+m)^2}{h\left[3(1+m^2) + (1+m^{1-\alpha})(m^2+m^{\alpha-1})\right]} \tag{A.5}$$

Equation A.5 is then used to estimate the bending angle (Θ) from the facing intercepted arc. The central angle of a circle is related to the bending curvature (κ) and the intercepted arc length (L) by

$$\Theta = \kappa L \tag{A.6}$$

where L is a fabrication parameter representing the length of the top layer and κ is calculated from Equation A.5. Equations A.5 and A.6 suggest that by selecting a pair of hydrogels with given swelling ratios (λ_1^3 and λ_2^3) and assigning the right fabrication parameters (h and L), the resulting hinge will bend with the desired curvature and bending angle.

To evaluate Equations A.5 and A.6, we made a range of hydrogel hinges from p-HEMA-based PEO_{10}-PU as the base layer and p-nIPAAm-based hydrogels with different types of PEO-PU forming the temperature sensitive top layer. A multi-step casting and polymerization process was used to make the hinges (Figure B.8, Supporting Information). The length of the p-nIPAAm-based hydrogels and the overall thickness of the hinge were also considered as fabrication parameters (Fig-

ure A.4a). The hinges remained flat in their dry state, as both materials had the same swelling ratios: $\lambda_1 = \lambda_2 = 1$ (Figure A.4b). By placing the dry hinges in water at 20 °C, however, each component began to swell differently. This disproportional swelling of the two hydrogel layers generated bending of the hinges as shown in Figure A.3c. Furthermore, by raising the temperature up to 60 °C, the swelling ratio of the p-nIPAAm-based hydrogels decreased until a new equilibrium shape was reached (Figure A.4d).

The radius of curvature and bending angle were optically measured for different pairs of hydrogels made with varying length and thickness. In Figure A.5a, the bending curvature is plotted against the ratio of linear expansion of top layer to bottom layer: λ_1/λ_2 (highlighted as layer 1 and layer 2 in Figure A.5a). As expected, no bending was noticed when the bilayers were made of p-HEMA-based PEO_{10}-PU hydrogels as both the top and bottom layers (filled diamond in Figure A.5a). For all the other bilayers with p-nIPAAm-based hydrogels as the top layer, bending was observed as shown by open symbols in Figure A.5a. The circles represent the bilayers at 20 °C and the squares represent the same bilayers at 60 °C. The model in Equation A.5 was able to predict the bending curvatures extremely well with only three input parameters: the linear extension ratios for the two hydrogel materials, which are material parameters, and the thickness of the bilayers, which is a fabrication parameter. The model also successfully predicts the direction of bending, with negative curvatures occurring when the ratio of linear extensions was less than one. In Figure A.5b, the bending angles predicted by Equation A.6 are plotted against measured bending angles for hydrogel bilayers. Two material parameters (linear extension ratios) and two fabrication parameters (thickness of bilayer and length of top layer) were needed in Equation A.6 to predict the bending angles. Again, very good agreement was observed between predicted and measured values.

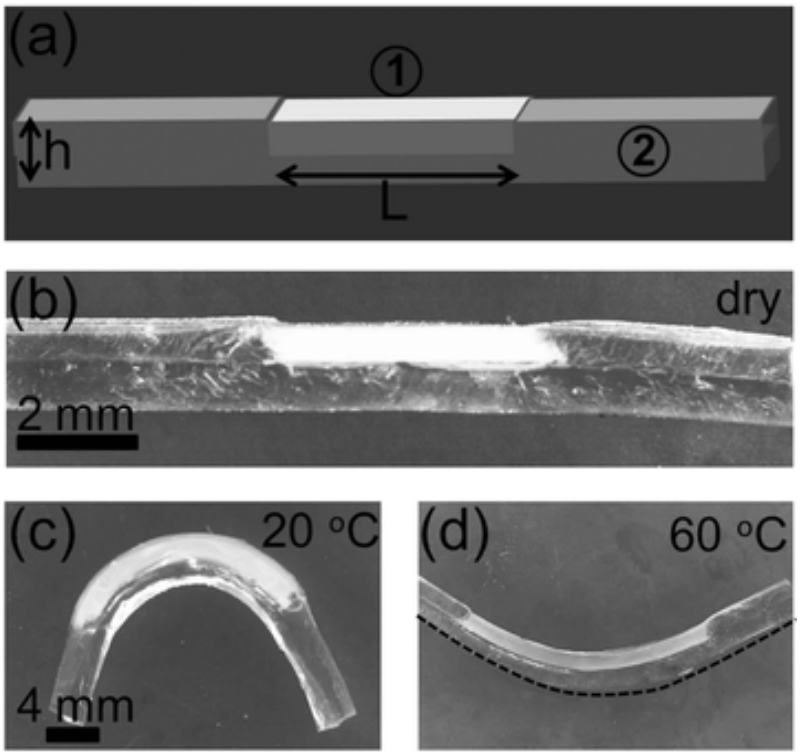

Figure A.4: Hydrogel bilayers: a) Schematic representation of a hydrogel hinge, made of the temperature-sensitive poly(NIPAM)based top layer (1) and the poly(HEMA)-based PEO_{10}-PU bottom layer (2). The fabrication parameters are h and L, as shown. Photograph of a hydrogel hinge shown in the dry state and b) the same hydrogel hinge when fully swollen c) at 20 °C and d) 60 °C. The broken line is to highlight the edge of the hydrogel.

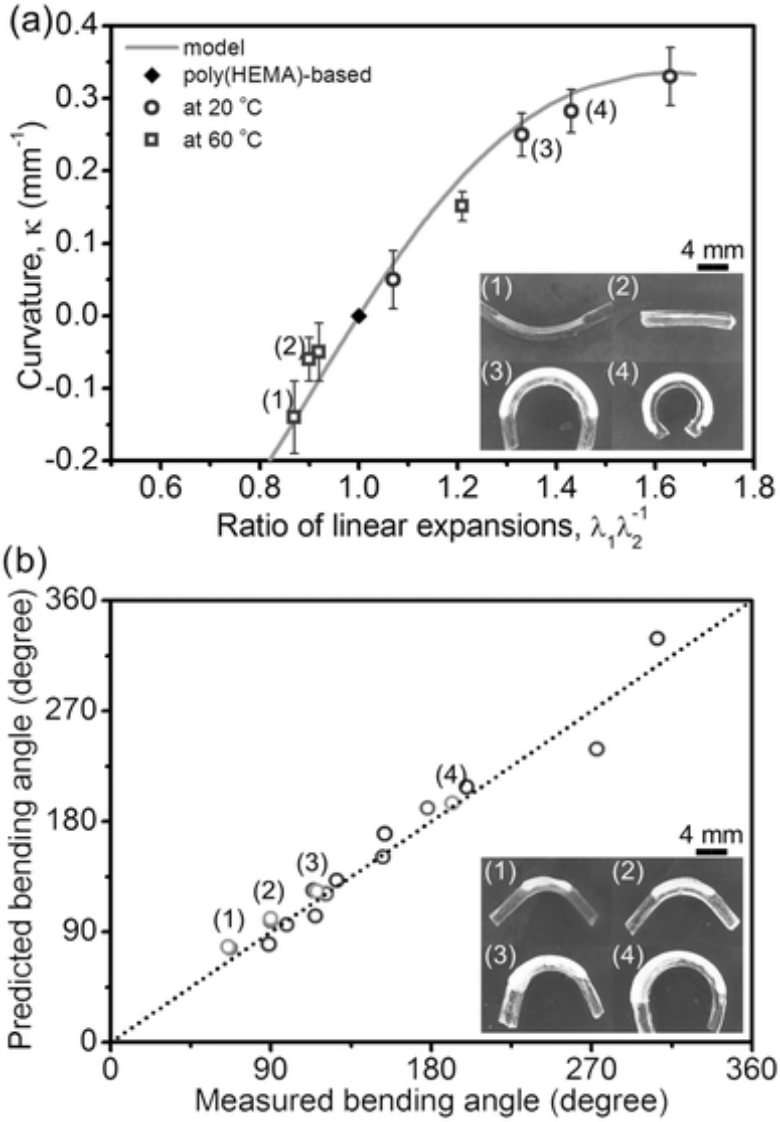

Figure A.5: Bending characteristics of hydrogel bilayers estimating only from the hydrogels' swelling ratios (λ^3) and fabrication parameters (thickness of bilayer and length of top layer): a) bending curvature as a function of ratio of linear expansion of top layer to bottom layer: λ_1/λ_2, and *b*) predicted bending angles against measured values. Photographs of samples are shown as numbered.

A.2.3 Hydrogels 3D printing

The shape predictions of Equations A.5 and A.6 were next used as a guide for printing hybrid hydrogel structures capable of transforming from one state to another upon hydration and temperature change. A custom-built extrusion printer capable of printing two different types of materials at different extrusion rates was used to prepare the designed structures. The ink deposition was made by two independently controlled miniature linear actuators mounted on the top of a small computer numerical control (CNC) milling stage. A spot UV lamp was used adjacent to the printer to illuminate the printed objects with a 300-450 nm UV light.

Prior to printing, the rheological properties of the inks were characterized using a rheometer with a cone-plate configuration. The ink rheological properties were mainly dictated by the long-chain PEO-PU content. The storage and loss moduli (G' and G'', respectively) both increased with increasing PEO-PU concentration. Also, G' and G'' had a power-law relationship with angular velocity (ω) in which $G' \approx \omega^{1.7-1.9}$ and $G'' \approx \omega^{0.9-1.1}$, resembling the expected viscoelastic behaviour of semi-dilute to concentrated polymer solutions. Zero shear viscosity (η_0) was also found to increase with PEO-PU concentration (c) following a power-law trend: $\eta_0 \approx c^{2.2-3.2}$, as expected for concentrated polymer solutions [45]. In general, inks with higher storage modulus were easier to print as they maintained their printed structure prior to and during the UV curing. However, higher pressures were needed to extrude these more viscous inks while retaining the same printing rate, which limited the maximum concentration of PEO-PU in the ink formulation that could be successfully extruded with our system. The Hagen-Poiseuille equation for laminar flow of a viscous ink with a viscosity of η passing through a cylindrical nozzle with a radius of r and length of l states [46]

$$u = \frac{r^2 \Delta P}{8 \eta l} \tag{A.7}$$

where u is the linear flow rate and ΔP is the pressure drop. For a stable printing process, the print speed is the same as the flow rate at which the ink exits

the nozzle. Thus, to maintain the print speed at a required rate, the applied pressure increases linearly with ink viscosity. The maximum pressure applied by the linear actuators in our set up was 94 kPa for a 5 mL syringe. Therefore, the concentration of PEO-PU in the ink formulation was adjusted to keep the ink viscosity below the maximum printable viscosity for a printing speed of 44.6 mm^3 min^{-1}. Using a CNC control program, all-hydrogel structures were printed from the HEMA-based PEO_{10}-PU ink as the nonactive material and the nIPAAm-based PEO_{10}-PU as the temperature sensitive material. The controllable printing parameters were the print thickness and the length of the printed active material. Equations A.5 and A.6 were used to define these printing parameters to achieve desired bending characteristics. The only material specification needed here was the linear expansion of crosslinked hybrid hydrogels after free swelling at 20 and 60 °C (Figure A.2).

Figure A.6 shows examples of a printed cubic box. The nIPAAm-based ink was printed first, and then partially UV cured for 10 min after which the HEMA-based ink was printed (Figure A.6a). After printing, samples were UV irradiated for another 40 min. The final printed objects had a total thickness of 1.75 mm and were completely flat (Figure A.6b). However, when brought in contact with water (20 °C), the p-nIPAAm-based PEO_{10}-PU hydrogel swelled more than the structural p-HEMA-based PEO_{10}-PU component. Consequently, the printed objects began to fold to their new hydrated states as defined by the model. Furthermore, the objects responded to the temperature raise as swelling ratio of p-nIPAAm-based PEO_{10}-PU collapsed at elevated temperatures, forcing the closed box to open up and transform back into a flat structure. This process was reversible and no delamination was observed at the interface of p-HEMA-based and p-nIPAAm-based hydrogels. As a comparison, a cubic box was also created from the same inks using a multistep molding and polymerization process (Figure B.9, Supporting Information). An equivalent shape transformation was demonstrated. We observed that, in general, Equations A.5 and A.6 were applicable to both fabrication methods. The main difference between moulding and 3D printing was the ease of manufacturing.

The 3D printing allowed us to fabricate the objects in one printing session, while the moulding/polymerization was essentially a multistep processing technique. Also, any change in the dimension or shape of object required a new mould design, whereas in 3D printing these modifications could be addressed by altering the G-code that controlled the moving stage. Moreover, human involvement could be minimized in 3D printing, which was in contrast to the multistep casting/polymerization, where the user had to oversee the process.

The incorporation of linear polymer chains capable of physical crosslinking (*i.e.*, PEO-PU) into the inks along with UV-curable monomers (*i.e.*, HEMA or nIPAAm) allowed the decoupling of inks' rheological behaviour from the gels' final mechanical and physical properties. The HEMA and nIPAAm monomers are both commonly used in biomedical applications; however, they could easily be replaced with any other hydrophilic monomer. Hence, this concept can be adapted to fabricate a variety of inks in which a variety of functional monomers can be used. Shape-morphing structures made by 3D printing of such functional hydrogels could potentially be used in biomedical applications where spatial constraints limit the initial shape of objects to flat surfaces only. After placed in their final position, these flat structures can later transform to their final 3D shape upon stimulation.

A.3 Conclusions

This study has shown that versatile 3D printable inks can be attained by incorporating linear PEO-PU polymers into UV curable monomer solution. A novel aspect of the inks proposed here is that the rheological properties of the ink prior to gelation are decoupled from the gelation process by using linear polymer chains capable of physical crosslinking. The rheological properties of the inks can be tailored by adjusting the amount of PEO-PU in the inks to fulfil the 3D printing requirements of the available extrusion-based printer. The resulting hybrid hydrogels were temperature sensitive with excellent mechanical proper- ties with almost full and immediate recovery after loading. It was also demonstrated that 3D shape transformation can

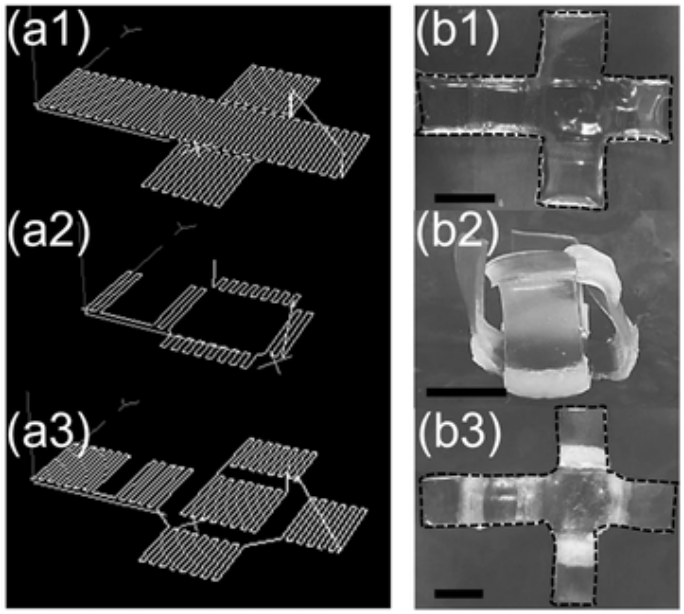

Figure A.6: The printing pattern used and the resulting print at various temperatures for a cubic box. Panels in (a) show the patterns for the print head movement to construct: a1) the base, a2) the actuating parts, a3) and their surrounding matrix. A series of images of the printed box are presented, picturing: b1) box as printed, b2) the same printed box at swollen state at room temperature and b3) its thermal response at 60 °C. The scale bar is 1 cm. The broken lines are to highlight the edge of the hydrogels.

be triggered by both hydration and temperature variation. The shape change is controlled by the material properties and fabrication parameters. A simple model was used to establish a correlation between material and fabrication parameters and the 3D structure of the hybrid hydrogels. This model was used as a guide to fabricate all-hydrogel hybrid structures capable of controlled and reversible shape transformation in response to hydration and heat.

A.4 Experimental Section

A.4.1 Ink Formulation

The ink formulations contained long polymer chains of PEO-PU, AKG as UV initiator, MBAAm as crosslinking agent, and HEMA or nIPAAm as monomers, all dissolved in ethanol. PEO-PU was purchased from AdvanSource Biomaterials. All other chemicals were purchased from Sigma-Aldrich and used as received. The ratio

of PEO-PU to monomer in the ink formulation was 1: 1, with the overall concentration of PEO-PU and monomer was 50 w/w %. The amount of UV initiator and crosslinking agent was adjusted based on monomer content at 2 mol% to reach the gelation point after 1 min of UV irradiation. The mixtures were stirred at 60 °C for 2 d to dissolve all components and achieve clear inks.

A.4.2 Ink Characterisation

Rheological properties of the inks were characterized using a TA AR-G2 rheometer with a cone-plate head configuration (1 , 40 mm with 30 μm gap). All measurements were performed under control temperature of 20 °C with solvent trap installed to prevent the loss of ethanol. Viscosity was measured under steady state condition with shear rate ranging from 0.01 to 100 s^{-1}. Viscoelastic properties of the inks were also characterized with frequency sweep from 0.01 to 100 Hz under constant strain of 0.1%. The effect of PEO-PU concentration on the rheological properties of the inks was explored by preparing inks with constant monomer content but varying PEO-PU concentration.

A.4.3 Hydrogel Preparation

To prepare hydrogel films for tensile and swelling testing, inks were injected between two glass slides separated with a 1 mm silicon gasket. Cylindrical hydrogels were also prepared for compression testing, by injecting the inks in a cylindrical mould. UV polymerization and crosslinking was performed by UV irradiation (300 nm) for 4 h using a photochemical reactor (Rayonet RPR-200). After polymerization, gels were removed from the molds and placed under constant flow of air to remove ethanol (20 °C, for 2 d). Dry hydrogels were immersed in Milli-Q water for 3 d to reach equilibrium. Fully swollen hydrogels equilibrated in water were used for further swelling ratio measurement and mechanical testing.

A.4.4 Hydrogel Characterisation

Differential scanning calorimetry (DSC) was employed to evaluate the phase transition behavior of water swollen p-nIPAAm-based PEO-PU hydrogels. Experiments were carried out on patted dry samples placed in aluminium pans, using a TA Q-100 DSC machine operating under constant flow of nitrogen gas. The scanning rate was fixed at 5 °C min^{-1} for heat–cool–heat cycles between 5 and 60 °C. Mechanical measurements were performed with a Shimadzu EZ-L universal tester equipped with a 500 N load cell. Hydrogel films were used for tensile testing and were cut into ribbons (5 mm width x 20 mm length, 10 mm gauge length), while hydrogel cylinders were used for compression testing (10 mm diameter x 10 mm height). The crosshead speed in compression and tensile testing was 2 mm min^{-1}. Compression cycling tests were performed on cylindrical hybrid hydrogels at a constant crosshead speed of 2 mm min^{-1}. After each load–unload cycle the maximum stress reachable at the end of next loading cycle was increased. The stress relaxation experiments were also conducted on cylindrical hybrid hydrogels in compression mode. Samples were loaded under constant crosshead speed of 2 mm min^{-1} until a 1 MPa stress was achieved. After this point the strain remained constant and stress decay was monitored against time. For all mechanical testing that was performed in compression mode, the cylindrical samples were fully immersed in water equilibrated at the desired temperature. For samples undergoing tensile testing, water at desired temperature was constantly applied on the surface of samples with a glass pipette. Swelling ratio of hydrogel films was calculated as the volume ratio of fully swollen hydrogels to fully dried samples, by measuring their dimensions at each state.

A.4.5 Multi-Step Hydrogel Structures Fabrication

Hydrogel hinges were made by a multistep molding process (Figure B.6, Supporting Information). HEMA-based PEO_10-PU ink was used as the nonactive component, and nIPAAm-based PEO-PU inks were used as the temperature sensitive component. First, HEMA-based ink was injected between two glass slides separated with a

0.8 mm silicon spacer, and then UV irradiated for 30 min. This process was repeated for the second layer of HEMA-based ink, with a second spacer added to further separate the glass slides. At this stage, additional spacers were also positioned on top of the hydrogel base that was made in the previous step. After the second round of UV irradiation, these spacers were removed and the empty space was filled with the nIPAAm-based inks, followed by the third round of UV irradiation. More complex objects such as an unfolded box were created following a similar method (Figure B.9, Supporting Information).

A.4.6 Hydrogel 3D Printing

The extrusion printer used for 3D printing of hydrogel inks consisted of two linear actuators (Zaber T-NA08A50-S-KT03U) mounted on a Sherline 8020 CNC milling stage (Figure B.10, Supporting Information). The linear actuators were placed parallel to each other, under which was a plastic holding to house two 5 mL syringes. Inks were loaded in these two syringes, and their plungers were attached to the linear actuators. By controlling the speed of actuators linear movement it was possible to adjust the extrusion rate from each syringe independently. A customized program was developed to control the actuators (C#, Visual Studio 12.0), while the CNC stage was controlled in the x, y, and z directions with Linux CNC EMC2 software. A Dymax BlueWave spot light emitting UV light in the range of 300–450 nm was stationed next to the printer to UV cure the printed objects. To ensure uniform curing, samples were cured in an aluminium lined UV opaque box, and the spot light was shone onto a curved surface to diffuse the light evenly. The total UV irradiation time was adjusted to expose the printed structures to the same amount of irradiation energy as the samples prepared for mechanical testing in the Rayonet photochemical reactor.

A.5 Acknowledgements

The authors wish to thank the Australian Institute of Innovative Materials for funding (Small Grant 268381012). The authors wish to acknowledge the support of the Australian National Fabrication Facility, Materials Node. S.N. is grateful to the Global Challenges program of the University of Wollongong for their support. R.G. would like to acknowledge the Australian Research Council for partial support under the Australian Laurate Fellowship scheme (FL110100196). The authors wish to additionally thank Dr. Patricia Hayes and Prof. Paul Calvert for insightful discussions, and Prof. Marc in het Panhuis for use of the 3D printing facilities.

3D/4D Printing Hydrogel Composites: A Pathway to Functional Devices

The past few years have seen the introduction of a number of 3D and 4D printing techniques used to process tough hydrogel materials. The use of 'colour' 3D printing technology where multiple inks are used in the one print allows for the production of composite materials and structures that can further enhance the mechanical performance of the printed hydrogel. This article reviews a number of 3D and 4D printing techniques for fabricating functional hydrogel based devices

The following is a stylistically edited version of the published paper:

S. E. Bakarich, R. Gorkin, S. Naficy, R. Gately, M. in het Panhuis, and G. M. Spinks, "3D/4D printing hydrogel composites: A pathway to functional devices," *MRS Advances*, vol. 1, no. 08, pp. 521–526, 08 Dec. 2015

A.6 Introduction

3D printing is an additive manufacturing technology that has been used to process hydrogel materials for tissue engineering applications. A major limitation in the use of hydrogels has been their poor mechanical performance but the last two decades has seen the development of a range of 'tough' hydrogels [48]. These developments have been followed by the introduction of new printing techniques that can form tough hydrogels into complex structures [49, 50]. The mechanical properties of these printed tough hydrogels tend to be inferior to those prepared using casting under optimal lab conditions. Table A.1 compares the mechanical parameters of alginate (Alg)/p-AAm ionic covalent entanglement (ICE) gels when cast and printed.

Table A.1: Summary of the mechanical properties of cast Alg/p-AAm ICE gels (data reproduced from [51]) and printed Alg/p-AAm ICE gels (data reproduced from [49])[a]

	E [kPa]	σ_T[kPa]	ϵ_f [%]	U [MJ m^{-3}]	Q
Cast	29	156	2300	≈ 2.5	7.1
Printed	66 ± 5	170 ± 30	300 ± 20	0.26 ± 0.01	6.7

The formation of composite materials is an established means of enhancing the mechanical properties of constituent materials. 'Colour' or multi-material 3D printers can print stronger reinforcing materials alongside tough hydrogel inks to form composites. In this article we demonstrate how 3D printing techniques can be adapted to fabricate functional hydrogel based devices.

[a] E is the elastic modulus, σ_T is the tensile strength, ϵ_f is the failure strain, U is the work of extension and Q is the swelling ratio

A.7 Experimental

A.7.1 Materials

All materials were used as-received and all solutions were prepared using Milli-Q water (resistivity = 18.2 $M\Omega$ cm). AKG photo-initiator was purchased from Fluka (Australia). AAm solution (40 %, for electrophoresis, sterile-filtered), alganic acid sodium salt (from brown algae with Brookfield viscosity 2 % in H_2O at 25 °C of 250 mPa s), calcium chloride (minimum 93.0 % granular anhydrous), ethylene glycol (rheology modifier), nIPAAm and MBAAm crosslinker were purchased from Sigma Aldrich (Australia). A commercial epoxy based UV-curable adhesive Emax 904 Gel-SC (Emax) was purchased from Ellsworth Adhesives (Australia).

A.7.2 Hydrogel Ink Formulations

An alginate ink for printing dissolvable support structures was prepared by mixing 3.75 mL of ethylene glycol in 11.25 mL of a 0.1 M calcium chloride stock solution. A spatula was then used to dissolve 450 mg of alganic sodium salt into the printing solution.

An Alg/p-AAm ICE gel ink was prepared by dissolving 4.50 mL of AAm, 38.7 mg of MBAAm, 36.9 mg of AKG and 3.75 mL of ethylene glycol in 6.75 mL of a 0.01 M calcium chloride stock solution. The ethylene glycol was used as a non-volatile co-solvent with the volume ratio of ethylene glycol to water fixed at 1:2.5. A spatula was then used to dissolve 450 mg of alganic sodium salt into the printing solution.

An Alg/nIPAAm ICE gel ink was prepared by dissolving 3 g of nIPAAm, 15 mg of MBAAm and 90 mg of AKG in 15 mL of a 0.01 M calcium chloride stock solution. A spatula was then used to dissolve 450 mg of alganic sodium salt into the printing solution.

A.7.3 3D Printing

Fibre reinforced hydrogels, adhesion test samples and a smart valve were all fabricated with an EnvisionTEC 3D-Bioplotter system that was coupled with a commercial UV-curing system. The patterned inks were cured with a Dymax BlueWave 75 Rev 2.0 UV Light Curing Spot Lamp System using a 19+ W cm^{-2} UV source with a 1 meter light guide. Digital models of tensile specimens and the multi-component valve were prepared with computer-aided design (CAD) software (Solidworks). The composite materials were designed by creating an assembly of separate parts. EnvisionTEC software was used to slice the digital models into a stack of two dimensional layers (250 μm thick) to determine the print path. Material files and internal structures were then added to each part within the assembly.

The extrusion inks were loaded into the 3D-Bioplotter in separate pressurized syringe barrels which were positioned into the temperature controlled print heads. Each barrel was fitted with a 23 gauge syringe tip (diameter 0.337 mm) and maintained at stable temperature of (25 °C for the Alg/p-AAm ICE gel and Emax inks and 10 °C for Alg/nIPAAm ICE gel ink) during printing. A pressure between 0.5 and 1 bar was used to extrude the inks and a head speed between 5 and 20 mm s^{-1} was used to pattern them. The inks were printed with a 0.5 mm resolution onto a poly(pyropylene) sheet when printing with the Alg/p-AAm ICE gel ink or a glass sheet cooled to 10 °C when printing the Alg/NIp-AAm ICE gel ink. The UV light was passed over each layer of patterned ink for 50 s and 200 s for the final layer. A spatula was used to remove any of the alginate based ink for printing sacrificial support structures once the print was finished. Finally the printed ICE hydrogels were immersed in 0.1M calcium chloride (72 hr) to fully crosslink the alginate.

Particulate reinforced hydrogels and gradient structures were fabricated with a custom built 3D printer. The 3D printer was built around a Sherline 8020 CNC milling stage and a novel syringe controlled deposition system made up of two Zaber T-LA60A-KT03 Miniature Linear Actuators mounted to the CNC gantry. Plastic tubing and a Y-adaptor was used to direct the flow from two syringes into a single

stream. A disposable static chaotic mixer with 12 mixing elements (Nordson EFD) was added below the Y-adaptor to insure blending of the two streams. A custom 3D-printed nozzle was designed to extrude a flat ribbon of material having a rectangular shaped outlet with dimensions 1.5 mm by 15 mm. An Opsytec Dr. Gröble 365 nm UV-LED smart light source was attached near the deposition system so that its illuminated area followed the print head to cure dispensed ink.

The extrusion inks were loaded into the 3D printer in separate syringe barrels. The Emax volume fraction was controlled using custom software (developed in C#, using Visual Studio 12.0) that allowed the two inks to be dispensed in different ratios by adjusting the speed of the two linear actuators. The net flow rate of combined material out of the nozzle had to remain constant to maintain consistency; thus the individual flow rates of the two materials from each barrel were adjusted relative to each other throughout the print. For gradient printing the flow rate of the two materials had to be linearly ramped; the speed of depression in one barrel was decreased from 100 % to 0 % while simultaneously the other barrel experienced a speed increase from 0 % to 100 %. The combined total rate of extension of the two linear actuators was set at a constant 180 μm s^{-1} when the milling stage was moved with a speed of 80 mm min^{-1}. The UV light using 100 % intensity followed the extrusion nozzle to set the blended composite structure by partially curing the two inks.

A processing scheme was applied to the composite ribbons after printing to improve their mechanical properties. The Dymax BlueWave 75 Rev 2.0 UV Light Curing Spot Lamp System using a 19+ W cm^{-2} UV source with a 1 metre light guide was used to complete the curing process. Each 30 mm length of ribbon was exposed to the spot of UV irradiation for 30 s. The composites were then immersed in 0.1 M aqueous calcium chloride solution for 72 hr to fully crosslink the alginate polymer network.

A.7.4 Adhesion Testing

An adhesion test was performed on a Shimadzu EZ-L Universal Mechanical Tester. An adhesion test sample was printed with Emax ends and a band of the Alg/p-AAm ICE gel. The adhesion sample was extended at a rate of 10 mm min^{-1} in the direction perpendicular to the Alg/p-AAm ICE gel band until failure and the position of failure was noticed. Four repeat tests were performed on each material with errors estimated from one standard deviation.

A.8 Discussion

Emax 904 Gel-SC is a commercially available epoxy based UV-curable adhesive that has been identified as a suitable ink for printing composite structures with the Alg/p-AAm ICE gel ink. These two inks can be incorporated into the one printing process because they have similar rheological properties, are both cured by UV initiated free radical polymerization reaction and display strong adhesion. [5] Adhesion between materials is important when forming composites for transferring stresses from the matrix onto the reinforcing phase. Adhesion is also important when fabricating multi-component devices as interfaces can act as a point of weakness in the devices structure. Figure A.7a. shows a 3D printed Alg/p-AAm ICE gel and Emax adhesion test sample clamped to a universal mechanical tester. Figure A.7b. shows that the strained sample fails through the hydrogel band and not at the interface of the two materials. This demonstrates a strong adhesion between the Alg/p-AAm ICE gel and Emax when the two inks are cured simultaneously side by side.

Fibre reinforced hydrogels have been made with a method that uses digital modelling and a 'colour' 3D printer to pattern two inks within the one structure. The models are made up of an assembly of two parts, one for the matrix and one for the fibre reinforcement. Fibres are designed as long thin volumes of material. When printing the models a different ink is assigned to each part of the assembly. Figure A.7c. is an example CAD model of a fibre reinforced tensile specimen and

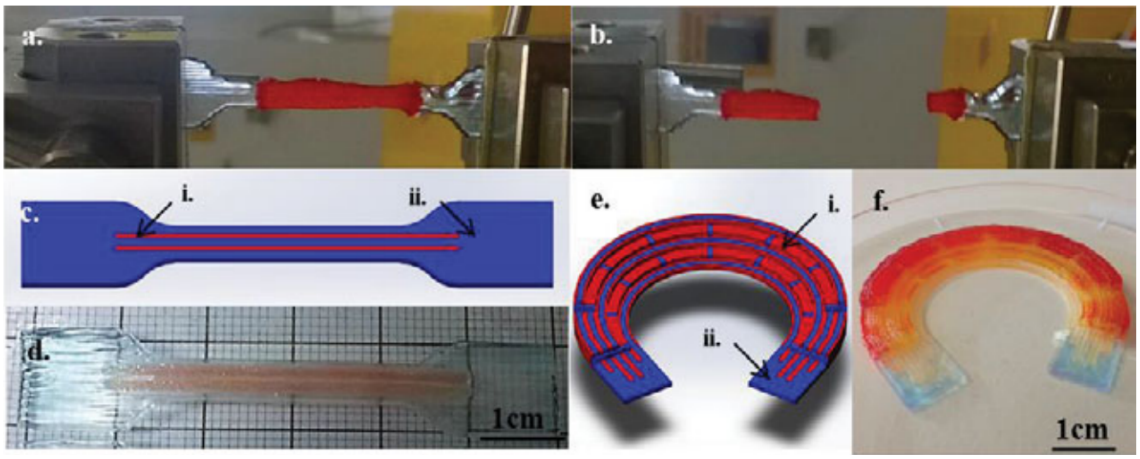

Figure A.7: Photographs of Alg/p-AAm ICE gel and Emax adhesion test sample (a.) before and (b.) after mechanical failure. (c.) CAD model and (d.) photograph of 3D printed fibre reinforced Alg/p-AAm ICE gel composite tensile specimen. Labels indicate components to be printed with (i.) Alg/p-AAm ICE hydrogel ink and (ii.) Emax. (e.) CAD model and (f.) photograph of 3D printed fibre reinforced Alg/p-AAm ICE gel composite artificial meniscus. Images were adapted with permission from [52]. Copyright (2014) American Chemical Society

Figure A.7d. is a photograph of the tensile specimen printed with the Alg/p-AAm ICE gel and Emax inks. The volume fractions of the printed materials can be altered by changing the number of fibers included in the CAD model. Tensile testing of the printed materials has shown that composites with higher volume fractions of Emax fibers display greater tensile strength and modulus [52]. The versatility of digital modeling enables these composites to be fabricated directly into complex shapes and useful structures. Figure A.7e. is a CAD model of an artificial meniscus and Figure A.7f. is a photograph of the artificial meniscus printed with the Alg/p-AAm ICE gel and Emax inks.

A novel extrusion based deposition system was used to print particulate reinforced hydrogels. The deposition system was designed with two digitally controlled syringe pumps that pushed the ink from two syringe barrels though a Y-adaptor into a single stream which flowed through a static mixer. The mixer ensured blending of the two inks before they were pushed out the extrusion nozzle. The Alg/p-AAm ICE gel and Emax inks are immiscible and phase separate when mixed together and so UV light was attached to the 3D printer so that the blended inks could be cured as soon as they were extruded to limit the phase separation. Figure A.8a. is

a macrosope image that shows the two phase structure of one these printed materials. Changing the extrusion rates of the two syringe pumps allowed for composites to be printed with various volume fractions of Emax. Mechanical characterisation showed that composites with low volume fractions of Emax (<50 %) behave like particulate reinforced composites. Custom software allowed for the extrusion rates of the two pumps to be ramped during the printing process to create gradients of material composition across the extruded ribbon. Figure A.8b. is a photograph of an artificial tendon containing two composition gradients that form a transition of modulus from one end to the other [35]. Figure A.8c. is a picture of the artificial tendon attached to a skeleton.

More functional hydrogel based devices can be fabricated with a 4D printing process that combines the digital modelling process used to print fibre reinforced hydrogels with a stimuli responsive hydrogel ink. 4D printing is an emerging technology for creating structures that change their shape on-demand over time. A stimuli responsive tough hydrogel ink was made by replacing the p-AAm component of the Alg/p-AAm ICE gel ink with PNIp-AAm. PNIp-AAm is a thermally sensitive hydrogel that exhibits reversible volume transition at a critical temperature (32-35 °C). Digital modelling allows for the design of structures that can harness this volume change in the same way that the skeleton harnesses the volume change of muscles to create movement. A smart valve that can open and close as a response to the temperature of the water flowing through the valve was printed to demonstrate the utility of this technique [53]. Figure A.9a. is a CAD model of the smart valve. Figure A.9b. is a photograph of the open smart valve after it had been exposed to a flow of 20 °C water and Figure A.9c. is a photograph of the closed smart valve after it had been exposed to a flow of 60 °C water.

A.9 Conclusions

We have introduced a number of 3D extrusion printing techniques used to make Alg/p-AAm ICE gel and Emax composite materials. The customization of 3D

Figure A.8: (a.) Macroscope image of a 3D printed particulate reinforced Alg/p-AAm ICE gel composite ribbon with an Emax volume fraction of 40 %. (b.) Photograph of an artificial tendon printed with Alg/p-AAm ICE gel and Emax gradient structures. (c.) Photograph of a 3D printed artificial tendon attached to a skeleton.

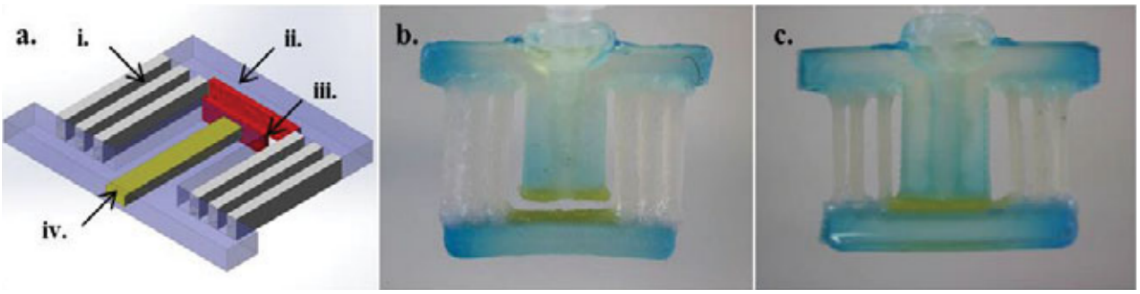

Figure A.9: (a.) CAD model of hydrogel valve. Labels indicate components to be printed with (i.) Alg/PNIp-AAm ICE hydrogel ink, (ii.) Emax, (iii.) Alg/p-AAm ICE hydrogel ink and (iv.) the alginate based ink for printing sacrificial support structures. Photographs of the 4D printed valve open (a.) when swollen in water at 20 °C and (c.) closed when swollen in water at 60 °C.

printers and writing of new software were important steps in the development of the new printing techniques. The different techniques allow for the formation of composites with multiple reinforcement morphologies. The development of these 'color' 3D and 4D printing techniques has provided a pathway to fabricate functional hydrogel based devices demonstrated by production of an artificial meniscus, artificial tendon and a smart valve.

3D Printing of Transparent and Conductive Heterogeneous Hydrogel-Elastomer Systems

A hydrogel-dielectric elastomer system, Poly-acrylamide and Polydimethylsiloxane, is adapted for extrusion printing for integrated device fabrication. A LiCl containing hydrogel printing ink is developed and printed onto treated PDMS with no visible signs of delamination and geometrically scaling resistance under moderate uniaxial tension and fatigue. We demonstrate a variety of designs including resistive strain gauge and ionic cable.

The following is a stylistically edited version of the published paper:

K. Tian, J. Bae, S. Bakarich, C. Yang, R. Gately, G. M. Spinks, M. in het Panhuis, Z. Suo, and J. Vlassak, "3d printing of transparent and conductive heterogeneous hydrogel-elastomer systems," *Adv. Mater.*, (*Currently under review*)

A.10 Introduction

Interest in stretchable electronics has grown significantly in recent years, driving a need for soft and stretchable materials that can sustain high strains and still fulfill their function in applications such as human wearable sensors for biomechanics studies and health monitoring [55–58], or feedback sensors in soft robotics [59–62]. Although many stretchable conductors exist, including liquid metals [63, 64], nanowires [65, 66], nanoribbons [67], and micro-cracked metals [68, 69], these materials have generally been unable to achieve high levels of optical transparency while maintaining high conductivities and stretchability; a feature that would enable their use in optogenetics [70] or allow optical imaging of the underlying substrate. Conventional strategies of incorporating metallic components with elastomers to attain stretchability also yield non-trivial failure modes such as liquid metal leakage[8] and hard-soft material interfacial failure [71]. The use of gels as conductors, where ions are the charge carriers instead of electrons, represents an entirely different approach that has gained popularity recently. Their high stretchability and transparency, when combined with recent improvements in toughness and stiffness [51, 72], have already enabled their use as stretchable electrical conductors [73, 74], capacitive strain sensors [75–77], and chemical/pH sensors [78]. Gel-based ionic circuits thus represent a unique class of devices within stretchable electronics. Conductive gels can be generally divided into those where the ions are provided by solvated salts [77, 79] (hydrogels) or by ionic liquids [76, 80, 81] (ionogels). Although immune to dehydration, ionogels have comparatively lower conductivities. Ionic liquids also interfere with the gel polymerization reaction, limiting the range of polymers that can

be used to synthesize ionogels [82]. By contrast, hydrogels are easier to synthesize, but they are susceptible to dehydration. Solvated hygroscopic salts may serve the dual purpose of increasing both their ionic conductivity and water-retention properties[26], though a balance must be struck between maximizing water-retention and ionic conductivity due to non-idealities of the electrolyte solution that reduce molar conductivity at high salt concentrations [83].

Fabrication of stretchable electronics using hydrogels requires integrating hydrogels with stretchable dielectrics such as dielectric elastomers; a process thus far primarily achieved via manual assembly of cast segments. If the field is to progress, advanced manufacturing techniques that integrate dielectric elastomers and hydrogels need to be developed [61]. Fabrication techniques specific to hydrogels have already been developed, including extrusion 3D printing [49, 76, 84, 85], digital projection based techniques [86], and screen printing [87, 88]. Extrusion printing techniques in particular are most easily capable of multi-material printing at high resolution and low costs [49, 52]. Recently, Robinson et al. fabricated a soft sensor with an ionic-liquid based gel and a silicone elastomer by combining soft lithography with extrusion printing [76]. Although recent studies have successfully fabricated stretchable electronics consisting entirely of soft materials, conductive hydrogels and dielectric elastomers, thus far these fabrications have relied on casting [73–75, 77] or a combination of extrusion printing with other methods [76].

Here, we describe a simple approach to 3D extrusion printing of soft, stretchable electrical devices integrating a conductive hydrogel and a dielectric elastomer with sub-millimeter resolution. We show that both types of materials can be integrated into a single device using a single fabrication process. We characterize the mechanical and electrical performance of the printed hydrogel and demonstrate the technique by printing a soft strain sensor. The device was fabricated using polyacrylamide (PAAm) hydrogel and poly-dimethyl-siloxane (PDMS) because of their widespread use, as well as their favorable electrical and optical properties. The hydrogel precursor consisted of a concentrated aqueous solution of a hygroscopic salt,

a compatible rheological modifier, and UV-initiated polymerization/cross-linking compounds. Lithium chloride was selected as the hygroscopic salt in a compromise between vapor pressure and ionic conductivity, and its concentration (7 mol L^{-1}) was set above peak conductivity, but below saturation in an aqueous solution [89]. The PDMS was a UV curing formulation to allow for rapid setting during the printing process (KER-4690, courtesy of Shin-Etsu Silicones).

A.11 Results and Discussion

Printing was performed using an extrusion 3D printer comprised of a precision positioning system, an ink extrusion system, and a hardware/software interface to control location and rate of material extrusion relative to the sample stage (Figure A.10a) [49]. The entire system was housed inside a nitrogen environment. The RH of the environment was fixed at 43 % by bubbling nitrogen through a saturated solution of potassium carbonate [90]. Significant variations in RH during the fabrication process can lead to elastic instabilities in the hydrogel surface as a result of hydrogel swelling [80], which can happen very quickly because of the high surface area to volume ratio of sub-millimeter features. Oxygen displacement was needed to prevent inhibition of the free-radical polymerization in the hydrogel precursor. *In situ* UV curing was used to partially set the extruded ink and prevent extensive spreading. This point is elaborated on later in this article during the discussion of rheological characteristics of the hydrogel precursor. Figure A.10b demonstrates our printing capabilities of complex hydrogel-elastomer designs by comparing the final printing shape to its printing trace and Figure A.10c highlights the optical transparency of the printed devices.

Selecting materials for extrusion printing requires the consideration of their rheological properties, since these properties dictate extrusion pressure, post-extrusion shape retention, and printing resolution. A shear-thinning characteristic is particularly desirable for extrusion, since this allows for lowered viscosity under the high shear rates involved in extrusion and a high viscosity post-extrusion. This is usually

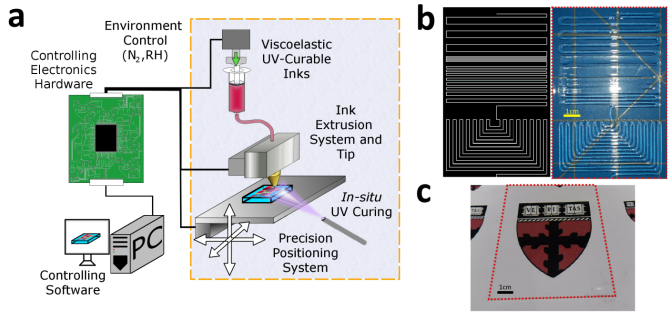

Figure A.10: a) Overall schematic of the 3D printing extrusion system used in this study. b) A side-by-side comparison of a patterned design and the final printed hydrogel-on-PDMS sample. c) The same printed sample placed over an image to demonstrate its complete optical transparency.

achieved through the addition of a rheological modifier, of which many are commercially available [91]. For this particular application, where the elastomer serves as a bulk dielectric as opposed to finer features, the resolution requirements for the extrusion printing of the PDMS are not as high as for the hydrogel. This allows the utilization of the UV-curing PDMS formulation without modification, despite its almost Newtonian behavior with viscosities at 4.8 Pa s at 0.1 s^{-1} and 4.5 Pa s at 102 s^{-1}. For applications where a higher resolution is required, many techniques and products are available to adjust the rheological behavior of the PDMS precursor [59, 76, 92–95].

A hydrogel precursor for extrusion printing must balance conductivity, stability, and rheology. A significant proportion of rheological modifiers used in extrusion printing are sensitive to the ionic strength of the precursor [34, 49, 52, 96], and may lead to precipitation [97–99] or flocculation [100] of the rheological modifiers at the high salt concentrations necessary for good electrical conductivity and water retention. This requirement excludes many of the modifiers that are routinely used for hydrogel printing. High-molecular weight polymers, however, are insensitive to the ionic strength of the precursor and have been used successfully in hydrogel extrusion printing [76, 85]. In this study, we use high-molecular weight polyacrylamide as a rheological modifier, because of its transparency and compatibility with the precursor formulation.

The rheology of the polyacrylamide/lithium chloride solution used to modify

the flow characteristics of the precursor was characterized by measuring its viscosity (η), yield stress (σy), and viscoelastic moduli (G',G''). The precursor rheology is dominated by the polyacrylamide; all other components in solution do not affect the viscosity significantly at their respective concentrations. We performed both viscometry and oscillatory rheology (Figure A.11). The storage modulus (G') plateaus at a modulus of approximately 555 Pa and exceeds the loss modulus (G'') at shear stresses below 570 Pa, indicating solid-like behavior up to this stress level (Figure A.11a); at stresses greater than 570 Pa, G'' exceeds G' and the precursor behaves more like a liquid. Thus, the precursor has an apparent yield stress of 570 Pa. Figure A.11b depicts the stress and viscosity as a function of shear rate obtained from viscometry measurements. The viscosity shows clear shear-thinning behavior with $\eta \approx$ 15,000 Pa s at low shear rates (10^{-2} s^{-1}) and η 5 Pa s at high shear rate (10^{2} s^{-1}). Extrapolating the linear portion of the stress-shear rate curve back to zero shear rates provides a Bingham yield stress of $\approx$ 550 Pa, which agrees well with the cross-over between G' and G''.

We estimate the shear-rate during extrusion using the generalized form of the Rabinowitsch-Mooney equation for a power-law fluid flowing through a cylindrical tube [101] of radius r,

$$\dot{\gamma} = (\frac{3n+1}{4n})\frac{4Q}{\pi r^3}, \tag{A.8}$$

where Q is the volumetric flow rate and n is the exponent of the power-law

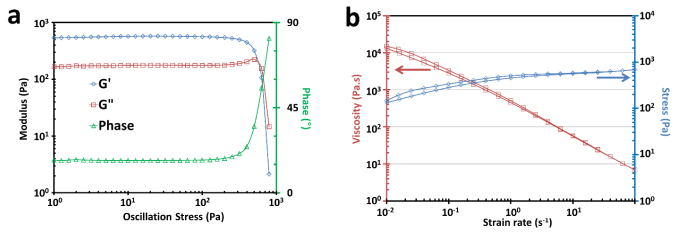

Figure A.11: Rheological analyses of the rheological modifier for the hydrogel precursor. a) Oscillatory rheology results showing shear storage (G') and shear loss (G'') moduli evolution of inks used over increasing shear stress. b) Viscometry results showing stress and viscosity against shear rate. Tests were begun at low shear rates and swept up, then back down to demonstrate a mild thixotropic effect.

describing the shear stress as a function of shear-rate, $\tau = K\dot{\gamma}^n$. By performing a power-law fit of the data in Figure A.11b, we obtain a value of 0.148 for the shear thinning exponent n in the high-strain rate region ($\dot{\gamma} > 1s^{-1}$). For a volumetric extrusion rate of 1 mm^3 s^{-1} and a 0.337 mm syringe tip diameter, the shear rate $\dot{\gamma}$ of the hydrogel precursor is $\approx$ 81 s^{-1}, with a corresponding viscosity of $\approx$ 7 Pa s. Immediately after extrusion, the viscosity increases to approximately 1,300 Pa s, assuming a shear rate of 0.1 s^{-1}. Other studies have achieved extrusion printing with viscosities of 10 Pa s at 10^2 s^{-1} and 10^2–10^3 Pa s at 0.1 s^{-1} strain rates [34, 49, 76]. Typical values for oscillatory rheological parameters in hydrogel extrusion printed inks place $G' \approx$ 350–3000 Pa and $\sigma y \approx$ 500-3000 Pa [76, 85]. This makes our precursor comparable in terms of rheological performance. These viscosity/G' values are insufficient, however, to ensure that the precursor retain its shape after printing over long periods of time. Since the hydrogel is UV curable, the simplest solution is to implement *in-situ* UV curing during the extrusion printing process to partially cure the inks as they are extruded from the syringe tip (Figure A.10a). Various hydrogel line geometries were generated by printing line stacks in both the lateral and vertical directions, specified as the x and z-directions respectively, at constant extrusion rate, stage velocity, and lateral/vertical center-to-center spacing (6.0 mm^3 s^{-1}, 7.5 mm s^{-1}, $S_x = 0.3$ mm and $S_z = 0.15$ mm respectively). To precisely design 3D structures of hydrogel printed directly on PDMS, we characterized the geometry of the printed hydrogel structures in terms of the number of lines (N_x and N_z) in the x and z-directions, respectively (Figure A.12 b-c). We note that the degree of spreading in the x-direction increases with N_z, but that the spreading saturates once three layers have been printed, indicating that building up stable 3D structures is possible. The spreading of the hydrogel precursor post-extrusion is governed by a balance between capillary, viscous, and inertial forces acting on the extruded geometries. We may determine the dominant force using the Ohnesorge number [102],

$$Oh = \eta/(\sqrt{\rho\gamma L}) \tag{A.9}$$

where, γ is the surface energy, ρ is the mass density, and L the characteristic length scale. Using conservative values, η 103 Pa s, γ 0.1 J m^{-2}, ρ 10^4 kg m^{-3}, and L $\approx$ 10^{-3} m, we observe that, indicating dominance of the viscous forces, as expected by the rheological design of the hydrogel precursor. The minimum level of lateral spreading was 0.8 mm, which can be observed by extrapolating Figure 3c to the y-intercept. This value can be decreased further by tuning the precursor rheology, increasing the *in situ* curing intensity, lowering the extrusion rates (Figure B.11), increasing the stage speed, or by utilizing a smaller size of syringe tip. Optical micrographs of multi-layer gel patterns showed smoothly merged surfaces (Figure A.12 d-f) and the formation of what are believed to be residual wetting layers on the gel edges. Optical profilometry was used to obtain cross-sectional profiles of the printed hydrogel lines (Figure A.12 g-h), which demonstrate that these profiles are nearly identical, indicating the reproducibility necessary for us to design and build 3D hydrogel structures.

Electrical testing of bulk cast hydrogel samples was conducted using a four-point probe configuration to establish the baseline electrical conductivity of the hydrogel. As shown in Figure A.13a, we observed ohmic conduction with a bulk conductivity of 10.39 $\pm$ 0.31 S m^{-1}, which is comparable to the conductivity of the corresponding aqueous salt solution[38]. By contrast, the conductivity of the printed lines, measured under conditions of controlled humidity at RH 43 %, was found to be 2.90 $\pm$ 0.40 S m^{-1}. This value is markedly lower than the bulk conductivity, but is most likely due to water loss post-extrusion. Although hydrogel water loss in open air will not be entirely avoided without the use of a sealant, such as by coating the hydrogel in an elastomer, the lithium chloride will allow the hydrogel to remain stable at a RH determined by the salt species and concentration. An aqueous lithium chloride solution increasing in mass percentage from 20 % to 30 % suffers a conductivity loss of 14 % [89] and the volumetric change from water loss alone would cause a 62 %

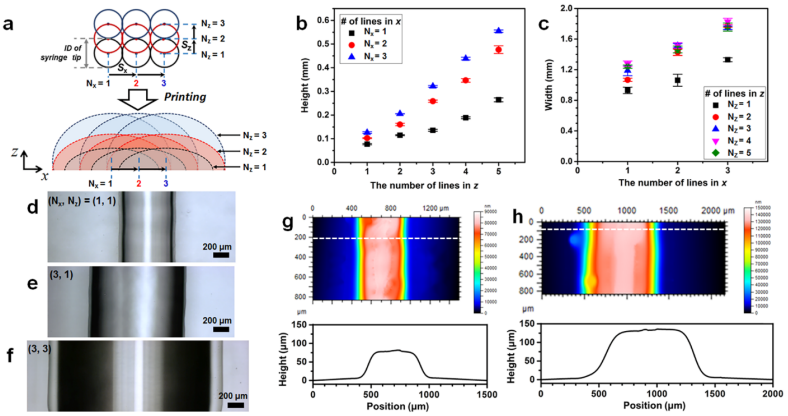

Figure A.12: a) Schematic illustration of the extrusion trace and the resulting geometry of multiple lines separated both laterally, by S_x in the x direction, and vertically, by S_z in the z direction. The number of lines in x and z is (N_x, N_z) = (3, 3), respectively. b) Height of gel lines as a function of N_z. c) Width of gel lines as a function of N_x. Optical micrographs of stacked layers of gel lines with d) (N_x , N_z) = (1, 1), e) (3, 1) and f) (3,3). Optical profilometry images and the cross-sectional profiles of gel lines with multiple hydrogel layers of g) (1, 1) and h) (3,1).

decrease in cross-sectional area, which together approximates conductivity loss to be at least 48 %. We characterized the resistance change of printed hydrogel lines printed on PDMS upon application of uniaxial tensile strain. The ideal case can be reasoned as follows: we let R and L, respectively be the resistance and length of a hydrogel line, and indicate their initial values with a subscript zero. We assume that the hydrogel is incompressible and the resistivity is independent of stretch. These assumptions predict that the ratio of current resistance over initial resistance is given by $R/R_o = (L/L_o)^2$. As the printed hydrogel lines are stretched, their resistances obey this relationship up to rupture of the samples at 50 % strain (Figure A.13b). This result suggests that the hydrogel lines are intact up to this strain, since damage in the hydrogel would cause a deviation from this expression. Tensile tests on freestanding hydrogel samples show that the printed gel is capable of stretching up to 150 % strain before rupture, further supporting the notion that the PDMS is the mechanically limiting component in this case. We also performed a fatigue test on a PDMS-Hydrogel sample at a strain of 20 % for one thousand cycles, and measured the resistance of the hydrogel at logarithmic intervals. Remarkably, there were no observable changes to the resistance of the device, nor were there visible signs of de-

lamination (Figure A.13c). To demonstrate transmission of AC electrical signals, we fabricated a simple analog to the ionic cable [74]: two parallel ionically conductive hydrogel wires were extruded onto a printed PDMS substrate, with the two terminals at either end serving as either an electrical input or output. The transfer function of the device was measured and fitted to a simple RC circuit model. Yang et al [74] demonstrated that the transmission of signals through an ionic conductor can be described using a special case of a transmission line model. According to the theory of ionic cables, the condition for negligible decay of the signal is $\omega\rho\epsilon l^2/(bd) \ll 1$, where ω is the signal frequency, l is the cable length, b and ρ are the thickness and resistivity of the ionic conductor, and d and ϵ are the thickness and permittivity of the dielectric. Using representative values, $\epsilon = 2.10^{-11}$, $\rho \approx 10^{-2}\Omega m$, $l = 10mm$, $b = 50\mu m$, $d = 50\mu m$ and let $\omega = 10^5 s^{-1} \approx 15kHz$, we evaluate the expression to be 0.08, indicating negligible signal decay. Using a printed ionic cable with similar dimensions, we have successfully demonstrated signal transmission of AC signals up to 15 kHz in frequency (Figure A.13d).

To demonstrate the capabilities of the printing process, we have extrusion printed a single-loop resistive strain gauge of hydrogel embedded within PDMS (Figure A.14a). The sensor has a gauge factor of 0.84, and remains linear up to 40 % strain (Figure B.12). The strain sensor was attached to the index finger of a nitrile glove using a thin layer of VHB adhesive tape (3M) and connected to a multi-meter to measure the resistance of the sensor as it underwent varying degrees of strain as a result of the bending/flexing of the digits of the glove (Figure B.13). This sensing capability was extended to all five digits of a human hand (Figure A.14). It can be observed that the strain gauge is sensitive enough to detect inadvertent finger motions of the ring finger in position two (Figure A.14c), as well as intermediate positions between being fully bent and fully straightened (Figure B.13b). We observed changes up to 30 % in the strain gauge resistance at maximum finger bending, corresponding to a strain of 36 %. No delamination or fracture was observed during the experiment, verifying our previous results on the durability and stretchability of the printed

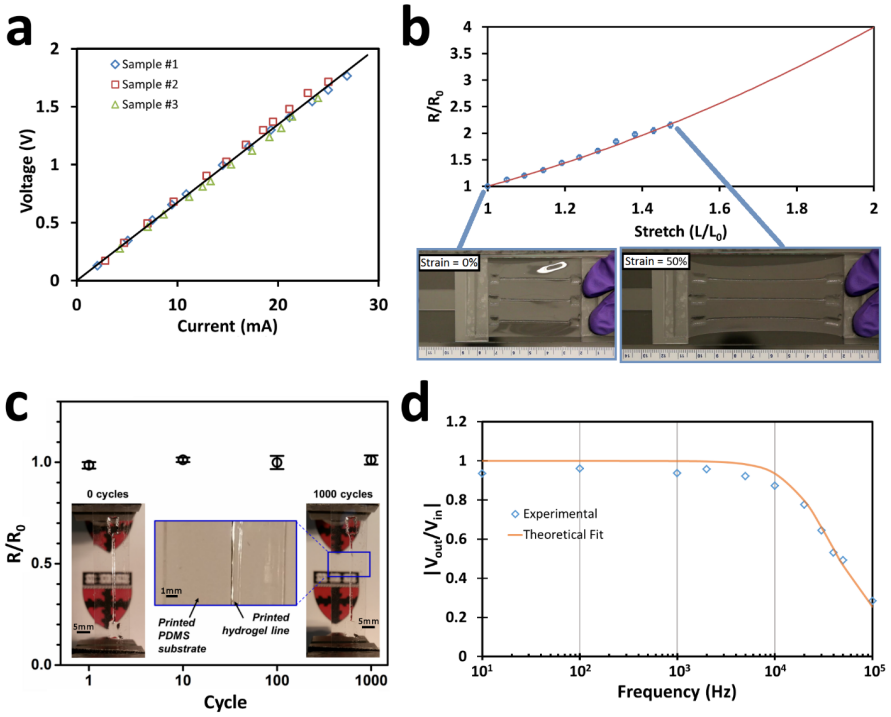

Figure A.13: Electrical characterizations of the hydrogel in either bulk or printed state. a) I-V curves obtained from 4-point probe measurements performed on bulk hydrogel samples. Sample dimensions were on average 30 cm long, 4.2 mm wide, and 3.5 mm in height, with an average measured resistance of 67 Ω; this corresponds to a conductivity of 10.39 ± 0.31 S m^{-1}. b) The normalized resistance of printed hydrogels on a PDMS substrate is measured as a function of stretch, plotted against the ideal geometric behavior. Photos illustrate the sample at initial (strain = 0 %) and fully stretched (strain = 50 %) states. c) The normalized resistance of printed hydrogels on a PDMS substrate as a function of fatigue cycle number. Uniaxial tensile strain cycles of 20 % strain were performed for up to 1000 cycles. No significant change to the resistance vs. strain behaviour was observed during our tests. Comparing images both before and after fatigue tests illustrate the lack of visible damage or delamination d) The transfer function of an ionic cable design is plotted against frequency. We perform a theoretical fitting of our results using a simple RC circuit model for the ionic cable and can observe a reasonable level of agreement between experimental results and theory.

laminates.

In conclusion, we have described a method for the 3D extrusion printing of an ionically conductive polyacrylamide hydrogel and a polydimethylsiloxane dielectric elastomer to fabricate soft ionic devices. By tuning the rheological behavior of the hydrogel precursor and performing oxygen plasma treatments of PDMS surfaces, it is possible to print and integrate hydrogels directly with PDMS at sub-millimeter resolution. This capability was demonstrated by the fabrication and functional verification of an ionic cable and resistance-based strain sensor. More complex geometries are readily designed and printed. The flexibility of the process allows one to replicate the design in an array or to print stacked devices for multi-axial strains. The strategies employed here to obtain the desirable printing resolution are applicable for any hydrogel-PDMS material system. This study provides a simple pathway to the fabrication of hydrogels and dielectric elastomers in an integrated fashion for stretchable electrical devices and soft robotics applications.

A.12 Experimental Section

A.12.1 Preparation of polydimethylsiloxane (PDMS)

A UV curable formulation of polydimethylsiloxane elastomer (Shin-Etsu Silicones, KER-4690 A/B) was provided by the manufacturer as a two-part precursor and was used in the recommended 1:1 ratio. After a 2 minute mixing cycle in a planetary centrifugal mixer (Thinky, ThinkyMixer ARE-300) at 2000 RPM, the precursor was used without further preparation and was cured via 365 nm UV light at a dose of 10 mW cm^{-2} for a period of 30 minutes, followed by an overnight bake at 65 °C. Prior to further printing, the PDMS was treated with an oxygen plasma (SPI Supplies, Plasma Prep II) at an O_2 pressure of 18 psi, vacuum pressure of 275 mTorr, and RF power of 80 W for 60 sec.

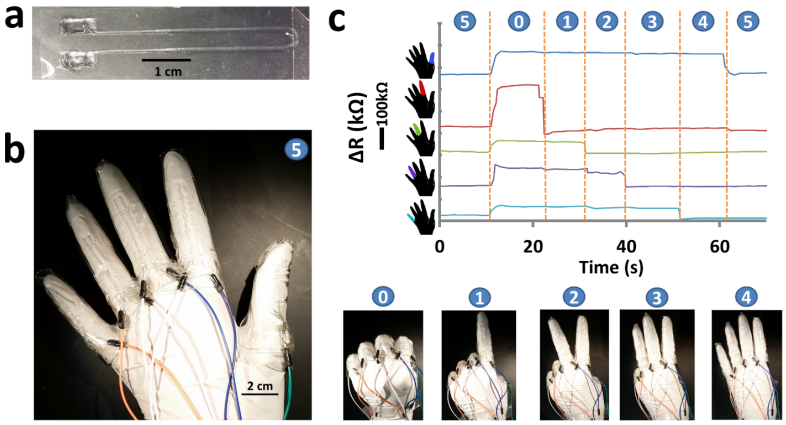

Figure A.14: An example of a printed hydrogel-elastomeric type device, where fairly arbitrary shapes and designs can be easily integrated into the system by virtue of the printing process. In this case a) a simple resistance-based strain gauge is replicated using the hydrogel as the conductor and PDMS as the encapsulating substrate. b) By attaching the sensor to a flexible glove and flexing the digit we are able to observe a change in resistance up to 30 % of its initial value at maximum finger bending and c) illustrate this process for a variety of hand gestures for each digits strain sensor resistance change over time.

A.12.2 Preparation of the hydrogel precursor

The precursor used in the printing process consisted of two components - the rheological modifier and the hydrogel component. The rheological modifier consisted of an un-crosslinked polyacrylamide solution made by UV exposing an acrylamide (AAm, Sigma-Aldrich, A8887) solution containing α-ketoglutaric acid (α-keto, Sigma-Aldrich) and N,N,N',N'-tetramethylethylenediamine (TEMED, Sigma-Aldrich, T7024) at 25 °C with the following ratios (w/w): 92.17 % Water, 0.073 % AAm, 0.00044 % α-keto, 0.00021 % TEMED. The hydrogel component consisted of AAm, α-keto, TEMED, lithium chloride (LiCl, Sigma-Aldrich, 746460), and N,N'-methylenebis(acrylamide) (MBAA, Sigma-Aldrich, 146072). This component was added to the un-crosslinked polyacrylamide solution and mixed using a planetary centrifugal mixer (Thinky, ThinkyMixer ARE-300) at 2000 RPM. Final precursor composition ratios (w/w) were: 63.15 % Water, 3.86 % PAAm, 9.05 % AAm, 18.43 % LiCl, 0.072 % MBAA, 4.95 % α-keto, 0.479 % TEMED.

A.12.3 Rheological Characterization

All rheological measurements were made using a TA Instruments Discovery HR-3 Hybrid Rheometer with a cone and plate geometry at a reference temperature of 25 °C. Oscillatory rheometry was performed on the polyacrylamide/lithium chloride portion of the hydrogel precursor using a frequency of 1 Hz and sweeping shear stresses from 1–500 Pa. Viscometry was also performed with shear rates ranging from 0.01 – 100 s^{-1}.

A.12.4 Device Fabrication

PDMS-Hydrogel precursors were directly printed onto a UV-resistant acrylic substrate (6.35 mm thickness, McMaster-Carr) rinsed with DI water followed by isopropanol and blown dry with nitrogen. A CNC milling machine (Sherline Products, 5400) was used as a positioning stage, upon which independent linear actuators (Zaber Technologies, T-LA60A) were mounted onto the z-axis of the stage as syringe pumps. Syringes (5 mL, Hapool Medical Technology Co) contained the precursors and were extruded through a 23 gauge blunted syringe tip (0.337mm ID, SAI Infusion Technologies). A displacement rate was prescribed to the actuators and the requisite extrusion force was applied to the syringe end. A steady flow of dry nitrogen piped through a saturated potassium carbonate (Sigma Aldrich) solution was used to purge the printing area of oxygen during the printing process and simultaneously fix the relative humidity. A 6 W UV LED (Instun, SK66) was used to initiate curing of the ink as it is extruded from the syringe at a dose rate of $\approx$ 3 mW cm^{-2}. Printed samples were then flood exposed to UV using an 8 W 365nm UV Lamp (UVP, UVLS-28 EL) in a nitrogen environment at an effective dose rate of $\approx$ 6 mW cm^{-2}.

Devices began with a printed PDMS layer that was fully cured and baked, as previously described. Prior to additional printing, the PDMS was treated with O_2 plasma and stored in DI water until immediately prior to the printing. While this plasma treatment process is incompatible with hydrogels already present on the

PDMS due to vacuum requirements, a UV-Ozone treatment may be substituted to achieve the same effect at a slower rate while maintaining hydrogel integrity [103]. After subsequent hydrogel and PDMS layers were printed, the device was exposed to the flood UV lamp. Since the curing of PDMS is inhibited by contact with water [104], the printed device was baked at 65 °C for 6 hours to drive the PDMS curing process to completion, followed by a DI water soak of 1 hour to rehydrate the hydrogel from the oven bake.

A.12.5 Sample Characterization

Cross-sectional images and measurements were made using a Coherence Correlation Interferometry (CCI) optical profiler (Taylor Hobson, CCI HD) with 5x and 20x objective lenses. DC electrical measurements were made using multimeters (Fluke, models 8846A and 175). A DC power supply (Dr.Meter, PS-305DM) was used to generate the current used in the four-point probe measurement. For the AC characterization, a waveform generator (Keysight, 33500B) and oscilloscope (Keysight, DSO-1004A) with passive probes (Keysight, N2862B) were used. Uniaxial tensile testing, for both stress-strain and fatigue experiments, was performed on a uniaxial tensile tester (Instron, 3342 Single Column UTS) using a strain rate of 50 mm min^{-1}. For the fatigue experiments, a maximum strain of 20 % was used.

Bibliography

[1] S. Naficy, R. Gately, R. Gorkin, H. Xin, and G. M. Spinks, "4D printing of reversible shape morphing hydrogel structures," *Macromol. Mater. Eng.*, 2016.

[2] T. Tørring, N. V. Voigt, J. Nangreave, H. Yan, and K. V. Gothelf, "DNA origami: A quantum leap for self-assembly of complex structures," *Chem. Soc. Rev.*, vol. 40, no. 12, pp. 5636–5646, 2011.

[3] P. W. K. Rothemund, "Folding DNA to create nanoscale shapes and patterns," *Nature*, vol. 440, no. 7082, pp. 297–302, 2006.

[4] S. Armon, E. Efrati, R. Kupferman, and E. Sharon, "Geometry and mechanics in the opening of chiral seed pods," *Science*, vol. 333, no. 6050, pp. 1726–1730, 2011.

[5] H. Liang and L. Mahadevan, "Growth, geometry, and mechanics of a blooming lily," *Proc. Natl. Acad. Sci. U.S.A*, vol. 108, no. 14, pp. 5516–5521, 2011.

[6] S. Felton, M. Tolley, E. Demaine, D. Rus, and R. Wood, "A method for building self-folding machines," *Science*, vol. 345, no. 6197, pp. 644–646, 2014.

[7] J. T. Early, R. Hyde, and R. L. Baron, "Twenty-meter space telescope based on diffractive fresnel lens," in *Optical Science and Technology, SPIE's 48th Annual Meeting*, International Society for Optics and Photonics, 2004, pp. 148–156.

[8] D. Pohl and W. Wolpert, "Engineered spacecraft deployables influenced by naturel," in *SPIE Optical Engineering+ Applications*, International Society for Optics and Photonics, 2009, pp. 742 408–742 408.

[9] Q. Cheng, Z. Song, T. Ma, B. B. Smith, R. Tang, H. Yu, H. Jiang, and C. K. Chan, "Folding paper-based lithium-ion batteries for higher areal energy densities," *Nano Lett.*, vol. 13, no. 10, pp. 4969–4974, 2013.

[10] Z. Song, T. Ma, R. Tang, Q. Cheng, X. Wang, D. Krishnaraju, R. Panat, C. K. Chan, H. Yu, and H. Jiang, "Origami lithium-ion batteries," *Nat. Commun.*, vol. 5, 2014.

[11] C. L. Randall, E. Gultepe, and D. H. Gracias, "Self-folding devices and materials for biomedical applications," *Trends Biotechnol.*, vol. 30, no. 3, pp. 138–146, 2012.

[12] R. Fernandes and D. H. Gracias, "Self-folding polymeric containers for encapsulation and delivery of drugs," *Adv. Drug Delivery Rev.*, vol. 64, no. 14, pp. 1579–1589, 2012.

[13] A. S. Gladman, E. A. Matsumoto, R. G. Nuzzo, L. Mahadevan, and J. A. Lewis, "Biomimetic 4D printing," *Nat. Mater.*, vol. 15, no. 4, pp. 413–418, 2016.

[14] J. L. Silverberg, A. A. Evans, L. McLeod, R. C. Hayward, T. Hull, C. D. Santangelo, and I. Cohen, "Using origami design principles to fold reprogrammable mechanical metamaterials," *Science*, vol. 345, no. 6197, pp. 647–650, 2014.

[15] E. A. Peraza-Hernandez, D. J. Hartl, R. J. Malak Jr, and D. C. Lagoudas, "Origami-inspired active structures: A synthesis and review," *Smart Mater. Struct.*, vol. 23, no. 9, p. 094 001, 2014.

[16] R. Kempaiah and Z. Nie, "From nature to synthetic systems: Shape transformation in soft materials," *J. Mater. Chem. B*, vol. 2, no. 17, pp. 2357–2368, 2014.

[17] T. Xie, "Tunable polymer multi-shape memory effect," *Nature*, vol. 464, no. 7286, pp. 267–270, 2010.

[18] C. M. Yakacki, "Shape-memory and shape-changing polymers," *Polym. Rev.*, vol. 53, no. 1, pp. 1–5, 2013.

[19] C. Liu, H. Qin, and P. Mather, "Review of progress in shape-memory polymers," *J. Mater. Chem.*, vol. 17, no. 16, pp. 1543–1558, 2007.

[20] J. Kim, J. A. Hanna, R. C. Hayward, and C. D. Santangelo, "Thermally responsive rolling of thin gel strips with discrete variations in swelling," *Soft Matter*, vol. 8, no. 8, pp. 2375–2381, 2012.

[21] J. Guan, H. He, D. J. Hansford, and L. J. Lee, "Self-folding of three-dimensional hydrogel microstructures," *J. Phys. Chem. B*, vol. 109, no. 49, pp. 23 134–23 137, 2005.

[22] W. Huang, B. Yang, L. An, C. Li, and Y. Chan, "Water-driven programmable polyurethane shape memory polymer: Demonstration and mechanism," *Appl. Phys. Lett.*, vol. 86, no. 11, p. 114 105, 2005.

[23] L. T. de Haan, V. Gimenez-Pinto, A. Konya, T.-S. Nguyen, J. M. N. Verjans, C. Sánchez-Somolinos, J. V. Selinger, R. L. B. Selinger, D. J. Broer, and A. P. H. J. Schenning, "Accordion-like actuators of multiple 3D patterned liquid crystal polymer films," *Adv. Funct. Mater.*, vol. 24, no. 9, pp. 1251–1258, 2014.

[24] M. Jamal, A. M. Zarafshar, and D. H. Gracias, "Differentially photo-crosslinked polymers enable self-assembling microfluidics," *Nat. Commun.*, vol. 2, p. 527, 2011.

[25] E. W. Jager, O. Inganäs, and I. Lundström, "Microrobots for micrometer-size objects in aqueous media: Potential tools for single-cell manipulation," *Science*, vol. 288, no. 5475, pp. 2335–2338, 2000.

[26] H. Okuzaki, T. Saido, H. Suzuki, Y. Hara, and H. Yan, "A biomorphic origami actuator fabricated by folding a conducting paper," in *Journal of Physics: Conference Series*, IOP Publishing, vol. 127, IOP Publishing, 2008, p. 012 001.

[27] K. Hiraoka, W. Sagano, T. Nose, and H. Finkelmann, "Biaxial shape memory effect exhibited by monodomain chiral smectic c elastomers," *Macromolecules*, vol. 38, no. 17, pp. 7352–7357, 2005.

[28] J. Leng, X. Lan, Y. Liu, and S. Du, "Shape-memory polymers and their composites: Stimulus methods and applications," *Prog. Mater Sci.*, vol. 56, no. 7, pp. 1077–1135, 2011.

[29] L. Ionov, "3D microfabrication using stimuli-responsive self-folding polymer films," *Polym. Rev.*, vol. 53, no. 1, pp. 92–107, 2013.

[30] Y. Mao, K. Yu, M. S. Isakov, J. Wu, M. L. Dunn, and H. J. Qi, "Sequential self-folding structures by 3D printed digital shape memory polymers," *Sci. Rep.*, vol. 5, 2015.

[31] Q. Ge, H. J. Qi, and M. L. Dunn, "Active materials by four-dimension printing," *Appl. Phys. Lett.*, vol. 103, no. 13, p. 131 901, 2013.

[32] M. Zarek, M. Layani, I. Cooperstein, E. Sachyani, D. Cohn, and S. Magdassi, "3D printing of shape memory polymers for flexible electronic devices," *Adv. Mater.*, vol. 28, no. 22, pp. 4449–4454, 2015.

[33] D. Raviv, W. Zhao, C. McKnelly, A. Papadopoulou, A. Kadambi, B. Shi, S. Hirsch, D. Dikovsky, M. Zyracki, C. Olguin, *et al.*, "Active printed materials for complex self-evolving deformations," *Sci. Rep.*, vol. 4, 2014.

[34] S. Hong, D. Sycks, H. F. Chan, S. Lin, G. P. Lopez, F. Guilak, K. W. Leong, and X. Zhao, "3D printing of highly stretchable and tough hydrogels into complex, cellularized structures," *Adv. Mater.*, vol. 27, no. 27, pp. 4035–4040, 2015.

[35] S. E. Bakarich, R. Gorkin, G. M. Spinks, *et al.*, "4D printing with mechanically robust, thermally actuating hydrogels," *Macromol. Rapid Commun.*, vol. 36, no. 12, pp. 1211–1217, 2015.

[36] S. Naficy, G. M. Spinks, and G. G. Wallace, "Thin, tough, ph-sensitive hydrogel films with rapid load recovery," *ACS Appl. Mater. Interfaces*, vol. 6, no. 6, pp. 4109–4114, 2014.

[37] I. Bischofberger, D. C. Calzolari, and V. Trappe, "Co-nonsolvency of pnipam at the transition between solvation mechanisms," *Soft Matter*, vol. 10, no. 41, pp. 8288–8295, 2014.

[38] M. J. Hore, B. Hammouda, Y. Li, and H. Cheng, "Co-nonsolvency of poly (n-isopropylacrylamide) in deuterated water/ethanol mixtures," *Macromolecules*, vol. 46, no. 19, pp. 7894–7901, 2013.

[39] S. Naficy, H. R. Brown, J. M. Razal, G. M. Spinks, and P. G. Whitten, "Progress toward robust polymer hydrogels," *Aust. J. Chem.*, vol. 64, no. 8, pp. 1007–1025, 2011.

[40] H. Qi and M. Boyce, "Stress–strain behavior of thermoplastic polyurethanes," *Mech. Mater.*, vol. 37, no. 8, pp. 817–839, 2005.

[41] S. Timoshenko, "Analysis of bi-metal thermostats," *JOSA*, vol. 11, no. 3, pp. 233–255, 1925.

[42] S. Jiang, F. Liu, A. Lerch, L. Ionov, and S. Agarwal, "Unusual and superfast temperature-triggered actuators," *Adv. Mater.*, vol. 27, no. 33, pp. 4865–4870, 2015.

[43] L. R. G. Treloar, *The physics of rubber elasticity (third edition)*, 1. Wiley-Blackwell, 1975, vol. 8, pp. 39–39.

[44] M. Rubinstein and R. Colby, *Polymer physics*. OUP Oxford, 2003.

[45] C. Shou-Zhong, "Empirical viscosity–concentration relationship for polymer solutions," *Polym. J.*, vol. 14, no. 6, pp. 501–504, 1982.

[46] G. K. Batchelor, *An introduction to fluid dynamics*. Cambridge university press, 2000.

[47] S. E. Bakarich, R. Gorkin, S. Naficy, R. Gately, M. in het Panhuis, and G. M. Spinks, "3D/4D printing hydrogel composites: A pathway to functional devices," *MRS Advances*, vol. 1, no. 08, pp. 521–526, 08 2015.

[48] X. Zhao, "Multi-scale multi-mechanism design of tough hydrogels: Building dissipation into stretchy networks," *Soft Matter*, vol. 10, no. 5, pp. 672–687, 2014.

[49] S. E. Bakarich, M. in het Panhuis, S. Beirne, G. G. Wallace, and G. M. Spinks, "Extrusion printing of ionic–covalent entanglement hydrogels with high toughness," *J. Mater. Chem. B*, vol. 1, no. 38, pp. 4939–4946, 2013.

[50] S. E. Bakarich, P. Balding, R. G. III, G. M. Spinks, and M. in het Panhuis, "Printed ionic-covalent entanglement hydrogels from carrageenan and an epoxy amine," *RSC Adv.*, vol. 4, no. 72, pp. 38 088–38 092, 2014.

[51] J.-Y. Sun, X. Zhao, W. R. K. Illeperuma, O. Chaudhuri, K. H. Oh, D. J. Mooney, J. J. Vlassak, and Z. Suo, "Highly stretchable and tough hydrogels," *Nature*, vol. 489, no. 7414, pp. 133–136, 2012.

[52] S. E. Bakarich, P. Balding, R. Gorkin III, G. M. Spinks, *et al.*, "Printed ionic-covalent entanglement hydrogels from carrageenan and an epoxy amine," *RSC Adv.*, vol. 4, no. 72, pp. 38 088–38 092, 2014.

[53] S. E. Bakarich, R. Gorkin III, R. Gately, S. Naficy, M. In het Panhuis, and G. M. Spinks, "3D printing of bio-inspired tough hydrogel composites with spatially varying materials properties," *Addit. Manuf.*, 2016, Under review.

[54] K. Tian, J. Bae, S. Bakarich, C. Yang, R. Gately, G. M. Spinks, M. in het Panhuis, Z. Suo, and J. Vlassak, "3d printing of transparent and conductive heterogeneous hydrogel-elastomer systems," *Adv. Mater.*, (*Currently under review*).

[55] Y. S. Rim, S.-H. Bae, H. Chen, N. D. Marco, and Y. Yang, "Recent progress in materials and devices toward printable and flexible sensors," *Adv. Mater.*, vol. 28, no. 22, pp. 4415–4440, 2016.

[56] N. Lu, C. Lu, S. Yang, and J. Rogers, "Highly sensitive skin-mountable strain gauges based entirely on elastomers," *Adv. Funct. Mater.*, vol. 22, no. 19, pp. 4044–4050, 2012.

[57] A. K. Bansal, S. Hou, O. Kulyk, E. M. Bowman, and I. D. Samuel, "Wearable organic optoelectronic sensors for medicine," *Adv. Mater.*, vol. 27, no. 46, pp. 7638–7644, 2015.

[58] A. Lmberis and A. Dittmar, "Advanced wearable health systems and applications-research and development efforts in the european union," *IEEE Eng. Med. Biol. Mag.*, vol. 26, no. 3, pp. 29–33, 2007.

[59] J. T. Muth, D. M. Vogt, R. L. Truby, Y. Mengüç, D. B. Kolesky, R. J. Wood, and J. A. Lewis, "Embedded 3D printing of strain sensors within highly stretchable elastomers," *Adv. Mater.*, vol. 26, no. 36, pp. 6307–6312, 2014.

[60] A. Frutiger, J. T. Muth, D. M. Vogt, Y. Mengüç, A. Campo, A. D. Valentine, C. J. Walsh, and J. A. Lewis, "Capacitive soft strain sensors via multicore–shell fiber printing," *Adv. Mater.*, vol. 27, no. 15, pp. 2440–2446, 2015.

[61] M. Amjadi, K.-U. Kyung, I. Park, and M. Sitti, "Stretchable, skin-mountable, and wearable strain sensors and their potential applications: A review," *Adv. Funct. Mater.*, vol. 26, no. 11, pp. 1678–1698, 2016.

[62] Y. Mengüç, Y. L. Park, E. Martinez-Villalpando, P. Aubin, M. Zisook, L. Stirling, R. J. Wood, and C. J. Walsh, "Soft wearable motion sensing suit for lower limb biomechanics measurements," in *IEEE International Conference on Robotics and Automation (ICRA), 2013*, 2013, pp. 5309–5316.

[63] M. D. Dickey, R. C. Chiechi, R. J. Larsen, E. A. Weiss, D. A. Weitz, and G. M. Whitesides, "Eutectic gallium-indium (egain): A liquid metal alloy for the formation of stable structures in microchannels at room temperature," *Adv. Funct. Mater.*, vol. 18, no. 7, pp. 1097–1104, 2008.

[64] A. Tabatabai, A. Fassler, C. Usiak, and C. Majidi, "Liquid-phase gallium–indium alloy electronics with microcontact printing," *Langmuir*, vol. 29, no. 20, pp. 6194–6200, 2013.

[65] S. Gong, W. Schwalb, Y. Wang, Y. Chen, Y. Tang, J. Si, B. Shirinzadeh, and W. Cheng, "A wearable and highly sensitive pressure sensor with ultrathin gold nanowires," *Nat. Commun.*, vol. 5, 2014.

[66] H. Yabu, K. Nagamine, J. Kamei, Y. Saito, T. Okabe, T. Shimazaki, and M. Nishizawa, "Stretchable, transparent and molecular permeable honeycomb electrodes and their hydrogel hybrids prepared by the breath figure method and sputtering of metals," *RSC Adv.*, vol. 5, no. 107, pp. 88 414–88 418, 2015.

[67] X. Feng, B. D. Yang, Y. Liu, Y. Wang, C. Dagdeviren, Z. Liu, A. Carlson, J. Li, Y. Huang, and J. A. Rogers, "Stretchable ferroelectric nanoribbons with wavy configurations on elastomeric substrates," *ACS Nano*, vol. 5, no. 4, pp. 3326–3332, 2011.

[68] S. P. Lacour, S. Wagner, Z. Huang, and Z. Suo, "Stretchable gold conductors on elastomeric substrates," *Appl. Phys. Lett.*, vol. 82, no. 15, pp. 2404–2406, 2003.

[69] Y. Xiang, T. Li, Z. Suo, and J. J. Vlassak, "High ductility of a metal film adherent on a polymer substrate," *Appl. Phys. Lett.*, vol. 87, no. 16, p. 161 910, 2005.

[70] I. R. Minev, P. Musienko, A. Hirsch, Q. Barraud, N. Wenger, E. M. Moraud, J. Gandar, M. Capogrosso, T. Milekovic, L. Asboth, *et al.*, "Electronic dura mater for long-term multimodal neural interfaces," *Science*, vol. 347, no. 6218, pp. 159–163, 2015.

[71] Z. Suo, "Mechanics of stretchable electronics and soft machines," *MRS Bull.*, vol. 37, no. 03, pp. 218–225, 2012.

[72] J. Li, W. R. K. Illeperuma, Z. Suo, and J. J. Vlassak, "Hybrid hydrogels with extremely high stiffness and toughness," *ACS Macro Letters*, vol. 3, no. 6, pp. 520–523, 2014.

[73] C. Keplinger, J.-Y. Sun, C. C. Foo, P. Rothemund, G. M. Whitesides, and Z. Suo, "Stretchable, transparent, ionic conductors," *Science*, vol. 341, no. 6149, pp. 984–987, 2013.

[74] C. H. Yang, B. Chen, J. J. Lu, J. H. Yang, J. Zhou, Y. M. Chen, and Z. Suo, "Ionic cable," *Extreme Mech. Lett.*, vol. 3, pp. 59–65, 2015.

[75] J.-Y. Sun, C. Keplinger, G. M. Whitesides, and Z. Suo, "Ionic skin," *Adv. Mater.*, vol. 26, no. 45, pp. 7608–7614, 2014.

[76] S. S. Robinson, K. W. O'Brien, H. Zhao, B. N. Peele, C. M. Larson, B. C. Mac Murray, I. M. Van Meerbeek, S. N. Dunham, and R. F. Shepherd, "Integrated soft sensors and elastomeric actuators for tactile machines with kinesthetic sense," *Extreme Mech. Lett.*, vol. 5, pp. 47–53, 2015.

[77] C. Larson, B. Peele, S. Li, S. Robinson, M. Totaro, L. Beccai, B. Mazzolai, and R. Shepherd, "Highly stretchable electroluminescent skin for optical signaling and tactile sensing," *Science*, vol. 351, no. 6277, pp. 1071–1074, 2016.

[78] G. Gerlach, M. Guenther, G. Suchaneck, J. Sorber, K.-F. Arndt, and A. Richter, "Application of sensitive hydrogels in chemical and ph sensors," in *Macromolecular Symposia*, Wiley Online Library, vol. 210, 2004, pp. 403–410.

[79] Y. Bai, B. Chen, F. Xiang, J. Zhou, H. Wang, and Z. Suo, "Transparent hydrogel with enhanced water retention capacity by introducing highly hydratable salt," *Appl. Phys. Lett.*, vol. 105, no. 15, p. 151 903, 2014.

[80] B. Chen, J. J. Lu, C. H. Yang, J. H. Yang, J. Zhou, Y. M. Chen, and Z. Suo, "Highly stretchable and transparent ionogels as nonvolatile conductors

for dielectric elastomer transducers," *ACS Appl. Mater. Interfaces*, vol. 6, no. 10, pp. 7840–7845, 2014.

[81] M. Li, J. Li, H. Na, and J. J. Vlassak, "Mechanical behavior of poly (methyl methacrylate)-based ionogels," *Soft Matter*, vol. 10, no. 40, pp. 7993–8000, 2014.

[82] P. Kubisa, "Ionic liquids as solvents for polymerization processes—progress and challenges," *Prog. Polym. Sci.*, vol. 34, no. 12, pp. 1333–1347, 2009.

[83] M. R. Wright, *An introduction to aqueous electrolyte solutions*. John Wiley & Sons, 2007.

[84] D. M. Kirchmajer, R. Gorkin III, *et al.*, "An overview of the suitability of hydrogel-forming polymers for extrusion-based 3d-printing," *J. Mater. Chem. B*, vol. 3, no. 20, pp. 4105–4117, 2015.

[85] R. A. Barry, R. F. Shepherd, J. N. Hanson, R. G. Nuzzo, P. Wiltzius, and J. A. Lewis, "Direct-write assembly of 3d hydrogel scaffolds for guided cell growth," *Adv. Mater.*, vol. 21, no. 23, pp. 2407–2410, 2009.

[86] D. Lee, H. P. Hong, M. J. Lee, C. W. Park, and N. K. Min, "A prototype high sensitivity load cell using single walled carbon nanotube strain gauges," *Sens. Actuators, A*, vol. 180, pp. 120–126, 2012.

[87] D. A. Pardo, G. E. Jabbour, and N. Peyghambarian, "Application of screen printing in the fabrication of organic light-emitting devices," *Adv. Mater.*, vol. 12, no. 17, pp. 1249–1252, 2000.

[88] S. E. Shaheen, R. Radspinner, N. Peyghambarian, and G. E. Jabbour, "Fabrication of bulk heterojunction plastic solar cells by screen printing," *Appl. Phys. Lett.*, vol. 79, no. 18, pp. 2996–2998, 2001.

[89] W. Haynes, *Crc handbook of chemistry and physics, 92nd edition*, ser. CRC Handbook of Chemistry and Physics. Taylor & Francis, 2011.

[90] L. Greenspan *et al.*, "Humidity fixed points of binary saturated aqueous solutions," *J. Res. Nat. Bur. Stand.*, vol. 81, no. 1, pp. 89–96, 1977.

[91] D. D. Braun and M. R. Rosen, *Rheology modifiers handbook: Practical use and applilcation*. Elsevier, 1999, pp. 71–191.

[92] T. Femmer, A. J. Kuehne, and M. Wessling, "Print your own membrane: Direct rapid prototyping of polydimethylsiloxane," *Lab. Chip*, vol. 14, no. 15, pp. 2610–2613, 2014.

[93] J. O. Hardin, T. J. Ober, A. D. Valentine, and J. A. Lewis, "Microfluidic printheads for multimaterial 3d printing of viscoelastic inks," *Adv. Mater.*, vol. 27, no. 21, pp. 3279–3284, 2015.

[94] S. Grilli, S. Coppola, V. Vespini, F. Merola, A. Finizio, and P. Ferraro, "3D lithography by rapid curing of the liquid instabilities at nanoscale," *Proc. Natl. Acad. Sci. U.S.A*, vol. 108, no. 37, pp. 15 106–15 111, 2011.

[95] T. J. Hinton, A. Hudson, K. Pusch, A. Lee, and A. W. Feinberg, "3D printing PDMS elastomer in a hydrophilic support bath via freeform reversible embedding," *ACS Biomater. Sci. Eng.*, vol. 2, no. 10, pp. 1781–1786, 2016.

[96] B. Duan, L. A. Hockaday, K. H. Kang, and J. T. Butcher, "3d bioprinting of heterogeneous aortic valve conduits with alginate/gelatin hydrogels," *J. Biomed. Mater. Res. A*, vol. 101, no. 5, pp. 1255–1264, 2013.

[97] A.-M. Hermansson, E. Eriksson, and E. Jordansson, "Effects of potassium, sodium and calcium on the microstructure and rheological behaviour of kappa-carrageenan gels," *Carbohydr. Polym.*, vol. 16, no. 3, pp. 297–320, 1991.

[98] P. H. von Hippel and K.-Y. Wong, "The effect of ions on the kinetics of formation and the stability of the collagen-fold*," *Biochemistry (Mosc.)*, vol. 1, no. 4, pp. 664–674, 1962.

[99] I. Donati and S. Paoletti, "Material properties of alginates," in *Alginates: Biology and Applications*, B. H. A. Rehm, Ed. Berlin, Heidelberg: Springer Berlin Heidelberg, 2009, pp. 1–53.

[100] A. Mourchid, E. Lécolier, H. V. Damme, and P. Levitz, "On viscoelastic, birefringent, and swelling properties of laponite clay suspensions: revisited phase diagram," *Langmuir*, vol. 14, no. 17, pp. 4718–4723, 1998.

[101] Q.-H. Nguyen and N.-D. Nguyen, *Incompressible non-newtonian fluid flows*, Y. Gan, Ed. InTech, 2012.

[102] G. H. McKinley and M. Renardy, "Wolfgang von ohnesorge," *Phys. Fluids*, vol. 23, no. 12, p. 127 101, 12 2011.

[103] Y. Berdichevsky, J. Khandurina, A. Guttman, and Y.-H. Lo, "UV/ozone modification of poly(dimethylsiloxane) microfluidic channels," *Sens. Actuators, B*, vol. 97, no. 2, pp. 402–408, 2004.

[104] J. Chen, R. Zjang, and W. Wang, "Fabricating microporous PDMS using water-in-PDMS emulsion," *RSC Publishing Blogs Home. Chips and Tips*, 2012.

Appendix B

Supporting Information

The supporting information for both body chapters and additional papers within the appendix

Conducting carbon nanofibre networks: dispersion optimisation, evaporative casting and direct writing

Table B.1: Summary of expense ($E_{\$}$) values obtained from the UV-vis absorbance data shown in Figure B.1 and Figure 3.1. Naming convention for the dispersions is as follwos, (ration VGCNF:GG)-VGCNF concentration, *e.g.*, "10:3-5" indicates a dispersion with VGCNF:GG ratio of 10:3 and VGCNF (C_{VGCNF}) and GG (C_{GG}) concentrations of 5 mg mL^{-1} and 15 mg mL^{-1}, respectively.

Dispersion	C_{VGCNF} (mg mL^{-1})	C_{GG} mg mL^{-1}	$E_{\$}$ (J mg^{-1})
10:2.5-1	1	0.25	36 ± 18
10:5-1	1	0.50	72 ± 18
10:7.5-1	1	0.75	108 ± 36
10:10-1	1	1.0	144 ± 36
10:12.5-1	1	1.25	216 ± 72
10:15-1	1	1.5	288 ± 72
10:3-1	1	0.3	36 ± 18
10:3-2.5	2.5	0.75	29 ± 14
10:3-5	5	1.5	21.6 ± 7.2
10:3-7.5	7.5	2.25	16.8 ± 4.8
10:3-10	10	3.0	14.4 ± 3.6
10:3-12.5	12.5	3.75	17.3 ± 4.3
10:3-15	15	4.5	19.2 ± 4.8
10:3-17.5	17.5	5.25	24.7 ± 4.1
10:3-20	20	6.0	36 ± 2

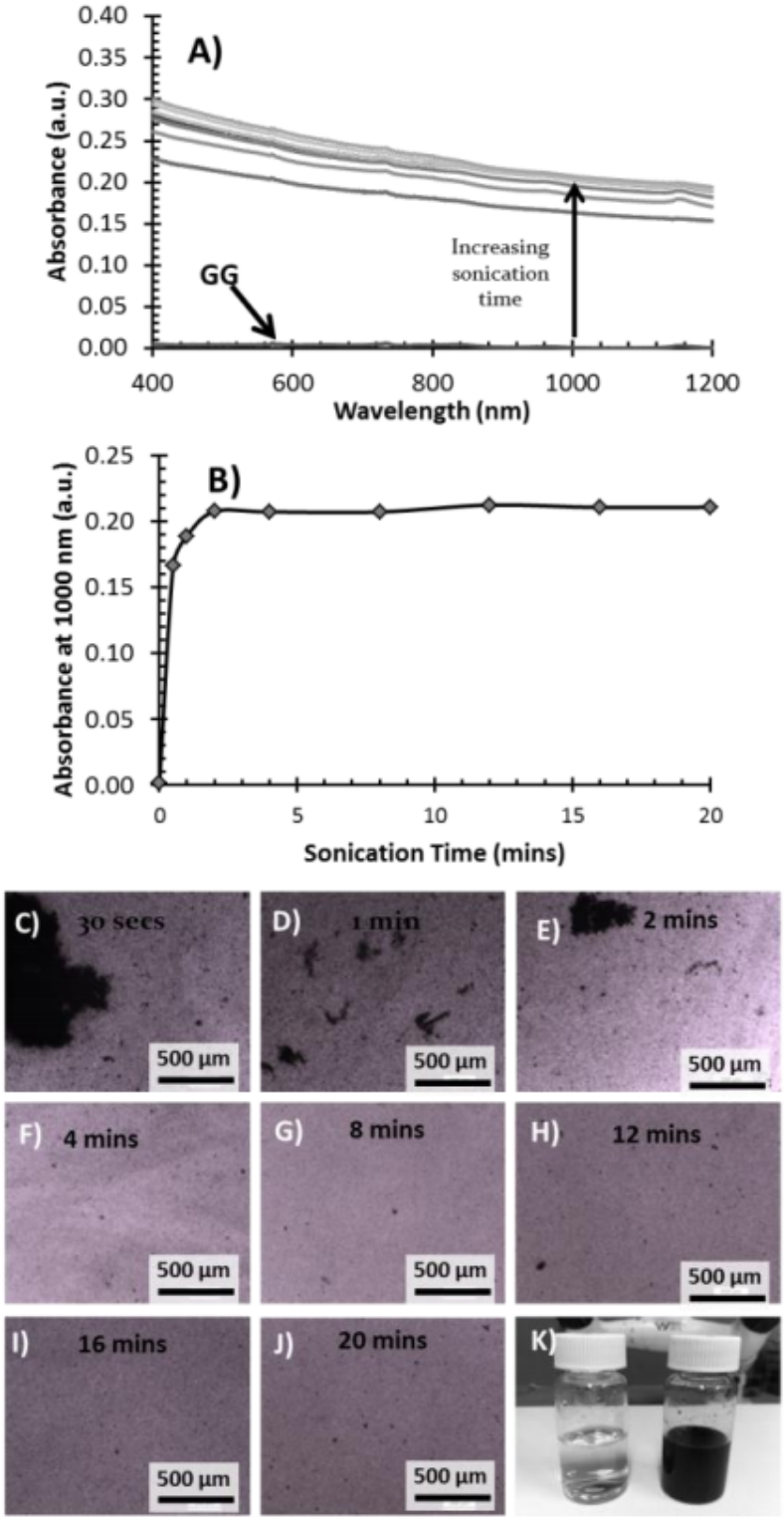

Figure B.1: (A) UV-vis-NIR absorbance versus wavelength of GG-VGCNF dispersions with equal GG and VGCNF concentrations of 1 mg mL^{-1}. Arrow indicates increase in sonication time. (B) UV-vis-NIR absorbance at 1000 nm as a function of sonication time at 6 W. (C-J) Optical microscopy images at different sonication times. (K) Photograph of the GG solution (left) and a completely dispersed GG-VGCNF dispersion (right).

4D Printing of Reversible Shape Morphing Hydrogel Structures

B.1 Dynamic Scanning Calorimetry (DSC)

DSC was performed on p-nIPAAm-based hybrid hydrogels. Hydrogel samples were patted dry first, then placed in standard DSC aluminium pans. The scanning rate was fixed at 5 °C min^{-1} for heat-cool-heat cycles spanning between 5 to 60 °C. The DSC curves are shown in Figure B.2 for all p-nIPAAm-based PEO-PU with the exception of p-nIPAAm-based PEO_{12}-PU, due to its overlap with p-nIPAAm-based PEO_{10}-PU. Note that the heat flow in Figure B.2 is not normalized to the mass of samples, and the curves can only be used to locate the transition temperatures.

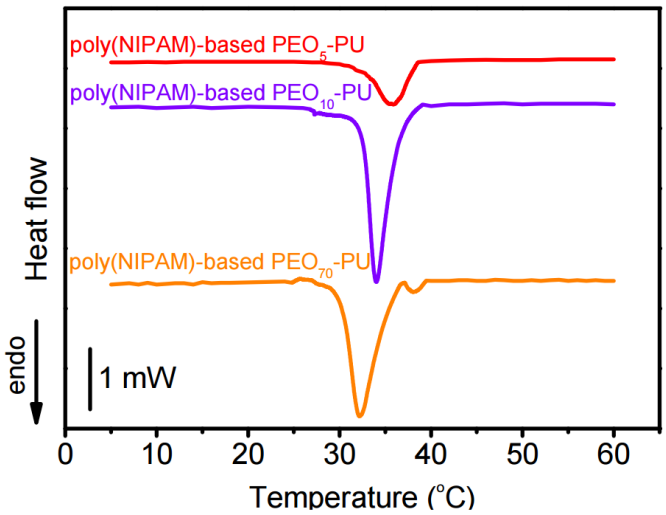

Figure B.2: Differential scanning calorimetry results for p-nIPAAm-based PEO-PU hydrogel with different PEO-PU component as indicated.

B.2 Mechanical Properties Comparison

The mechanical properties of the hybrid hydrogels were characterized in compression and tension to evaluate their performance in possible load-bearing applications. Compression tests were performed on hydrogel disks (10 mm diameter x 10 mm height), immersed in water at the desired temperature. Figure B.3a represents examples of compression stress-strain curves for p-HEMA- and p-nIPAAm-based PEO_5-PU hydrogels. The maximum compression strength sustained by p-HEMA- and p-nIPAAm-based PEO_{10}-PU hydrogels equilibrated at 20 °C was, respectively, 4770 ± 40 and 2930 ± 60 kPa. However, at 60 °C, p-nIPAAm-based PEO_{10}-PU

hydrogels did not demonstrate compressive failure within the maximum force limit of the available load cell. The maximum compression stress recorded for this hydrogel at 60 °C was 5500 kPa which was reached at 74 % of compression strain. For tensile testing, hydrogel strips (5 mm width x 20 mm length, variable thickness according to the degree of swelling) were used under tension. Examples of tensile stress-strain curves for p-HEMA- and p-nIPAAm-based PEO_{10}-PU hydrogels are shown in Figure B.3b. Maximum tensile strength achieved by the p-HEMA-based hydrogels was 642 ± 27 kPa with elongation at break of 119 ± 18 %. The p-nIPAAm-based hydrogels had a tensile strength and elongation at break of, respectively, 397 ± 9 kPa and 68 ± 7 % at 20 °C, and 1150 ± 15 kPa and 275 ± 14 % at 60 °C.

In Figure B.4, tensile mechanical properties of p-HEMA- and p-nIPAAm-based PEO_{10}-PU hydrogels are compared with conventional hydrogels, double networks, homogeneous hydrogels, slip-link hydrogels and nanocomposite hydrogels, in terms of tensile strength vs. elongation at break [1]. At 60 °C, the p-nIPAAm-based PEO-PU hydrogel had strength and elongation at break comparable to other tough hydrogel systems. However, both p-HEMA-based PEO_{10}-PU hydrogel and p-nIPAAm-based PEO_{10}-PU at 20 °C performed similar to less swollen conventional hydrogels.

Overall, the tensile properties of p-HEMA- and p-nIPAAm-based PEO-PU hydrogels are close to tough double network gels. Unlike the double networks, the main source of mechanical enhancement observed in the hybrid hydrogels developed here originates solely from the PEO-PU network. In double network hydrogels, the topological combination of both networks results in an enhanced mechanical perfor-

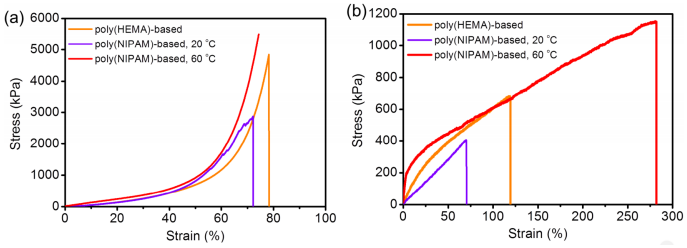

Figure B.3: Representative stress-strain curves of fully swollen p-HEMA-based and p-nIPAAm-based PEO_{10}-PU hydrogels tested in compression (a) and in tension (b). No temperature sensitivity was observed for p-HEMA-based hydrogels, hence mechanical data for 20 °C is shown only for this material.

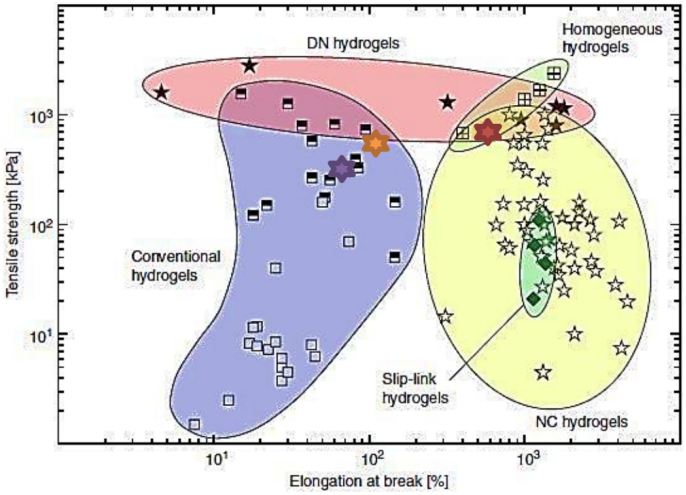

Figure B.4: Mechanical comparison between hydrogels produced here (large stars) with other hydrogel systems. Modified from Naficy *et al.* (2011) with permission from CSIRO Publishing [1]

mance, while each single networks component is inherently weak [2]. In contrast, the tensile strengths and elongations at break of the hybrid hydrogels investigated here were between those of the stronger pure PEO-PU hydrogels and the covalently crosslinked single network hydrogels of p-HEMA or p-nIPAAm. The reduced performance of these hybrid hydrogels compared to the pure PEO-PU component can be explained by the diluting effect of water and p-HEMA or p-nIPAAm network. A network that is diluted beyond its free swelling is always subject to the internal stresses, even when there is no external force applied. At 20 °C, the concentration of the load bearing PEO_5-PU network was ≈ 27 % in p-HEMA-based PEO5-PU and ≈ 10 % in p-nIPAAm-based PEO_{10}-PU hydrogels, while the pure PEO_{10}-PU hydrogel fully swollen in water had a solid concentration of 50 %. The higher strand density of PEO-PU in the latter pure network enhances its capacity to sustain the external stress. The negative effect of dilution on the mechanical performance of these hydrogels was further highlighted when mechanical properties of the p-nIPAAm-based PEO_{10}-PU hydrogel improved by raising temperature to 60 °C, where the concentration of PEO_{10}-PU network increased to 32.9 % upon deswelling of p-nIPAAm network.

The p-HEMA- and p-nIPAAm-based PEO_{10}-PU hydrogels also exhibited a great degree of hysteresis recovery after consecutive loading/unloading cycles in compres-

sion tests with incremental increase of maximum stress applied in each of cycles (Figure B.5). The final stress in the last cycle was kept well below the ultimate compression strength of the hydrogels. Both p-HEMA- and p-nIPAAm-based PEO_{10}-PU hydrogels had small hysteresis at 20 °C, suggesting small amount of energy dissipation in each cycle. The p-nIPAAm-based PEO_{10}-PU hydrogels at 60 °C, on the other hand, showed considerable hysteresis and energy dissipation in each cycle. The overall behaviour of hybrid hydrogels resembled that of thermoplastic polyurethanes with a softening feature after each loading-unloading cycle [3]. After each loading-unloading cycle, the hybrid hydrogel was slightly more compliant, however, unlike covalently crosslinked networks, the reloading curve in the subsequent cycle is always above the unloading curve in the previous cycle.

The stress relaxation of hybrid hydrogels under constant strain was also found to be very similar to that of PEO-PU component, which again is an indicative of the mechanical dominance of PEO-PU network in the hybrid hydrogels Figure B.6. Stress relaxation tests were performed on hybrid hydrogels under compression. Hydrogel samples were cut into 10 mm x 10 mm cylinders, place in the mechanical tester, and then compressed at 2 mm min^{-1} until a stress of 1000 kPa was reached. Samples remained under compression while stress was recorded against time for 120 sec, after which stress was released by raising the crosshead. This process was repeated three consecutive times with no considerable difference was observed between cycles. Figure B.6 shows examples of stress relaxation curves for p-HEMA-based and p-nIPAAm-based PEO_{10}-PU hydrogels (a,b). Figure B.6 also presents a comparison between hybrid hydrogels and their constituting PEO-PU component (c).

B.3 Modulus vs. Linear Expansion Ratios

Moduli of fully swollen hybrid hydrogels were measured in tensile and compression tests at 20 °C and 60 °C. Figure B.5 shows the Young's moduli of all hybrid hydrogels against the inverse of linear expansion ratio of hydrogels. The expansion ratio (λ) of hydrogels was calculated as the cubic root of swelling ratio of hydrogels assuming

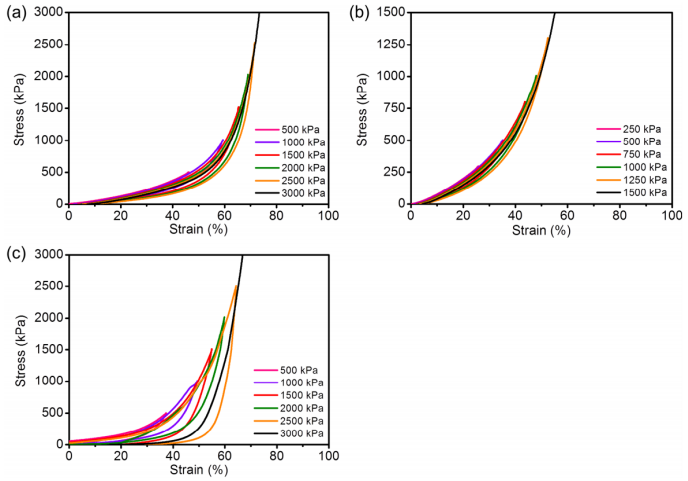

Figure B.5: Compression loading-unloading cycles for (a) p-HEMA-based PEO_{10}-PU, (b) p-nIPAAm-based PEO_{10}-PU at 20 °C and (c) p-nIPAAm-based PEO_{10}-PU at 60 °C. The ultimate loads applied in each cycle on p-nIPAAm-based PEO_{10}-PU at 20 °C was half the other two systems to avoid reaching mechanical failure before the end of the fifth cycle.

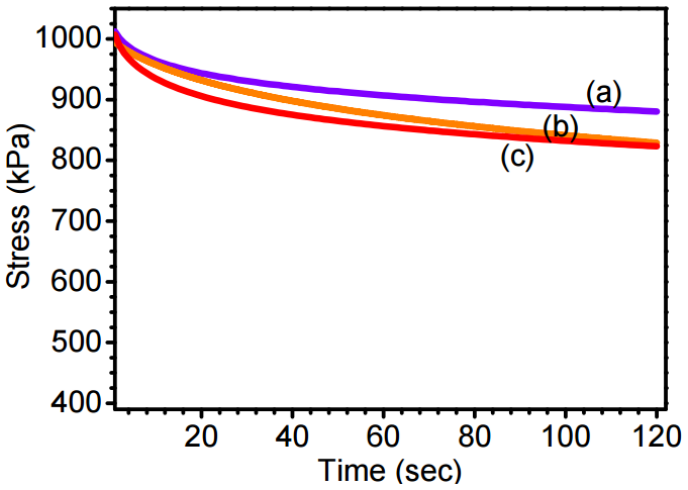

Figure B.6: Stress relaxation of p-HEMA-based PEO_{10}-PU (a), p-nIPAAm-based PEO5-PU (b) and PEO_{10}-PU (c). All samples are fully swollen at room temperature

all hydrogels swell/deswell isotropically: $\lambda = \sqrt[3]{Q}$. According to rubber elasticity theory, there is a linear relationship between the modulus of a swollen network and the inverse of its linear expansion ratio: $E \approx E_0\lambda^{-1}$, where E_0 is the modulus of the dry network. Moreover, both swelling ratio and dry network modulus are dictated by the network structure. In the cases where the main controlling network parameter is the degree of crosslinking can be related to the equilibrium swelling ratio by: $E_0 \approx Q^{-\vartheta}$ where ϑ is determined based on the nature of interaction between polymer chains and solvent molecules. For θ-solvents $\vartheta = 8/3$, for athermal solvents $\vartheta = 1.75$, and for good solvents $\vartheta = 1.75$ or $8/3$ depending on the extend of swelling. Considering that $Q = \lambda^3$ this results in $\upsilon = 3\vartheta$, where $E \approx \lambda^{-\epsilon}$ (see main text). The resulting relationship between modulus of a swollen network and its linear extension ratio due to equilibrium swelling is: $E \approx \lambda^{-\alpha}$ with $\alpha = \upsilon + 1$. The measured modulus for all hydrogels made in this study is plotted against λ in Figure B.7. The solid line in Figure B.5 represents $\alpha = 6.9$ which is close to the expected value for networks swollen in good solvents ($\alpha = 6.25$).

B.4 Hybrid Hydrogel Structures Preparation

Hydrogel hinges were prepared in a multi step process as shown in Figure B.8 with details presented in the Experimental Section. Briefly, the first layer (hinge base)

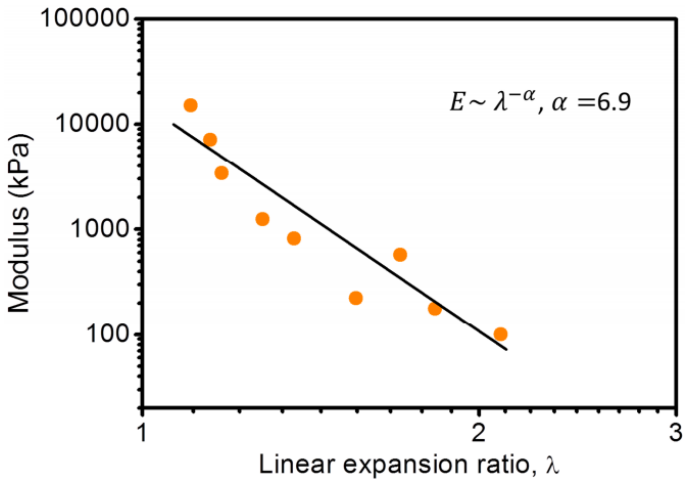

Figure B.7: Young's modulus as a function of linear expansion ratio (λ)

was polymerized by placing ink 'A' between two glass slides separated with a silicon spacer (0.8 mm). After UV irradiation for 30 min, glass slides were opened and a second silicon spacer was placed on the top of the first spacer. Another spacer with the same thickness was also placed on the already UV cured hydrogel 'A'. For the second time, ink 'A' was injected to fill up the remaining space left between glass slide at the top and hydrogel 'A' at the bottom (step (2)). In step (3), the third spacer was removed and the gap was filled with ink 'B', followed by UV irradiation. The width of the third spacer determined the length of the active part formed on top of the hinge.

A similar method was used to create more complex structures, such as an unfolded box, where the printed object was capable of transforming from its flat state to a closed box upon hydration and then open up again in response to temperature (Figure B.9). For this example, the outer silicon spacer was cut into the outline of the unfolded box, and the same sequence of polymerization steps as described for a single hinge were repeated here.

B.5 3D Printer

A picture of 3D printer and the UV curing system is shown in Figure B.10. Video S1 (found in supporting information online) shows the printer in action.

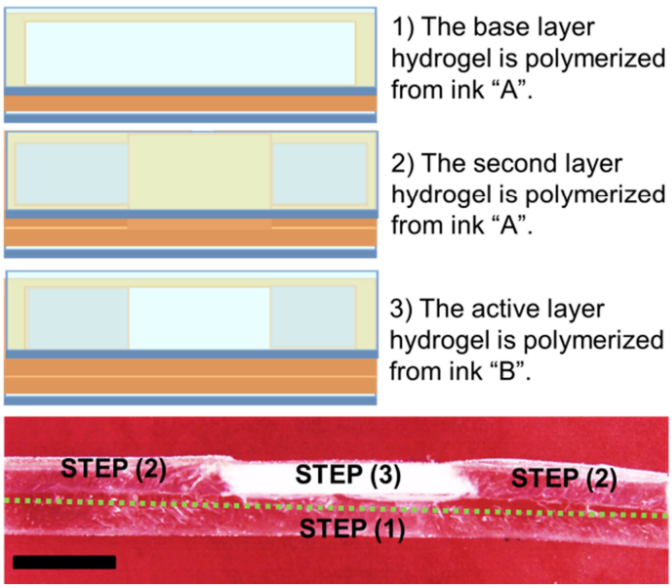

Figure B.8: Multi-step preparation process for hydrogel hinges: steps (1) and (2) are to form the base and the body of the hinge, while in step (3) the active material is formed on the top layer. The dotted line highlights where the boundary of hydrogel 'A' formed in step (1).

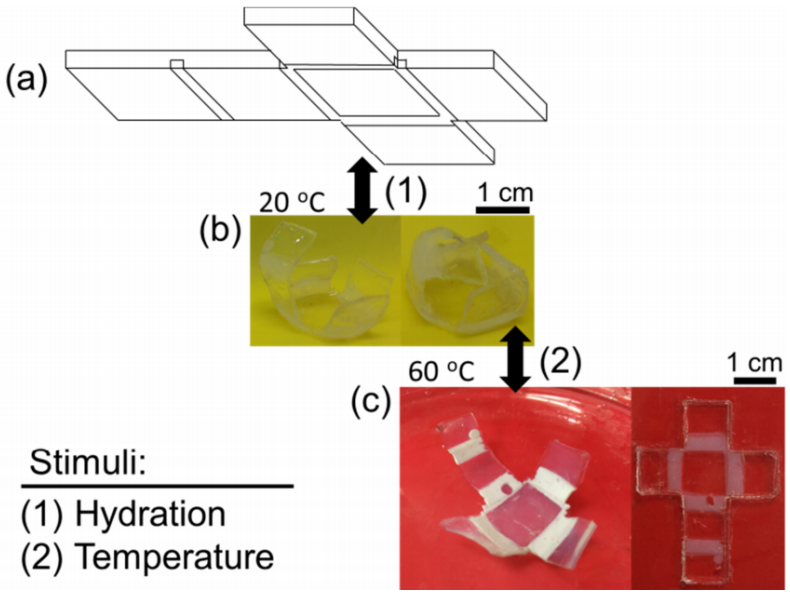

Figure B.9: An example of a hybrid hydrogel box, made by a multi-step process similar to the one presented in Figure B.8. An unfolded box was molded in three steps (a). The flat object was responsive to hydration and began folding into a closed box (b). By elevating the temperature from 20 °C to 60 °C, the temperature sensitive p-nIPAAm-based hydrogel deswelled forcing the box to fully open up (c).

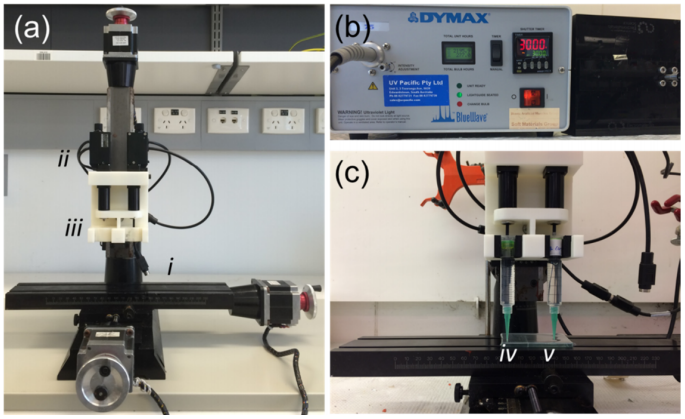

Figure B.10: Photographs of the extrusion printer (a), the UV curing system (b) and the syringes loaded with inks (c). Panel (a) shows the CNC stage (i), the linear actuators (ii) and the syringe holder (iii). Panel (c) shows syringes loaded with a non-active ink (HEMA-based) (iv) and an active ink (NIPAM-based) (v)

3D Printing of Transparent and Conductive Heterogeneous Hydrogel-Elastomer Systems

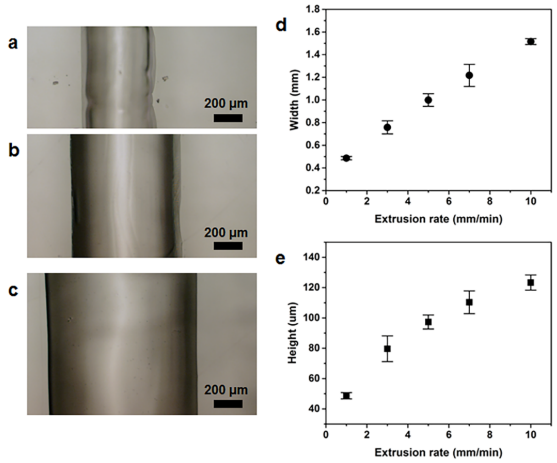

Figure B.11: Variations in hydrogel geometry by only nominal extrusion rate variation, keeping stage velocity (450 mm min^{-1}), extrusion height (300 μm) and extrusion tip diameter (337 μm) constant. We illustrate gel geometry with optical micrographs of the printed hydrogel on top of PDMS substrate at (a) 1, (b) 3, and (c) 5 mm min^{-1} extrusion rates. (d) shows a plot of the relationship between extrusion rate and final line width, with what appears to be a linear correlation. (e) A similar plot for final gel height versus extrusion rate.

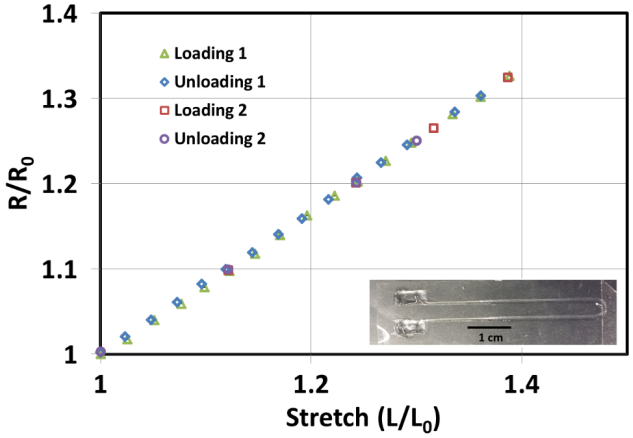

Figure B.12: Resistance change of a stretched strain gauge sample, demonstrating a linearity of the resistance change response for this design up to 40 % strain.

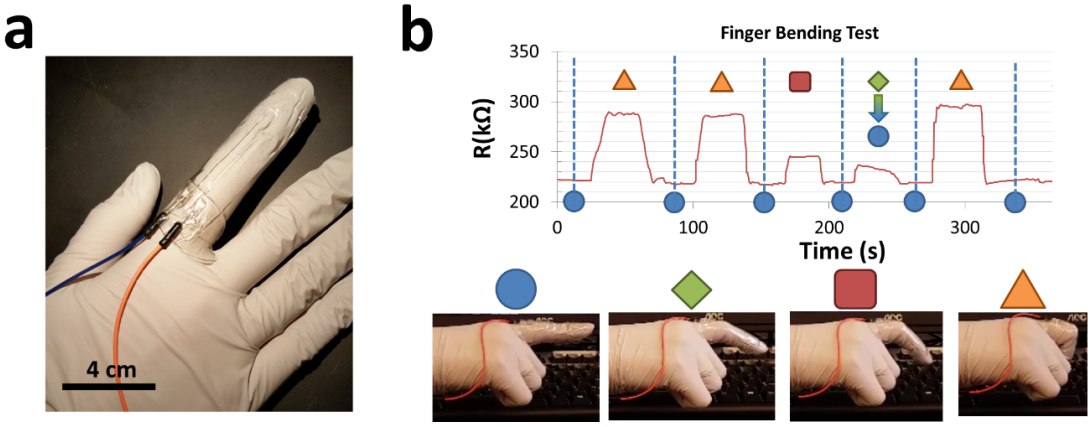

Figure B.13: A single strain gauge is mounted onto the index finger and held in various positions while the resistance is recorded. (a) Illustrates the mounting of the strain gauge using VHB tape and leads connecting the gauge. (b) Illustrates the various positions alongside the time-trace of the gauge's resistance. The mildly bent position (green diamond) is gradually straightened to the default position, whereas others were more rapidly transitioned from straight to bent positions.

Bibliography

[1] S. Naficy, H. R. Brown, J. M. Razal, G. M. Spinks, and P. G. Whitten, "Progress toward robust polymer hydrogels," *Aust. J. Chem.*, vol. 64, no. 8, pp. 1007–1025, 2011.

[2] J. P. Gong, "Why are double network hydrogels so tough?" *Soft Matter*, vol. 6, no. 12, pp. 2583–2590, 12 2010.

[3] H. Qi and M. Boyce, "Stress–strain behavior of thermoplastic polyurethanes," *Mech. Mater.*, vol. 37, no. 8, pp. 817–839, 2005.